CHARACTERISATION OF TORREFIED CARBON FOR CARBON DIOXIDE CAPTURE AND COFIRING APPLICATION

ODIRA VANATIUS ATUEYI

A thesis submitted in partial Fulfilment of the Requirements for the

Degree of

Doctor of Philosophy

University of Strathclyde

Department of Chemical and Process Engineering

Glasgow, United Kingdom

November 2020

DECLARATION OF AUTHENTICITY AND AUTHOR'S RIGHTS

‘This thesis is the result of the author’s original research. It has been composed by the author and has not been previously submitted for examination, which has led to the award of a degree.’

Signed:…O.V ATUEYI…… Date:……20/11/2020

ACKNOWLEDGEMENT

This thesis is a product of my four years of academic commitment. Getting over these years, combined with my family life, I consider this period the most challenging time in my life. Having ended on a good note, I would like to express my profound appreciation to my PhD supervisors – Professor Ashleigh Jane Fletcher and Dr Jun Li, for guiding me through the path of widening my knowledge in the field of adsorption science and bioenergy applications in the industry. Their guidance throughout my PhD program was supportive, without which my laboratory works, coupled with the disruptions imposed by the COVID-19 global pandemic crisis, would have added more frustration to my research progress.

My progression from the Master's degree program to a PhD research, both in Chemical and Process Engineering at the University of Strathclyde, was not without the supports from the administrative staff of the Department of Chemical and Process Engineering. The laboratory technicians were very supportive; Mr Ian Airdrie was always helping out during my inter-departmental laboratory project engagements, and I appreciate him for this. My special thanks go to the following persons; (1) Nze Akachukwu Sullivan Nwankpo (2) Mr Paulinus Akajemeli and Mrs Nnenna Akajemeli, (3) Mr Japheth Chuks Ngobili, (4) Mr Peter Mozie, and (5) Prophet Chika Ezeh, for their unconditional support, trust and prayers through the entire period of my PhD program.

Also, I would not seize to recognise the words of encouragement from my beloved mother, siblings, in-laws, uncles and family friends, who at every point, encouraged me that all will end in praises despite my study challenges. The special prayers from my wife (Joy) and lovely kids (Zikorachim and Manuel) were like an ice breaker at every struggling moment. For the financial support, I remain indebted to the Federal Government of Nigeria for the dual scholarship awards for my Master and PhD studies through her Petroleum Technology Development Fund. As a result, I would always make myself available any time in the future, where I am called upon to serve my country Nigeria in any capacity. Above all, I give all the glory to the alpha and omega "God Almighty" for the life and provisions throughout my studies.

ABSTRACT

Increased carbon dioxide (CO_2) emissions across the globe, and the resulting atmospheric levels, have become the subject of many scientific studies in recent times. Managing and reducing CO_2 emissions has remained a challenge for scientists and researchers in carbon capture science, despite technology advancements. Although recent technologies deployed suggest an improvement from the classical approaches, there is a need to explore other alternatives to optimise process performance and to reduce the cost of carbon capture and sequestration processes.

In this study, torrefaction technology was employed to develop 'torrefied carbon' using renewable carbonaceous materials, such as Iroko (IR - hardwood) and Scottish Pine (SP - softwood), for CO_2 capture from the combustion stacks of coal-powered plants. The study was divided into two parts: (a) developing the torrefied carbon using selected torrefaction conditions, at temperatures of (290 ^oC, 320 ^oC, 350 ^oC and 380 ^oC), a residence time of 60 min and heating rate (10 $^oC\ min^{-1}$), under CO_2 atmosphere. The second is testing the torrefied carbons for CO_2 adsorption potential and cofiring applications. The physicochemical characteristics of the torrefied carbons, such as hydrophobicity, calorific values and ultimate analysis, as well as the torrefaction performance indicators, such as energy gain, energy consumption, mass density and mass yield, amongst others, were assessed, allowing the fuel quality and potential use of the torrefied carbon once entirely spent for CO_2 capture in same power plant to be evaluated.

Given the results obtained, the torrefaction performance indicators showed there is energy gain for the selected torrefaction conditions. The highest energy gain values of 104 and 102 were found for the SP and IR, respectively, at the torrefaction condition of 320 °C, at a residence time of 60 min. The calorific values of the torrefied carbons developed at 320 °C and 350 °C, where - IR (26.49 MJ kg^{-1} and 26.75 MJ kg^{-1}) and SP (26.13 MJ kg^{-1} and 29.12 MJ kg^{-1}), respectively, which were higher than those of the low-ranked coal (23.20 MJ kg^{-1}) investigated. For the adsorption studies, the torrefied carbons developed at 350 °C showed the highest CO_2 adsorption capacity for both IR and SP carbons. The thermodynamic study of the CO_2 adsorption using the Langmuir and isosteric heat of adsorption suggests the existence

of heterogeneous surface sites' on the torrefied carbon surfaces. The CO_2 adsorption shows low heat of adsorption, given the values of the isosteric heat, for IR320 (-45 KJ mol^{-1}), IR350 (-58 KJ mol^{-1}), SP320 (-28 KJ mol^{-1}) and SP350 (-41 KJ mol^{-1}), an indication that the CO_2 adsorption process is governed by physisorption.

The kinetics of the CO_2 adsorption of the torrefied carbons followed the Double Exponential Model, described by two distinct rate-determining steps. The rate of CO_2 adsorption on the torrefied carbons appeared fast, given the equilibration time of an average of < 8 min for the IR and 11 min for the SP carbon, suggesting that the short time of equilibrium based on the Pressure Swing Adsorption process indicates a good potential from the materials on a kinetic basis. Within the study context, it was determined that the torrefied carbons could be employed for cofiring in coal-powered plants following a CO_2 capture process. Although the structural features exhibited by the torrefied carbons were not fully explored in this work, due to the research limitations, the study opens up an opportunity into the potentials of torrefied carbon utilisation as a cost-intensive alternative in CCS applications.

DEDICATION

This work is dedicated to the memory of those who lost their lives during the 2019/2020 COVID-19 global pandemic crisis.

TABLE OF CONTENTS

LIST OF FIGURES

LIST OF TABLES

Chapter 1 : INTRODUCTION

1.0 Overview

As the global energy demand continues to increase, concerns around climate changes have motivated many researchers to seek new ways of developing energy-efficient processes with minimal Carbon dioxide (CO_2) impact on the environment. With fossil fuels dominating the primary energy source, accounting for about 81% of the global energy production mix, it is accompanied by a release of ~ 30 x 10^{12} kg of CO_2 annually [1]. According to a study by Le Quéré *et al.* in 2017, China, the United States, India and the 28 EU countries alone account for ~ 59% of the global CO_2 emissions, with China commanding 27% of this share [2]. As a result, it is evident that there is an urgent need to shift global energy production towards low carbon alternatives. Although many of the World's energy governing bodies have made collaborative efforts to encourage the use of clean process technologies, future forecasts still favour the use of fossil fuels in the short term. The reliance on the use of fossil fuels-based technologies has been attributed to the favourable levelised cost of electricity, representing the average price an electricity-generating asset must realise when deployed in the market to break even over its lifetime [3].

A thorough scientific assessment of future climate conditions has also shown that climate change due to greenhouse gas (GHG) emissions is real and have attributed this to human activities, which could pose significant dangers if unchecked. Given the current trends, and to contain the increasing GHG levels, while encouraging the use of fossil fuels, a promising alternative is to capture CO_2 emissions from large stationary sources for subsequent geological storage. Although a number of natural sinking measures for CO_2 trappings, such as forestation and ocean utilisation, have helped reduce CO_2 levels in the atmosphere, capturing CO_2 from industrial sources has become the leading option due to a need to prevent significant CO_2 emissions large point sources.

High CO_2 emission in industries has been contained by a process known as Carbon Capture and Storage (CCS). This process entails using sorbent materials with an affinity for CO_2 and with the tendencies to capture CO_2 gas from emission points when loaded in the CCS unit of

an operational coal-fired power plant. More so, for enhanced CO_2 capture performance, the sorbent material must meet certain conditions of the flue gas emitted from the stacks of coal combustion systems. Also, given that coal is an impure hydrocarbon composed of varying heteroatoms and inorganic components depending on the source, its combustion will emit different fractions of gaseous and solid products. The CCS unit's location for flue gas pre-treatment processes will also affect the extent of CO_2 separation [4]. An example of flue gas composition emitted from a coal-fired power plant in operation is shown in Table 1-1.

Table 1-1- An example of flue gas composition from a coal-powered plant and the plant's operating condition [4]

Component	**Flue gas (pre-treatment)**
N_2	75-80%
CO_2	12-15%
SO_2	1800 ppm
NO_x	500 ppm
H_2O	5-7%
O_2	3-4%
CO	< 100 ppm
Hg/As	ppb
Particulates	10-20 mg Nm^{-3}
Pressure (mbar)	0.1
CO_2 partial pressure (mbar)	0.012-0.015

Based on flue gas composition, sorbent materials are required to have the potential to desorb captured CO_2 at relatively low regeneration energy. They should maintain high CO_2/N_2 selectivity, with good CO_2 adsorption capacity, at conditions such as 0.15 bar and 40 °C, considered relevant for post-combustion CO_2 capture [5]. Presently, the mechanism of CO_2 capturing under the flue gas operating conditions remain a challenge in practice, as there is yet to be developed sorbent material that could perform optimally under these conditions.

Although a wide range of sorbent materials have been developed and tested for application in different post-combustion CO_2 capture schemes, the achievement of optimum performance still poses a challenge for researchers in the field of carbon capture science. Therefore, this research aims to characterise a class of renewable sorbent material developed for CO_2 capture applications in a CCS unit integrated into a coal-powered plant. To appreciate where this work will have an impact, it is necessary to understand the science of CO_2 and how this fits into the global and industrial context.

1.1 The science of CO_2, greenhouse effect and global warming

Carbon dioxide, identified in 1750 by Joseph Black, a Scottish scientist, was characterised as an odourless, colourless, slightly acidic and non-flammable gas [6]. As a gas, the triple-point behaviour suggests that beyond the critical points of 72.8 atm (73.76 bar) and 31.1 °C (304.25 K), CO_2 neither exists as a pure liquid or gas (i.e., it becomes indistinguishable), as shown in the phase diagram, Figure 1-1.

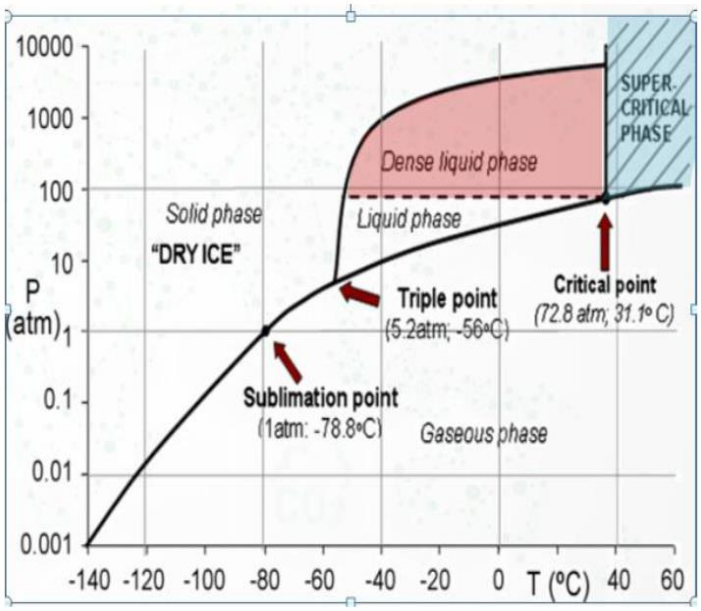

Figure 1-1- Phase diagram of pure CO_2 [7]

By contrast, in the solid-state, CO_2 is referred to as ‘dry ice’, with its Lewis structure showing how two oxygen atoms bonded to one carbon atom at an angle of 180 °[6]. Also, the negative charge of the oxygen atoms from the CO_2 molecules is evenly distributed around the ground state's carbon atom. With the electronegativity value of oxygen being 3.5 and that of carbon 2.5, this results in a net electronegativity value of 1 [8]. Therefore, by summing the bonds polarity vectors, with each pointing in the direction of the two oxygen atoms, this cancels out, resulting in a zero dipole moment. It is due to this reason that CO_2 is considered a non-polar molecule.

Furthermore, the way in which electrons distribute symmetrically across the bonded atoms of the CO_2 molecule causes it to interact with infrared radiation [10]. CO_2 has a strong radiative forcing (RF) (i.e., ability to trap emitted radiation), which accounts for its capacity to influence the atmospheric energy balance. The RF measures the difference between incoming solar radiation and outgoing infrared radiation as a function of the GHG concentration, its warming capacity, residence time and spatial distribution [9]. Any variation in these factors beyond acceptable limits can result in the cooling or warming of the atmospheric energy [10]. The warming or cooling capacity shows the potency of an emitted gas to act as a GHG. Aside from CO_2, other GHGs such as methane, ozone, nitrogen oxides, and several halogenated compounds also contribute to the trapping of converted heat introduced by sunlight, due to their warming effect and longevity in the atmosphere, and helps keep the Earth warm, via a phenomenon known as the ‘greenhouse effect’ [6]. The greenhouse effect is, by means, a natural way in which the Earth regulates its temperature, without which it would be covered in a pool of ice. However, due to rapid global industrialisation, albeit other artificial addition of GHGs into the environment, researchers have reported that CO_2 contributes ~ 60% to global warming [6].

Svante Arrhenius, a Swedish scientist, was the first to suggest a link between CO_2 emissions and global warming, as evident in his paper titled ‘On the influence of carbonic acid in the air upon the temperature of the ground’ [11]. At the time, he opined that the Earth’s average surface temperature was around 15 °C due to infrared absorption of water vapour and CO_2 present in the atmosphere, which could potentially increase proportionally with CO_2 emission

levels [11]. Although his findings were not convincing at the time, due to a belief that other natural phenomena, such as solar activity and ocean circulation, could cancel out CO_2 pollution, in the late 1940s, using infrared spectroscopy, CO_2 contributions to global warming were generally accepted [11].

1.2 CO_2: emission sources and the global drive towards meeting emission reduction targets

Although notable emission sources of CO_2 have mainly been associated with energy generation activities in the power sector, those from other anthropogenic sources, such as organic waste disposal, deforestation and land-use changes for agricultural purposes, also contribute significantly [12]. As of 2013, two sectors, namely-electricity/heating and transportation, have accounted for about two-thirds of the total global CO_2 emissions, as shown in Figure 1-2.

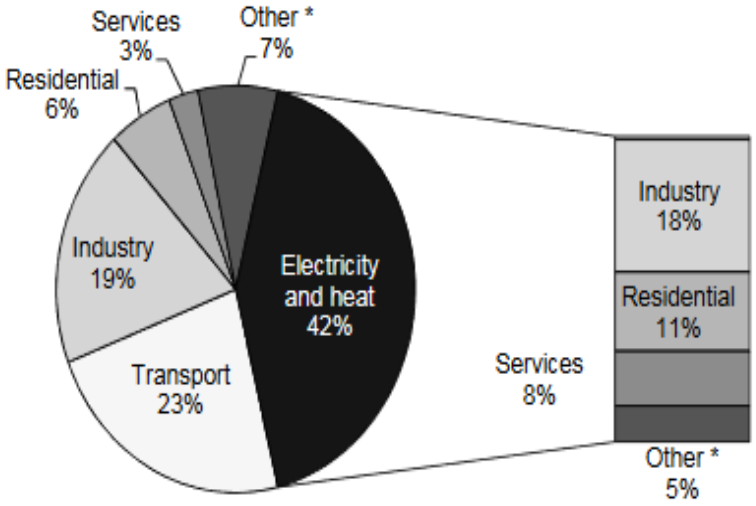

Figure 1-2-Global CO_2 emissions according to sector [13]

According to the International Energy Agency (IEA) report of 2019, energy demands across the globe increased by 2.3% from the previous year, showing as the fastest pace ever recorded in past decades. The increase has been associated with the robust growth in the global economy and the stronger heating and cooling demands from a number of countries

[14]. Consequently, CO_2 emissions increased by 1.7% to 33.1 gigatonnes (Gt), with coal utilisation for power generation surpassing 10 Gt, accounting for 30% of all energy-related CO_2 emissions [14]. Fossil fuel utilisation for energy production has dominated the power generation mix over the past decades, given their proven reliability, flexibility and having been considered as an economical means of energy production. Although fossil fuel usage may drop slightly in coming decades, given recent developments of other cost-effective energy technologies, there is a need to decarbonise the existing energy mix, by promoting less carbon-intensive alternative energies.

However, given the current standpoint, the implementation of existing alternatives may become a daunting challenge. The IEA has warned that, by 2050, it would be beneficial to reduce CO_2 emission from all energy-related processes to half their 2007 figures (29 Gt CO_2 yr^{-1}) [15]. Also, following the Organisation for Economic Co-operation and Development (OECD) baseline, the forecasted GHGs concentration worldwide is expected to reach approximately 685 ppm by mid-century and more than 1000 ppm by 2100. Additionally, the CO_2 level has been projected around 530 ppm in 2050 and 780 ppm in 2100 [16]. More so, with the IEA's '450 ppm' proposal, being the maximum allowable CO_2 emissions necessary to meet the Conference of Parties (COP)-21 and the Paris Agreement objectives, a recent report by Muna Loa laboratory, shown in Figure 1-3, suggests that the average ambient concentration of CO_2 as of October 2020 is ~ 412.04 ppm [17].

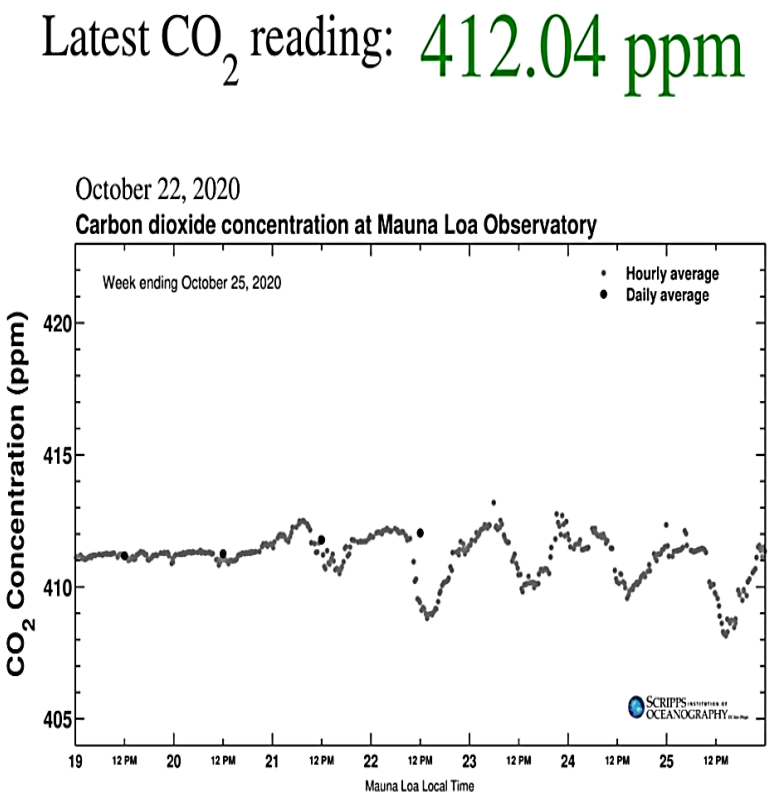

Figure 1-3-Atmospheric CO_2 concentration as of October 2020, adapted from Scripps Institution of Oceanography, UC San Diego [17]

The 412.04 ppm level shows that CO_2 concentration in the atmosphere is increasing and may reach 570 ppm earlier than predicted by the Intergovernmental Panel on Climate Change (IPCC) [18]. The increasing trend of CO_2 into the atmosphere had also been investigated in a study by Le Quéré *et al.,* where a comparative analysis of yearly average anthropogenic CO_2 emission and other natural sinking measures showed an apparent discrepancy [2]. However, based on the discrepancies in CO_2 imbalance, several changes have been witnessed across the globe, with recent happenings including; a rise in sea levels, propagating flooding [18]; poor cropping due to the Earth's rising temperatures, and reported extinction of several animal species occasioned by extreme weather conditions, amongst other devastating effects imposed by these conditions [12].

Due to the impacts of CO_2 emissions on human and natural systems, the United Nations (UN) and the World Meteorological Organisation founded the IPCC in 1988 [19]. The UN, through her United Nation Framework Convention on Climate Change (UNFCCC), aligned with the

visions of the Kyoto Protocol Accord, where 37 nations signed into the first truly global emission reduction commitment to reduce their country's 1990 CO_2 emission levels by 5%, from 2008 to 2012 [20]. Following this, in 2015, at the UN climate change conference held in Paris, 197 parties further committed to a new 'Paris Agreement', with a common purpose to reduce the global temperature to well below 2 °C, and to drive commitments that would limit future rises [19]. In this agreement, individualised targets were set out for the participating countries based on their economic strengths. Despite the agreement put in place, only 30 metric tonnes of annual CO_2 capture has been reported from all industrial activities as of 2017 [21]. As of 2017, the commitments from the 197 countries to contain their CO_2 emissions have been weakened by the United States decision to withdraw from the international climate change pact, despite being the world's second-largest CO_2 emitter [22].

Based on the preceding information, it is now evident that there is a need to review CO_2 capture technologies currently being employed across the industry. Researchers have already suggested three effective means: making energy production processes more efficient, promoting the use of renewables, and adopting the CCS application [23] [24]. Furthermore, based on a combined report of a study by the IEA and the OECD, regarding scenario 2050 predictions, energy efficiency improvements and CCS implementation have been highly recommended [25]. However, with the high cost of CCS implementation, contrasted with associated economic benefits, reducing the cost of CCS has become imperative and is the focus of this research.

1.3 CO_2 capture technologies and challenges pertinent to existing capture technologies

In industry, capturing CO_2 emissions from different industrial sources can be undertaken in a range of capture contexts, thereby preventing CO_2 entry into the atmosphere. The choice of capture alternative depends on the nature of the industrial operation, but generally, the activity accounts for ~ 70-80% of the entire capture and sequestration costs [26]. Nowadays, three capture routes commonly employed in the industry are - Pre-combustion, Oxyfuel combustion and, Post-combustion capture, as described in Figure 1-4.

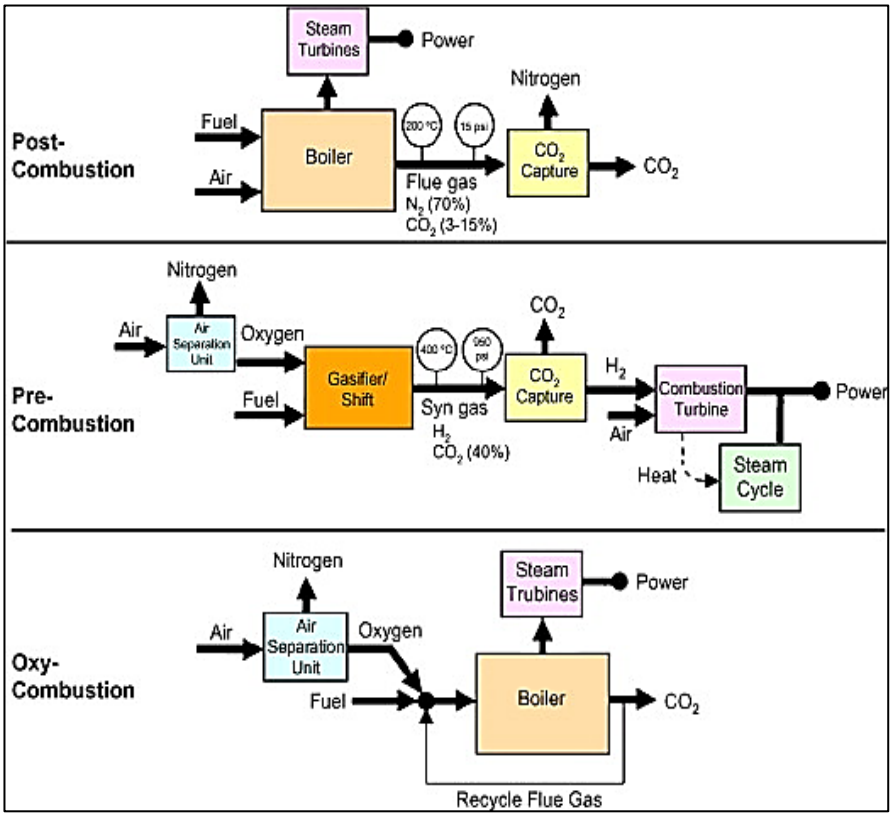

Figure 1-4-An overview of types of CO_2 capture processes [24]

Although these capture routes have been employed in various applications, they are associated with individual advantages and disadvantages, which have become the focus of many research studies. Following CO_2 capture, subsequent stages entail the transportation and compression of captured CO_2 via pipelines to safe underground storage sites where they may find usefulness for other industrial purposes.

1.3.1 Pre-combustion carbon capture

Pre-combustion capture is characterised by a relatively high-pressure process, during which CO_2 capture begins with the conversion of primary fuels by gasification into a synthetic gas-a mixture of carbon monoxide (CO) and hydrogen (H_2). The primary fuel conversion process aims to generate H_2 but is accompanied by ~ 10 tons of CO_2 per ton of H_2 being produced [27]. The initial products (CO and H_2) undergo a water-gas-shift reaction with steam, from where CO_2 is produced and captured, leaving behind a rich source of H_2.

Pre-combustion capture processes can be scaled to meet intended process objectives. Trending research efforts on the pre-combustion capture process now focus on improving the catalyst efficiency of the water-gas shift reaction for more H_2 and CO_2 production, and also reducing the energy penalty associated with the process. Also, given that CO_2 separation occurs under high-pressure, pre-combustion capture processes incur reduced energy penalties (~ 20%), compared with those of post-combustion capture (~ 30%), even at 90% CO_2 recovery. This has been attributed to the low volume flow rates of the CO_2 emission flux pressure from the combustion systems [28]. For pre-combustion capture, the increased concentration of CO_2 in the flue gas stream contributes to lowering the energy penalty of the process by ~10 -16%, almost 50% that of post-combustion capture processes [28].

1.3.2 Oxy-fuel combustion capture technology

In oxy-fuel combustion capture, the process employs pure oxygen (~ > 95%) in place of air for primary fuel combustion. Pure oxygen utilisation facilitates complete combustion of the fuel, producing H_2O and CO_2, with high CO_2 concentration generated in the product stream, with zero nitrogen. With high CO_2 level present in the product stream, its separation becomes much easier, as water vapour, produced alongside, would be removed by cooling [28]. The introduction of oxygen in this process may demand a stand-alone air separation process unit for O_2 production, which would make the capture process more costly.

Oxy-fuel combustion capture systems can capture nearly 100% of CO_2 in the product stream due to the absence of nitrogen in the combustion product stream. An integrated cooling system employed for water vapour removal from the product stream accounts for the separation process's lower energy requirement. An innovation, known as chemical looping oxy-combustion technology, has recently been considered a competitive means of lowering the energy penalty associated with oxyfuel CO_2 capture processes [26]. The chemical looping employs metal oxide particles for selective oxygen transport from the combustion air reactor to a fuel reactor, where CO_2 is separated.

1.3.3 Post-combustion capture technology (PCCC)

Post-combustion capture describes CO_2 capture from a combustion flux, a process often referred to as an 'end of pipe' solution for CO_2 separation. It requires the integration of a Carbon Capture Unit (CCU), where CO_2 is captured at up to 80-90% recovery using wet or dry sorbents [27]. The wet process is mainly employed for the PCCC, given the propensity to accommodate large flue gas emission fluxes, with variable CO_2 gas density, where the CO_2 fraction in the flue gas is up to 10-15% [26]. A typical benefit of PCCC is that most by-products from combustion, such as NO_x, SO_x, and water vapour, are removed from the flux before CO_2 capture.

Although the cost of PCCC operation may seem high, due to the incorporation of certain pre-treatment processes, like desulphurisation, necessary before the CO_2 separation, the energy penalty associated with such routes has been reported to be ~ 25-35% of the entire CO_2 separation cost [27]. With such incurred energy penalty, the effect would be an increase in the cost of electricity generation, due to loss of net power plant efficiency by ~30%, with a further reduction of the power plant's efficiency by ~11% [27]. As PCCC allows for retrofitting to both new and existing power plants without affecting the plants' operations, another significant challenge for sorbents is the inability to process high emission flux, resulting in low separation efficiency. Therefore increased purity of the flue gas is necessary to lengthen sorbent usage; in most cases, SO_2 and NO_2 values < 10 ppmv are recommended [27].

1.4 CO_2 capture applications based on post-combustion capture technology

As the PCCC method is the focus of this research, a review of the CO_2 capture technology is necessary to understand the advantages and disadvantages of their application in the industry. PCCC is an easily applied technology for existing CO_2 emission sources and may allow for the use of wet and dry sorbents for CO_2 separation. There are five main techniques for CO_2 separation: chemical and physical absorption/adsorption, membrane separation, and cryogenic separation. These techniques are still in use in industry, as shown in Figure 1-5 and are discussed in the next section.

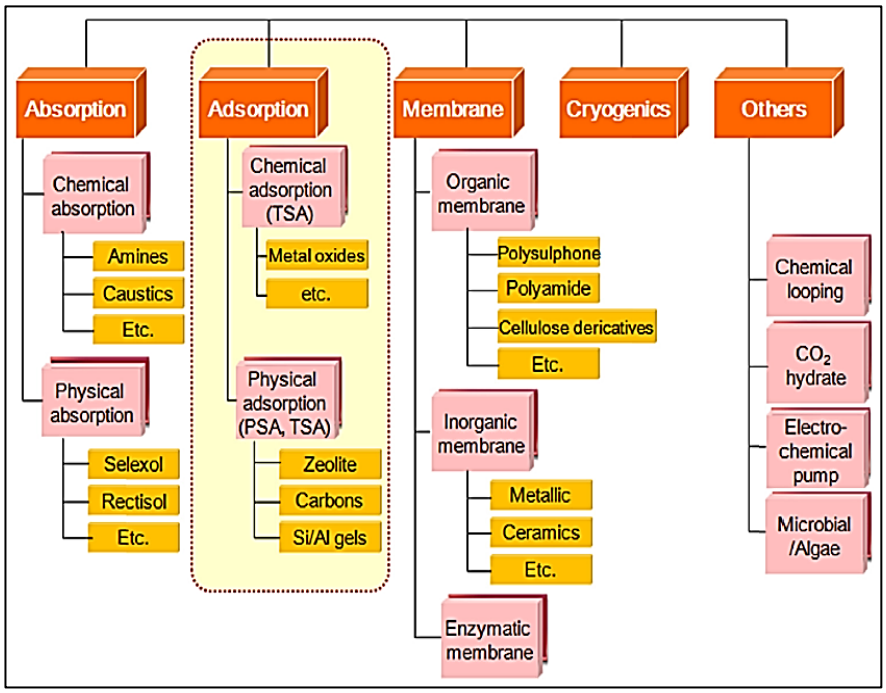

Figure 1-5- Post-combustion capture technology applications [26]

1.5 CO_2 capture by absorption

CO_2 capture by absorption mechanism suggests a wet process, using a physical (when absorption occurs without chemical reaction) or chemical (where a chemical reaction is required, and new chemical compounds are formed) method. Chemical methods are more prevalent in the industry and are employed in processing large-scale CO_2 emission sources with high or low CO_2 partial pressures [26]. A comparative analysis of the two methods is shown in Table 1-2. The most dominant process used in the industry is due to economics and a few disadvantages discussed in the next section.

Table 1-2-Comparison of chemical and physical absorption

Chemical absorption	Physical absorption
High absorption heat is required	Low heat of absorption is common
Increasing absorption temperature achieves desorption, and where the pressure is high, the reduction applies.	Desorption is achieved mainly through the reduction of system pressure (i.e., flashing) or by additional heating of the solvent
Ability to reduce the acid gas level to a minimum	Removal of acid gas is limited to some extent
Absorption is unrestrained by the partial pressure of the feed gas	Absorption capacity depends on the feed gas partial pressure.

1.5.1 Chemical absorbents

1.5.1.1 Amine solvent CO_2 absorption capture

Typically, CO_2 absorption, employing amine solution, requires an absorber and a stripper unit, where CO_2 rich flue gas is contacted with an amine solution in a column counter-current fashion, as shown in Figure 1-6. Across the industry, the feed gas is usually fed at a temperature of ~ 40-60 °C, while CO_2 desorption occurs at ~ 120-140 °C [29].

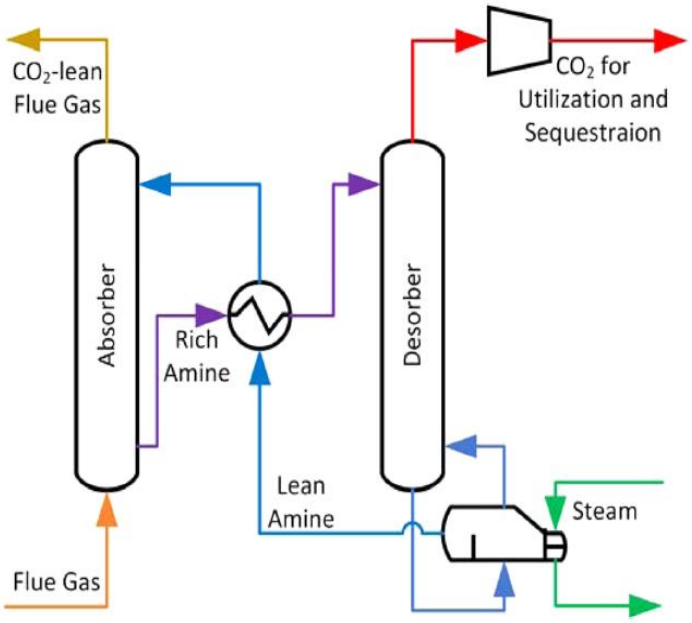

Figure 1-6-Process overview of monoethanolamine (MEA) CO_2 scrubbing process [29]

Amines that are commonly employed for CO_2 absorption are a class of alkanol amines, namely-primary MEA, secondary (diethanolamine-DEA) and tertiary forms (N-methyl diethanolamine-MDEA), with each containing a minimum of one (OH^-) and an amine group [30]. The CO_2 reaction affinity of these amines are in the order of primary > secondary > tertiary [31], while their respective loading efficiency is tertiary > secondary > primary [30]. Bishnoi and Rochelle validated the loading capacity of the tertiary amine on CO_2. They reported a capacity of 1 mol of CO_2 mol^{-1} of amine, while those of the primary and secondary amine fall within the region of 0.5-1 mol of CO_2 mol^{-1} of amine [31].

During CO_2 capture using MEA, the CO_2 being an acidic gas, acts as a solute while reacting with the amine, acting as a Bronsted base. With a saturated hydrocarbon bonding of the amine / OH group, the amine compound donates a lone pair of electrons from its nitrogen species to the carbon atom of the CO_2 molecule. The chemistry of the ionic speciation equilibria, following the disassociation of the CO_2 in the aqueous amine solution, as described by the Zwitterion mechanism, results in a stable carbamate compound being formed, as represented through Equations 1.1 to 1.4 [31] [29].

$$R_1R_2NH + CO_2 \leftrightarrow R_1R_2NH^+COO^-(zwitter\ ion) \quad \text{Equation 1.1}$$

$$R_1R_2NH^+COO^- + CO_2 + R_1R_2NH \leftrightarrow R_1R_2NCOO^-\ (carbamate) + R_1R_2NH_2^+ \quad \text{Equation 1.2}$$

$$2R_1R_2NH + CO_2 \leftrightarrow (R_1R_2NH_2^+)(R_1R_2NCOO^-) \quad \text{Equation 1.3}$$

$$R_1R_2NH + CO_2 + H_2O \leftrightarrow (R_1R_2NH_2^+)(HCO_3^-) \quad \text{Equation 1.4}$$

The Zwitterion mechanisms for the primary and secondary amines were initially proposed by Caplow in 1968 [32], while Donaldson and Nguyen found the tertiary reaction scheme [33]. These primary and secondary reactions, which occur sequentially, trigger ammonium carbamate formation under anhydrous conditions and further convert the carbamate to bicarbonates following a hydrolysis reaction [31]. More so, given the amine behavioural differences, other compounds with steric characteristics, such as the 2-amino-2 methyl-1-propanol (AMP), whose amine groups are attached to the secondary or tertiary carbon atom, has been considered as an alternative for CO_2 capture. The AMP's affinity to reduce carbamate stability creates room for its hydrolysis into bicarbonate formation [31]. The hydrolysis is a function of chemical stability, controlled by system temperature and molecular structure, and it helps to free more amine molecules for further reaction with more CO_2 to enhance equilibrium loading [29].

Although amine-based solvents have proven effective for CO_2 capture applications, they are fraught with several drawbacks, including capacity loss over time, corrosion of system pipings; reduction in net plants' efficiency; and a significant increment in electricity cost [23]. Also, different degradation forms experienced, such as thermal, oxidative and carbamate polymerisation, have been reported [29]. Thermal degradation has been noted to occur within the stripping unit of an absorber. It is occasioned by the high operating desorption temperature, resulting in amine chain by-products formation. The oxidation degradation resulting from oxygen (often > 5%) in the flue gas dissolving into the amine solvent creates some by-products like oxalate and hydroxyethyl [34]. Additionally, the carbamate degradation triggered by the high-temperature exposure of the amine solution at the stripper unit during regeneration may lead to the formation of 2-oxazolidone. And upon further reaction with the MEA, it produces 1-

(2-hydroxyethyl)-2-imidazolidone and other species, like dihydroxyethylurea and N-(2-hydroxyethyl)-ethylenediamine [35].

All these by-products affect the performance of MEA to capture more CO_2 with time, thus requiring fresh solvent make-up to compensate for the natural decay. Additionally, according to Arnold et *al.*, ~ 2.2 kg of MEA is needed to capture 1 ton of CO_2 [36]. A techno-economic and environmental assessments carried out by Rao and Rubin suggest that, if an aqueous MEA of 30 wt % is used for CO_2 capture from a coal-fired power plant, about 80% increase in electricity cost is likely, with the energy demand estimated at around 4.2 GJ tonne^{-1} of CO_2 capture [37]. This, therefore, calls for the development of alternative processes to further reduce the energy spent during CO_2 regeneration processes compared with those of MEA technology.

1.5.2 Physical sorbents

1.5.2.1 Selexol process

The Selexol process is one of the physical methods employed for CO_2 and H_2S separation from flue gases containing large concentrations of these acidic gases. In this process, CO_2 is captured without a chemical reaction taking place. The solvent often used for the process is the dimethyl ethers of polyethylene glycol (DMPEG) [$CH_3(C_2H_4O)nCH_3$], acting as a weak Lewis base, where the value of *n* varies from 2 to 9 [38].

According to Burr and Lili, DMPEG can work efficiently for CO_2 absorption within a temperature range of -18 °C to 175 °C [38]. During the process, CO_2 separation is achieved by a two-stage configuration of two absorber and stripping units. The solvent enters the first absorber at temperatures below ambient, where H_2S gas is scrubbed and, after stripping with steam, the second absorber removes CO_2, before solvent regeneration. Alternatively, the CO_2 laden solvent may be subjected to several flashing stages (pressure reduction) to enhance its bulk removal, resulting in complete CO_2 desorption due to its reduced solubility under low partial pressure conditions of the DMPEG [38].

The merits of DMPEG use are its low vapour pressure, less toxic nature, and the ability to tolerate moisture in the flue gas; hence, no heat or water wash is necessary for solvent recovery [30]. Secondly, on account of the high viscous nature of DMPEG in low-temperature environments (5.6 cp at 25 °C), the CO_2 mass transfer efficiency within the absorption system may be limited, given that reduced temperatures favour gas solubility in physical solvents, which may be a disadvantage [38]. The related energy consumption associated with this process has been linked to power, heating, and cooling systems demand valued around 0.1080 kWh kg^{-1} CO_2, 0.2238 kWh kg^{-1} CO_2 and 0.5590 KWh kg^{-1} CO_2, respectively, with the difference accounted to other auxiliary equipment [39].

1.6 CO_2 capture by adsorption

CO_2 capture by adsorption mechanism suggests using solid-based materials, where adsorption occurs by physical or chemical processes. In chemical adsorption, bonds are formed when CO_2 molecules interact physically or chemically with the solid sorbent. Adsorption processes are attractive for CO_2 separation, and the advantages they offer include; no liquid waste products, and the sorbents have low influence of contaminants, like SO_2, H_2O, on separation. Although many adsorbents have been discussed in the literature, some of the sorbents shown in Figure 1-5 are commonly employed for commercial applications and are presented in the next section. The physical sorbents interact with CO_2, with their adsorption process governed by the van der Waals weak intermolecular forces. The chemical sorbents are those propelled by chemical reaction forces, dominating during the CO_2 capture process.

1.6.1 Physical sorbents

1.6.1.1 Activated carbons

Activated carbon (AC) represents one of the classical forms of carbonaceous adsorbents that have found application in both medicine and fluid mixture separation. They are considered safe and relatively low-cost, given their origination from sources like tree barks, coconut shells, woody biomass, straws, etc. [40]. In industry, they are synthesised by employing physical or

chemical methods involving two-step developmental processes: carbonisation and activation. The physical method entails partial carbonisation of the precursor materials, at temperatures < 764 °C, and under an inert atmosphere, resulting in a rudimentary porous body of the parent material [41]. This is followed by thermal activation of the carbonised material using oxidants like steam or CO_2 at temperatures between 764-1000 °C, to aid enlargement and narrowing existing pores within the carbon structure [41].

By contrast, chemical methods employ chemical agents, such as acids (H_3PO_4) or bases (KOH) as activators (to avoid tar formation), for the activation processes, after carbonisation of the precursor materials at temperatures ranging from 400-800 °C [41]. Although these agents have been effective as activators, several studies have shown that specific agents, when utilised at varying proportions, can alter the physicochemical characteristics of the AC developed [42]. An instance is a study carried out by Hayashi *et al.*, where AC was produced using potassium hydroxide (KOH) as an agent, resulting in an AC with surface areas >1000 m^2 g^{-1}, however, such a process comes with significant environmental and corrosion consequences to the process systems [43].

Despite the challenges associated with AC's production with uniform pore characteristics [44], other issues remain the high energy consumption during the development process owing to dual thermal stages. Several researchers have opined that an energy reduction is likely where a one-step activation process is employed [45]. However, from the context of CO_2 capture, the importance of surface chemistry has been shown, by incorporating certain functional groups via impregnation on the AC surface during activation, to enhance CO_2 capture affinity. This evidence has been validated in a number of studies, where metal oxides, amines and nitrogen modified ACs, promoted CO_2 adsorption capacity via electrostatic interaction, though at the expense of a reduction in porosity of the AC, where the agents are not uniformly dispersed onto the carbon surface structure [46].

Given the above, it is evident that carbonisation and activation processes promote porosity formation in AC, explaining the increased van der Waals forces exhibited by AC in physical adsorption scenarios. However, weaker interactions are also expected when employing untreated AC due to low surface areas and porosities. As a result, since CO_2 is an acidic gas,

capturing the gas using AC would be enhanced by introducing basic functionalities onto the AC surface to provide anchoring sites for CO_2 attraction.

1.6.1.2 Zeolites

Zeolites are microporous crystalline forms of aluminosilicate originating from alkali or alkali earth metals and are synthesised for different industrial applications. Zeolites are characterised by interconnecting pore channels in cages of sizes between 0.5 -1.2 nm, that occlude gas diffusion [47]. The structure consists of tetrahedra of SiO_4 and AlO_4, assembled into polyhedral building units, where the silicon and aluminium atoms reside at the polyhedra corners, encircling oxygen (O) atoms [48]. This assemblage results in a three-dimensional framework, whose tetrahedrons can be tuned by altering the Si/Al cation ratios or exchanging the (Si^{4+} and Al^{3+}) in the zeolite [30]. The size of a zeolite cage depends on the type of exchange cation, and the number of oxygen atoms shared in the tetrahedral, as both influence zeolite adsorption properties. Researchers have reported that cation types, such as Si, Li, Al and Na, can influence the heat of CO_2 adsorption with increasing monovalent charge density [49].

The employment of zeolites for CO_2 capture, particularly those of NaX, zeolite 13X and zeolite 5A, are used as a benchmark for the performance of newly developed adsorbents [5]. Their preference is due to their molecular sieving behaviours, and the high electrostatic affinity for CO_2, with up to 5.5 mmol g^{-1} of CO_2 adsorption capacities reported [47]. According to a study carried out by Jadhav *et al.* on modified zeolite 13X with MEA, amine impregnation results in increased CO_2 adsorption at 30 °C by a factor of 1.6, compared with an unmodified zeolite, thus explaining the roles of surface agents and cationic effects on the zeolite structure [50]. Despite zeolites being proven to offer certain advantages for CO_2 adsorption, key drawbacks have been identified, including low CO_2 capture and selectivity over nitrogen in post-combustion capture scenarios [30]. These behaviours have been linked to CO_2/N_2 competition for adsorption sites in zeolite pore channels, as the kinetic diameters of CO_2 (0.33 nm) and nitrogen (0.36 nm) are too close to permit distinct separation [51]. Also, with water vapour present in flue gases, this limits the adsorption capacity of zeolites for CO_2, due to the tendency

of H_2O molecules to compete on adsorption sites, as they bind to the cationic species, thus limits CO_2 access to pores due to reduced electrical field gradient within the cages [51].

Wang et *al.* also studied the effect of moisture on hydrophilic zeolites, such as NaX, where CO_2 adsorption capacity was reported to decrease by 60% upon loading of the zeolite with 3.4 mmol of H_2O g^{-1} [52]. Also, in a recent study by Beltrao et *al*., on zeolites derived from coal ash for CO_2 capture; the zeolites exhibited high affinity for CO_2 and water [53], inferring that, with the presence of moisture, alongside captured CO_2, this may increase regeneration temperatures to above 300 °C [30]. This characteristic of hydrophilic zeolites contrasts with the hydrophobic version due to their higher Si to Al ratio, where CO_2 separation has been reported to consume a lower amount of energy, e.g. 0.13 GJ $tonne^{-1}$ of CO_2 uptake for zeolites configured in hollow fibre membranes [54]. Furthermore, given that most CO_2 adsorption with zeolites is executed under pressure or vacuum swing adsorption processes, pressures above 2 bar have been recommended as suitable for usage; however, this may also require higher regeneration energy demand, leading to substantial process energy losses [51].

1.6.2 Chemical sorbents

1.6.2.1 Amine functionalised Metal-Organic Frameworks (MOFs)

The use of Metal-Organic Frameworks (MOFs), an inorganic-organic hybrid material for CO_2 capture, has attracted considerable attention over the years, after their initial proposal by the Yaghi group [55]. They are a family of crystalline porous and non-porous materials that result from the coordination of metallic clusters (inorganic) and basic organic groups, called ‘linkers’ [47]. Their structures are such that they possess open metal centres. However, a number of MOFs are non-porous, and the attributes are related to the intertwined nature of the organic constituent and metallic ions coordination. The synthesis process of MOFs allows for tunability of the geometry, sizes and functionalities, which have resulted in the development of many different types of MOFs, with remarkable adsorption properties and surface areas ranging from 1000-10000 m^2 g^{-1} [56].

Adsorption sites in MOFs can be enhanced by using slim organic linkers, compared with bulky ligands. The slim organic linkers can create smaller pore networks that favour gas adsorption [56]. However, despite using slim linkers, which yield high MOF porosity, fragile frameworks may also become evident due to large void space creation [56]. This may arise from the incompatibility of selected chemical groups to satisfy MOF coordination conditions [57]. MOFs have been reported to exhibit high CO_2 adsorption capacity, especially when dealing with pure CO_2 adsorption systems, even at high pressures. Additionally, their adsorption capacity reduces when exposed to gas mixtures and flue gases from power plants, owing to the low partial pressure nature of the flue gas stream [26]. Also, recent studies on CO_2 capture from flue gas have shown that MOFs are reactive to moisture present in flue gases, and may lose mechanical strength and durability over time, and, based on the high cost of their manufacture, this limits their application in PCCC [30].

It has also been suggested that the introduction of chemically functionalised groups into a MOF structure can create a composite solid with an affinity to adsorb weakly acidic CO_2. The chemical functionalisation is viewed as offering the possibility of a donor-acceptor relationship between the MOF and the CO_2. The chemical groups can be incorporated into the MOF structure by direct functionalisation or post-synthesis via grafting techniques [58]. Lin et *al.* employed a direct synthesis method to incorporate an amine group onto MIL-101 (Cr), using OH- assisted hydrothermal treatment, as shown in Figure 1-7. Their findings showed an increased MOF surface area of 1675 $m^2\ g^{-1}$, with a CO_2 adsorption capacity of ~15 mmol g^{-1} at 25 °C, exhibiting a Type I adsorption isotherm, which suggests the presence of micropores within the MOF pore structure [57].

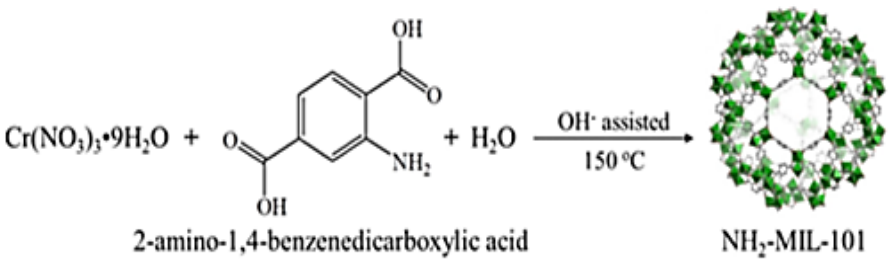

Figure 1-7-Amine-functionalised MIL -101 (Cr) via direct OH-supported hydrothermal process [58]

Contrary to this, other techniques for amine support, such as post-synthesis (amine immobilisation), which can open up the metallic coordinate sites on the MOF structure, have shown a disparity in adsorption performance. In a study by Kim *et al.* on immobilised diethylenetriamine (DETA) grafted on Cr coordination sites of MIL-101 (Cr), a significant reduction in surface area, in addition to low CO_2 capture performance, was evident at low pressures [59]. This disparity infers that, aside from the nature of different chemical groups, different synthesis pathways can influence the adsorption properties of MOF. While it has been shown that amine-functionalisation of MOFs coordinated via direct synthesis promotes CO_2 capture performance, the post-synthesis approach via grafting could result in pore blockages being introduced within the MOF pore network. These may reduce the surface area and pore volume of MOF, leading to loss of adsorption sites.

Given the above, it is evident that employing direct synthesis offers a more advantageous pathway for MOF functionalisation, however, this feature can be extended by the opening of more metallic sites, inducing interpenetration and ion exchange characteristics within the host structure.

1.6.2.2 Organo-functionalised mesoporous silica

Mesoporous silicas are a group of adsorbent composites produced from the incorporation of supramolecular aggregates of ionic surfactants that act as a soft organic template and an inorganic silica framework [60]. The resulting structural framework provides outstanding textural and surface characteristics, such as increased surface area, large pore volume and more surface OH group. The large OH group available on the mesoporous silica surfaces provides anchor sites that enable diverse post-synthesis functionalisation with other organic guest species as support [58].

1.6.2.3 Amine-impregnation

For the amine-impregnation process shown in Figure 1-8, the polyethyleneimine (PEI) is introduced into the silica material as a support, after dissolution in a polar solvent, before infusion into the silica pore network [61]. According to Hedin et *al.,* a trade-off needs to be

established before loading organic group onto silica, whose pores must not be too narrow, otherwise, an increase in density of the organic support can create little room within the pores that could limit gas transportation [47]. Additionally, the estimation of the pore volume of the silica material is necessary before impregnation to ensure effective distribution of the chemical species within the silica structure channels.

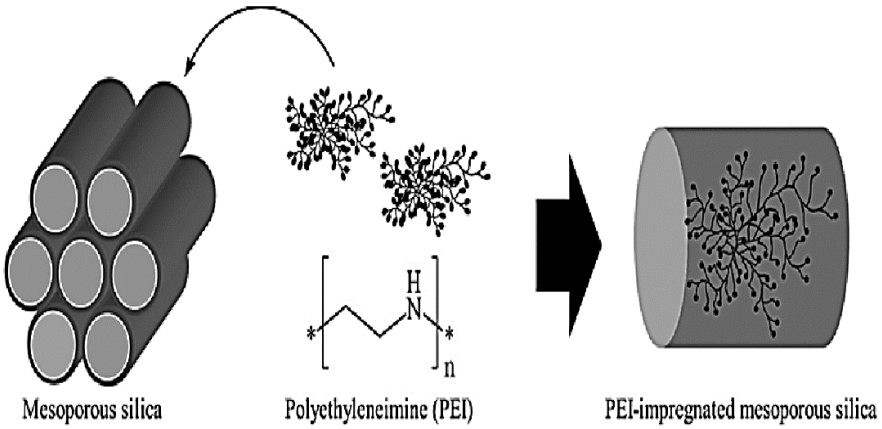

Figure 1-8-Amine-functionalised mesoporous silica via physical impregnation method [61]

Regarding amine support, researchers have investigated the influence of amine impregnation on CO_2 capture performance [62, 63]. In a study by Yue et *al.* on CO_2 capture of mesoporous SBA-15 impregnated with tetraethylenepentamine (TEPA), a CO_2 adsorption capacity of 3.93 mmol g^{-1} was reported [64]. Also, in a comparative study by Chen et *al.* [58] and Qui et *al.* [65], under the same experimental conditions, higher CO_2 adsorption was observed for TEPA-containing sorbents compared with PEI-containing sorbents. The variation in adsorption capacity was attributed to the higher density of the amino group and the less viscous nature of the TEPA, compared to the PEI, which results in a reduction in affinity sites for CO_2 interaction [63]. Additionally, Son *et al.* lent further credence to this view, where PEI impregnated into varying mesoporous silica and carbonaceous materials for pure CO_2 adsorption at 75 °C, showed that the pore size of the support material is a determinant factor for enhanced adsorption kinetics, resulting in adsorption capacity of 3.02 mmol g^{-1} [66].

Despite the impressive CO_2 capture performances of amine-impregnated mesoporous silicas, some studies have reported that a lack of chemical bonding between the support and the

organic species could result in the leaching of organic species from the support under high-temperature cyclic adsorption and regeneration processes [58]. The findings were validated in a study by Hicks et a*l.,* where TEPA-impregnated mesoporous silica, employed for CO_2 adsorption under cyclic operation, reduced the CO_2 capture performance due to leaching of the TEPA support [67]. Other findings suggest that with oxygen presence in flue gases, the material's performance could be affected by its oxidation, thus questioning the longevity of amine impregnated silica [47].

1.6.2.4 Post-synthetic functionalisation (grafting) technique

As an alternative to addressing the drawbacks associated with the use of amine impregnation, such as lack of thermal stability due to leaching of the organic supports, other methods like 1) chemical grafting, 2) co-condensation, and 3) incorporation of organic groups as bridging components into the pore walls of mesoporous silicas, using organosilica precursors, have been proposed [60]. The grafting method entails modifying the mesostructured silica pore cavity by inducing a reaction between the $(R'O)_3$ SiR type and the hydroxyl group present on the silica surfaces shown in Figure 1-9 [60].

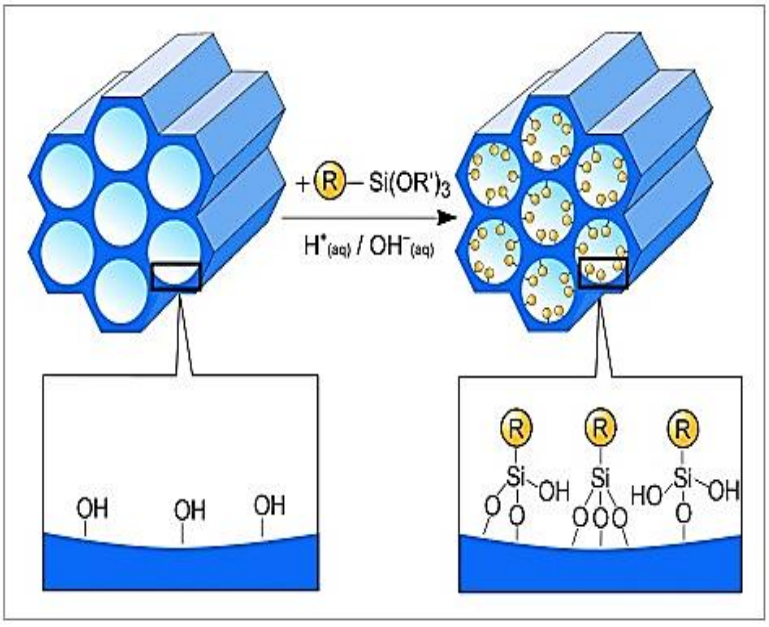

Figure 1-9-Chemical modification of mesoporous silica by post-synthetic grafting method [60]

As shown in Figure 1-9, an increase in the concentration of OH^- group on the mesoporous silica surfaces have been suggested to promote the loading efficiency of amine species; however, the strength of such functionalisation depends on the nature of the organic residue (R) [60]. A study carried out by Leal *et al.* on the CO_2 adsorption of 3 -aminopropyl triethoxysilane (APS) grafted into silica gel under anhydrous and hydrated conditions, evident that the amino species reacted with the CO_2 [68]. The APS-grafted silica gel under the anhydrous condition shows a CO_2 uptake of 0.41 mmol g^{-1}. However, those grafted under hydrated condition showed an adsorption capacity of 0.89 mmol g^{-1} at similar adsorption temperature conditions [68].

The impact of the various amine grafting conditions on the APS-silica, and the water-aided silica, shows that the CO_2 uptake may be associated to the extent of the surface grafting, influenced by APS diffusion into the silica pores, as well as the number of silanol groups present on the silica surface, in addition to the porosity of the support [30]. Furthermore, it is instructive to note that since chemical grafting takes place at the silica pore centres, excessive grafting may limit molecular diffusion of gas species due to likely induced pore blockages that could reduce the sorbents' porosity.

1.6.2.5 Co-condensation (direct synthesis) technique

Aside from the techniques discussed above, another approach employed for organo-grafted mesoporous silica synthesis is co-condensation of silane [$(RO)_4Si$ (TEOS or TMOS)] and organosilane of the type $(R'O)_3SiR$, in the presence of a structure-directing agent (SDA), acting as an organic template [30]. Although SDA is employed for the synthesis of pure mesoporous silica, however, the synthesis pathway can be provided by a surfactant (organic template) with an amphiphilic character, from where the organic residue is covalently projected into the silica pore, thus making the organic residue become an integral part of the silica matrix, as shown in Figure 1-10 [30].

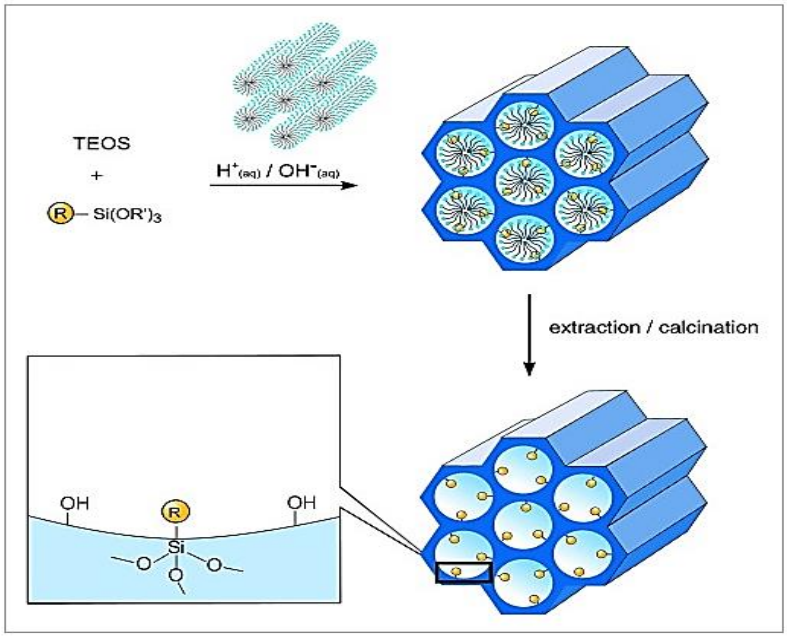

Figure 1-10-Co-condensation technique for organic modification of mesoporous silica [60]

By employing co-condensation, the synthesis approach eliminates potential pore blockages, as the organic units, which anchor onto the silica surfaces, are homogeneously distributed in contrast to the grafting technique [60]. Although uniform distribution is evident, one significant drawback is ensuring that the functional support does not exceed 40 mol% in the reaction mixture, else a less ordered mesoscopic product may result [60]. This is because an increased proportion of the $(R'O)_3SiR$ in the reacting mixture may lead to homocondensation reaction, occasioned by a variation in the hydrolysis rates and condensation of the structurally different precursors. This phenomenon is associated with the co-condensation technique, as it prevents the functional group's homogenous distribution into the silica framework. Another problem is that the increased loading of the support material could reduce pore size, volume and surface area of the organo-silica material [60].

Generally, although the chemical grafting and direct synthesis techniques result in the formation of highly stable CO_2 capture adsorbent, the extent of guest species introduced into the silica pore is restrained by the number of silanol groups present on the mesoporous silica surfaces. The introduced species can result in lower CO_2 uptake compared with other adsorbents developed by other modification routes.

1.7 Membrane technology for CO_2 capture

Membranes have found usefulness for CO_2 separation in gas streams of small volumetric flow rate, where they act as a filtering media. They are mainly employed for CCS applications for H_2/CO_2 separation in pre-combustion capture schemes, CO_2/N_2 separation for post-combustion, and O_2/N_2 separation oxyfuel combustion [69]. Before separation using membranes, the flue gas is first wet-scrubbed and cooled to the working temperature of the membrane, during which the target gas selectively passes through the membrane, with the heavy components of the feed stream retained, as described in Figure 1-11. Although different membranes exist, such as organic (polymeric), inorganic (zeolites), enzymatic, and dense (non-porous), the effectiveness of CO_2 separation is a function of the membrane pore characteristic relative to the size of the target gas molecule, as well as the affinity of the gas toward the membrane material [69].

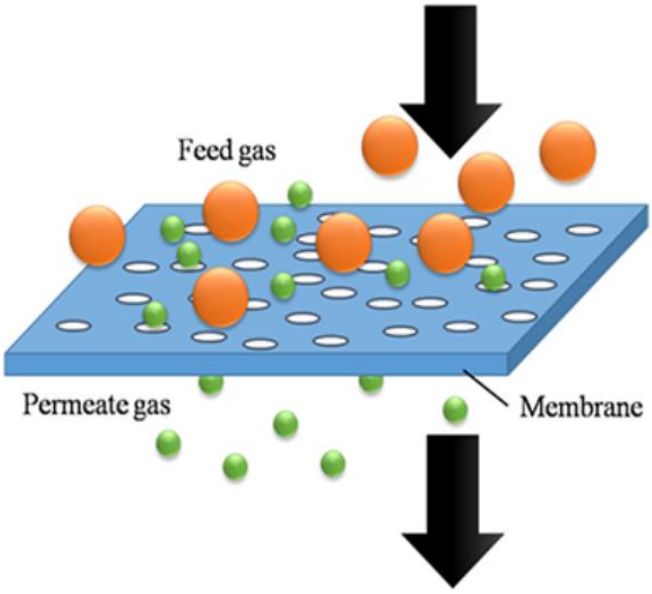

Figure 1-11-Schematic representation of binary gas mixture membrane separation [69]

Polymeric membranes are mainly employed for gas transport, while the inorganic types are used in highly selective separation processes [69]. During membrane separation, as the amount of CO_2 permeation increases, the efficiency of the membrane decreases with time due to the effects of contaminants present in the feed stream, thus, creating technical constraints to the membrane performance relative to permeability and selectivity [69]. These two factors

can also be varied during membrane design and development to meet specific CO_2 capture performance needs.

In addition to the seeming advantages of membranes, such as requiring low energy and zero need for regeneration, the disadvantages include the inability to process large volumes of gas streams, operating at temperatures above 100 °C and fouling of the membrane system when operating under high-pressure conditions have been reported [70]. As a result, there is a need to incorporate high-cost modules and recycling systems, which may increase process complexity, energy consumption and costs [71]. Compared with other CO_2 capture techniques, membranes are insensitive to sulfur and other trace elements found in flue gases; however, they are suitable in removing a required amount of CO_2 from gas streams rather than the absolute quantity [69].

1.8 CO_2 separation using Cryogenic systems

Cryogenic CO_2 separation from flue gas streams entail compression, cooling, and fractional condensation processes, executed at low temperatures that result in a phase change of the CO_2 gas. In post-combustion capture scenarios, CO_2 laden dry flue gas is first cooled, compressed and brought down to a desublimation temperature, typically around -100 °C to -135 °C, where the CO_2 gas precipitates as a solid before undergoing an expansion process [72]. The final product, being a mixture of CO_2 in the liquid phase and nitrogen in the gaseous phase, can further be separated by fractionation. Cryogenic CO_2 separation has been reported to favour flue gas stream separation with high CO_2 contents (> 90%) [72]. The CO_2 capture efficiency for such systems is dependent on the operating conditions during the expansion process. Specific operating conditions for desublimation, such as < 1 atm, at -135 °C and -120 °C, have reported CO_2 recovery of ~ 99% and 90%, respectively [72].

Until recently, newly targeted solutions for CO_2 separation based on advanced cryogenic separation have shown that energy penalties, ice formation (e.g., frozen water) and economics of the cryogenic CO_2 separation processes can be reduced [73]. These were demonstrated in a study by Xu *et al.* on a cryogenic CO_2 capture during coal-based hydrogen production, where a reduction in cold energy demands of the operation was reported to be ~ 0.395 MJ kg^{-1}, for

90% and 99% CO_2 recovery and purity, respectively [74]. Also, in a study carried out by Tuinier *et al.,* on a cryogenic CO_2 capture from flue gas system operated dynamically, whose cold energy source was provided by a liquefied natural gas, a simultaneous separation of water and CO_2 on account of differences in their dew and sublimation temperatures were reported, thus averting the problems of clogging and pressure drops [75]. Given the seeming increase in cold energy demand of cryogenic CO_2 separation, another significant pressure challenge is how to insulate the cryogenic packed beds to prevent loss of sensible and latent heats [73]. More so, this cold energy requirement for refrigeration is high, given that specific component of the flue gas, such as moisture, have to be removed before cooling the gas stream in order to avoid blockages [71].

1.9 Criteria for CO_2 adsorbent performance

As can be seen from the performance characteristics of several sorbent materials employed for CO_2 capture in PCCC technologies, it is evident that sorbent choices are a critical aspect of the CO_2 capture process. A summary of key criteria that sorbent materials must meet is discussed in the next section.

1.9.1 Selectivity for CO_2

The selectivity (*S*) indicates the extent to which a sorbent material has an affinity for CO_2 molecules, in the presence of other gas components within a gas stream mixture, at any given condition [76]. Given that flue gas streams emitted from coal-powered plants contain a high fraction of N_2 (75-80%) and a low percentage of O_2 (3-4%), as shown in Table 1-1; a good sorbent material should be able to demonstrate high CO_2 selectivity over other gas components in the flue gas stream. As a parameter, *S* has a direct relationship with the purity of captured CO_2, which is critical for the CO_2 sequestration economics [77]. Therefore, for a given separation, the highest *S* value is considered a good choice. Also, while the sorbent material should demonstrate high CO_2 capacity, this should also be the case in the presence of water vapour in the flue gas stream. Water vapour presence is a determinant factor for

consideration in the type of sorbent material used for CO_2 component separation, given their hydrolytic stability.

1.9.2 CO_2 adsorption capacity

The adsorption capacity, also known as the working capacity, or CO_2 delta loading, is a critical performance criterion that helps determine the size of an adsorption system, the associated energy penalty, and the purity of CO_2 capture in an adsorption process. It can be estimated from the purge-to-feed ratio of a given adsorption operating condition. For working capacity comparison with different sorbent materials, the equilibrium conditions, such as temperature and partial pressure at any given point, must be specified. Adsorption capacity, when related to temperature swing adsorption processes, is the difference in the CO_2 captured amount between the low temperature/purity, likened to the adsorption process, and the high temperature/high purity, notable for the regeneration and desorption stages for a given cycle operation [78]. Equation 1.5 can be employed for the estimation of working capacity during CO_2 capture processes [79]:

$$[CO_2]_{working\ capacity} = \left[mCO_{2(adsorption)} - mCO_{2(desorption)}\right]/m_s \qquad \text{Equation 1.5}$$

Where,

$mCO_{2\ (adsorption)}$ = CO_2 loading at adsorption conditions, mmol g^{-1}

$mCO_{2\ (desorption)}$ = CO_2 loading at regeneration conditions, mmol g^{-1}

m_s = sorbent mass, g

Adsorbents with excellent working capacities have been reported with the ability to reduce the energy penalties associated with CCS processes, and values > 3 mmol g^{-1} are often considered as good choices for CO_2 separation [4].

1.9.3 Kinetics of adsorption and desorption

The kinetics of sorption represent the time control of the adsorption/desorption processes occurring in a given fixed-bed adsorption system. A sorbent material needs to exhibit fast kinetics under flue gas operating conditions as a dynamic factor. Although fast kinetics are crucial for adsorption processes, as they reflect how quickly the adsorption system attains equilibrium, slow kinetics would reduce the working capacity, with both cases governed by sorbent's surface chemistry materials. In some instances, sorption kinetics are controlled by the extent of CO_2 interactions with the adsorbent's surface functional groups. This is also, despite the mass transfer and diffusional resistances between the gas phase and the sorbents' surface structure.

1.9.4 Resistance to attrition

A sorbent's resistance to attrition is related to the mechanical strength of the material and the nature of the processes where it's being utilised. The criterion is crucial, given that an increase in the level of attrition may result in frequent replacement rates of sorbents, owing to physical breakdown and mechanical wear and tear of being circulated in an adsorption bed. For example, a sorbent material needs to possess excellent microstructural and morphological stability in an adsorption process. Low attrition will increase the sorbent's tendency to capture more CO_2 over several cyclic regeneration stages, despite changes in selected operating parameters, such as high volume flowrate of the flue gas, vibrations, and temperature, which may induce apparent fragmentation of the sorbent. Also, there are tendencies that sorbent disintegration may occur via abrasion or crushing; therefore, the sorbent's mechanical strength is crucial for reduced makeup rates and reduction in the cost of CO_2 capture.

1.9.5 Chemical stability

The stability of sorbents is often related to how well they behave under thermal and oxidising environments. For flue gases comprising other gas constituents, sorbent's choice would need to consider the cost implication of frequent sorbent replacements. As most studies have shown, sorbents that react with CO_2, also react chemically with SO_2. An example is the amine-

based absorption process, where toxic by-products are generated, given the oxidising environment induced by O_2 present in the flue gas [35]. Consequently, it is crucial to reduce these impurities by employing pre-treatment processes such as desulphurisation (sulphur removal) to enhance the sorbent's stability and adsorption capacity.

1.9.6 Capture cost

The cost of CO_2 capture represents another criterion worth considering during CCS applications. This is beneficial from the perspective of the overall CO_2 capture process economics. When the cost of sorbent development is considered, this may also form part of the entire CO_2 capture process. It would further permit the trade-off between the capital and operating costs involved in a CO_2 capture process to be known. In a study conducted by Susarla *et al*. on the energy and cost of CO_2 capture, using zeolite 13X for CO_2 separation from flue gas containing 15% CO_2 emitted from a 500MW power plant, under PCCC scenario, it was reported that CO_2 capture cost was around US$30.4-36.7 per tonne of captured CO_2 [80]. Similarly, Ho *et al*. carried out a comparative analysis of CO_2 capture from a 500MW subcritical lignite power plant operation, using 30 wt% MEA solvent, and reported a cost of US$70 $tonne^{-1}$ [81]. The disparity in capture cost suggests that CO_2 capture cost may be lower where an adsorbent material is utilised.

Given the high cost of CO_2 capture, this further weakens the global drive towards CCS commercialisation. Furthermore, from the perspective of sorbent development, a study by Tarka *et al*. using \$10 kg^{-1} as a reference point to undertake a sensitivity analysis versus economic performance, reported that \$5 kg^{-1} spent on sorbent development presents an exemplary scenario, and also, any cost close to \$15 kg^{-1} is seen as uneconomical [82]. Therefore, to make adsorption processes more economical, the cost of sorbents for CO_2 capture application should not exceed \$10 kg^{-1} to compete well with other CO_2 capture alternatives.

1.9.7 Adsorbent regeneration

Sorbent regeneration often comes via pressure reduction or heating and cooling processes, leading to slow degradation of sorbent materials. For a typical cyclic operation, energy consumption is considered favourable if it is substantially low. The ease with which a sorbent material is regenerated will ultimately reduce the cost of a separation process. These attributes are necessary for ideal adsorbent development, and it is doubtful that a single adsorbent will meet all of the required characteristics. However, in the current study, two regeneration alternatives have been considered - Pressure Swing Adsorption (PSA) and Temperature Swing Adsorption (TSA) processes. Their associated advantages and disadvantages are discussed in the next section. The Temperature Swing Adsorption process has been considered to enable comparison with the MEA solvent absorption system, where the regeneration energy has been reported to be ~ 4530 kJ kg^{-1} CO_2 [82]. Also, since coal-powered plants emit low-grade thermal energy, this heat produced during combustion could be an additional energy source for sorbent regeneration.

1.9.7.1 Pressure Swing Adsorption

Pressure Swing Adsorption (PSA) technology, referred to as a 'heatless process', was patented in 1932. It was first demonstrated in an oxygen enrichment experiment by Charles Skarstrom in 1960 [83]. The process entails selective adsorption of a target gas component in a gas stream upon contacting with sorbents loaded in a fixed bed. An equilibrium state is achieved during the process when a gas stream enriched in the more strongly adsorbed component is produced, following a reduction in the target gas component's partial pressure or the system pressure. By principle, the PSA system 'swings' between the high pressure in the feed (for the adsorption steps) and the low pressure necessary for the desorption process, as described in Figure 1-12, thus allowing for re-use of the sorbent.

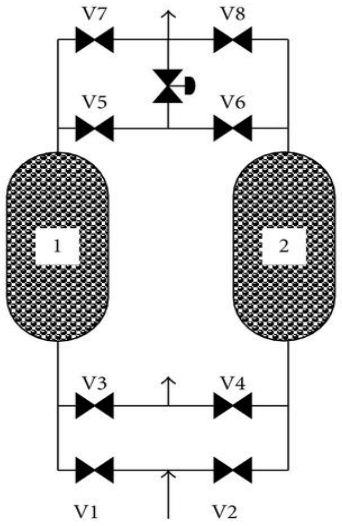

C1	Feed	Blow	Purge	Press
	V1, V7	V3	V5, V3	V1
C2	Purge	Press	Feed	Blow
	V6, V4	V2	V2, V8	V4

Figure 1-12-Skarstrom four-cycle-two-column PSA process with non-steady state complementary stages [84]

Although the PSA process appears relatively simple, it can become complex where several unsteady-state complementary stages are integrated. These stages would enable such a process to be operated under cyclic conditions to promote product purity and recovery. Given that a PSA unit's performance is determined by the nature of the sorbent employed, an increase in the number of adsorber unit, with more pressure equalisation steps, will promote recovery of a target gas component [85]. However, for CO_2 post-combustion capture scenarios, adsorption is carried out at pressures higher than ambient, with desorption achieved near sub-atmospheric pressure levels. More so, where the CO_2 concentration in the flue gas is low, adsorption may take a longer time to complete.

Despite the added benefit of the PSA process, a number of studies have shown that its implementation is challenging for CO_2 capture processes in large scale emission sources. This is attributed to a need for vacuum creation during the desorption/regeneration process, which is a crucial parameter causing trade-offs between CO_2 separation and energy consumption [86]. Also, the energy consumed during the process often comes from the electric power

demands of the vacuum pumps and the fans required to overcome the pressure drop in the column, and these may induce a form of energy penalty to the entire capture process [86]. Additionally, owing to the high volumetric flowrate of flue gas from the stacks of combustion systems during post-combustion capture scenarios, the size of a PSA unit that would accommodate such a high flowrate flue gas stream at low CO_2 gas density might become an issue to maintain a suitable fluid velocity and the subsequent pressurisation steps. The low velocity of the flue gas (i.e. pressure drop per unit length) may result in gas channelling and poor distribution of the feed stream through the adsorption column. As a result, this might demand multiple adsorption columns for CO_2 separation, creating a footprint issue compared with absorption counterparts [86].

1.9.7.3 Temperature Swing Adsorption

The Temperature Swing Adsorption (TSA) process is often applied for post-combustion CO_2 capture in industry. It operates between low-temperature adsorption and high-temperature desorption processes. After achieving sorbent saturation by adsorption, the reactor temperature is raised further, at constant concentration and pressure, to promote desorption, broken into pre-heating and regeneration stages. During the pre-heating stage, heating is continued up to a set regeneration temperature, when desorption begins, with high CO_2 concentration leaving the reactor at a low flowrate, actioned by thermal expansion [87]. Following this, while the CO_2 recovery rate is low, the regeneration phase is initiated by introducing a purge gas to complete the desorption process. The purge gas introduced simultaneously, sweeps the CO_2, and removes the sensible and reaction heats from the reactor, as the reactor's temperature cools to the adsorption temperature. This precooling process further opens the sorbents' adsorption sites, ready for another cycle of adsorption–regeneration process, provided the sorbent does not suffer degradation or attrition. A typical illustration of a TSA cycle operation is described in the 4-step cycle process shown in Figure 1-13.

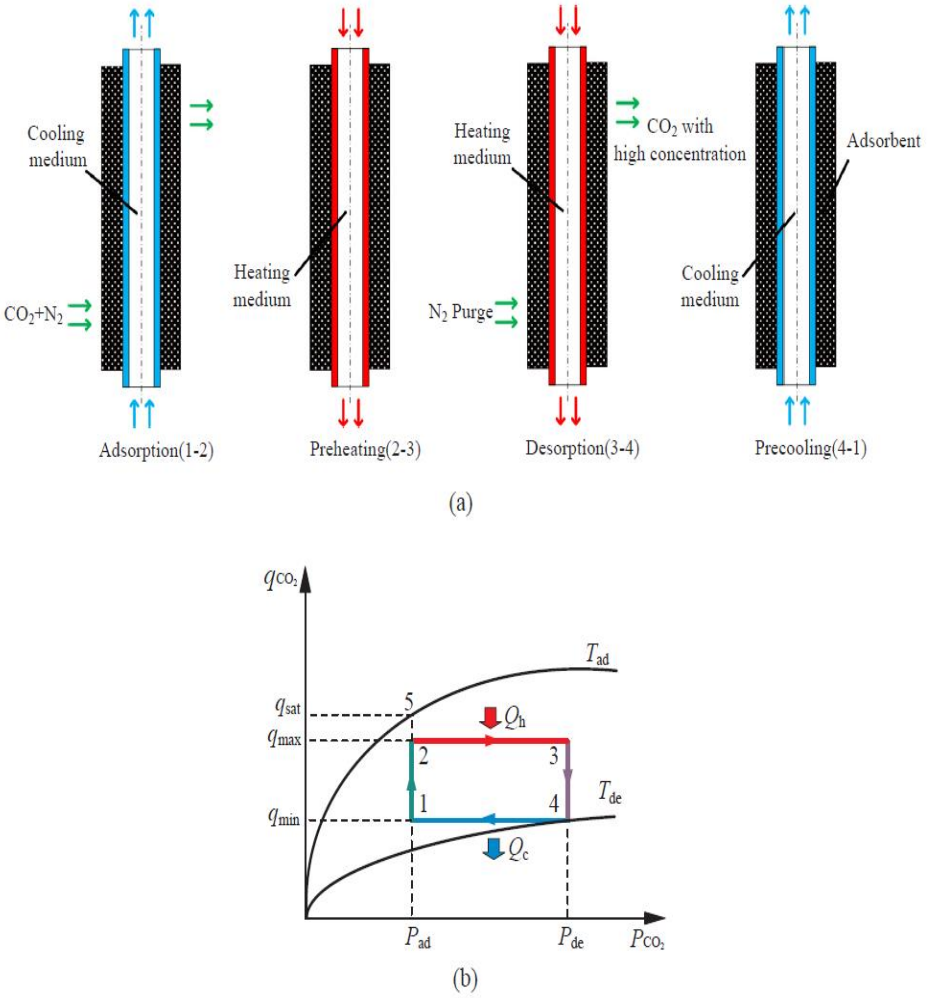

Figure 1-13-A typical description of a 4-step Temperature Swing Adsorption cycle in (a) and the related thermodynamic diagram in (b) [88]

In a 4-step TSA cycle, the energy requirement of the thermal cycling would most often come from the heat supplied to the bed before attaining the regeneration temperature, where the temperature is maintained through completion of the desorption stage. Although other contributing energy sources, such as those from the fan and vacuum pumps, are needed to overcome the beds' pressure drop, the primary energy contributor is related to the heat supplied to the reactor. Across the industries, an increase in the bed's temperature does not generally complete the regeneration process, but the introduction of hot gases, which serve as a purge, helps facilitate complete desorption.

Due to the low heat capacity of gases, large volumes of the purge gases are sometimes expended, making the process an energy-intensive one, even as the gas specie recovered

suffers dilution with the purge gas. Direct heating may also result in frequent sorbent replacement. And to avoid this, some researchers have opined that, by adopting indirect heating and cooling processes, providing for no contact between the coolant and the sorbent, this can aid systems optimisation, depending on the choice of cycle parameters, which could help achieve excellent CO_2/N_2 separation performance [87].

1.9.7.4 Regeneration energy estimation for TSA processes

As a parameter for comparing sorbent performance for CO_2 capture based on a TSA process, the regeneration energy per kg of an adsorbed gas is critical [87]. Since it is favourable for a TSA process to minimise energy losses, energy consumption must, therefore, serve as a benchmark for analysing the performance of different sorbents at different regeneration temperatures. For a given TSA process, the heat of desorption can be estimated from the amount of recovered CO_2 and the isosteric heat of adsorption. The thermal energy applied for the sorbent regeneration would often be translated into an equivalent energy loss (KWh) [89]. Therefore, any difference in heat consumed and expended for the desorption process would represent the energy necessary for heating auxiliary equipment and other associated heat losses [87].

In CCS processes, the electric power that drives the CO_2 separation unit is usually drawn from the heat generated from the integrated power plant's combustion system. However, where a large amount of energy is spent on the regeneration processes, the power plant may experience an energy penalty for not delivering the optimum energy required to meet the intended electricity production balance. The energy penalty has often been attributed to the excessive fuel demand for a fixed net power output needed to make up for the CCS unit's power supply. Therefore, reducing the energy penalty is crucial from an economic point, and this can be achieved where CO_2 separation efficiency is high, using appropriate sorbent material. As the current research is limited to accounting for regeneration energy spent during CO_2 separation under a TSA arrangement, other energy considerations and losses, such as mechanical, compression and auxiliary works, are typical of a complete CCS energy process requirements are not investigated. According to an investigation carried out by Lee *et al.,* using an amine-based solvent system, the regeneration energy entails the sum of reaction enthalpy

between the amine and the CO_2, the sensible heat provided for the desorption of CO_2 from the loaded amine solution, and the latent heat of vaporisation necessary for the regeneration of amine vapours [89].

Contrary, the case of amine absorption is different for the adsorption system. The energy applied accounts for the sorbent's working capacity, the heat capacity, the regeneration temperature, and the process's adsorption heat [90]. The adsorption case is related to the current work; hence, a model developed by Berger and Bhown may be adopted to estimate the energy requirement for CO_2 / N_2 separation [78]. The sensible heat necessary for sorbents' heating may come from an indirect heating process, followed by a hot purge gas sweeping process. Therefore, the thermal energy required for regeneration would be calculated using the sum of the sensible heat provided for the bed heating and the energy necessary for desorption of CO_2 / N_2 (equivalent to the adsorption heat) for a given adsorption cycle by employing Equation 1.6 [91];

$$Q_{reg} = m_{ads} C_{p,ads} \Delta T + \Delta H_{ads} \qquad \text{Equation 1.6}$$

Where

Q_{reg} = Regeneration heat (kJ)

ΔH_{ads} = heat of adsorption of CO_2 and N_2 (kJ mol^{-1}) → [$nCO_2\,\Delta H_{ads}\,CO_2 + nN_2\,\Delta H_{ads}\,N_2$]

ΔT= temperature difference between adsorption and regeneration (K)

$C_{p,ads}$= sorbent specific heat capacity (kJ kg^{-1} K^{-1})

m_{ads} = mass of adsorbent (kg)

nCO_2 and nN_2 = respective moles of species recovered from bed heating.

1.10 Summary

Chapter 1 of this work has unpacked the challenges currently being faced across the globe regarding climate change. A review of previous works by researchers have shown that several measures have been explored in industries to contain CO_2 entry into the atmosphere from significant scale sources using different sorbent materials. A summary of CO_2 capture sorbents, including their pros and con, is shown in Table 1-3.

Table 1-3 - Summary of merits and demerits of sorbent types for CO_2 capture

CO_2 capture technology	Advantages	Disadvantages
Chemical sorbents	1) CO_2 capture and sorption capacity are usually high. Ease of manufacturing in some cases depending on sorbent type.	Support species might experience leaching at high temperature. High regeneration energy may be required. Chemical stability is often low due to possible dilution of other gas components in flue gas streams.
Physical sorbents	CO_2 capture and sorption capacity is usually high. CO_2 capture is based on a physical process; hence less regeneration energy is required.	Sorbents' may be stable under an oxidising environment in the presence of other flue gas components.

As shown in Table 1-3, it is evident that different sorbents that have been employed for CO_2 capture applications in industries have their associated merits and demerits. As a result, the development of alternative sorbents could address the operational imbalance and the requirements of CO_2 capture from large point emission sources, like the coal-powered plants. Addressing the imbalance would require using sorbents with a high affinity for CO_2 in the presence of other gas components in the flue gas. Such sorbent also needs to exhibit fast kinetic and be chemically stable, while reducing the energy penalty is crucial for cost-saving to optimise process performance. Considering the criteria for CO_2 capture performance, as discussed in Section 1.9, Chapter 2 of this work would look at a review of other literature studies regarding sorbent development from renewable sources for CO_2 capture. The adsorption theory would also be discussed relative to sorbent materials' performance and how torrefied carbon would fit into the CCS application context.

Chapter 2 : LITERATURE REVIEW AND RESEARCH OBJECTIVES

2.0 Introduction

This chapter provides a background of the processes involved in torrefied carbon development from renewable sources, such as woody biomass. A thermochemical conversion process, known as torrefaction, is discussed, along with associated techniques employed for characterising torrefied carbon. Given that the torrefied carbons intended for this work are aimed for a dual-purpose application, such as CO_2 capture and cofiring, relevant adsorption theories for assessing the performance of sorbents' and fuel characterisation would be discussed.

The choice of woody biomass was put into perspective to guide the torrefied carbon development to permit comparison with other sorbents' employed for CO_2 capture in industries. To validate the choice of theoretical techniques supporting the experimental data obtained in this work, the techniques would extensively be discussed, with their equations, associated models, assumptions and the limitations for a given technique, critically appraised to justify their use. This would be followed by Chapter 3, which provides the methodology adopted for the experimental techniques utilised.

2.1 Biomass

Biomass represents any material originating from a biological or agricultural means that is convertible to bioenergy [92]. The history of biomass dates back thousands of years, when materials such as wood, following different conversion means, were transformed into various types of heating media for domestic applications. In plants, for example, the photosynthetic process is responsible for biomass (CH_mO_n) formation. During the process, CO_2, which is absorbed by plants, is catalysed by the chlorophyll in the plants, which transforms the absorbed CO_2 into carbohydrates, which forms the plant's building blocks, as shown in Figure 2-1 [93].

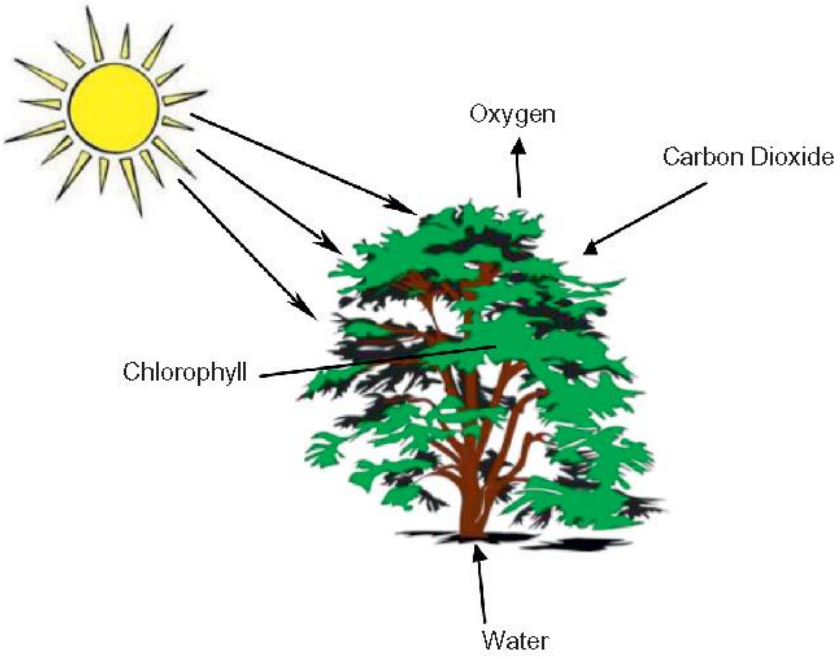

Figure 2-1- The formation cycle of plant biomass [93]

When biomass undergoes combustion, by-products are formed; for example, the CO_2, which plants once absorbed, are emitted, resulting in zero CO_2 inventory. This is the reason biomass is considered to be a carbon-neutral fuel [94]. Biomass conversion into different fuels is dependent on the specific property inherent in a particular biomass source. According to IFP Energies Nouvelles, ~ 5% of the total biomass worldwide can be employed for energy generation, capable of meeting nearly 26% of the global energy demand, equivalent to six billion metric tons of oil [95].

2.2 Plant biomass

The American Society of Agricultural and Biological Engineers previously grouped biomass into primary, secondary and tertiary categories, sometimes referred to as first, second and third-generation biomass by further classification [96]. The first generation represents agro-based feedstock with large carbohydrate potentials, which are sourced mainly from crops, like sugar cane, corn, sugar beets, etc. This biomass set poses a significant risk to the global food supply and is often employed in biofuels production. The second category of biomass comprises by-products from the wood industry, such as tree barks, leaves, floor residue from process plants, post-consumer residues, and other waste wood debris from urban settings.

Also, a number of dedicated energy crops fall under this category and are often referred to as lignocellulosic feedstock. They are usually grown for bioenergy applications and could come from the short-rotation woody or perennial herbaceous energy crops [97].

The short rotation coppices are fast-growing tree species, such as American sycamore, sweetgum, hybrid poplar, willow, black locust, loblolly pine, etc. They are adaptable with better resistance to diseases [97]. However, growing these crops on arable land requires intensive care, and today, they are either burned alone or used in cofiring applications with coal to make electricity. The perennial herbaceous energy crops are less woody and grassy and are usually collected after the harvest cycle. Some commonly used energy-related perennial herbaceous plants are switchgrass, miscanthus and reed canary, and they mostly reproduce, with a lifespan > 15 years [98]. Finally, the third generation biomass (tertiary) comes from algae, and they seem to offer greater energy yield compared to the other generation classes [93].

In general, woody biomass is grouped into hard-and softwoods, which are readily available. The hardwoods are known for their ease of resprouting from stumps after harvest, while the softwoods exhibit high carbon contents. The woody biomass comprises the lignocellulosic compounds, namely-hemicellulose, cellulose, and lignin, at varying proportions. Other components, such as ash and extractives (organics, lipids, and essential oils), occur in dimensions subject to the biomass type [93]. Under high thermal environments, the biomass organic constituents are devolatilised depending on the percentage proportion of the biomass type components [99]. The lignocellulosic compounds, namely-hemicellulose, cellulose, and lignin, are discussed in the next section.

2.3 Lignocellulosic biomass

As explained in Section 2.2, the plant biomass's secondary category is found in the tree trunks and branches. They are non-starchy, containing the lignocellulose fractions, namely - lignin, cellulose and hemicellulose [93]. They are neither digestible nor constitute a part of the global food chain, and their utilisation for energy applications does not threaten the World’s food supply. These components of the lignocellulosic biomass are polymeric. They are formed by

millions of associated units and are positioned at different layers within the plants' secondary cell wall, as shown in Figure 2-2.

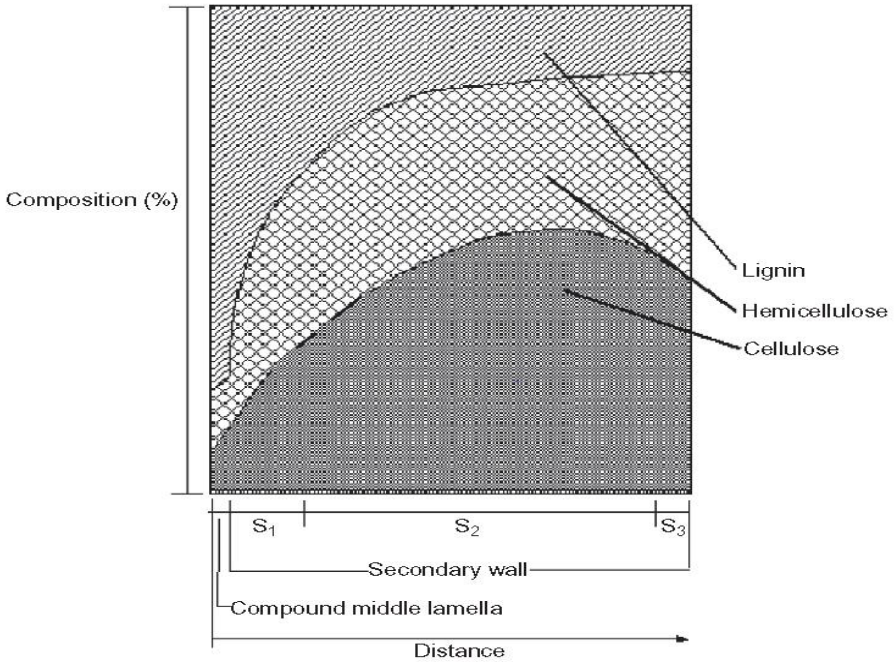

Figure 2-2- Percentage distribution of the lignocellulose fractions in a wood structure [93]

2.3.1 Lignin

Lignin is amorphous and constitutes highly cross-linked polymers integrated into plants' secondary cell wall without a known structure [93]. The molecular formula is represented by $[C_9H_{10}O_3\ (OCH_3)_{0.9\text{-}1.7}]_m$, with the *m* indicating the degree of polymerisation [100]. Lignin occupies about 25-35% fraction of the lignocellulose components in plants, and they account for ~10-25% of the plant's dry matter, sharing both hydrophilic and hydrophobic group complexes [101]. It fills the voids between the cellulose, hemicellulose, and pectin components of the plant's cell wall [102]. However, owing to the covalent bonding shared by Lignin with other plant pectin components, it acts as a cementing agent that confers stability to the entire plants' cell wall [103].

Diebold and Bridgwater suggest that Lignin exists as a 3-dimensional polymer, as a combination of 4-propenyl phenol, 4-propenyl-2methoxy phenol and 4-propenyl-2,5-dimethoxy phenol [104]. The dominant monomeric unit found in Lignin comes from the benzene group

family; however, in softwoods, over 95% of coniferly (4-hydroxy-3-methoxy-cinnamyl) form of alcohol units are present, while those found in hardwoods are dominated by syringyl, a class of phenols [105] [106]. Lignin contents in hardwoods ~ 18-25% have been reported to be more reactive than those found in softwoods containing 25-35%, which is attributed to the presence of more syringyl. When lignin is subjected to heat treatments, it decomposes at around 280-500 °C, producing a complex mixture of polyhydroxylated and alkylated phenol compounds, following cleavaging and scissoring of bonds [106].

2.3.2 Cellulose

Cellulose is composed of repeating d-glucose (C-6 sugar) units in a linear form, housed within the secondary cell wall of plants, with the generic formula represented by $(C_6H_{10}O_5)_m$ [106]. It is considered the most abundant organic lignocellulose fraction on Earth, with ~35-55% present in biomass by weight [101]. It makes up the fibres in woods and is insoluble, with polymeric units showing high molecular weights (up to 500,000) and polymerisation levels up to 10,000 [102]. Cellulose composites confer rigidity to the plant's cell walls via its microfibril-like network within the carbohydrate matrix, enclosed in a hemicellulose pool and lignin bodies. Under heat treatment, it degrades at a temperature ~ 240-350 °C, producing dry cellulose and levoglucosan [107]. The structure withstands thermal depolymerisation well, compared to hemicellulose. The unstructured region within the cellulose structure possesses hydration waters, as shown in Figure 2-3, with several OH^- groups present, and these are evaporated following rupturing during heating processes.

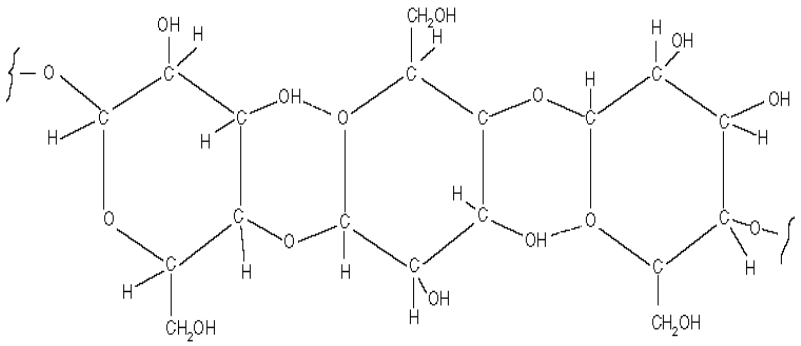

Figure 2-3-Chemical structure of cellulose [93]

2.3.3 Hemicellulose

Hemicellulose constitutes different monosaccharides, ranging from monomers like d -xylose, d-mannose and methyl glucuronic, representing 20-40% of a plant's matter, with a chemical formula of $(C_5H_8O_4)_m$, with *m* indicating the degree of polymerisation [106]. The presence of short side chains in hemicellulose, as shown in Figure 2-4, reduces their strength and tendencies to form hydrogen bonds across the polymeric chains. Klass reported that the polymerisation degree of hemicellulose is < 100-200. The composition and amorphous nature are dependent on the biomass type, with notable differences at the various parts of the plant [102].

When hemicellulose is subjected to 200-260 °C, it decomposes, yielding more gases than tar, due to stripping of its monomers' side branches [107]. Hemicelluloses in hardwoods are more reactive than those found in softwoods due to their varying proportions in the wood types, and these are evident during thermal processes. According to Basu, this behaviour is attributed to the high content of 4-o-methyl glucuronoxylan present in the hardwood, compared with the arabino-glucuronoxylan and galactoglucomanans found in softwoods [93].

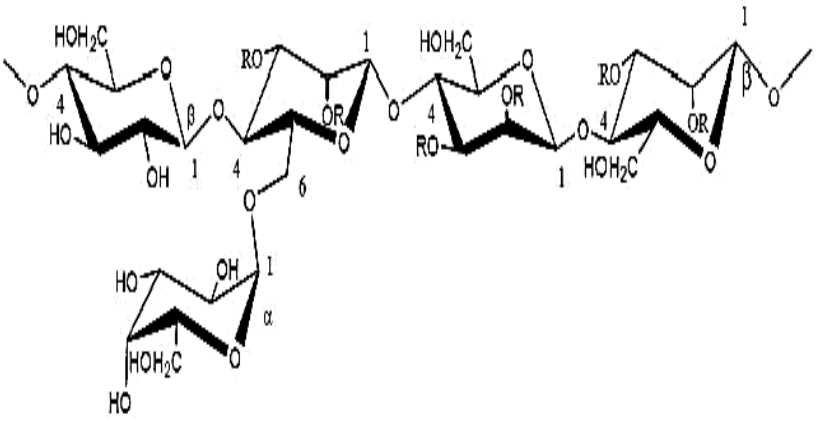

Figure 2-4-Chemical structure of hemicellulose [107]

2.4 Biomass use for energy application

The chemical energy stored in biomass underlies the motivation behind its consideration as an alternative replacement for fossil fuels. The complete replacement of fossil fuels is not entirely possible presently; however, biomass employment for cofiring would reduce GHG emissions. This approach has proven cost-effective, as CO_2 abatement costs for cofiring are much lower than when cofiring is not utilised in CCS [93]. A study by Basu has also reported that employing cofiring with biomass fraction at <10%, when fully established, can potentially reduce coal-powered plant performance drawbacks [93]. Van Loo and Koppejan suggested that an insignificant effect on combustion efficiency is likely during cofiring application when using ~ 3 to 5% of biomass, of moisture content < 10% [108]. Also, given a study carried out by Kasman and Berg, they concluded that biomass cofiring minimises the chances of alkali chloride formation, which is likely to react with traces of sulfur or aluminium silicate found in coal, and may trigger corrosion in biomass-powered systems [109]. The advantages of biomass cofiring have shown that the separation cost of CO_2 can be reduced in CCS applications for a typical PC plant, as shown in Figure 2-5 [93].

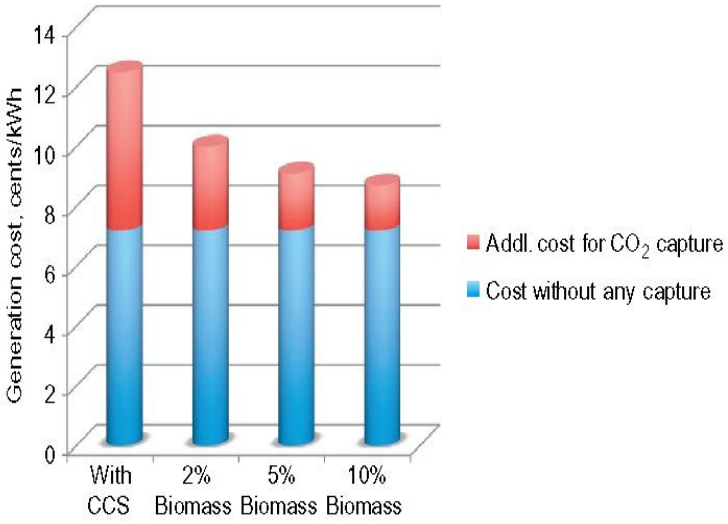

Figure 2-5-Cost of electricity with carbon capture and sequestration and carbon capture and sequestration-biomass cofiring percentage [93]

Given that biomass emits none or a reduced amount of NO_X, SO_X, mercury and fly ash compared to coal, this makes them adaptable for cofiring applications. The presence of calcium in biomass also provides a means of sulfur absorption that may have been released during co-combustion. Aside from this, when biomass is cofired with coal, it helps reduce N_2O emission, another major GHG, resulting from additional side reactions that may be occurring with the elements present in the biomass [110].

From a CCS perspective, cofiring in existing coal-fired systems can avoid significant levels of CO_2 being released during energy generation. However, findings have shown that using 100% biomass could pose technical constraints due to disparities in their properties compared with coal [93]. Although there are varying cofiring options, namely (a) direct cofiring, (b) indirect cofiring (gasification), and (c) parallel cofiring, each of these options have its process risks. For example, direct cofiring may cause interference with the boiler cofiring capability, which may often result in a need to reduce the biomass to coal ratio to < 5% [111]. In gasification, the separate handling of biomass may lead to vaporisation of alkalis in the biomass, which has the potential to cause fouling, slagging, and corrosion in the boiler tubings, while parallel cofiring increases the capital cost of operation, having to separately manage two boiler systems, as shown in Figure 2-6 [93].

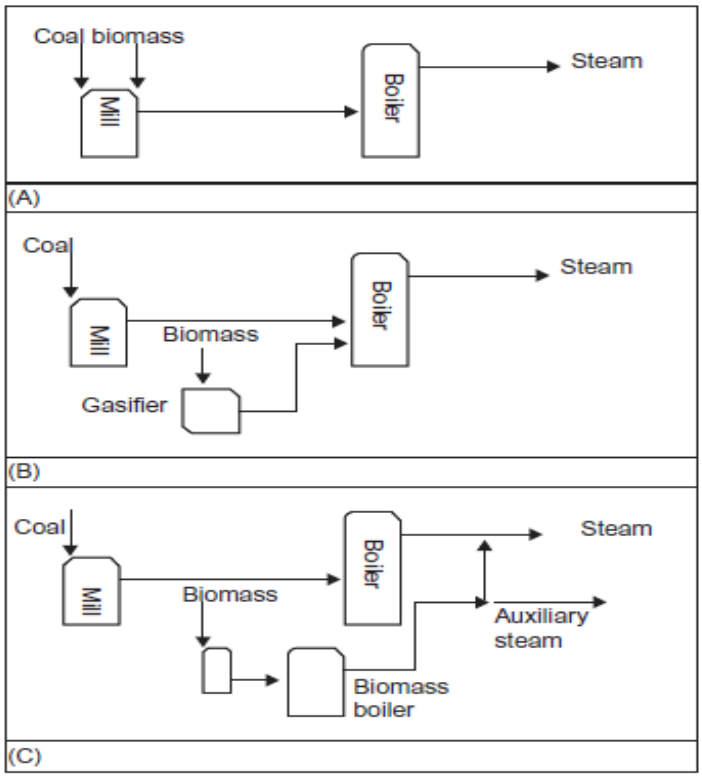

Figure 2-6-Options for biomass cofiring with coal [93]

Despite the benefits associated with the use of biomass, there seem to be drawbacks that make them unsuitable for cofiring applications. These include low bulk densities and the different varieties' fibrous nature, making their grinding very difficult and energy-intensive. Also, storage difficulties may be encountered due to these materials' tendency to absorb moisture over an extended storage period, thus allowing for harmful fungus growth [100]. More so, the rising cost of bioenergy production, land use for growing energy crops, and the possible unavailability of agricultural wastes, amongst other factors, may hinder biomass commercialisation. As a result, pre-treatment technologies, such as mechanical and thermal processing, have been employed to address these problems, resulting in different kinds of products like torrefied carbons, amongst other industrial chemicals and synthetic fibres [94].

2.5 Pre-treatment of biomass (torrefaction process)

Torrefaction is a means of improving biomass properties using heat treatments. The term originates from the French word '*torréfier',* meaning 'to roast', and was first used in the 1930s during a trial experiment for biomass utilisation as fuel for gasification purposes. Later, an industrial demonstration in the metallurgical industry, under the Pechiney process, employed torrefied wood feedstock as a reducing agent and coke alternative for silicone production [93]. Conventionally, torrefaction is alternatively known as slow pyrolysis. It is traditionally carried out in a non-oxidative environment at temperatures between 200-300 °C, resulting in a partly decomposed solid, with a characteristic change in the material features, as shown in Figure 2-7 [112].

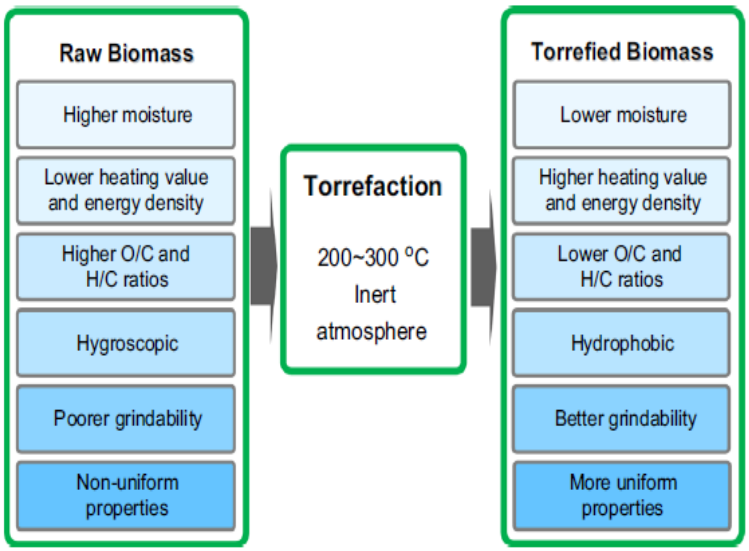

Figure 2-7-Property variations in biomass via torrefaction. Adapted from [100]

Contrary to the conventional methods, Uemura *et al*. suggested that the presence of oxygen, even at a minute fraction in a torrefaction reactor, could be beneficial to the formation of certain by-products [113]. The process begins with heating the biomass to the desired set temperature, where it dwells for a given time known as the residence time. Typically, torrefaction is grouped into light, mild and severe stages, on account of the operating temperature range, namely: 200-235, 235-275 and 275-300 °C, respectively [114]. Thermal conversions usually occur at a relatively low heating rate (< 50 °C min^{-1}), with residence times

of ~ 60 min (+/-) [112]. While higher heating rates have been reported to promote liquid yields, lower heating rates favour solid product formation [115]. Ragland, Aerts and Baker, also pointed out that the thermal conductivity of woody biomass increases at the rate of ~ 0.2% per °C, resulting in a 10% increase per 50-degree temperature rise [116]. Some selected properties of the solid product, such as microporosity, a type of pore network found in porous materials, are often developed at lower heating rates. By contrast, rapid heating rates promote macropore (a type of pore) formation, with both micro and macropores significant for gas adsorption processes [115]. Other products obtainable from torrefaction vary according to temperature ranges, with tar production occurring at temperatures of 300-320 °C, and this is the reason torrefaction in most cases is limited to a temperature of 300 °C [117].

2.6 Types of torrefaction

2.6.1 Wet torrefaction

This type of torrefaction is referred to as hydrothermal carbonisation (HTC). It entails the pre-treatment of biomass in a hot compressed aqueous medium under saturated vapour pressure. The process occurs at temperatures ranging from 180-260 °C, for about 5-240 min, before employing explosive decompression, which helps rupture the fibrous structure of the biomass [100]. During HTC, water, CO_2, and other compounds are cleaved from the biomass structure, resulting in high char yield production with improved energy density and calorific value. Wet torrefaction has been reported to enhance the biomass's properties compared with the conventional methods [118]. These have attributed to the fact that biomass upgrading in the aqueous phase entails adding additives, such as acids, to improve the wet torrefaction processes. Additionally, Lynam *et al.* suggest that the inclusion of a particular solution, e.g., acids or other materials, to the aqueous phase promote carbonisation, yielding improved torrefied biomass [119].

2.6.2 Oxidative torrefaction

Oxidative torrefaction is performed under air-induced conditions within a temperature range of 200-300 °C. This approach is considered cost-effective, given the elimination of the use of inert gases. The oxidative reaction is exothermic, and as a result, less external energy demand is required, unlike the endothermic biomass torrefaction cases. Given that torrefaction is carried out in an oxidative environment, the reaction rates are faster, and they are promoted by shorter residence times. Wang *et al.* investigated the influence of oxidative environment during torrefaction and reported that they support rapid decomposition of the biomass, even at reduced torrefaction time and temperature [120]. Another study carried out by Rousset *et al.* using Eucalyptus wood, torrefied under 21 mol% oxygen over different temperatures, agrees with these findings [121], thus supporting the argument presented by Uemura *et al.*, with an indication that increased oxygen levels affect the charring and energy yield of torrefied biomass.

2.6.3 Steam torrefaction

Steam torrefaction, otherwise known as steam explosion, employs saturated or superheated steam for the biomass pre-treatment and is usually performed at 200-260 °C for 5-10 min, followed by a rapid decompression process [122]. Following the steam explosion, low molecular weight volatile matters are liberated. Unlike in conventional torrefaction, the torrefaction severity, in this case, is determined by increasing the steam temperature or explosion time. It has also been reported that improved torrefied biomass properties could be obtained using this process compared with those of non-oxidative torrefaction, even at lower temperatures and treatment times [123].

2.7 Parameters controlling torrefaction processes

2.7.1 Temperature

Temperature is one parameter that significantly influences torrefaction. It brings about the destruction of biomass building blocks, thereby altering the nature of the by-products. Prins

reported a change in the weight of solid residues across different torrefaction temperatures [117]. Their findings concurred with the results reported in a similar study by Deng *et al.*, but with a noticeable change in compositional elements and weight loss [124]. Although the temperature remains a significant factor, Bergman *et al.* suggested that different biomasses induce different reactions even under similar torrefaction conditions, as is evident for the case of fibrous and woody biomasses [112].

According to Cielkosz and Wallace, disparities often witnessed in mass yields are governed by an exponential function (t/T), relating to the temperature (T) and time (t) of treatment, with increased temperatures bringing about low mass and energy density of the torrefied material [125]. The temperature influence during torrefaction is also closely related to the size of the given biomass material. As the biomass size becomes small, the temperature gradient between the exposed surface and the core also becomes smaller due to little heat resistance, comparable to larger biomass sizes, where a finite temperature gradient may exist [93]. This suggests that the core temperature is very significant during biomass decomposition compared to the external surface temperature. This is why torrefaction set temperature slightly overshoots by one or two degrees; a case often witnessed during bench-scale laboratory experiments. The degree of overshoot is a function of the extent of thermal flux through the core of the biomass material, as well as its size; an indication of exothermic reaction occurrence.

2.7.2 Residence time

Residence time also affects the properties of biomass during torrefaction. It is known as the time during which the biomass dwells in the reactor after being heated to the desired set temperature before cooling under a flow of inert or non-inert gases [126]. Although the torrefaction time is less significant than temperature, a minimum or maximum residence time can result in different final products' degradation characteristics, such as grindability [127]. The effect has also been reported in a study by Arias *et al.*, where the residence time affected the grindability of eucalyptus wood torrefied at the temperature range of (220-500 °C), with slight improvement recorded for the torrefaction carried out at 240 °C for residence times beyond 30

min [128]. These findings were supported by Pimchuai [129] using five different biomass samples, who concluded that increased dwell time promotes torrefied solids formation with better calorific value. By contrast, a study carried out by Stelt *et al.* noted that longer torrefaction time results in lower mass yield product and an increased energy density solid, but the effect was less pronounced after 60 min [130].

2.7.3 Heating rate

The heating rate, measured in °C min^{-1}, as a controlling parameter, influences the extent to which secondary degradation reactions occur during torrefaction as it affects by-product distribution [131]. Heating rate effects have been noted to favour the production of large amounts of tar precursors, which are commonly evident in the devolatilization stages of biomass degradation, where cracking and reforming of vapours are supported by high temperature and residence time conditions. According to Di Blasi, chars gasification reactivity is influenced by high heating rates and shorter residence times, owing to limitations to induce secondary char production at this stage [132].

Kumar *et al*. further suggest that the impacts of heat and mass transfer within the biomass increase with increased heating rates [133]. However, other researchers who investigated the effect of heating rates on products composition reported that such changes are related to the distribution of by-products. Also, secondary reactions often dominate at higher heating rates, resulting in high gas yields production [134]. Given that lower heating rates result in the formation of char residues due to repolymerisation of the intermediate products, higher heating rates, by contrast, lead to the creation of gas products due to re-decomposition reactions, and a given rate can result in an extensive fragmentation or minimisation of the secondary reactions. Therefore, an economic balance needs to be established in overcoming heat transfer limitations, and a great deal of attention is necessary to understand the mechanism associated with the entire conversion process.

2.7.4 Use of gas medium (inert and non-inert)

Although torrefaction has traditionally been carried out under an inert atmosphere, several studies have investigated non-inert and oxidising gases' influence on lignocellulosic biomasses' energy characteristics. In this light, biomass conversion effects under the flow of N_2, O_2 and CO_2 atmospheres, at varying concentrations and temperature (220, 250 and 300 ^oC) conditions were investigated for solid-phase conversion by Uemura *et al.*, using palm kernel shell [135]. Their findings reported that the severity order of torrefaction using the different gases is in the order of $O_2 > CO_2 > N_2$, with the van Krevelen plots evidencing a commonality in the trend of the various gases. In the case of torrefaction with CO_2, whose effects were more pronounced, particularly at 300 ^oC, the severity may have been induced by the CO_2 compared to N_2. The thermal conductivity of CO_2 gas may have permitted higher heat transfer through the surface gas films, more elevated than the nitrogen gas. Also, the chemical effects induced by the CO_2 may be associated with the Boudard reaction between the CO_2 gas and the carbon surfaces [135].

Other researchers also torrefied eucalyptus wood chips, of sizes 10 × 40 × 80 mm, under 21 vol.% of oxygen at 240 and 280 °C in a fixed bed reactor, and reported the solid product energy yield decreasing considerably at 280 °C [136]. They also opined that the torrefaction rate was more enhanced at 280 °C, compared to 240 °C. These findings correlated well with the study carried out by Lu *et al.*, where torrefied oil palm fibre and eucalyptus wood chips, investigated under nitrogen and an air atmosphere at 250-350 °C, reported that torrefaction in air results in lower solid and energy yields than with N_2 [137]. Wang *et al.* carried out a similar investigation using spruce sawdust in 21 vol.% oxygen at 260-300 °C and found that an oxygen atmosphere results in a slightly weaker torrefaction product; however, they concluded that non-oxidative torrefaction produces better solid yield results than oxidative torrefaction [138].

2.7.5 Feed (particle) size

The particle size of biomass may range from a whole tree to the smallest piece of sawdust, including processed woody pellets. The variation in size affects torrefaction reaction rates from

a thermal flux's perspective within the biomass interior, thus, influencing product formation. As torrefaction entails thermal flux movement by convection from the reactor onto the material's external surface before conduction into the inner part, the enormity of torrefaction influences the products. As reported by Prins *et al.,* for wood pyrolysis below 300 °C (particle size < 2 mm), the influence of heat transfer was of little importance considering the particle size [117]. Additionally, Peng *et al*. investigated pine sawdust's torrefaction of varying sizes (< 1 mm). They found that increased rates at higher temperatures affect the mass yield of the solid products, given the size of feed investigated [139]. These discrepancies in the mass yield suggest the extent to which the thermal flux through a given size of biomass under various heating rates influences solid yield.

The feed size, which governs the extent of thermal flux, is a function of the Pyrolysis and Biot numbers. While the Pyrolysis number expresses the ratio between the external surface heat transfer to that of the torrefaction reaction rate, on the contrary, the Biot number shows the ratio of heat convection through the external surface of the material and the heat conduction through the material core [93]. The biomass behaviour under varying thermal fluxes is related to the fraction of the lignocellulose components within the different biomass type. The influence is more evident upon the subjection of the biomass to similar experimental conditions. Prins *et al.* provided an insight into the behavioural disparity of lignocellulosic biomass constituents while comparing hard and softwoods under similar experimental condition. They reported a lower mass yield for the hardwoods compared to the softwoods and attributed this to the difference in their hemicellulose contents [117]. Given this, it was concluded that hardwoods promote the acetic acid release, while softwoods favour formic acid formation, even under the same torrefaction conditions, due to more xylan constituents in the hardwood [117].

2.8 Mechanism of torrefaction and the heating stages

During torrefaction, the dominant transport mechanism is the thermal flux that modifies the biomass's inherent properties due to heat impact. The mechanism involved can be broken into five different heating stages, described by temperature-time and heat load-dependent profiles, as shown in Figures 2-8 and 2-9 [112].

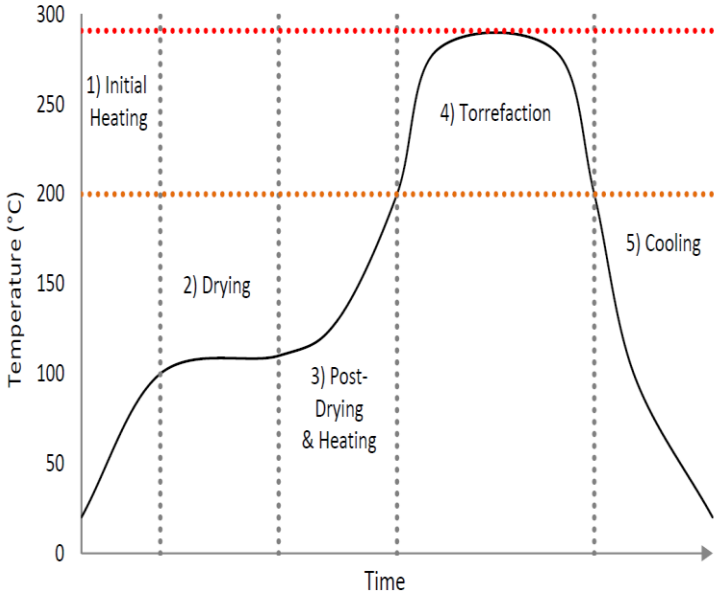

Figure 2-8-Temperature-time profile during biomass torrefaction [112]

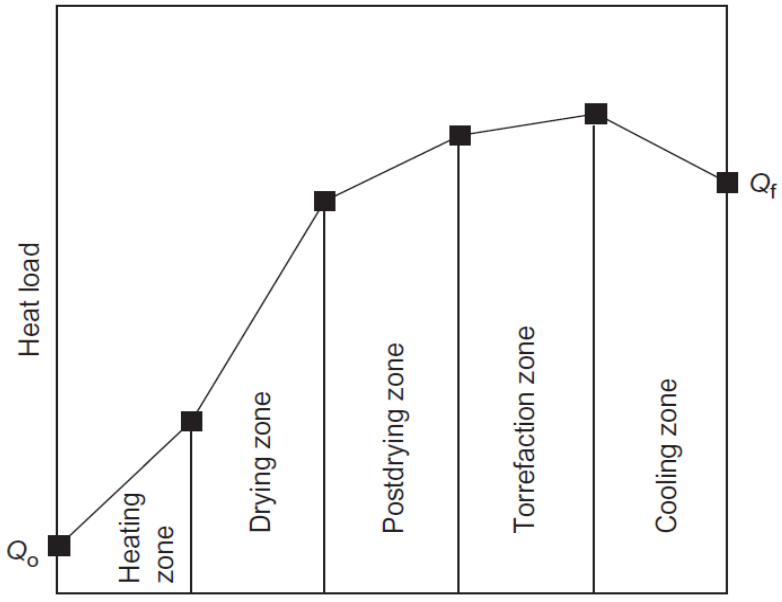

Figure 2-9-Heat load profile of biomass sample undergoing torrefaction [140]

Stage 1 defines the initial heating (pre-drying) stage, considered as a non-reactive drying period during which the biomass is heated above room temperature to about 100-105 °C, with no marked changes noticeable in the chemical compositions [141]. This results in the

evaporation of all physical moisture that is present in the biomass, with the energy spent represented by Equation 2.1 [94]:

$$Q_{pd} = M_{f1} C_{pw} (100 - T_o) / h_{upd} \quad \text{Equation 2.1}$$

where, Q_{pd} = energy required for pre-drying

C_{pw} = specific heat of biomass

M_{f1} = mass of raw biomass

T_o = temperature of feed

h_{upd} = energy efficiency factor for pre-drying (accounting for furnace heat losses)

The value of C_{pw} is dependent on the temperature and moisture content of the wood, at a given temperature, for which, at temperatures below 106 °C for various wood species, Equation 2.2 can be applied for the determination of C_{pw} [140]:

$$C_{pw} = 0.266 + 0.0116\,(\theta - 273) \quad \text{Equation 2.2}$$

Where, θ = Biomass temperature (^{o}C)

Contrary to Equation 8 proposed by Jenkins, and given the temperature limitations, TenWolde *et al.* suggested a generic equation that may be employed for estimation of specific heat capacity (C_p) of dry woods, at any given temperature, represented in the form of Equation 2.3 [142]:

$$C_P\,(dry) = 0.1031 + 0.003867\theta \quad \text{Equation 2.3}$$

Alternatively, the heat capacity of any biomass *(CH_mO_n)* can also be evaluated using the empirical equation based on Kopp's rule, by summing the atomic heat capacities of the individual elements that constitute the solid in its solid-state [143] [144]. An example of dry woody biomass heat capacity at different temperatures, based on percentage moisture fraction, is shown in Table 2-1 [116].

Table 2-1-Heat capacity of dry woods at different temperatures [116]

Temperature (K)	heat capacity (kJ kg^{-1} K^{-1})			
	c(dry)	c(5%)	c(12%)	c (20%)
280	1.2	1.3	1.5	1.7
300	1.3	1.4	1.7	1.9
320	1.3	1.5	1.8	2.0
340	1.4	1.6	1.9	2.2
360	1.5	1.7	2.0	2.3

Stage 2, also referred to as the drying stage, is often considered the most energy-intensive stage of torrefaction, where all the free moisture inherent in the biomass is evaporated. This occurs before the biomass attains the critical moisture level, where the temperature begins to rise. Upon attainment of the critical moisture level, the evaporation rate diminishes, and a further increase in temperature brings about an additional energy demand represented by Equation 2.4 [93]:

$$Q_d = L\, M_f M\, / h_{ud} \qquad \text{Equation 2.4}$$

where Q_d = Energy spent on drying stage

M_{f1} = mass of raw biomass

M = Mass of moisture in M_f (%)

L = Heat of vaporisation of water at 100 °C ~ 2,260 kJ kg^{-1}

h_{ud} = Efficiency of energy used for drying section

Stage 3, known as the post-drying heating stage or reactive drying, during which the biomass heating progresses toward the onset of torrefaction at 200 °C. The bound waters associated with the biomass material are freed at this stage, while structural deformity is evident alongside light volatile fractions [93]. Energy demand at this stage is relatively low, given that the material would have been dry; hence, the sensible heat gained can be estimated from Equation 2.5 [93]:

$$Q_{pdh} = M_f(1 - M)C_{pd}(1 - 100))\, / h_{u,pdh} \qquad \text{Equation 2.5}$$

where, Q_{phd} = Energy spent for drying stage

C_{pd} = Specific heat dry biomass (from stage 2)

$h_{u,pdh}$ = Efficiency of energy used for the post-drying section

M_{f1} = mass of raw biomass

T_t = Temperature onset of torrefaction

Stage 4 is known as the torrefaction stage, where extensive depolymerisation of the biomass structure commences at ~200 °C. Components of the biomass, such as hemicellulose, begin to degrade at this temperature due to breaking the C-C and C-H bonds in the biomass structures [141]. The extent of torrefaction causes a marked change within the biomass structure, while reactions above this temperature, within 250-300 °C, as reported by Prins *et al.,* are considered exothermic [117]. Little energy is required at this stage to compensate for inevitable heat losses from the reactor, which may be represented by Equation 2.6 [93]:

$$Q_{tor} = H_{loss} + M_f\,(1 - M)X_t \qquad \text{Equation 2.6}$$

where Q_{tor} = Energy spent on torrefaction stage

H_{loss} = Heat loss from reactor (furnace) into ambient (related to reactor design)

X_t = Parameter governed by the extent of heat absorbed for torrefaction stage (kJ kg^{-1})

M_{f1} and M = mass of raw biomass and mass of % moisture in M_{f1}

Stage 5 is the cooling stage after torrefaction, prior to the biomass being removed from the reactor at room temperature (T_p). The torrefied biomass cools naturally to the desired temperature, with no noticeable mass loss. However, a number of studies have shown that heat extracted during the cooling stage could be recycled as a heating medium for further torrefaction process [93]. Although energy addition is negligible during this stage, extracted heats from the product may be represented by Equation 2.7 [93]:

$$Q_C = M_f(1 - M)\,MY_{db}C_{pt}(T_t - T_p) \qquad \text{Equation 2.7}$$

where, Q_c = Extracted energy (energy out)

MY_{db} = Mass yield after torrefaction

M = Mass of moisture in M_f (%)

C_{pt} = Specific heat of the biomass at chosen torrefaction temperature

T_t = Torrefaction temperature

T_p = Final cooling temperature (starting room temp)

M_{f1} = mass of raw biomass

2.9 Energy balance of torrefaction

As explained in the previous section, the heating requirements at the different stages (1 to 4) may be considered the energy demand of a given torrefaction process, which may be equated to the cooling stage's extracted energy. However, in cases where the reactor design parameters are lacking, a rough estimate using the generic pyrolysis equation may be applied for quick energy balance calculations using Equation 2.8.

$$m_{fuel}H_{fuel} = H_{pyr} + m_{char}H_{char} + m_{vol}H_{vol} \quad \text{Equation 2.8}$$

where, m_{fuel} = mass of raw biomass (fuel)

H_{fuel} = heating value of raw biomass

m_{char} = mass of solid product

H_{char} = heating value of char

m_{vol} = mass of volatile matters produced

H_{vol} = heating value of volatile liberated

H_{pyr} = energy spent in process (energy consumption)

Figure 2-10 shows a typical energy and mass balance of a torrefaction process. However, for a bench-scale torrefaction experiment using a vertical or horizontal tube furnace, which can be viewed as a direct heating method, the biomass material is usually loaded in a crucible and placed inside a reactor, eliminating the influence of loading rate.

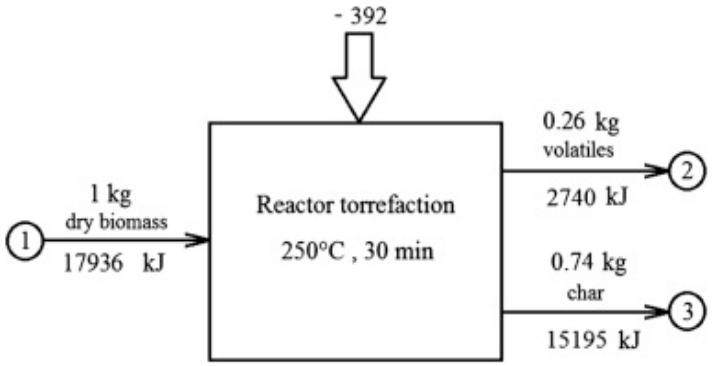

Figure 2-10- Energy and mass balance of torrefaction at a different operating condition [145]

Even though most torrefaction processes occur under the flow of a gas medium, energy and material balances can be evaluated on a static basis. In principle, although the entire energy-related stages are grouped into 5, the primary unit operations identified are drying (pre-drying, drying and post-drying), torrefaction, and cooling, with each having its associated energy load requirement that can be factored into the entire process energy picture. Following the identified stages mentioned above, the heat load required for the drying stage, up until the onset of torrefaction at 200 °C (T_t), may be represented by the sum of the energy load for stages 1, 2 and 3, expressed as Q_d [93]. However, since heat losses are inevitable from the reactor during the successive drying stage operations, the actual heat demand, taking consideration of the heat losses, may be represented as Q'_d [93]:

$$Q'_d = Q_d/(1 - X_d) \qquad \text{Equation 2.9}$$

where, X_d = total fraction of heat loss during drying stages 1-3

Furthermore, because torrefaction is considered a gradual decomposition process of biomass, the biomass may require a higher residence time to allow for both exothermic and endothermic reactions to occur, with heat demand at this stage small or even negligible. Therefore, the total energy load (Q_{total}) necessary for the torrefaction stage (Q'_{tor}) can be equated to the heat extraction from the reactor (Q_c), depending on the reactor insulation factor. Given this, the total energy load for each of the drying stages 1 to 3 and that of the torrefaction stage 4, representing the sum of energy added to the torrefaction process, equals Equation 2.10 [93]:

$$Q_{total} = Q'_d + Q'_{tor} \qquad \text{Equation 2.10}$$

After torrefaction, the torrefied biomass cools down to the starting or room temperature (25 °C), during which heat energy given off may be recovered from the (cooling) operation (Q_c). Therefore, based on the energy balance principle regarding the heating stages, the total heat load for the torrefaction (Q'_{tor}) may be equated to the partial heat energy recoverable from the cooling stage process, from where the final energy balance can be estimated using Equation 2.11:

$$Q'_{tor} + Q'_d = Q_c \qquad \text{Equation 2.11}$$

However, where all parameters relating to the reactor design are not available, the Q_c shown in Equation 2.12 may be employed to estimate the equivalent total energy utilisation for a torrefaction process.

$$Q_c = M_f\ (1 - M) M Y_{db} C_{pt} (T_t - T_p) \qquad \text{Equation 2.12}$$

Despite Equation 18, other alternative equations have been considered for determining energy consumption during torrefaction processes. According to Chen et *al.*, heat input during a torrefaction process is conveyed by the carrier gas, whose enthalpy is a function of the carrier gas's specific heat capacity at the selected torrefaction temperature range [146]. Also, considering the incremental changes in enthalpy of the carrier gas, this allows for energy input (consumption) of such process to be estimated, by taking into account, the molar flow rate of the carrier gas and the residence time of the torrefaction process, as shown in Equation 2.13,

where ΔH_T, is obtained from the specific heat capacity of the gas, as suggested by Cengel [147]:

$$E_{(in)} = \Delta H_T \times Q \times t \quad \text{Equation 2.13}$$

where,

E_{in} = energy input (kJ)

ΔH_T = enthalpy of carrier gas (kJ kmol^{-1}) [$\Delta H_T = \int_{25}^{T} C_p \, dC$)].

$C_p = a + bC_p + cC_p^2 + dC_p^3$, [for CO_2 gas, a = 22.26 KJ (kmol.K)$^{-1}$, b =-5.981 x 10^{-2} KJ (kmol.K)$^{-1}$

c =-3.501 x 10^{-5} KJ (kmol.K)$^{-1}$, d =7.469 x 10^{-9} KJ (kmol.K)$^{-1}$]

Q = molar flow rate of CO_2 gas (kmol min^{-1}) - 100 ml min^{-1} used = 4.082 x 10^{-6} kmol min^{-1} as reported in [148] for N_2.

t = torrefaction residence time (min)

T(upper limit) = torrefaction temperature selected

T_{25} = room temperature (25 °C or 298 K)

2.9.1 Mass balance of torrefaction

The mass balance of a torrefaction process is related to the nature of the torrefaction process employed (wet, oxidative or steam). For a batch process such as the one considered in this research, the inputs to the reactor are the loaded raw biomass samples, the N_2 or CO_2 gases, while the output splits into the solid and the gaseous products-classified into condensable and noncondensable by-products; such as water, acids and other gaseous products, as evidenced in the study by Tumuluru *et al.* [103].

However, as the current study is limited only to analysing the torrefied solid product from the torrefaction process for CO_2 capture application, the final solid mass would be determined by

carrying out a simple mass balance, based on the difference in weight of the sample before and after torrefaction. The results obtained thereon would also help estimate the mass and energy yield for each torrefaction process. A diagrammatic representation of the mass balance for a typical wet torrefaction process is shown in Figure 2-11, and it is expressed in Equation 2.14.

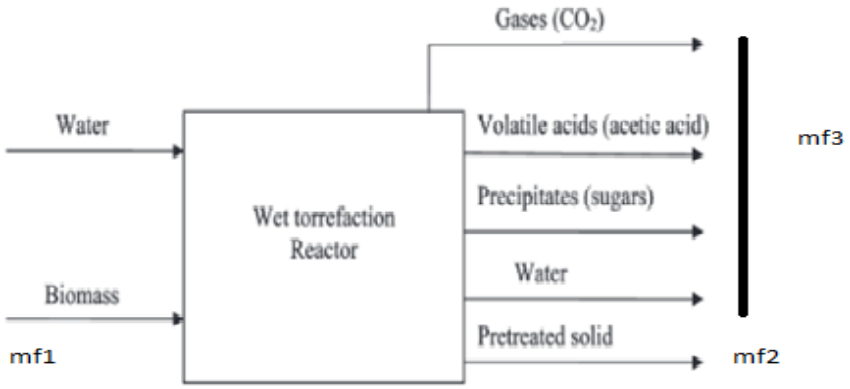

Figure 2-11-Typical mass balance for a wet torrefaction process [149]

Mass Balance Equation (solid product)

$$M_{f1}(initial\ mass) - M_{f2}\,(final\ mass) = M_{f3}(mass\ loss) \qquad \text{Equation 2.14}$$

2.10 Behaviour of lignocellulosic components during torrefaction

The degradation of lignocellulosic constituents of biomass under torrefaction occurs during both endothermic and exothermic reaction temperature regimes. However, due to variation in the original compositions, the components react differently without displaying a combined effect [150]. Under mild pyrolysis conditions, part of the oxygen within the hemicellulose structures is consumed during the exothermic reaction scheme, bringing about hemicellulose degradation. The same applies to lignin, but given its increased content, the reaction may be more extreme during decomposition [151].

For cellulose, the decay occurs via an endothermic reaction scheme due to oxygen depletion. However, in this case, the reaction can be progressed towards the exothermic with increasing torrefaction condition, enhancing tar formation [152]. Yang *et al.*. reported an independent

behaviour of the different lignocellulosic components using thermogravimetry technique and found that under light torrefaction conditions (at 220 °C), the hemicellulose fraction degrades faster with a maximum weight loss distinct at 268 °C [153].

Conversely, the cellulose and lignin components were slightly affected at this temperature. While the maximum mass loss for cellulose occurred at 355 °C, the lignin decomposed slowly due to its high thermal resistivity, as evident in Figure 2-12. Contrary to these findings, Chen and Kuo's related study, based on increasing torrefaction temperature at a fixed residence time, reported a proportional degradation of the lignocellulosic components with increasing temperature lines [114].

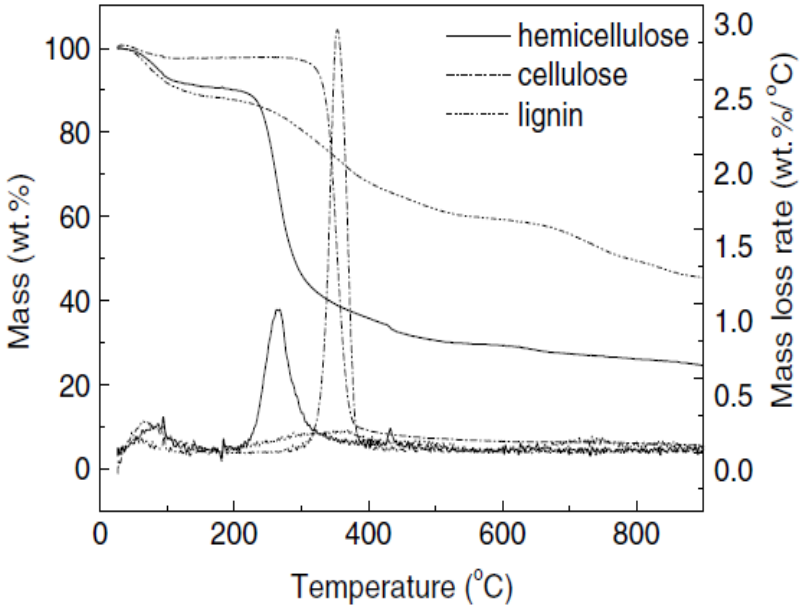

Figure 2-12- Pyrolysis of lignocellulosic components via thermogravimetry study [153]

2.11 Products of torrefaction process

Products formation during torrefaction results from the decomposition of the biomass constituents into solids and volatiles [141]. The volatile products constitute condensable (liquid) and non-condensable (gaseous) products, whose formation is governed by torrefaction severity. Prins *et al.* reported that steam is the primary volatile product, alongside other organics, with the gaseous product consisting of 80% CO_2, 20% CO, and small fractions of H_2 and CH_4 [154]. The degradation that led to varieties of these products does not occur entirely

due to temperature variation. The non-condensable products formed are a consequence of dehydration and decarboxylation reactions taking place within the biomass matrix, and not limited to degradation, resulting in the formation of CO, CO_2, and a fraction of CH_4, while the condensable products, namely lipids, organics, carbon and water are also being formed [93] [112].

The liquid organic fraction liberated may be separated by further unit operations into acetic acid and formic acid. The liquid products from hardwoods such as acetic acid and those from softwoods, i.e., formic acid, are not the same in most cases [117]. The difference in product distribution may be akin to the percentage difference in their hemicellulose contents. CO_2 production has been attributed to the decarboxylation reactions of sugar moieties, while CO formation is linked with reactions that occur when the steam, liberated during dehydration, reacts with CO_2 within the resulting pores [155]. The cumulative mass loss from each of the lignocellulosic constituents in the biomass after torrefaction may account for the total decline in the solid product's weight by the simple application of a material balance. Typical product composition formed during torrefaction is shown in Figure 2-13.

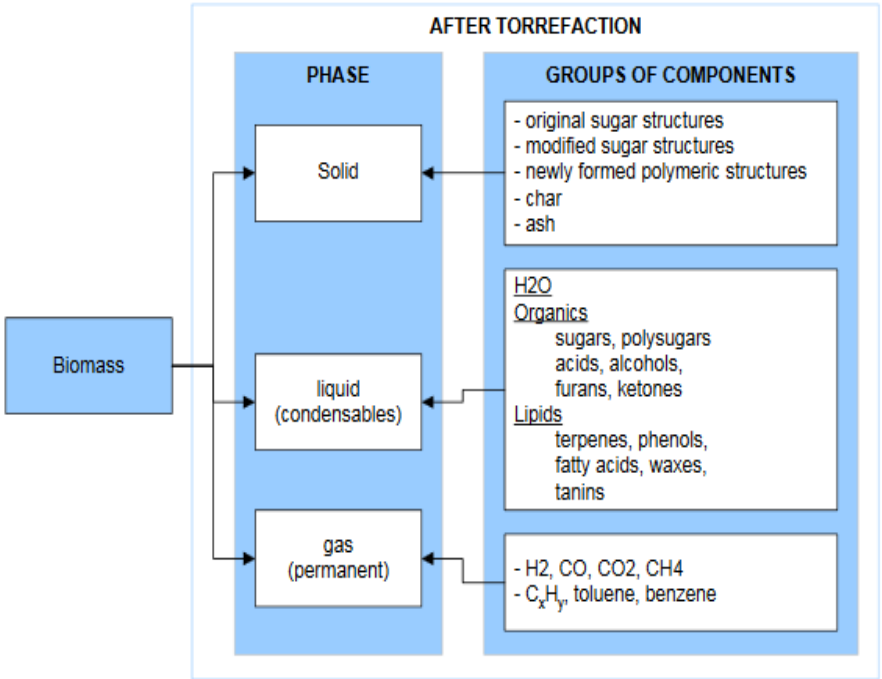

Figure 2-13-Products resulting from a torrefaction process [112]

Solid product yield varies in composition, texture and mass, as the moisture content in the starting material continues to reduce while volatiles are being given off. The moisture often appears in the form of -OH groups linked to the hemicellulosic and cellulosic structures. More so, as most adsorption processes occur around the polar region in porous solids, increased heating will promote a hydrophobic product formation with a non-polar behaviour [156]. Cellulose is a highly crystalline matter, and the reduction of the -OH group within its structure will further improve its crystallinity, thus preventing moisture access to the adsorption binding regions within the structure [156]. Kymalainen and co-workers studied the changes in the -OH groups of woody biomass following mild pyrolysis. Their findings suggest reducing OH groups with increasing temperature, as shown in Figure 2-14 [156]. This shows the impact of temperature on the -OH group present in the cellulose structure.

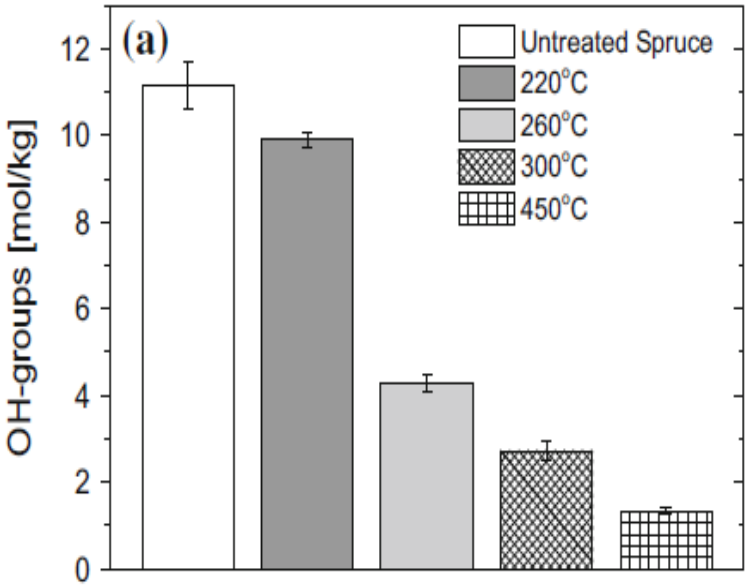

Figure 2-14-OH group change following pyrolysis of woody biomass at different temperatures [156]

2.12 Chemistry of torrefaction processes

As mentioned previously in Section 2.3, the lignocellulosic constituents make up the biomass building blocks in several mono and polysaccharides' fractions. For a greater insight into torrefaction chemistry, it may be logical to study the dominant units' behaviour in each of the lignocellulosic components during reactions from an independent point as a determinant factor for torrefaction performance.

In a study by Prins *et al.* on weight loss kinetics of different woody biomass, using xylan as a reference for hemicelluloses, xylan's thermal decomposition commenced at a temperature of 200 °C, with an increase in weight loss observed [117]. The findings agreed with the study reported by Shen [157], suggesting that early hemicellulose degradation was due to the splitting of glycosidic bonds of the xylan side units, constituting 4-o-methyl glucuronic acid and O-acetyl, in a series of chemical reactions. The reactions bring about the formation of an unstable transitional compound, 1,4-anhydro-d-xylopyranose, which further undergoes side reactions with other xylan side units. Furthermore, Werner *et al.* distinguished the thermal behaviour of xylan extracted from coniferous and deciduous woods, where a remarkable difference at the onset of degradation was attributed to xylan variations in the different wood type [158].

For cellulose decomposition, Chen *et al.* investigated dextran's thermal behaviour as cellulose reference [114]. Cellulose is known to compose of β-d-glucopyranose linked by glycosidic bonds, whose decomposition is slightly affected compared with the hemicellulose even at the same temperature. The weight loss under different torrefaction temperature is shown in Figure 2-15.

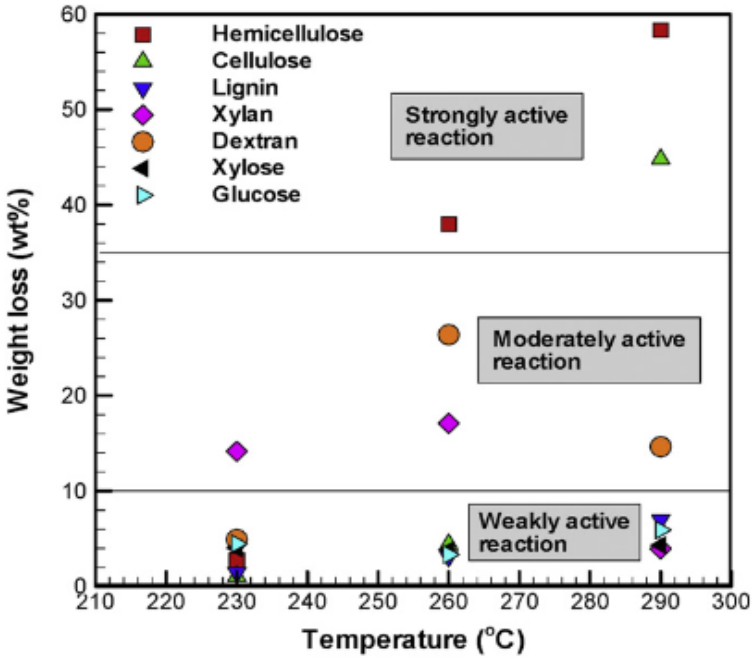

Figure 2-15-Weight loss kinetics of lignocellulose at different temperatures for 1hr [114]

Cellulose decomposition can be seen to occur via a three-step process, as reported by Kilzer and Broido [159]. One is at a temperature of 220 °C, under an endothermic reaction where the cellulose structure becomes dehydrated, producing anhydrocellulose. The second stage involves a competitive reaction at 280 °C, during which levoglucosan forms following the reorientation of anhydro-α-D-glucopyranose due to depolymerisation process, under the same endothermic regime. The third stage, exothermic, entails the decomposition of anhydrocellulose due to C-C and C-O bonds' rupturing within the cellulose structure. This sequence brings about emanation of levoglucosan radicals as shown in Figure 2-16, in the absence of oxygen bridging associated with the monomeric chains, and where hydride ion transfer occurs along the carbon-carbon chain, this induces I-6 oxygen linkages [160].

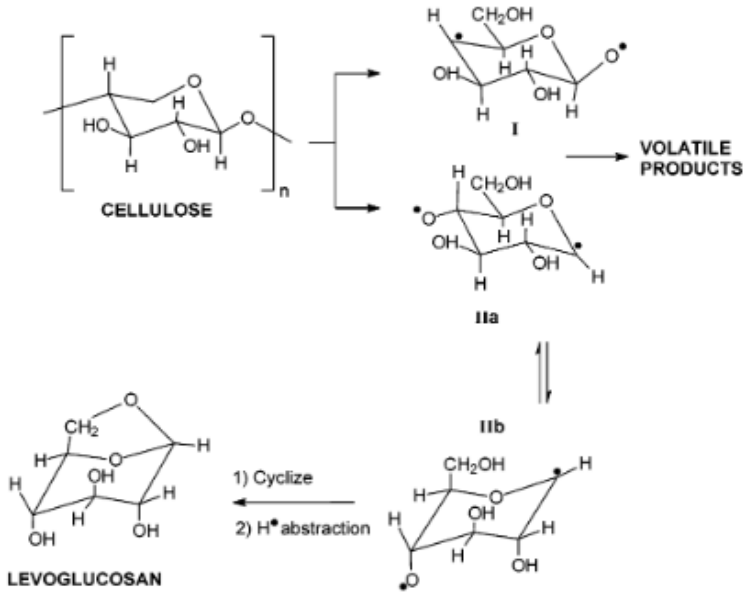

Figure 2-16-Cellulose decomposition mechanism following pyrolysis [107]

According to a study carried out by Jiang *et al*. on different lignin classes, their decomposition follows a free radical emanation route, where ether bond linkages are reduced due to scissoring of the methyl and hydroxyl radicals occurring along the C-C chains [105]. These reaction schemes promote phenols and chars' formation due to lignin's resistivity to thermal dehydration [160].

In general, wood chemistry under pyrolysis induces several reaction steps, including dehydration and depolymerisation reactions due to bond scissoring, resulting in moisture removal, carbonyl, and carboxyl radical reaction, which, upon devolatilization, produces CO and CO_2 [100].

2.13 Kinetics of torrefaction

Based on kinetics, torrefaction processes can be presented by a single-step kinetic model, according to Repellin *et al.,* as shown in Equation 2.15 [161]. However, the single-step kinetic model has been criticised by many researchers, owing to the inability to predict possible by-product distribution along the biomass degradation lines, as the model assumed that char conversion to volatile ratio is constant [162].

$$M_{f1} \rightarrow V + M_{f2}$$ Equation 2.15

Where M_{f1} = mass of raw biomass material

V = volatile liberated

M_{f2} = mass of torrefied solid

By considering likely possible reactions, Di Blasi and Lanzetta put forward a refined model, following the study of xylan decomposition, and suggested that biomass decomposition reaction follows a sequential and parallel mechanism described by a two-step mechanism, as shown in Figure 2-17 [162].

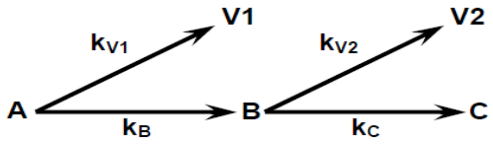

Figure 2-17-A two-stage kinetic reaction scheme of biomass decomposition [162]

Where,

A (M_{f1}) = mass of raw biomass

C (M_{f2}) = mass of torrefied biomass

B = intermediate product

V1 and V2 = volatile products at different reaction stages

K_B and K_C = arrhenius rate constants

According to the Di Blasi and Lanzetta model, the initial stage represents when competitive production of volatiles and transitional products occurs, consequent to depolymerisation and cleavage of the xylan bond monomers at a fast rate. The second stage entails decomposing the cleaved sugar moieties, which occurs slowly due to cellulose decomposition, compared with the first stage, accounting for the hemicellulose decomposition. The result of the kinetic

study agrees with the findings reported by Bach *et al.* [163], where the initial stage was confirmed as proceeding at a higher conversion rate, compared to the penultimate step, based on the rate constant values.

Also, based on a different perspective, Branca and Di Blasi presented a kinetic model of wood pyrolysis [164]. They classified the kinetics according to the different reaction zones via three sequential steps at different temperatures, namely-depolymerisation, devolatilisation and charring.

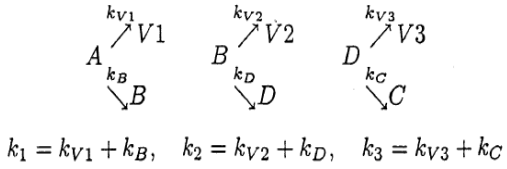

Figure 2-18- Three-step kinetic mechanisms of wood pyrolysis [164]

Where,

A (M_{f1}) = mass of raw biomass

C (M_{f2}) = mass of torrefied biomass

B = intermediate product

V1 and V2 = volatile products at different reaction stages

K_B and K_C = arrhenius rate constants

K_D = third stage reaction rate constant

D = third stage reaction by-product

Overall, based on the literature review on biomass torrefaction, it is evident that different types of product are obtainable at different torrefaction levels and conditions. The products (solid, liquid and gas) formed reflects the reaction state at a given stage of the torrefaction process. As a result, the choice of torrefaction condition would ultimately influence the nature of the desired product. However, while the current work aims to develop a renewable sorbent 'torrefied carbon', the choice of torrefaction conditions are vital in meeting the study objectives. Therefore, the next section of this work would undertake a literature review surrounding sorbent's application in adsorption processes. Adsorption theory would be tested on the sorbent's performance, following their characterisation based on the torrefaction conditions applied, which would reveal, in detail, the property changes as governed by torrefaction performance.

2.14 Adsorption basics

Adsorption is a consequence of saturation of unbalanced forces on a solid surface, allowing the attraction of gas molecules to condense onto it [165]. The atomic theory provides further clarity because atoms exposed on solid surfaces are incompletely bound, and therefore, are energetically favoured to attract molecules of opposite charges to condense onto themselves. According to quantum–mechanical theory, these atoms close to each other are often separated by a distance, where a quantum state is established. However, the consequence of a change in one atom's electronic cloud density induces a corresponding electrical moment on another atom, causing attraction [166]. The attraction force $U_A(r)$, which occurs from a short distance, where the individual atoms exhibit a form of potential energy, is represented by Equation 2.16 [166]:

$$U_A(r) = -C/r^6 \qquad \text{Equation 2.16}$$

Where C = polarisabilities of the atoms (-ve sign indicates attraction)

r = distance between the atoms

In addition to the attraction (dispersion) force, a repulsion force also dominates at close proximity, where an overlap of the atomic orbital occurs, expressed as $U_R(r)$ in Equation 2.17 [166]:

$$U_R(r) = b/r^6 \qquad \text{Equation 2.17}$$

Where b = an empirical constant

Given the above, the attraction and repulsion forces at play at interfaces account for adsorption phenomena, as outlined by the Lennard-Jones potential diagram in Figure 2-18.

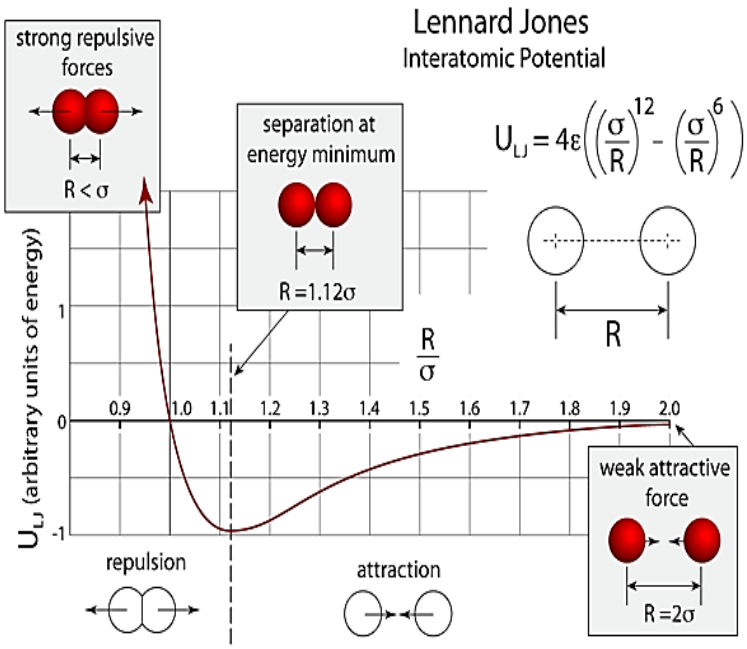

Figure 2-19-The Lennard-Jones potential – atoms in motion, indicating regions of attraction and repulsion [167]

Furthermore, by virtue of the energy potential exhibited by the gas molecules within an evacuated system, only a limited amount of the gas molecule would be removed from the gas phase and either held to the surface of the solid or move freely over the surface in a two-dimensional fashion [168]. This behaviour of the gas molecule, which is occasioned by a drop in the energy potential, is such that their distance from the solid surface must be at the very minimum for adsorption to occur. The 12-6 Lennard-Jones describe the overall interaction energy between the adsorbed gas molecule and the solid surface in the form of pairwise interaction, expressed by Equation 2.18 [167]:

$$U(r) = 4\varepsilon[(\sigma/r)^{12} - (\sigma/r)^{6}] \qquad \text{Equation 2.18}$$

Where

Ɛ = well depth, a measure of attraction extent (the deeper, the stronger the attraction)

U (r) = intermolecular potential between atoms (when U (r), r = σ)

σ = Distance at zero intermolecular potential

r or R = distance between centres of two atoms.

For gas adsorption systems, the interphase comprises the adsorbent, the gas and the adsorptive space, as shown in Figure 2-20. As illustrated, the gas molecules in their adsorbed state are known as adsorbate; however, while in the gas phase, they are known as adsorptive [169]. Before an adsorbate is formed, mass transport of gas molecules must precede the adsorption taking place, during which a molecular layer of the adsorbed species is formed. Further surface interactions may result in different types of adsorption, either physical or chemical [170].

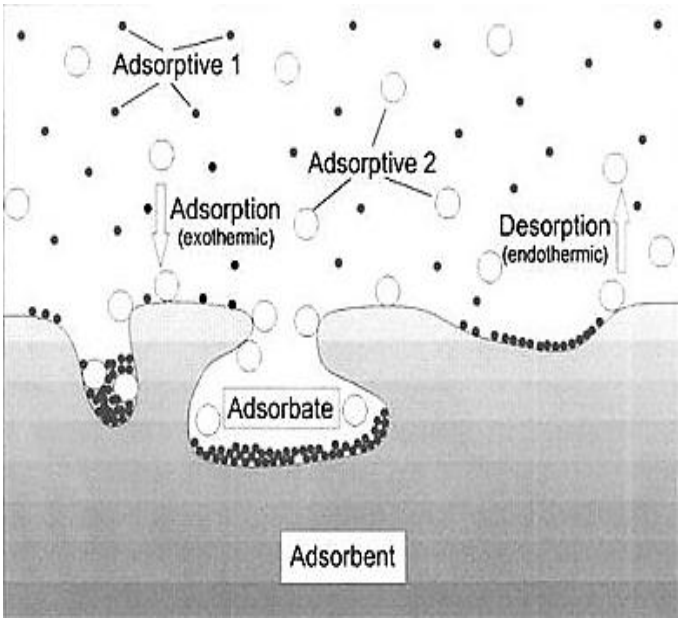

Figure 2-20-Description of adsorption-desorption phenomena [169]

Since thermodynamic parameters govern adsorption processes, factors such as pressure and temperature may affect adsorption at equilibrium. These factors may promote the surface interaction of reactant species at their different levels, enabling them to attain the desired activation energy necessary for a physical or chemical reaction to occur [168]. From the sorbent perspective, consideration is also given to the structure in terms of shape, size, pore size/shape distribution and chemical constituents. However, adsorption capacity would ultimately depend on the ease of adsorbate transportation into the sorbent material's interior surface.

2.15 Physical and chemical adsorption

As explained in the previous section, the extent of surface interaction and reaction classify adsorption processes into physisorption or chemisorption, with their distinct characteristics shown in Table 2-2.

Table 2-2-Adsorption types and their notable properties [171]

Property	**Physical Adsorption**	**Chemical Adsorption**
Nature of forces	van der Waals	reaction forces
Heat of adsorption (kJ mol^{-1})	20 - 40	>80
Adsorption rate	occurs rapidly	occurs slowly
Desorption process	easy, following pressure reduction or temperature increase	difficult, an increase in temperature required for bonds breaking
Specificity	non – specific as any gas can be adsorbed on a sorbent surface	strongly distinct, and it largely depends on the nature of the sorbate and sorbent
Molecular coverage	unimolecular or multilayer may form	a unimolecular layer is formed

During physical adsorption, gas molecules are attracted to sorbent high energy sites by van der Waal forces of attraction. These forces are propelled by dipole interactions or short-range forces, which lend credence to the nature of bonding strength [168]. Therefore, for such weak interactions, lower heats of adsorption, slightly higher than those of adsorbate heat of sublimation, are expected. However, in cases where ionic adsorbents are employed, the electrostatic field present will also contribute to the adsorption energy [166]. Since both monolayer and multilayers can be formed during physical adsorption, the process may occur

at low temperatures between any surface and gas. The first layer formed is held firmly onto the sorbents' surface, compared with the subsequent layers.

By contrast, for chemical adsorption, target gas molecules, while arriving at the adsorption interface, react covalently with exposed electrons at the high energy binding sites on the sorbents' surface, forming a chemical bond. For the case of activated chemisorption, gas molecules must overcome the activation energy barriers before sorbent-sorbate complexes are formed [172]. The activation energy, which is high, and attained slowly, is why chemical adsorption is considered a slow process. Although energy is supplied for the activated adsorption, such thermal energy must be sufficiently high to surmount the surface interaction barriers. The consequence of the high activation energy is higher heat of adsorption following the exchange of valence electrons. The heat generated during this time can provide a means of measuring the bonding strength of the adsorption process [166]. A description of the potential energy diagram for an adsorption process, where physisorption, chemisorption and activated chemisorption dominates, is shown in Figure 2-21. The physisorption and chemisorption potential wells are differentiated by their depths E_P and E_c, respectively, while the activation barrier is with height E_{conv} [172]

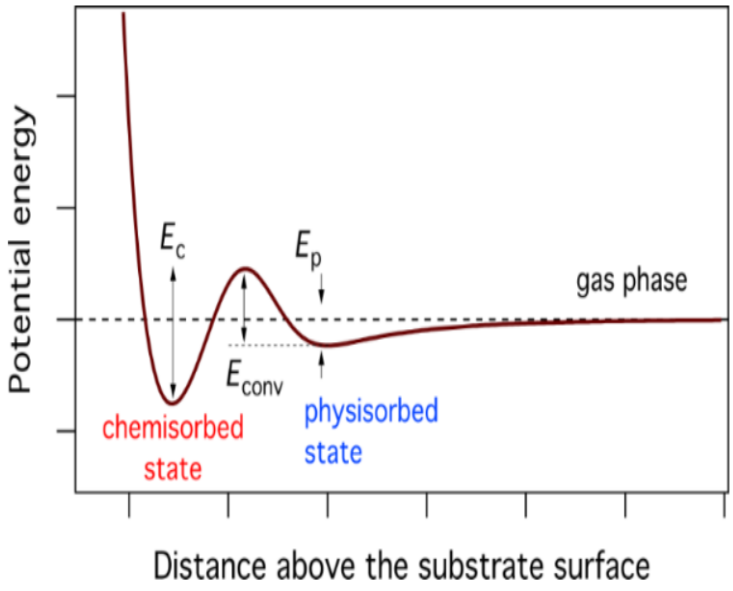

Figure 2-21- Potential energy diagram of an adsorption process [172]

In general, although surface interactions occur in both adsorption cases, low heats of adsorption suggests a lower heat of desorption and vice versa. Both adsorption types described can be reversed by a desorption process, involving a slight increase in temperature or pressure reduction of the adsorption system. This process would remove the adsorbed species from the sorbent surface by elevating their energy state from the foot of a potential well and push them back into the gas phase [170]. While physical adsorption is readily reversible, chemical adsorption may sometimes require a dissociation process or excessive heating to separate the adsorbate from the solid surface [168].

2.16 Adsorption thermodynamics

Adsorption being a spontaneous process results from a reduction in an adsorbent's surface energy and the degree of freedom of the adsorptives. The process's thermodynamics are defined with respect to the phase equilibria between the bulk phase (usually a gas) and an adsorbed phase (considered to be liquid-like). Based on this, the adsorption energy comes from the effects of both potential and kinetic molecular interactions, after which the gas molecules, initially moving freely in a 3-dimensional fashion, reduces to 2-dimensional when equilibrium is attained, as the system entropy (ΔS) decreases. Therefore, an increase in the disorder of an adsorption system will cause ΔS to be positive due to increased molecular activity of the adsorptive, whereas if the ΔS is negative, this will result in condensation of the adsorptive onto the adsorbent, with the entropy expressed by Equation 2.19 [173]:

$$\Delta S = \int \partial Q_{rev} / T \qquad \text{Equation 2.19}$$

where Q_{rev} = amount of heat transferred into the system

T = temperature

As a rule of thumb, where the system temperature increases, the gas molecules' kinetic behaviour increases, hence ΔS increases. This is why physisorption processes are unfavourable at high adsorption temperatures due to increased molecular interaction that prevents settling of adsorptive on sorbent surfaces. Similarly, as the adsorption system's

pressure increases, gas molecules become closer to each other and, therefore, less disordered; hence, the ΔS at such case reduces. Given this, it can be inferred that physisorption would dominate at lower temperatures and relatively increased pressure. For concentration, an increase in the gas species concentration will shift the adsorption equilibrium towards the adsorbed phase in line with Le Chatelier's principle. As controlled by the temperature, pressure, and concentration, this entropy change determines the phase that a given system will prefer. This suggests that any change in the thermodynamic parameters of adsorption can affect the nature of the process. These changes in the behaviour of the system are also accompanied by a change in the free energy (ΔG) of the system, represented by Equation 2.20:

$$\Delta G = \Delta H - T\Delta S \qquad \text{Equation 2.20}$$

where

ΔG = free energy

T = system temperature

ΔH = enthalpy of reaction

ΔS = system entropy

The free energy, being the driving force that accounts for all chemical reactions, brings about product formation, in this case, the adsorbed gas (adsorbate). The sign of ΔG at any given time determines the direction taking by the system towards equilibrium attainment; in which for (–ve) value, the reaction must occur, while for ΔH (–ve), this infers that the adsorption process will always be exothermic, given the decrease in the heat content of the reaction system [168]. If ΔG equals zero, the system is said to be in a state of equilibrium, and where (ΔG > 0), the reaction becomes non-spontaneous [173]. Thermodynamically, since adsorption is likened to a phase transition process, where an adsorptive in the gaseous phase condense into a liquid-like state, the process can be related to a classical vapour/liquid equilibrium system. Hence, with such a system, adsorption heat can be explored for the heat change accompanying phase transition using the Clausius-Clapeyron equation [168].

2.16.1 Determination of heat of adsorption from Clausius-Clapeyron equation

By definition, phase changes occur at a given temperature and pressure, at equilibrium, when $\Delta G = 0$ [174]. Therefore, by relating the saturated vapour pressure (P^{sat}) of the gas molecule with the boiling temperature (T_b) and the difference in molar volume in the vapour phase and the adsorbed phase in equilibrium, the heat change of an adsorption system can be estimated. Furthermore, based on the assumption that [175]:

- molar volume of adsorbed phase is much smaller than that of the vapour molar volume;
- vapour phase behaves like an ideal gas (no interaction between the molecules), and;
- variations in the heat of vaporisation are neglected, meaning that it is independent of the system temperature;

then the Clausius-Clapeyron equation, shown in Equation 2.21, can be applied for the determination of the heat change associated with the adsorptive condensation into a liquid-like adsorbed state [168]:

$$\partial \ ln \ P \ / \ \partial T = \Delta H_{vap} \ / \ RT^2 \qquad \text{Equation 2.21}$$

where

ΔH_{vap} = heat of vaporisation

R = universal gas constant (8.3142 J mol $^{-1}$ K^{-1})

T = temperature

P = absolute pressure

Upon rearrangement of Equation 2.21, following integration, the Clausius-Clapeyron equation can be re-written in the form of Equation 2.22:

$$ln\,P = -\,\Delta H_{vap}\,/\,RT + C$$ Equation 2.22

where

C = ΔS/R, from where the change in the entropy of an adsorption system can be determined.

2.17 Porosity in solid materials

Porosity is the term used to describe small openings in a solid, expressed as the ratio of total accessible volume to that of the volume occupied by 1 g of the solid [176]. Almost all solids contain these openings, whose role is to allow for the passage of materials through them, for example, gas molecules or vapours during an adsorption process. The openings sometime result during the sorbents' development following thermal or activation processes, enlarging the inherent porous structure. The structure of porous materials can also be tuned during the development stages to induce various pores that constitute the solid's internal and external surface area [177]. By nature, the external surfaces are the surfaces outside of the pore and are non-porous, wider than they are deep, while the internal surfaces are the imperfections that are deep than they are wide, within the pore walls [178].

For adsorption applications, porosity only offers the volume of space within the sorbent that gas molecules can access to reach the high energy binding sites on the sorbent's internal surface. As porosity does not directly impact the adsorption phenomenon, the capacity for adsorption would ultimately depend on the pore accessibility relative to the size and shape of the adsorptive [178]. Additionally, the pore morphology, which describes the shape in terms of pore width, volume and roughness and the availability of highly polar surfaces, may also influence the extent of an adsorption process [179]. In practice, pores are classified according to their shape or exposure to an external fluid, with the total pore volume ascribed to the sum of both open and closed pores. However, the open pores are those applicable for adsorption purposes [180].

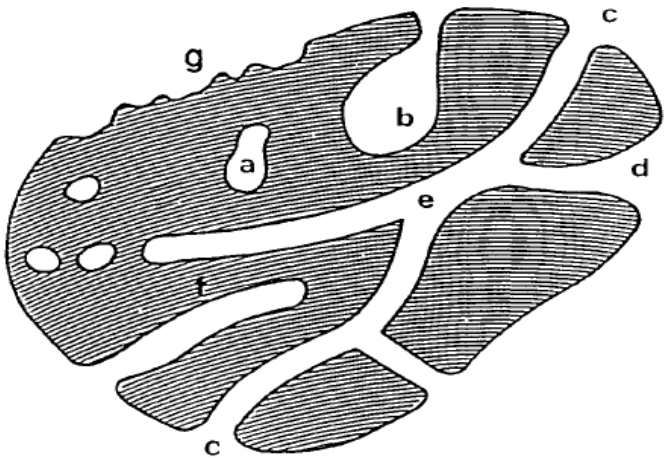

Figure 2-22-Different types of pores in a porous solid [180]

As shown in Figure 2-22, pore **(c)** is defined as a transport pore, which provides continuous pore interaction with an external fluid. It can also affect the macroscopic property of the sorbent [180]. The other pores leading to the external surfaces, such as pores **(b), (d)** and **(f),** are known as open pores. Pore **(b)** is open at one end and is very useful for adsorption, while pore **(a),** referred to as a closed pore, appears isolated and unsuitable for adsorption [180]. Pore **(e),** which is opened at both ends, permits gas molecules' transportation from one external surface to another on a time-dependent basis.

2.17.1 Pore classification

Although porosity in solids is classified on the basis of the extent with which the pores are exposed to an external fluid, the International Union of Pure and Applied Chemistry (IUPAC) further categorise them based on their sizes, as shown in Table 2-3, namely; the micropores (with sub-divisions), the mesopores and the macropores [181]. Each pore introduces peculiar adsorption characteristics that reflect their structural behaviour based on the non-uniformity of shapes and pore alignments [182].

Table 2-3-Pore classification according to sizes [182]

1Å = 0.1 nm (nanometre)

Pore type	Size range
Ultramicropore	<0.7 nm
Micropore	>0.7 nm < 1.4 nm
Supermicropore	>1.4 nm < 2 nm
Mesopore	> 2 nm < 50 nm
Macropore	> 50 nm

2.17.1.1 Microporosity

Micropores result from defective packing arrangements within a bulk solid, leading to interconnection and subdivision of pores, such as ultra and super micropores. They are usually of width < 2 nm, and their adsorption mechanism appears continuous due to the overlapping of force fields of opposite pore walls [183]. Micropore volumes are usually in the range of 0.1-0.4 $cm^3\ g^{-1}$, with surface areas nearing 1000 $m^2\ g^{-1}$ and above [177]. The ultra micropores are those of width < 0.7 nm and are often responsible for activated diffusion in porous solids. This is due to the constrictive nature of their pore networks relative to the adsorptive size. Adsorption in ultra micropores exhibits molecular sieve action and are favourable at a low relative pressure range < 0.01 [183].

The supermicropores, on the other hand, are of width ranging from 1.4-2.0 nm and favours adsorption at relative pressures > 0.01 < 0.15, but with the adsorption mechanism following a co-operative pore-filling process [183]. However, with the supermicropores limited to 2 nm and the ultramicropore 0.7 nm, multilayer formation during adsorption is likely; once a definite saturation pressure limit is established. While the pore volume remains the determining factor for adsorption in micropores, the adsorption process may not always extend to multilayer formation, with a subsequent filling of the pore width with an adsorbate [183]. As a standard, the surface area of micropores can be determined from the Langmuir equation. However, this may sometimes be misleading, given that pore volume has been suggested to be a more reliable means for micropore characterisation, as suggested by Dubinin [184].

2.17.1.2 Mesoporosity

Mesoporous materials originate from either indigenous or created means- the indigenous results from stronger defective packing, associated with shrinkages within a parent material, following carbonisation or activation processes [40]; the latter is linked with molecular holes created following a controlled activation process, thus forming pores of sizes > 2 nm < 50 nm [181]. The surface area of mesopores ranges from 10 to 100 m^2 g^{-1}, with the pore volume similar to the micropores [177]. Their low surface areas suggest weak fluid-fluid interactions within the pore walls. Mesopores sometimes overlap with the micropores within a given pore network and helps provide a means for adsorptive transportation [181].

Adsorption in mesopores can be described by three distinctive stages. Firstly, adsorption takes place initially on the narrow pore walls, inducing monolayer formation at low-pressure regions. Secondly, after the pore has reached its limit with increasing relative pressure, it behaves like an open surface. At this point, further adsorption then takes place on the already established monolayer since not all the adsorbed molecules are in direct contact with the adsorbent. Thirdly, with further adsorption extending into multilayer build-up, the sorbate interacts between selves, condenses and nucleates into a liquid-like phase (vapour-liquid transition), leading to capillary condensation [183].

2.17.1.3 Macroporosity

Macropores result from structural defects in the form of cracks and fissures. As a result of the developed pore width, adsorption in macropores occurs on a layer to layer basis, which is familiar with non-porous solids [178]. Their pore sizes which are > 50 nm, are broader than those of mesopores and micropores, and, based on this characteristic, they offer fewer advantages for adsorption due to weaker adsorbate interaction.

Despite the aforementioned, macropores may be helpful as a transport pore for gas molecules onto the high energy binding sites of sorbent materials, but mainly when pore overlapping or mixtures exist in a typical porous solid. Furthermore, adsorption here is promoted at higher pressures but on a step-wise pattern, which does not happen through all the pore spaces, but

at proximity to the pore walls [185]. For macropores, owing to their low surface areas, usually < 2 $m^2 g^{-1}$, negligible adsorption is typical without capillary condensation taking place; however, they can be characterised using the mercury porosimetry technique [184].

2.18 Interpretation of Adsorption phenomena

2.18.1 Adsorption Isotherm

An adsorption isotherm represents the amount of gas adsorbed by an adsorbent in (mmol g^{-1}), upon achievement of equilibrium, as a function of temperature, pressure and interaction potential [178]. The isotherm reflects the adsorbed molecules' average potential energy within a finite volume element (the pore), exerted by the repulsive and attractive forces [186]. Proposed in the 1940s by Brunauer, Deming, Deming, and Teller (BDDT), the isotherm is classified into six types (I to VI); however, with recent advances in the adsorption science, it has been classified into eight types, with classes I to VI shown in Figure 2-23, based on IUPAC recommendations [178].

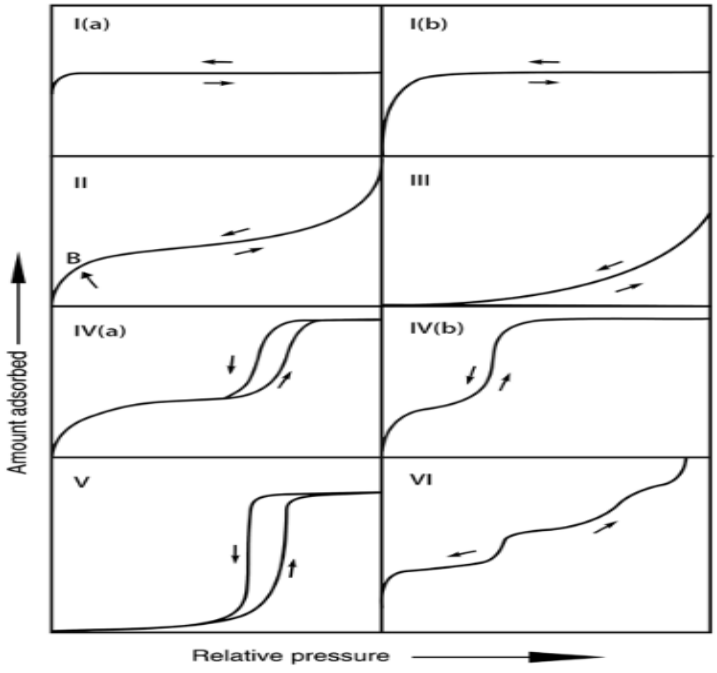

Figure 2-23-Classification of adsorption isotherm [187]

Generally, all adsorption processes described in the literature fall into one or a combination of the IUPAC classified isotherms. By contrast, the desorption isotherm represents the reversal of the adsorption condition, following a reduction in the adsorption system's pressure or an increase in the adsorption system's temperature. If adsorption occurs below the adsorptive gas's critical temperature, the isotherm is often expressed based on relative pressure; otherwise, in terms of absolute pressure [187]. Although adsorption isotherms help provide the basis for the choice of a sorbent in processes, it does not offer information regarding the kinetics of the process or the contact time to limit the solute concentration in a given process condition [168].

2.18.1.1 Adsorption isotherm (types and characteristics)

Type I isotherms are exhibited mainly by microporous adsorbents, such as activated carbons and several zeolites, and it also depends on the adsorptive. The isotherm shape is concave to the lower P/P^o regions of the isotherm. During adsorption, the pores are filled with adsorbate up to their saturation limits, say at $P/P^o < 0.1$, owing to stronger adsorbate interaction due to pore width overlapping effect [176]. However, with little or no further adsorption taking place, this may be attributed to the inability to access the adsorbent's micropore volume relative to their sizes. The Type I isotherm is reversible, despite the strong interaction between the sorbent and the sorbate. The difference between Type I (a) and I (b) isotherms is linked to the widening nature of their pore size distribution, in which many Type I isotherms obey the Langmuir equation, with the limiting plateau representing monolayer adsorption on the pore wall [168].

Type II isotherm displays both concave and convex curves at different P/P^o regions of the isotherm. It is frequently exhibited in adsorption on non-porous and macroporous solids, whose diameters are broader than micropores. The shape of the isotherm at the concave region characterises monolayer formation, followed by an unlimited multilayer. The unrestricted multilayer formation is due to the availability of finite volume elements above the external surface or the pore size exposed larger than the adsorptive diameter. As evident in Figure 2-23, the inflexion (B) point occurs near completion of the monolayer within the concave

region, noted by a sharp knee. However, where a gradual curvature separates the inflexion point and the onset of continuous multilayer formation, this may make the adsorbent characterisation difficult [178].

Type III isotherms display a convex curve over the entire P/P^o region of the isotherm, which indicates no distinct monolayer formation. The convex nature reflects a weakness in adsorbate-adsorbent interaction, resulting in low uptakes at the low P/P^o region, which is more peculiar to non-porous and macroporous sorbents. In this case, once the adsorption layer is established, with increasing P/P^o, molecular clusters may form on the already established layer, and subsequent layers may be produced before completion of adsorption on the first layer. Adsorption here creates a discontinuous layer of molecules not controlled by van der Waal forces. As a result, this leads to a sharp uptake towards the higher P/P^o region of the isotherm, with the adsorbed amount restricted at saturation pressure [168]. With adsorption not limited at $P/P^o = 1$, this suggests that heat of adsorption at layer one formed < the adsorbate heat of liquefaction, causing the adsorption to proceed. At this stage, the adsorbate interaction with the adsorbed layer established is higher than the interaction with the adsorbent surface [168].

Type IV isotherms share similarities with Type II isotherms at the concave and mid-pressure regions. At high P/P^o, a slope is evident at increased uptake as the mesopores are filled up. Similar to the Type II isotherm, the inflexion point near completion of the monolayer indicates the porous solid's adsorption limit. Type IV isotherm is typical with mesoporous adsorbents, whose pore sizes may restrict the formation of multilayer and capillary condensation phenomena [188]. The notable feature of Type IV(a) is the formation of a hysteresis loop, occasioned by capillary condensation, in cases beyond the critical pore width (> 4 nm). On the other hand, the Type IV (b) isotherm, although still applicable to mesopores, has pore sizes that must fall within the critical diameter to permit reversible adsorption.

Type V isotherms show similar characteristics to Type III isotherms but account for weak adsorbate-absorbent interaction potentials at low relative pressure ranges. The limiting uptakes at the mid pressure region of the adsorption isotherm suggest the likelihood of adsorption occurring via pore-filling processes. With evidence of hysteresis, such can be

exhibited by both micro and mesoporous adsorbents [176]. For Type V adsorption at high P/P^o, adsorbate clustering initiates pore-filling. An example of such is the adsorption of water vapour on hydrophobic sorbents, and also, in the case of phosphorous gas adsorption on NaX (Zeolite) [166].

Type VI isotherm is a particular case of adsorption occurring in a stepwise (layer by layer) pattern, with the adsorbed layers formed, attributed to subsequent single layer completion. Each adsorption layer's height represents the maximum adsorption capacity, with the sharpness being a function of the adsorption system type and temperature. Type VI isotherm is familiar with adsorbents with high homogeneous and non-porous surfaces [189].

2.18.2 Hysteresis loops

As shown in Figure 2-23, in the cases of Type IV(a) and V adsorption isotherms, there are marked deviations where the adsorption/desorption branches are not identical, occurring within the multilayer bounds at certain P/P^o regions. This non-reversible adsorption condition which often starts from the higher P/P^o region of the multilayer bounds, results in an adsorption phenomenon known as hysteresis. The hysteresis can be considered an intrinsic property of the vapour-liquid phase transition in a finite volume system [183]. The theory was first advanced by Zsigmondy, where he suggested its close connection with capillary condensation theory [190]. According to Zsigmondy, gas vapour condensation within the pore wall for irreversible hysteresis does not entirely wet the capillary walls, owing to impurities. Additionally, Foster argues that such a loop may be due to delayed meniscus formation during multilayer formation in open pores during adsorption. Similarly, the desorption pathway has been attributed to condensation effects [191].

2.18.2.1 Capillary condensation

The capillary condensation phenomenon, which occurs progressively, has been related to the pore size distribution's nature, and the stages can be explained using Figure 2-24. During adsorption, sorbents' pores are filled progressively by the sorbate due to force fields exerted on them by the pore walls, bringing about a mono adsorption layer (A). However, as the

adsorption system pressure increases from the bulk, multilayers (B), which are larger in sizes relative to the pore dimensions, may begin to form. As these layers accumulate (initiation of the hysteresis loop) at certain critical P/P^o region, they draw closer to each other (C) due to stronger van der Waals interaction. At this point, the vapour in the pores condenses into a liquid-like phase due to the capillary condensation [187]. The condensed liquid further forms a hemispherical meniscus at this saturation pressure limit, when the pores are being filled, as shown in stage (D).

This added mechanism suggests that thermodynamic equilibrium is not attained over the adsorption branch. The same applies to the desorption branch if part of the condensate becomes trapped within the pore cavities, causing a gap between two curves of different pathways, under the same conditions [190]. The hysteresis loop closes through desorption after the condensate stabilises. However, at an appropriate vapour pressure, lower than that which initiates pore condensation, when the pore entrance becomes unblocked, the retained condensate begins to evaporate, as shown in (E). After this, the desorption process follows the same process as the adsorption by desorbing the multilayer film in equilibrium with the vapour in the core of the pore and the bulk gas phase (F). The ease of this desorption of condensate from the individual pores may depend on whether a clear channel exists linking the pore to the outer surface.

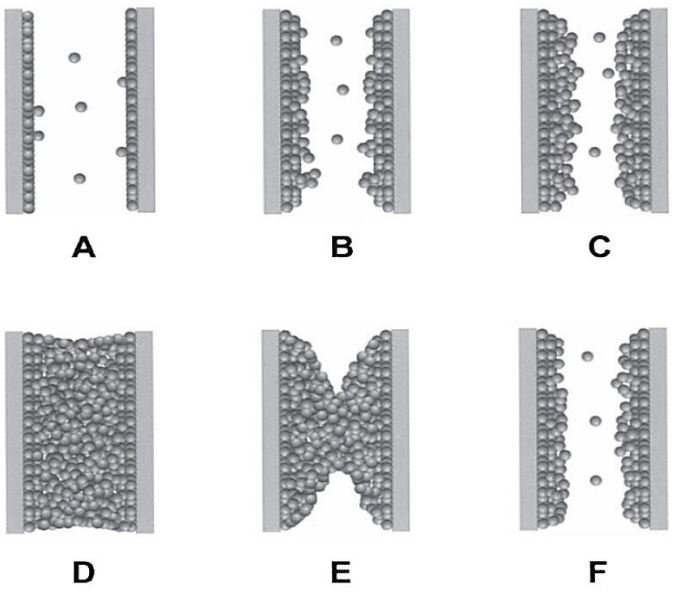

Figure 2-24-Capillary condensation mechanism [192]

2.18.2.2 Types of hysteresis loop

According to the IUPAC classification of 1985, hysteresis loops are categorised into four different types (H1 to H4), to a large extent, based on interpretation of the capillary condensation phenomena [183]. However, given the recent advances in material characterisation, the hysteresis loop has further been extended by two more types, namely, the H2 (b) and H5, Figure 2-25 [187]. Each of the six hystereses has particular features and associated mechanism, which relates to pore structure characterisation.

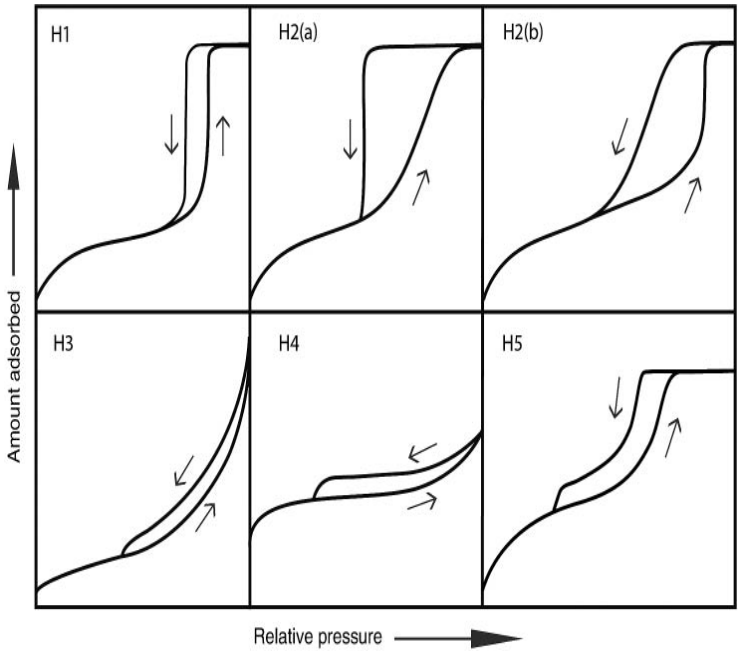

Figure 2-25-Classification of hysteresis loops [187]

Type H1 is associated with sorbents with a narrow range of pore size, such as mesoporous carbons. The pores of such sorbent materials are classified as rigid, and the adsorption isotherm linked to the Type H1 has a well-defined plateau at high P/P^o, which makes it possible to assess the pore volume. A notable feature of the Type H1 loop is the upper and lower closure points at the boundary curves, which are almost parallel. Here, pore connectivity effects are minimal, and the narrow loop suggests delayed condensation in the adsorption branch.

Type H2 splits into H2 (a) and H2 (b) types, exhibited by complicated pores, whose shapes are not well-defined. The steep descent of the desorption branch of the Type H2 (a) has been attributed to pore blocking in a narrow pore neck or due to cavitation-induced evaporation of the adsorbed liquid [187]. Pore network effects and cavitation resulting in bubble formation within the pores account for the forces acting on the liquid due to pressure changes (reduction). For type H2 (b), the steep loop descent also exists and is associated with pore blocking, but in this case, the size distribution (width) of the pore is much broader, leading to a gradual descent of the desorption branch, unlike those of type H2 (a). The hysteresis loop exhibited here is more pronounced for certain mesoporous ordered materials developed following hydrothermal treatments.

Type H3 shows no plateau at higher P/P^o regions. The main features are the low closure points on the desorption branch and a sharp uptake at high P/P^o, which in the case of nitrogen adsorption at -196 ^oC, is located in the region of 0.42 P/P^o [190]. Here, the adsorption branch is associated with the Type II isotherm, and the closing region of the desorption branch corresponds to the cavitation-induced P/P^o region. Examples of this hysteresis type are common with the adsorption of non-polar gases by montmorillonite clays [193].

Type H4 is somewhat similar to Type H3, with no apparent plateau being established, and is commonly seen in Types I and II isotherms. However, the noticeable difference here is the higher uptake at low P/P^o [187]. The uptake exhibited at the low P/P^o region indicates micropore filling. Type H4 hysteresis loops are found in selected zeolites, as well as micro and mesoporous carbons

Type H5 although unusual**,** is often associated with adsorbents with a mesoporous structure that possess a combination of open and partially blocked pores, for example, plugged hexagonal template silica [187].

Conclusively, Types H3, H4 and H5 are noted for their sharply descending desorption lines, generally located within a narrow range of P/P^o (~ 0.4 -0.5), peculiar to N_2 at -196 ^oC [106]. Adsorption hysteresis has shown to be familiar with mesoporous materials. Although pores' size allowed for capillary condensation and evaporation to occur, the pore fillings and emptying

follow the same approach for microporous materials. The causes and effects of hysteresis are yet unclear, but this has been attributed to the nature of the adsorption condition, as well as the sorbent's structure [187]. A number of studies have reported that low-pressure hysteresis loops in selected adsorbents may be linked with an artefact of experimental practices, such as imperfect degassing [165]. Generally, by increasing the adsorption system pressure, hysteresis shifts, and by increasing the temperature, hysteresis shrinks. Also, at critical adsorption temperature condition, hysteresis disappears, while in the presence of varying pore configurations, adsorbate, and adsorbent, different kinds of hysteresis may result [190].

2.19 Adsorption Theories

Theories always guide new experimental developments and are regularly tested for consistency with process technology advancements. The science of adsorption, which has further developed, follows ongoing interplays between theory and experiment. Although no theory was in existence before 1914 for interpreting the adsorption phenomenon; however, in 1916, Langmuir developed a theory, which by extension, underpinned the derivation of many equations employed in understanding adsorption science.

2.19.1 Langmuir Adsorption Isotherm

Langmuir conceived the theory of van der Waal's attraction and repulsion forces at the boundary layer of phases in continuous transition and related them to the adsorption phenomena. Langmuir found that during such a chemical process, a unimolecular layer is formed on a sorbent surface [168]. Given van der Waal's theory, Langmuir explored a kinetic means to arrive at a model based on the conviction that when gas molecules strike on solid surfaces, an elastic or inelastic collision may result [168]. This behaviour exhibited by the gas, which may occur infrequently, could cause them to reflect (elastic) from the solid surface without losing kinetic energy. However, where an inelastic collision dominates, a loss of kinetic energy of the gas under motion will result in the gas molecules condensing on the solid surface for a short time before moving back (evaporating) into the gas phase, where they enjoy some degree of freedom [84].

As a result of the time lag with which the gas molecule stayed on the solid surface and held by van der Waal forces, Langmuir accounted for this to be responsible for adsorption [84]. Also, where the molecular evaporation process occurs slowly, a unimolecular layer of the adsorbing gas is formed when equilibrium is established. These mechanisms of adsorption and evaporation occurring dynamically can influence the rate of an adsorption process. In developing the equation supporting these views, Langmuir believed that adsorption rates depend on pressure and availability of vacant sites on sorbent surfaces [168]. By contrast, the desorption rate relies on the extent of sorbents' surface coverage, as well as the energy of activation, which the adsorbate must attain at an equal or higher level before desorbing from the surface. Therefore, Langmuir described the relationship between the unimolecular surface coverage as a function of partial pressure, under isothermal conditions, by assuming that [176]:

- gas molecules behave ideally, such that the potential energy due to intermolecular forces between them is less significant;
- adsorbent surfaces consist of a 2-dimensional array of energetically homogenous energy sites, known as the potential well of same energy level, where adsorption is localised;
- only one molecule can be accommodated on any available vacant site to form a monolayer, where additional layers do not build up;
- lateral interaction of gas molecules is negligible, suggesting that the energy state of an adsorbed gas is independent of the neighbouring one.

Given the above assumptions, Langmuir equated the number of gas molecules evaporating from the solid surface after striking, to the number condensing onto it, as described by the reaction Equation 2.23. This guides the derivation of the Langmuir Equation 30, whose isotherm takes a linear form based on partial pressure.

$$A(g) + S(s) \leftrightarrow A.S\ (at\ interface) \qquad \text{Equation 2.23}$$

$$\frac{P}{V} = \frac{1}{KV_m} + P/V_m \qquad \text{Equation 2.24}$$

Therefore, the Langmuir equation can be tested against experimental data by plotting P/V values against P [168]. When fitting the experimental data, obtaining a straight line is necessary, although not a condition for the theory applicability. A slope 1/ Vm is determined from this plot, from where the specific surface area of the adsorbent is found [166]. By contrast, where the plot deviates from linearity, the value of the monolayer capacity (V_m) obtained would mean the excess measured amount due to structural defects on the adsorbent surface [194].

Also, the value of K is indicative of adsorption strength. Where the value is high, it suggests high molecular affinity. At this point, the monolayer capacity tends to unity, as against the low-pressure regime where the K value is small [195]. Furthermore, V_m and K values are both temperature-dependent and vary from different Langmuir isotherm at different temperatures. The Langmuir isotherm is said not to be obeyed at higher pressures when the plot of P/V against P deviates from a straight line, an indication of an adsorbent surface inhomogeneity, resulting in a variation of the V_m values, which thus infers that the Langmuir equation is not applicable and cannot account for these changes [168].

2.19.2 Criticism of the Langmuir model

- The assumption that adsorbent surfaces possess vacant sites of the same energy level has been disputed in many experiments. V_m values obtained vary at low and high-pressure regions, owing to surface heterogeneity, with adsorption sites spreading over different energy levels [196].

- The model cannot be applied to Type II to Type VI isotherms at high-pressure conditions but is limited to Type I isotherms. This reason is due to reported deviations from linearity beyond the low-pressure regions of the isotherm.

- Langmuir assumed the non-existence of adsorbate lateral interaction at the surfaces, whereas evidence of weak forces between neighbouring molecules has been reported

[195]. This weak interaction from neighbouring molecules results in a variation of adsorption heat on sorbent's energy sites, subject to molecular self attraction or repulsion.

- Langmuir assumed that a monolayer forms on solid surfaces, which is not always the case, as researchers have proved the potentials of multilayer formation after the monolayer. This assumption was disputed with the variation of adsorption energy at different adsorption layers produced [189].

2.19.3 Brunauer-Emmett-Teller (BET) isotherm model

Given the development of Langmuir theory that accounts for unimolecular adsorption, Langmuir noted that multi-molecular adsorption layer formation is likely with gases at pressures nearing their saturation limits [84]. Based on this notion, the Langmuir model was further extended by Brunauer, Emmett, and Teller (BET) in 1938 to account for multilayer formation [176]. A number of assumptions relied on by BET for the extension of the Langmuir equation are that:

- adsorption is localised on fixed sites of equivalent sizes and energy level;
- no lateral interaction exists between the adsorbed molecules;
- each adsorbed layer formed acts as a 'site' for subsequent ones, and that the multilayers formed are unrestricted;
- only the adsorbed gas molecules directly in contact with those in the adsorptive phase experience dynamic equilibrium; the rates of condensation and evaporation are similar for all layers after the first;
- adsorption enthalpy (ΔH_{ads}) for all layer formed outside the first is equivalent to the enthalpy of liquefaction (ΔH_L) of the adsorbed gas.

Based on the assumptions above, the BET equation was derived relying on Langmuir's kinetic interpretation. However, it accounted for the sorbate interaction at each adsorption layer,

where condensation and evaporation rates are assumed to be same for all layers after the first, as described by Equations 2.25 to 2.27:

$$A\,(g) + S\,(s) \leftrightarrow A.S\,(first\ layer) \qquad \text{Equation 2.25}$$

$$A(g) + A(g)\,S(s) \leftrightarrow A_2\,S\,(second\ layer) \qquad \text{Equation 2.26}$$

$$A(g) + A_2(g)\,S(s) \leftrightarrow A_3\,S\,(multilayer)\ and\ so\ on\ \ldots. \qquad \text{Equation 2.27}$$

Therefore, by extension, the BET Equation 2.28 has now been widely accepted by many researchers for use in modelling adsorption isotherms and the characterisation of adsorbents [176]:

$$\frac{P}{V(P^o - P)} = \frac{1}{V_m}C + \left(C - \frac{1}{V_m\,C}\right)P/P^o \qquad \text{Equation 2.28}$$

Where, P^o = saturation vapour pressure (mmHg)

P = equilibrium pressure (mmHg)

V = adsorbed volume at pressure (P) expressed as a molar quantity (mbar)

V_m = complete monolayer coverage expressed as a molar quantity (mbar)

C = a dimensionless constant relating to adsorption enthalpy, as represented in Equation 2.29:

$$C = e^{[\frac{\Delta H_A - \Delta H_L}{RT}]} \qquad \text{Equation 2.29}$$

Where, ΔH_A = enthalpy of adsorption of the first adsorption layer (J mol^{-1})

ΔH_L = enthalpy of liquefaction for second and subsequent adsorption layer (J mol^{-1})

R = universal gas constant (8.3142 J mol^{-1} K^{-1})

T = adsorption temperature (K)

Also, given the assumption that adsorbate evaporation and condensation at subsequent layers after the first are equal, the constant C relates the energy of adsorption at the first layer [187]. The shapes of adsorption isotherm Type I to VI can indirectly suggest the extent of surface interaction for a typical adsorption process. Where the value of C approaches unity, ΔH_A becomes smaller, an indication of the existence of weak adsorbate-adsorbent interaction. However, where the C value is large, it suggests that adsorption enthalpy is greater owing to increased surface interaction. As a result, the isotherm knee would look sharp, and Point B, which defines the limit of monolayer formation, becomes evident [187].

Furthermore, researchers have suggested that C values should ideally be > 150 to demonstrate adsorption occurring on high energy sites [180] [187]. However, values of C < 50 may suggest possible overlapping between the mono and multilayers formed, which may lead to a doubtful value of the monolayer capacity (V_m) [187]. Under the BET model, the C value is a determinant factor of the isotherm shape, just as K is for the Langmuir model. The linear range within which a reasonable value of C may be determined falls within the BET P/P^o region of 0.05-0.35, as the experimental data often deviate above and below this range. Therefore, upon linearization of Equation 2.28 and plotting the values of $P/V(P^o-P)$ against P/P^o, a straight-line graph with slope (s) [C -1 /V_m C], intercept (*i*) (1/V_m C) and constant C would be used for determination of the BET surface area. Alternatively, a combined equation for V_m and C can be expressed in the form of Equation 2.30 and 2.31 [176]:

$$V_m = 1/(s+i) \qquad \text{Equation 2.30}$$

$$C = \left(\frac{s}{i}\right) + 1 \qquad \text{Equation 2.31}$$

2.19.3.1 Criticism of the BET model

- One major criticism of the BET model is the uncertainty surrounding the correctness of C values. This arises as several studies have shown that the C value must be positive for the V_m value to be realistic, as a negative C value will suggest one outside the BET range. Also, a

clear knee isotherm is necessary as a condition for an acceptable C value, which in most cases, C values > 100 is favoured [197].

- Another limitation is the discrepancy regarding the V_m values obtained upon linearization of the BET model. Many studies have reported that accurate values of V_m are restricted to the linear region of the BET plot (i.e., 0.05-0.35 P/P^o) for the Type II and IV (a) isotherms, as the equation deviates from the experimental data at high-pressure regions, attributed to the negligence of sorbate lateral interaction [180]. Hence, for an accurate value of V_m to be determined, monolayer formation must be fully established before multilayer formation.

- The assumption that adsorbed layers are infinite at saturation pressure has been disputed in many studies, where molecular layers formed were limited upon exposure of the solid to saturation pressure [197].

- The assumption that adsorption sites are energetically equal has also been discredited in several experiments, following a marked variation/reduction in adsorption heat with surface coverage, as reported in Drain and Morrison's study, due to surface heterogeneity [198].

2.19.4 Determination of BET surface area

Although not always significant in the analysis of microporous adsorbent, the surface area is vital as a parameter for comparing different adsorbents. It provides a fingerprint of the probe accessible area, representing the effective area available for adsorption by a given adsorptive [187]. After determining the monolayer capacity from experimental data, using the Langmuir or BET model, it is possible to determine the surface area with the knowledge of the average molecular cross-sectional area occupied by the adsorbate molecule within a completed monolayer. The relationship between the BET surface area and the monolayer capacity is expressed in Equation 2.32 [187]:

$$S = V_m \times A_m \times L \qquad \text{Equation 2.32}$$

where, S = specific surface area ($m^2\ g^{-1}$),

L = Avogadro's constant, 6.0221367 x 10^{23} (molecule mol^{-1})

A_m = adsorbed molecule cross-sectional area over the completed monolayer (m^2 $molecule^{-1}$)

V_m = monolayer capacity, expressed as a molar quantity, (mmol g^{-1})

As described above, it is evident that the BET surface area determination depends on adsorptive choice, the adsorption operating temperature, and the procedure adopted in locating the P/P^o range, within which the BET equation is applied. However, in both cases of using the Langmuir and the BET model, the surface area obtained may be flawed by the assumptions upon which these theories were founded. Importantly, in the case of adsorption in micropores, which follows a volume filling process, locating the exact point B may be challenging, and extreme caution should be exercised. Therefore to address the above limitations and the subjectivity in evaluating the BET V_m value, a procedure proposed by Rouquerol for determining the appropriate location within the BET linear region is beneficial in cases where micropores are present, and this requires that specific criteria must be met, as listed below [199]:

- the plot of n (P^o-P) values against P/P^o should continue to increase with a corresponding increase in P/P^o, for the region restricted for the BET application.

- BET plot obtained from the data within the restricted BET range should be linear, with the intercept on the ordinate being positive, from where a reliable value of C can be determined.

- values of P/P^o from where the corresponding value of V_m is obtained should fall within the selected BET range.

- where the above criteria are met, the point where the monolayer formation establishes at P/P^o can be recalculated, within 10%, by inputting the C value into the expression 1/ ($\sqrt{C}$ + 1) provided V = V_m is stated in the BET equation.

2.20 Analysis of microporous materials

As the shape of a physisorption isotherm is dependent on the extent of sorbate-sorbent interaction at any given operating condition; however, at the monolayer adsorption region, the sorbent structure influences the shape of the adsorption isotherm. By contrast, the sorbent structure is less pronounced in depicting the isotherm shape for adsorption occurring at the multilayer adsorption region, as the multilayer thickness depends on the equilibrium pressure. Although an adsorbed film of uniform thickness represents a characteristic density profile, it is often assumed that the pore wall's film thickness is uniform. Such statistical thickness can be explored by normalising the adsorption isotherm.

2.20.1 t-plots method

The t-plot method, proposed by Lippins and De Boer, is one such method utilised for comparing the adsorption isotherm of microporous materials relative to standard Type II adsorption isotherm [200]. The plot represents an experimental isotherm, where the adsorbed amount is plotted against the corresponding adsorbed layer thickness over the P/P^o range. For this, the multi-layer formed during adsorption is modelled mathematically to determine the statistical thickness over the corresponding P/P^o range. The model may utilise an appropriate thickness equation, such as the one shown in Equation 2.23, dedicated for carbon-based adsorbents to calculate corresponding t values for the given P/P^o ranges on the isotherm [201] [202].

$$t = 0.88\,(\frac{P}{P^o})^2 + 6.45\,\left(\frac{P}{P^o}\right) + 2.98 \qquad \text{Equation 2.33}$$

The resulting t-curve (t vs adsorbed amount) established is compared with the experimental test isotherm. Any disparity in the shape of the experimental isotherm from the standard t-curve would suggest a departure of the t-plot from linearity. The model is only valid within narrow P/P^o ranges (0.2-0.5) for adsorption occurring after monolayer formation before the onset of capillary condensation. As a result, the t-plot is considered unsuitable for analysing highly microporous materials as adsorption through them occur outside of this range. Hence,

to account for the validity, the P/P^o range applied for such analysis may be adjusted for the best linear t-plot to be obtained. If the isotherm is identical with the shape of the standard Type II isotherm for nonporous materials or mesoporous solid, a straight line passing through the origin will be evident, and the slope (s) allows the external surface area (S_t) of the microporous sorbent to be determined using Equation 2.34.

$$S_t = s\ X\ 15.47 \qquad \text{Equation 2.34}$$

If micropores are absent within the sorbent structure, there would be a good agreement between the t-area, S_t, and the surface area (S_{BET}) obtained using the BET method [200]. However, where a small fraction of micropores are present in the sorbent structure, the t-plot will be extrapolated to the adsorption axis. The positive intercept (i) obtained becomes equivalent to the micropore volume (V_p), which can be estimated using Equation 2.35.

$$V_p = i\ X\ 0.001547\ (cm^3) \qquad \text{Equation 2.35}$$

2.20.2 Dubinin-Radushkevich (DR) model

Dubinin, in 1947, lent credence to the Polanyi potential theory and recognised certain aspects of the theory that aided the application of the concept of the volume filling of micropores. Although Dubinin achieved moderate success in accounting for adsorption in micropores, the significant problem was the inability to extend the theory to non-porous materials and the characterisation of microporous structures [184]. Due to lack of success in describing adsorption in micropores, Dubinin and Polanyi developed the volume filling theory of micropores, where adsorption is governed by a pore-filling mechanism rather than on layer to layer basis [203].

According to the hypotheses put forward by the Polanyi potential theory, adsorption phenomena are attributed to long-range dispersion forces that emanate from sorbent surfaces, resulting in the formation of adsorption layers [204]. Here, Polanyi suggests that adsorption layers formed are due to compressive forces, occasioned by a fall in adsorption potential, when gas molecules are attracted to a sorbent surface. This led Polanyi to provide a

quantitative treatment that correlates the energy of adsorption to the adsorbate density. With an assumption that the sorbate behaves like an ideal gas, he accounted for temperature independence with the adsorption potential, represented by Equation 2.36 [205]:

$$A = -\Delta G = RT\ ln(P^o/P) \qquad \text{Equation 2.36}$$

where, P = equilibrium pressure (mbar)

P^o = saturated vapour pressure (mbar)

T = temperature (K)

R = universal gas constant (8.314 J mol $^{-1}$ K $^{-1}$)

A = adsorption potential (J)

Based on the potential theory, Dubinin established that the adsorption potential (A) could be given a thermodynamic meaning, describing it as the differential molar of adsorption, expressed in terms of negative change in free energy (-ΔG), as shown in Equation 2.36. Because micropore sizes are comparative to adsorbate molecules' kinetic diameter, the successive formation of adsorption layers on the pore walls becomes impossible. It is here that the surface area losses significance as a means for characterising micropores. Dubinin then recognised the importance of micropore volume over the surface area, by introducing a second parameter that represents the degree of fractional pore filling (θ = W/W_o), as per Equation 2.37 [205]:

$$\theta = \frac{W}{W_o} = \int (A/E_o) \qquad \text{Equation 2.37}$$

With further assumption that the pore size distribution is Gaussian, and by combining Equation 2.36 and 2.37 and introducing a scaling factor, the well-known Dubinin-Radushkevich Equation 2.38 and its linearized version Equation 2.39 were developed [203] [205]:

$$\frac{W}{W_o} = exp[-(B\ T^2)/\beta^2(log(P^O/P)^2)] \qquad \text{Equation 2.38}$$

$$log\, W = log\, W_o - D\, log^2(\frac{P^O}{P})$$ Equation 2.39

where

W = adsorbed amount in the micropore when adsorption potential is A.

W_o = micropore volume (maximum at A = 0)

β = similarity constant

E_0 = characteristic adsorption energy for a reference vapour, usually benzene

$B = (2.303R)^2 k$

$D = B\, T^2/ \beta^2$ (a constant that measures the pore size distribution of the adsorbent)

Therefore, the suitability of the DR equation can be tested using Equation 2.39. Using a plot of $log\, W_o$ against $log^2(P/P^o)$, a straight line results, with a slope of $D = B\,(T/\beta)^2$ and an intercept of $log\, W_o$, from where the surface area, effective pore size, micropore capacity (W_o) and characteristic energy of the adsorption system can be determined. Also, where the density of the adsorbed phase is known, the micropore volume (V_{micro}) can be determined using Equation 2.40:

$$V_{micro} = W_o \times density\ correction\ factor$$ Equation 2.40

Where the density correction factor for CO_2 gas at 0 ^oC is 1.5876×10^{-3} [206].

Despite the benefits of using the DR equation for the characterisation of microporous materials, it has been reported that the equation is limited in application to homogenous microporous sorbents with a narrow pore size distribution [203]. This, therefore, fails to linearize where heterogeneous surfaces dominate the sorbent structure. Hence, to overcome this deficiency, a modified version of the DR equation, proposed by Dubinin-Astakhov (D-A), Equation 2.41, is often applied [203].

$$ln\,W = lnW_o - Dlog^n(\frac{P^O}{P})$$ Equation 2.41

where

n = Dubinin-Astakhov parameter

W = adsorbed amount in the micropore when adsorption potential is A.

W_o = micropore volume (maximum at A = 0)

D = B T^2/β^2 (a constant that measures the pore size distribution of the adsorbent)

The DA equation included the parameter 'n' to account for surface heterogeneity, and it has been reported that the value of 'n' is ~ 2 for porous carbon-related adsorbents, while values of 4-6 are suggested for zeolite materials [203]. Also, in situations where the value of n is not an integer, such a heterogeneous system can be explained as having a broad pore size range; hence, the DR equation represents the sum of contributions from the pore size ranges.

Furthermore, although varying cases may arise where it becomes challenging to utilise the DR equation in the generalised form, as they may require a high computation level, an alternative interpretation of the generalised equation may be by visual analysis. Figure 2-26 represents a linear plot of the DR equation functions and their likely deviations from linearity. Any deviation from the normal Gaussian distribution helps predict the pore size distribution within a porous material.

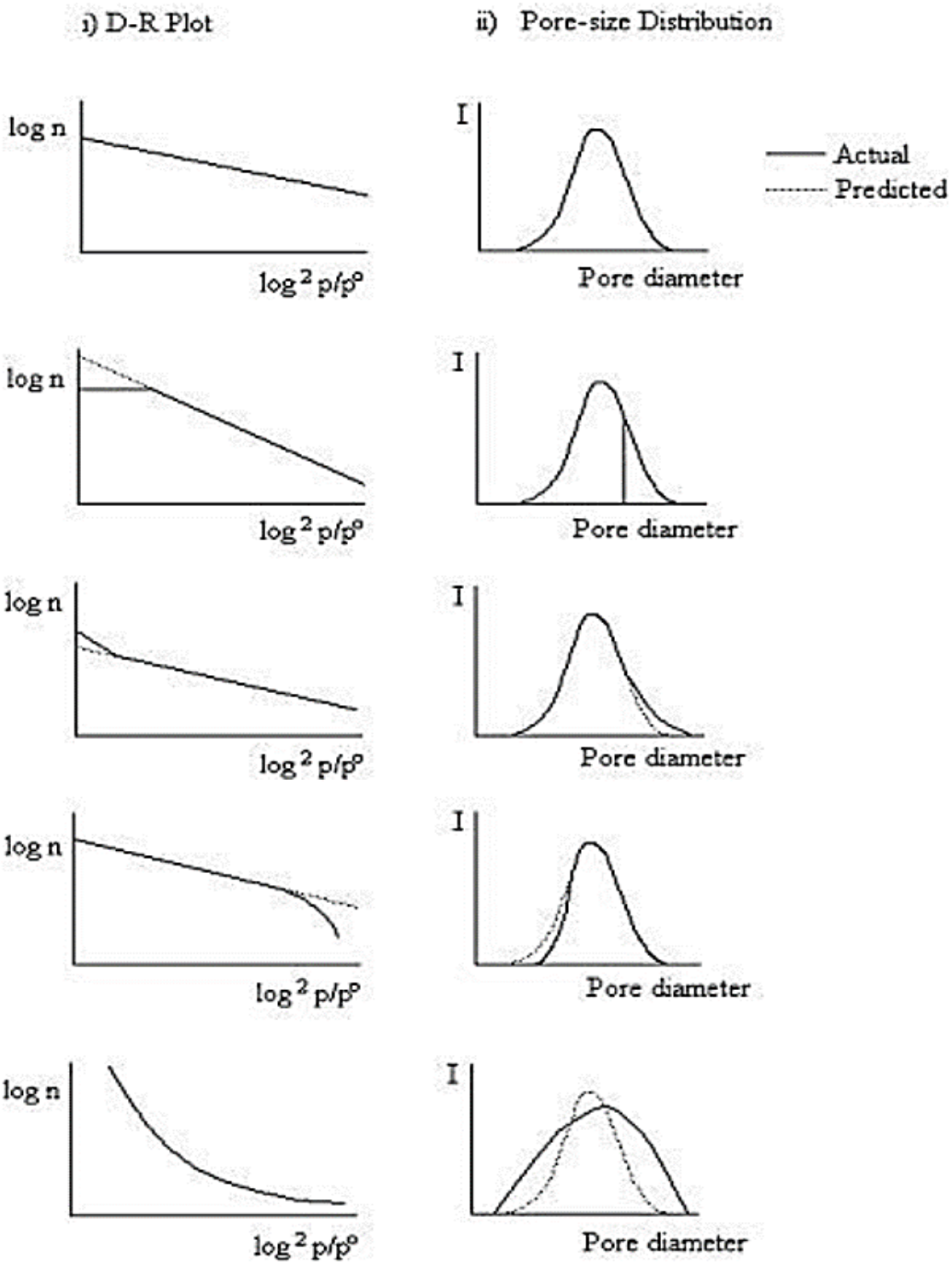

Figure 2-26-Potential variations of the DR Plot and its relation to the nature of Pore-Size Distribution [207] [208].

2.21 Analysis of mesoporous materials

The analysis of mesoporous solids has a relationship with the concept of capillary condensation. Given that adsorption in mesopores initially occur on the pore walls as if the pores are narrow with high energy potential, subsequent pore filling continues with an increase in relative pressure until the 50 nm mesopore size limit is attained. It is at this stage that the pore is said to behave like an open surface.

2.21.1 Brunauer- Joyner-Halenda (BJH) theory

The method proposed by Brunauer, Joyner and Halenda (BJH) is has been employed to analyse pore size distribution (PSD) and total pore volume in mesopores based on the modified Kelvin equation. The Kelvin equation was developed, given an earlier study by Zsigmondy in 1911, who described the relationship ($P < P^o$) between the equilibrium pressure over a concave meniscus of a liquid and the vapour pressure at the same temperature, permitting vapour condensation into a liquid-like form in a porous material [40]. Also, since the establishment of a complete meniscus is a condition at saturation, however, by assuming a cylindrical pore that is radially filled with liquid sorbate, Kelvin related the vapour pressure above the meniscus of the liquid to the diameter of the containing pore and suggested that the vapour pressure of the liquid droplet with radius (r_k) increases with decreasing r_k [171] [40]. Thus, it is based on this account that the vapour pressure lowering over a cylindrical capillary is expressed in terms of the Kelvin Equation 2.42 [171]:

$$ln\left(\frac{P}{P^o}\right) = -2\gamma V_L / r_k RT \qquad \text{Equation 2.42}$$

where

r_k = kelvin radius of curvature

R = universal gas constant (8.314 J K^{-1} mol^{-1})

T = absolute temperature (K)

γ = surface tension (dyne cm $^{-1}$)

V_L = liquid sorbate molar volume (m^3 mol^{-1})

Figure 2-27 shows that r_k, is the radius at which pore condensation occurs at a corresponding P/P^o, but cannot be described as the actual pore radius. This is because an adsorbed film has already been established at the onset of adsorption and remain on the pore wall at a certain thickness (t) during desorption. Therefore, to enable accurate estimation of the pore size, it became necessary to account for the multilayer thickness (t) established during the onset of adsorption [40].

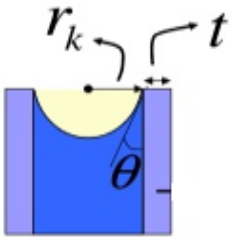

Figure 2-27- Cross-section of open-ended cylindrical pore showing the pore radius (r_k) and the adsorbed layer thickness (t)

Given the inability of the Kelvin equation to account for the influence of fluid-wall interaction in the containing pore capillaries, BJH, in 1951, proposed a means of estimating the PSD and total pore volume in mesoporous solids, to account for the thickness of an adsorption layer based on the assumptions that [209]:

- all pores are open-ended and cylindrical without a porous network.
- although the BJH agrees with the views of the Kelvin equation, however, for the case of the hemispherical liquid-vapour meniscus at zero contact angle (well-defined surface tension), the Kelvin equation could be modified to Equation 2.43:

$$ln\left(\frac{P}{P^o}\right) = -\left[\frac{2\Upsilon V_L}{r_p}RT\right]cos\,\theta \qquad \text{Equation 2.43}$$

where

r_p = actual radius of the pore (nm)

R = universal gas constant (8.314 J K^{-1} mol^{-1})

T = absolute temperature (K)

γ = surface tension (dyne cm^{-1})

V_L= liquid sorbate molar volume (m^3 mol^{-1})

θ = angle between the physically adsorbed layer and capillary condensate radius (r_k)

Therefore, where the thickness of the adsorbed layer is considered, and with the angle between the physically adsorbed layer and capillary condensate radius being zero, the effective radius of the pore radius becomes the sum of the multilayer thickness and the radius (r_k) obtained from the Kelvin Equation 2.43, resulting in r_p, expressed in the form of Equation 2.44 and 2.45 [209]:

$$r_p = r_k \cos\theta + t \qquad \text{Equation 2.44}$$

$$r_p = r_k + t \qquad \text{Equation 2.45}$$

where r_p = actual radius of the pore (nm)

r_k = kelvin pore radius (nm) (from the Kelvin equation)

t = thickness of the adsorbed molecular layers at a corresponding relative pressure

ɵ = contact angle (where cos 0 = 1)

For practical utilisation of Equation 2.44, the procedure assumed that emptying the capillary condensate follows a stepwise manner over the corresponding reduction in P/P^o, during which the average pore radius also decreases. The amount of adsorptive lost in each step represents the core volume of pores emptied at that step; hence a functional relationship between P/P^o and r_k is represented by Equation 2.46 [201] [209]:

$$r_k(nm) = -0.415 \,/\, log_{10}\,(\frac{P}{P^o}) \qquad \text{Equation 2.46}$$

Therefore, to estimate the total pore volume (V_p), it is taken that the limited adsorbed amount (mmol g^{-1}), which occurs at P/P^o 0.995, when the pore is assumed to be filled, is converted to volume adsorbed [201], using Equation 2.47:

$$V_p = \frac{m}{\rho} = n.M/\rho \qquad \text{Equation 2.47}$$

where,

V_p = total pore volume ($cm^3\,g^{-1}$)

ρ = liquid density at saturation ($g\,cm^{-3}$)

m = adsorbent mass (g)

n = number of moles

M = adsorbed amount (g)

However, considering a case where the surface area is confined to a network of non-intersecting cylindrical pores, the total pore volume can be estimated using Equation 2.48, a relationship with the average pore radius.

$$r_{ap} = 2V_p \,/\, S_{BET} \qquad \text{Equation 2.48}$$

where,

S_{BET} = BET specific surface area ($m^2\,g^{-1}$)

r_{ap} = average pore radius (nm)

The result from the pore sizes (r_p) is then represented by a plot of $\Delta V_p/\Delta r_p$ against r_p, known as the pore size distribution, where ΔV_p is the pore volume obtained from the desorbed amount over a corresponding reduction in pressure, using the desorption branch of the isotherm.

2.22 Adsorption kinetics

As described in Section 2-15, it is evident that adsorption rates are a function of the energy of impact of the adsorptive onto the sorbent surfaces, driven by the temperature of an adsorption system. The impact of temperature variation may result in the rate of gas molecules penetration into the interior part of a sorbent being reduced or increased. Consequently, this would result in slow or high adsorption capacity. Additionally, where the adsorption system's temperature is increased up to a certain limit, the adsorption rate would also increase correspondingly, provided the activation energy of the adsorptive is attained. Since adsorption processes entail molecular diffusion, the kinetic analysis is necessary to determine system performance, hence the use of adsorption reaction or diffusion models to describe the kinetics of a given process [210]. The reaction model looks at adsorption chemical reaction kinetics from an entire process perspective; however, it does not account for the actual course regarding the stages involved [210]; therefore, it is crucial to explore the kinetics using the diffusion model.

2.22.1 Diffusion mechanism

From a diffusional viewpoint, it has long been established that most adsorption processes are controlled by diffusion through the layers at proximity to the boundaries of the sorbent particles [166]. McBain first established such hypothesis in 1919, where he opined that '*true adsorption is nearly instantaneous. And any lag at present can be accounted for by the time required for the dissipation of the heat evolved, or the comparative inaccessibility of a portion of the surface of a porous adsorbing agent.'* [211]. Given the above statement, it can be seen that, in the absence of lag, the estimation of adsorption rates may nearly be immeasurable.

However, where a porous sorbent is present, the steps involved may provide a means of assessing the mechanisms associated with adsorption kinetics. The adsorption diffusion model describes adsorption as taken place via four consecutive stages, namely [210] [212] (i) mass transport of the gas species to the sorbent surface, (ii) diffusion of the gas species across the liquid film at the boundary surface of the sorbent (iii) pore diffusion within the pores, and finally, (iv) adsorption and desorption process from active sites. As the kinetic process is

controlled by either of the rate-limiting steps, (ii) and (iii), the extent of diffusion would also ultimately depend on the pore size, as well as the relative ratio of pore width and the size of adsorptive [213]. Consequently, it is necessary to understand four variants of diffusional regimes such as (a) gas diffusion, (b) Knudsen diffusion, (c) surface diffusion and (d) activated diffusion which may become evident [214].

Gas diffusion occurs where the pore size is larger than the mean free path, in which case the adsorptive moves freely, and molecule-molecule collisions become more frequent. The mean free path defines the average distance a molecule travels between collisions. For Knudsen diffusion, the molecule sizes are closer to the pore size, causing the mean free path to be slightly shorter; hence molecule-wall collision dominates. The surface diffusion is evident when the mean free path is greater than the pore size, resulting in the adsorbate molecules becoming too close to the sorbent surface, with diffusion occurring via the movement of gas species along the surface of the pore walls. For activated diffusion, pore sizes are close to the kinetic diameter of the adsorptive; and here, the energy barrier at pore entrances limits molecular penetration rates; therefore, gas species must overcome the energy barrier to enter the pore. Also, it is pertinent to note that, for diffusion in polymeric materials, different forms of diffusion, described as Fickian, Case II (non-Fickian) and anomalous (non-Fickian), may be evident [215].

2.22.1.1 Fickian diffusion (case I)

Fickian diffusion is related to Fick's theory, which assumed that the flux of a diffusing substance through a unit area is directly proportional to the concentration gradient, described as Case I or Fickian diffusion, and represented by [216]:

$$J = -D\partial C/\partial x \qquad \text{Equation 2.49}$$

where,

J = flux per unit area of material (mol m^{-2} s^{-1})

C = concentration gradient of diffusing substance (mol m^{-3})

x = flux direction measured over the cross-sectional area of the material (m^2)

D = coefficient of diffusion ($m^2\ s^{-1}$)

As shown in Equation 2.49, it is evident that Fickian diffusion is concentration-dependent and may entail substance transportation from an area of higher concentration to that of lower concentration in the direction of diffusion. Although such a transport process may not represent gas species' movement, especially in transport pores, pores such as the micropore invalidate this view, as surface diffusion often dominates here. Another fundamental criterion for Fickian diffusion is that the surface concentration attains equilibrium upon a change in conditions, which remains unchanged through the sorption process [216]. Hence any deviation from Fickian diffusion may be likened to a consequence of the rates with which changes occur within the sorbent structure in response to external stresses experienced by the sorbent [216]. Generally, the rate of diffusion for any given process is represented by Equation 2.50 [217]:

$$M_t/M_e = kt^n \qquad \text{Equation 2.50}$$

where

M_t = sorbate uptake at time (t) in (g)

M_e = sorbate uptake at equilibrium (g)

k = rate constant (s^{-1})

n = diffusional exponent, relating to the nature of diffusion

Equation 2.50 can be employed to describe the mechanism of adsorption using a plot of ln (M_t/M_e) versus ln (t), from where n representing the slope may be determined. For Fickian diffusion, the value of n is 0.5, an indication that M_t/M_e is not directly proportional to t; however, in cases where n = 1, the mass change becomes proportional to t, making the process a concentration-independent one, defined as Case II diffusion [217].

2.22.1.2 Linear Driving Force Model (case II)

As case II represents a concentration-independent one, diffusion here follows a linear driving force (LDF). The characteristic feature of the LDF is that an initial induction time is established at the film surface boundary. Also, a small Fickian precursor is ahead of this front at the boundary, with a developed sharp and well-defined front advancing into the polymeric material at a constant velocity, resulting in the uptake amount increasing linearly with time [215] [218]. As a result, the advancing front is seen as controlling diffusion at a constant velocity, and the diffusion process proceeds at a much quicker rate. The LDF model is represented by Equation 2.51:

$$\frac{M_t}{M_e} = 1 - e^{-kt} \qquad \text{Equation 2.51}$$

where

M_t = sorbate uptake at time (t) in (g)

M_e = sorbate uptake at equilibrium (g)

k = rate constant (s^{-1})

For the LDF model, plot ln (1-Mt/Me) against t produces a straight line from where *k*, representing the rate constant, is determined from the slope. The LDF, as a mass transfer model, has been utilised in many cases for evaluating the kinetics of adsorption in porous materials.

2.22.2 Non - Fickian / Anomalous Diffusion model

Anomalous diffusion cannot be employed to characterise Fickian or Case II diffusion. This is because diffusion here is time-dependent relative to the cooperative motions required to accommodate diffusant distress within the polymeric structure. For this case, the value of n ranges from $0.5 < n < 1$ [216]. A number of early researchers, such as Park and Crank, investigated non-Fickian diffusion of a penetrant molecule into a polymeric structure by

introducing the concept of swelling, akin to changes induced by internal stress gradients in the polymeric material, based on time-dependent surface concentrations. Although the model developed were useful in predicting several features of non-Fickian diffusion, however, they were unable to present a clear prediction of the sharp front [219]. Additionally, Frisch suggested that polymers below their glass transition temperature limits often experience a time-dependent change in molecular relaxation times and surface concentration, required to maintain sorption-equilibrium at boundary interfaces [220]. This may suggest that the torrefied carbons developed in this work may experience a similar non-Fickian diffusion mechanism within their pores.

2.22.3 Stretched Exponential (SE)

For a complex condensed matter system that undergoes swelling-stress-relaxation processes, which results in molecular rearrangements, the stretched exponential (SE) function may be useful in describing kinetics. Additionally, Zeng and Xu suggest that such a complex system, characterised by a change in structure due to induced stresses, needs to be modelled by introducing a number of parameters into a model framework to help fit the experimental data [221]. For an adsorption system, the SE model, which is a form of a larger nested model, takes the form of Equation 2.52:

$$\frac{M_t}{M_e} = A(1 - e^{(-kt)\beta}) \qquad \text{Equation 2.52}$$

where

M_t = sorbate uptake at time (t) in (g)

M_e = sorbate uptake at equilibrium (g)

k = rate constant (s^{-1})

A = constant (A = 1, when $M_t = M_e$)

β = exponential parameter

Given that gas species diffusion into porous structures, experiencing anomalous diffusion, undergo a relaxation process, Fletcher *et al.* reported that SE model derivation for different physical mechanisms shares a common underlying mathematical structure [222]. Therefore, the exponential parameter β with a value of 0.5, represents a one-dimensional process governed by a distribution of relaxation times, while the value of $\beta = 1$ represents those governed by a single relaxation time. The case $\beta = 1$ is similar to the LDF model; however, changing from LDF to SE model indicates a change in the process relaxation time, from a single value to a case of distribution of relaxation times [222].

2.22.4 Nested Kinetic Models

Several researchers have suggested the modelling of adsorption kinetics as a complete set of nested equations. Bagley and Long, in 1954, investigated the adsorption rates of acetone vapours and methanol on cellulose acetate [223]. They found that diffusion rates of the penetrants into the polymer structure exhibited a two-stage process behaviour. The first, which is fast, aligns with Fick's law and only involve an elastic expansion of the polymer network without causing any change in the polymer structure. Additionally, the first process is seen as proceeding a ‘quasi-equilibrium state, a state in which the system deviates from equilibrium by an insignificant amount (i.e., a slow process) and does not obey the Fick’s law.

The second kinetic process, which exhibits a slow process, involves altering the polymer structures rather than exhibiting an ordinary diffusion [223]. As the two-step processes exhibited Fickian and non-Fickian behaviours, Fletcher *et al.* suggest modelling such kinetic profiles over an incremental change in pressure for adsorption occurring in porous sorbents is possible using a series of nested equations. The nested model, based on the double exponential and double stretched exponential, could provide a better picture of the diffusional processes involved in the adsorption process kinetic [222].

2.22.4.1 Double exponential (DE)

The DE model has been employed in the description of adsorption kinetics of gas species on porous materials. The study by Wilczak and Keynote investigated the adsorption kinetics of lead (II) and copper (II) unto activated carbon using the DE model [224]. They reported that the sorption kinetics could be divided into two steps. The first step, being the rapid phase, involves internal and external diffusion, while the second process, described as being slow, is governed by intraparticle diffusion. The two-step mechanism with two rate-limiting steps, and rate constants (k_1 and k_2), can be described by the DE model, as represented in Equation 2.53 [222] [210]:

$$\frac{M_t}{M_e} = A_1(1 - e^{-k_1 t}) + (1 - A_1)(1 - e^{-k_2 t}) \qquad \text{Equation 2.53}$$

where

M_t = sorbate uptake at time t (s) in (g)

M_e = sorbate uptake at equilibrium (g)

k_1 = rate constant (s^{-1}) for the first process (fast)

k_2 = rate constant (s^{-1}) for the second process (slow)

A = fractional contributing parameter for to k_1 and k_2 (where $A_1 + A_2 = 1$) and $1 - A_1 = A_2$)

However, where the rate constant k_1 is far greater than k_2, this suggests that the fast process can be assumed negligible in describing the entire process kinetics [210]. The values of A_1 , A_2 , k_1 and k_2 can be determined from a plot of M_t/M_e against t [210]. Additionally, since it has been known that diffusion rates through porous solids are dependent on the structural features of the material, Fletcher *et al.* also proposed that describing the kinetics by two processes with a single relaxation time suggests that the slow process would entail diffusion through pores that require high energy of activation, while the fast process represents a case of diffusion in pores with low energy of activation [222].

2.22.4.2 Double stretched exponential

A parent model that could better describe two processes' adsorption kinetics with a single relaxation time is the Double Stretched Exponential (DSE). The model is different from the DE model with the inclusion of two β parameters, the β_1 and β_2, as shown in Equation 2.54.

$$\frac{M_t}{M_e} = A_1\left(1 - e^{(-k_1 t)\beta 1}\right) + (1 - A_1)\left(1 - e^{(-k_2 t)\beta 2}\right) \quad \text{Equation 2.54}$$

where:

β_1 = exponential parameter for the first process

β_2 = exponential parameter for the first process

N/B – all other terms in the equation have been defined earlier in previous sections

Equation 2.54 can be reduced to the DE model by setting the exponential β_1 and β_2 parameters to 1 and the SE model with the A parameter set as 1, thus reducing the model to account for a one-rate controlling process as the LDF.

2.23 Summary

Chapter 2 of this work has presented a review of previous studies on biomass torrefaction and the theories governing adsorption processes. The characterisation techniques discussed have offered an insight into the relevant characteristics expected of sorbent materials and how they may guide in evaluating CO_2 adsorption performance. Based on the evidence provided, it can be seen that sorbents' developmental processes can influence their adsorption properties, such as porosity and surface functionality. Sorbents' performance can be benchmarked against each other, and a suitable characterisation technique will expose similar characteristics for comparison when utilised.

Consequently, it is anticipated that by tuning the inherent properties of carbonaceous materials, such as biomass, by employing "torrefaction", the resulting structure may be utilised

for CO_2 capture and cofiring application. Therefore, this research is focused on studying the CO_2 capture potentials of torrefied carbons and their application for CCS. As CCS processes involve the regeneration of captured CO_2 following an adsorption cycle, energy expended during the regeneration process is a significant concern. However, to compensate for expended energy, torrefied carbons developed in this work would be such that, once they are fully utilised for CO_2 capture in an adsorption system, they can be recycled as fuel for cofiring in the same power plant integrated into the CCS unit. The purpose is to offer a closed-loop approach for the CO_2 capture process from coal-powered plants, using torrefied carbons for the CCS and cofiring application.

To meet the research's intended objectives, it may be necessary to analyse selected soft- and hardwood's torrefaction performance under varying torrefaction conditions. Torrefaction performance indicators, such as - the mass yield, energy yield, energy gain, atomic ratio, calorific value and hydrophobicity of the untreated and torrefied carbon samples, would assess the sorbent and fuel qualities. Additionally, the torrefied carbons' chemical and elemental properties via the ultimate analysis and the Fourier transform infrared spectroscopy may help identify the functional groups present in the untreated and torrefied carbon samples. An adsorption study aimed at determining the surface area of torrefied carbons using the BET method under the nitrogen adsorption at -196 °C, as well as the characterisation of the torrefied carbons using CO_2 at 30 °C, would provide information on the equilibrium capacity of the CO_2 adsorption process under the varying adsorption temperature condition.

Furthermore, following the adsorption process, the determination of thermodynamic and kinetic parameters of the CO_2 adsorption using an appropriate kinetic model at the selected adsorption temperature condition would enable a comparison of the torrefied carbon performance with other sorbents used in industries. This would inform future potentials of using torrefied carbons in reducing energy consumption in processes. The post CO_2 adsorption HHV analysis of the spent torrefied carbons would expose the recycled fuel quality and the suitability for cofiring in the intended system. The characterisation technique employed in this work is described in Chapter 3, and the results obtained, given their analysis, is discussed in subsequent sections.

Chapter 3 : EXPERIMENTAL METHODS

3.1 Materials and methods

3.1.1 Sample preparation

For the torrefaction experiments presented in this work, two woody biomass samples, namely Iroko (IR) and Scottish Pine (SP), were utilised. The Iroko wood samples of about 3 kg were purchased from the Timber market at Enugu State, Nigeria. The Iroko wood was sourced from a forest situated at Ondo state (south-west) Nigeria. Similarly, the Scottish Pinewood samples of similar amount were collected from the Glasgow Wood Recycling company. These wood samples were cleaned during the collection with a cotton material to ensure that contaminants, such as sand and soil, were manually removed. Also, coal samples used for the experiment were collected from Dangote Cement Plc's factory, at Ibese, Ogun State, Nigeria, in a pulverised form of size < 1.2 mm. As received, the samples were stored in a polythene bag and kept in a dry cupboard under room temperature to prevent their degradation and loss of moisture.

Each untreated IR and SP sample was reduced into cubed-size shape, of length and width, between 4-7 mm. The choice of sample size for the experiments was to enable recovery of suitable torrefied solid product for use in the CO_2 adsorption studies and fuel characterisation. Additionally, it is anticipated that smaller sized samples < 2 mm would be further reduced under selected torrefaction conditions. As in previous studies, most torrefaction experiments using woody biomass have been limited to using sample sizes of 1 mm [101] [117] [139]. Therefore, during the woody biomass cutting process, the powdery particles of < 2 mm recovered from the samples were characterised using the thermal gravimetric technique. The 4-7 mm IR and SP samples were used for the torrefaction experiments under a CO_2 gas atmosphere as the inert gas.

3.1.2 Equipment used for the study

- An ABB MB300 Series Fourier Transform Infrared Spectroscopy (FTIR) using the Horizon MB^{TM} FTIR software to obtain spectral information of the samples for characterisation;
- A Perkin-Elmer Series II CHNS/O 2400 analyser at the University of Glasgow was used for the analysis of the elemental composition of the coal sample, as well as the untreated and torrefied carbon samples;
- A Micromeritics Accelerated Surface Area and Porosimetry Analyser (ASAP) 2420 was employed for the surface area and pore size analyses of the samples;
- An Intelligent Gravimetric Analyser, from Hiden Isochema Limited, was used for the CO_2 adsorption studies of the torrefied samples;
- The thermal properties of the samples and the proximate analysis were carried out using a Thermogravimetric Analyser (Netzch STA 449 F1 Jupiter);
- A Carbolite MFT 12/38/250 tube furnace, integrated with Eurotherm 2132 PID controller, was used to carry out the torrefaction experiments;
- Kruss Drop Shape Analyser (DSA100), v1.92 was used for contact angle measurements to assess the untreated and torrefied carbon samples' hydrophobicity.

3.2 Sample characterisation

3.2.1 Proximate analysis

Before carrying out the torrefaction experiments, it was necessary to comprehend the samples (IR and SP) thermal properties. Proximate analysis was carried out using NETZSCH Simultaneous Thermal Analyser (STA) (model: 449 F3A-1141-M, Germany); a combined Thermal Gravimetric Analyser and Differential Scanning Calorimetry (DSC) instrument, shown in Figure 3-1. The Thermal Analyser includes a highly sensitive balanced chamber for

weighing samples and a silicon-carbide furnace to heat samples up to 1700 °C. Although high sensitivity weight measurements of the samples may be influenced by a number of undesirable forces, such as; the buoyancy and thermal forces, which may be acting on the balance; the sample and the sample pan, however, the TGA has an integrated computer software program to account for these forces.

Before loading samples for analysis, an alumina crucible was placed on a null balance drive system which applies a force to the balance movement. The null balance within the TGA instrument balance chamber supports the sample pan and the reference pan. This helps maintain the balance in an equilibrium position to enable sample weighing during heating. After a stable weight was achieved and tareing of the balance, the crucible was removed. And for a given sample of the IR and SP sample, of sizes < 1.2 mm recovered during the cutting process, approximately 18.50 mg (+/-1 mg) were weighed out and loaded into the alumina crucible. Following this, the crucible was placed back on balance and lowered into position before initiating the sample analysis.

Figure 3-1-NETZSCH Simultaneous Thermal Analyser used for the thermal analyses

The proximate analysis was programmed to align with the British Standard-BS1016 method, based on Ottaway's adopted procedure [225]. Gas flow was activated, and once the sample weight stabilised under the N_2 flowing gas at a rate of 50 cm^3 min^{-1}, the temperature was raised to 105 °C, at a heating rate of 20 °C min^{-1}. The sample heating at 105 °C continued at this rate for ~ 20 min to enable moisture removal from the sample. Next to this, the temperature was ramped to 950 °C, where the sample was heated and stayed for ~ 7 min to enable the liberation of volatile matters. Once this stage was completed, the thermal environment was switched to oxidative (oxygen) at the same heating rate of 20 °C min^{-1}, where the oxygen gas flow at the rate of 50 cm^3 min^{-1} was maintained. The temperature was reduced to 750 °C, and the sample was held for another 20 min. After the final stage, which resulted in ash production, the final mass was stabilised for about 1 hr after switching the gas to N_2 flow to permit cooling down of the reactor. The changes by mass of the samples under the different heating regimes were recorded using the Proteus software. The mass percentage fraction of the samples were extracted from the TGA curve generated.

3.2.1.1 Calculation of compositions

The proximate analysis was employed to characterise the biomass samples for the composition of moisture, volatile matter, ash, and fixed carbon contents. Calculations were performed using Equations 3.1 to 3.4 as per procedure in Ottaway [225]. The fixed carbon content of each sample was obtained by difference.

$$\%\, moisture = 100\,[\,1 - \frac{m_{105}}{m_{initial}}] \qquad \text{Equation 3.1}$$

$$\%\, volatile\ matter = 100\,\left[\,1 - \frac{m_{950}}{m_{initial}}\right] - \%\, moisture \qquad \text{Equation 3.2}$$

$$\%\, ash = 100.m_{ash}/m_{initial} \qquad \text{Equation 3.3}$$

$$\%\, fixed\ carbon = 100 - [\%\, moisture - \%\, volatile\ matter - \%\, ash) \qquad \text{Equation 3.4}$$

where,

$m_{initial}$ = initial mass (measured under the flow of N_2 at 50 $cm^3 min^{-1}$ at room temperature)

m_{105} = mass of sample after heating at 105 °C (measured under flowing N_2)

m_{950} = mass of sample after heating at 950 °C (measured under flowing N_2)

m_{ash} = mass of the sample after combustion in (O_2/air) at 750 °C)

3.3 Experimental investigation

3.3.1 Choice of torrefaction condition

The choice of CO_2 gas for the torrefaction experiment was to promote a sustainable closed-loop system of using torrefied carbons for CCS applications. Additionally, the use of CO_2 for the torrefied carbon development would further optimise CO_2 capture process economics. Although different gases, such as - Ar, N_2, O_2 and NH_3, have been reported for use in biomass torrefaction [135], CO_2 gas has been considered suitable for modifying the physicochemical characteristics of biomass [226]. The choice of CO_2 gas for this work is further supported by the findings reported by Saadon *et al*., where the grindability of biomass torrefied with CO_2 was better than the case of the same biomass torrefied with nitrogen gas, making it more suitable for energy application [227]. Also, as the current work is focused on CO_2 capture from the combustion stacks of coal-based power plants, the CO_2 effluents can further be recycled for torrefied carbon development, thus lending further support to ensuring a sustainable closed-loop system.

For the choice of torrefaction temperature, as explained in Sections 2.6 and 2.7, different torrefaction types and conditions have been known to enhance biomass properties for fuel applications; however, most studies reported have limited their findings to torrefaction temperature conditions below 300 ^oC. More so, at temperatures < 300 ^oC, torrefaction conditions have been categorised into light, mild and severe cases, based on the temperature regimes. These regimes also impact differently on the mass and energy balances of a given

torrefaction process. The torrefaction condition of 250 °C, over a residence time of 30 min, has been described as light torrefaction and was applied for biomass utilisation for fuel applications in [228]. The mild temperature range of 250-270 °C had been employed for biomass enhancement for commercial and energy reduction in processes. However, for the severe torrefaction case above 300 °C, little analysis has been performed on the potential use of torrefied carbon for other industrial applications, such as carbon capture. Hence, the choice of temperatures > 300 ^{o}C and a residence time of 60 min as used in the current work was aimed to study the characteristic feature of torrefied carbons and their suitability for carbon capture applications.

Additionally, the choice of 320, 350 and 380 °C would permit a comparison of the impacts of changing torrefaction condition, as shown in other studies, to contribute to the body of knowledge. Aside from this, CO_2 adsorption studies of using torrefied carbons have not been investigated in greater detail in past studies; hence, the findings from the current work would provide more insight on the impacts of other torrefaction controlling parameters in torrefied carbon development. The other parameters considered in this work are the residence time and the heating rate (constant), as shown in Table 3-1, given their importance in biomass structural modification during torrefaction. These choices have been supported by other findings from other studies, as little investigation had been carried out on CO_2 adsorption studies of torrefied carbons.

Table 3-1-Torrefaction condition used for this work

Material	Temperature (^{o}C)	Residence time (min)	Condition
IR	290	60	IR-290
IR	320	60	IR-320
IR	350	60	IR-350
IR	380	60	IR-380
SP	290	60	SP-290
SP	320	60	SP-320
SP	350	60	SP-350
SP	380	60	SP-380

(Heating rate of 10 ^{o}C min^{-1})

3.3.2 Experimental set-up

The torrefaction experiments were carried out using a horizontal tube furnace of length 56 cm. The tube is made from a borosilicate ceramic material. The tube is of length 75 cm, with outside and inside diameters of 3 cm and 2.5 cm, respectively (tube thickness = 0.5 cm). The furnace heating is controlled by Carbolite MTF 12/38/250, integrated with Eurotherm 2132 PID controller.

The experimental set-up comprises a beaker containing distilled water to receive the condensable volatiles, a CO_2 gas cylinder, and a flow meter to regulate the flow of CO_2 gas from the gas cylinder through the reactor. A stopper (cork) fitted at each end of the 75 cm tube is pierced at the centre to allow for the inflow and outflow of CO_2 gas and the volatiles produced following the torrefaction process. The schematic description of the torrefaction experimental set-up is shown in Figure 3-2.

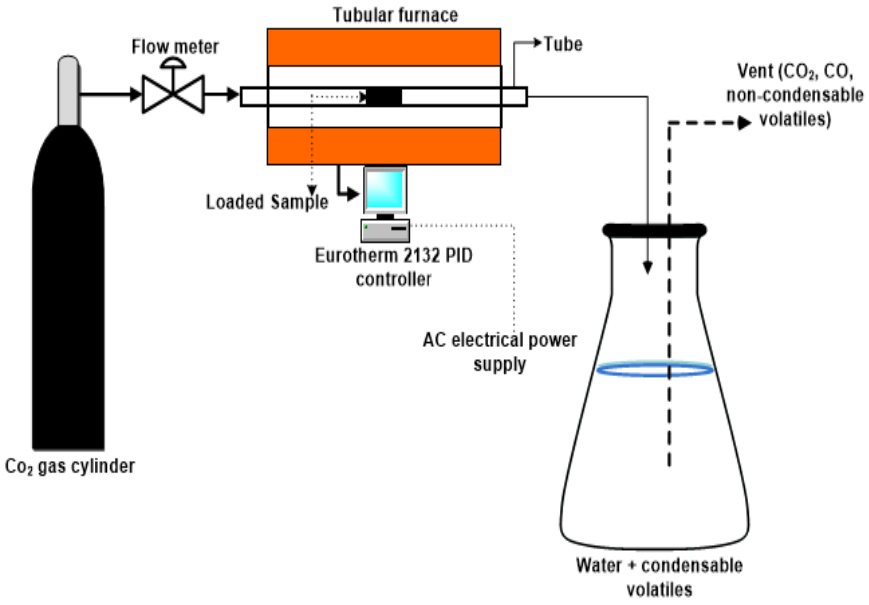

Figure 3-2- Schematic diagram of the torrefaction experimental set indicating the components

3.3.3 Torrefaction operation process

For each torrefaction experiment, IR and SP samples of about 1.6 g (+/- 10%) were loaded into a boat like shaped crucible (weight-14.6857 g) and positioned at the centre of the 75 cm ceramic tube before slid through to the centre of the 56 cm length furnace. After this, the stopper was attached to the tube outlet to a beaker containing distilled water to receive condensable-volatile products. The non-condensable volatile products are made to pass through to the venting system. CO_2 gas from a vertical cylinder was supplied through the reactor tube at the rate of 100 ml min^{-1} initially for about 5 min at room temperature to create a non-oxidative atmosphere within the tube.

Following this, a heating program of 10 °C min^{-1} was applied to the master PID controller based on selected torrefaction conditions under the CO_2 gas continuous flow. A residence time of 60 min, representing the dwell time, during which the loaded sample stays in the reactor was programmed. Once the dwelling time is attained, CO_2 gas continues to flow through the reactor to facilitate the cooling down of the reactor and the torrefied carbon sample. After the reactor cools down to room temperature at the end of each torrefaction cycle, the torrefied carbon was carefully removed and kept for further analysis. Each torrefaction cycle was repeated three times for consistency and confidence in the results, and the key performance indicators (KPI) were estimated. The KPIs, such as the mass yield, energy yield, energy density, enhancement factor and energy gain, are discussed and the results presented in the subsequent chapters of this report.

3.3.3.1 Determination of mass yield

After the torrefaction, the mass and energy balance was determined based on the solid and volatile product by difference. The initial mass (M_{f1}) of the raw biomass sample reduces to (M_{f2}) after torrefaction due to loss of volatile components (M_{f3}). Although Equation 2.14 may be utilised in determining the fraction of volatile given off, the mass yield was estimated using Equation 3.5:

$$Mass\ Yield\ (MY_{db}) = \frac{M_{f2}}{M_{F1}} \times 100\% \qquad \text{Equation 3.5}$$

where

M_{f2} = mass of torrefied product on a dry basis (db)

M_{f1} = mass of untreated sample on db

MY_{db} = mass yield on db

In this case, the mass yield is distinguishable from other results obtainable from a typical drying process. The torrefaction case is concerned with the changes occurring within the organic component of biomass materials on a dry basis.

3.3.3.2 Determination of energy yield

The energy yield (E_y), which represents the fraction of the biomass's energy-rich components retained following torrefaction, was due to the loss of the samples' energy-lean fractions. The energy yield is obtained from a calculated ratio of the higher heating value (HHV) of the solid product to that of the raw feed (i.e., the enhancement factor) and it is determined using Equation 3.6 [229]:

$$E_y(wt.\%) = (MY_{db}) \times (HHV_{torrefied}\ /HHV_{untreated}\ ) \qquad \text{Equation 3.6}$$

where, $HHV_{product}$ = higher heating value of torrefied solid product (MJ Kg^{-1})

HHV_{feed} = higher heating value of feed (untreated sample) (MJ Kg^{-1})

The result of the solid products' energy yield realised from the torrefaction processes is discussed in Chapter 4.

3.3.3.3 Determination of energy density, enhancement factor and energy gain

Energy densities, representing the extent of valuable chemical energy stored per unit mass of torrefied biomass, were determined following the selected biomass materials' partial

combustion. The energy density is associated with biomass calorific value in terms of the HHV or low heating value (LHV). In principle, the HHV represents the quantity of heat liberated, following the combustion of a specific amount of fuel (primarily at 25 °C), while accounting for the heat involved in the moisture removal [94]. By contrast, the LHV (net calorific value) defines the quantity of heat liberated, upon complete combustion of a given amount of fuel, without accounting for the heat of vaporisation of the products formed, whose value is always less than the HHV. [230]. The energy density (E_D) for the solid phase was calculated using Equation 3.7:

$$Energy\ Density, E_D = E_Y / M_Y \qquad \text{Equation 3.7}$$

where E_D = energy density

E_Y = energy yield

M_Y = mass yield

Additionally, another indicator used in evaluating the torrefaction performance is the enhancement factor (E_F) of the HHV, expressed by Equation 3.8. The indicator assesses the degree of torrefaction of the untreated sample, and where the value obtained > 1, it suggests there is relative gain per unit mass of the torrefied sample. Therefore, the greater the value (above unity), the higher the energy gain.

$$Enhancement\ factor\ (E_F) = \frac{HHV_{torrefied}}{HHV_{untreated}} \qquad \text{Equation 3.8}$$

Furthermore, although the enhancement factor, by implication, increases with increasing torrefaction severity, the extent of increment might be detrimental to the mass product yield. Given this, it becomes necessary to determine an optimum condition for torrefaction performance. The energy gain method proposed by [231] was employed as a better response variable/indicator, and the values were determined using Equation 3.9.

$$Energy\ gain\ (E_G) = \frac{\left[\frac{HHV_{torrefied} - HHV_{untreated}}{HHV_{untreated}}\right]}{\left[\frac{Mass_{untreated} - Mass_{torrefied}}{Mass_{untreated}}\right]} * 100$$ Equation 3.8

For the current work, the enhancement factor and the energy gain, for the torrefied IR and SP samples, under the different torrefaction process conditions were estimated and discussed in Chapter 4.

3.4 Analysis of torrefied carbon as fuel

After torrefaction, the torrefied carbons were analysed for fuel properties and CO_2 capture potentials. The analysis was to determine the changes impacted by the selected torrefaction conditions using various analytical techniques. For the analysis, a small amount of the torrefied solid product was weighed out and crushed into smaller sizes, < 1.2 mm, using a small laboratory mortar and pestle. Also, for the torrefied carbon sample size required for the CO_2 adsorption analysis, smaller fractions were cut from the torrefied solid product. The procedures for analysis of the result are explained in the subsequent sections.

3.4.1 Hydrophobicity of the samples using contact angle techniques

Contact angle experiments were employed to analyse the untreated and torrefied carbons' wettability. The Kruss Drop Shape Analyser (DSA1) v1.92, shown in Figure 3-3, was used. The benefit of such analysis was to determine the angle of contact between solid, liquid and vapour, which are influenced by specific forces, namely: the interfacial tension between the liquid and the surrounding vapour, the interfacial tension between the solid and the vapour, and also the interfacial tension between the liquid and the solid. The net result of the hydrophobic and hydrophilic interactions between the solid surface molecules and liquid molecules, following the deposition of a liquid droplet unto the solid surface, is the exhibition of a characteristic angle of contact that indicates a relative attraction of moisture on the torrefied solid surface. Like most liquid, water is known to have the capacity to wet solid surfaces and produce a contact angle due to its polar nature.

Figure 3-3-The photograph of Kruss Drop Shape Analyser (DSA100) used for the wetting investigation

So, for this analysis, a sessile-drop measurement method was employed. The Kruss instrument was programmed to analyse a circular droplet (circular method), where the contact angle was estimated from the circular arc and the baseline intersecting it. The baseline is the boundary between the drop contour and the surface of the liquid. Once the sample to be analysed was placed onto a horizontal surface, the high-resolution camera was focused on the sample. After this, approximately 5 µL of water was taken from a beaker containing distilled water using a pipette and was dropped onto the sample surface.

For measurements to be taken, the camera was focused on the image of the water droplet. The image was recorded and transferred to the analysis software, following a manual adjustment of the baseline, until a blue baseline was observed. Once the blue line matches the water droplet's actual base on the sample surface, representing where the water droplet meets its reflection, the contact angle measurements were taken. The pictures of the measurements were captured three times, allowing for the average value of the contact angle to be determined. The analysis error limits were within the range of (0.02-0.68%) for each sample analysed.

3.4.2 Ultimate analysis (CHN) of the samples

The CHN elemental analysis of the untreated and torrefied carbon samples was carried out at the University of Glasgow Chemistry laboratory, using Perkin-Elmer Series II CHNS/O 2400 analyser (Figure 3-4). The samples' analyses were carried out, using atropine and cysteine as the calibration standard compounds, with known k-factor. The k-factor was based on the analysis of these organic compounds with known elemental compositions. The procedure adopted for the ultimate analysis aligns with the European Standard BS EN 15104:2011 [232]. It aimed to analyse the percentage composition of carbon, hydrogen and nitrogen in all samples investigated. Before analysis, the Perkin-Elmer Series II analyser was tested for gas leakage and was set to a temperature of about 900 °C for the sample combustion. After this, ~ 2 mg (+/- 0.5 mg) of the calibration standard and those of the coal, untreated and torrefied samples, respectively, of sizes < 90 µm, were loaded into a tin capsule, which was weighed and folded. Also, for every four samples analysed, a new calibration standard is prepared for analysis to ensure the unknown samples' elemental composition results are consistent and reliable.

Figure 3-4-The Perkin-Elmer Series II CHNS/O 2400 analyser used for the study

Following this, each sample was analysed in triplicate, during which the calibration standard and the sample for analysis was dropped into the reaction chamber. Oxygen gas was then dosed in an excess amount to enable the sample in the reaction chamber to be combusted within the combustion tube, thus, producing gaseous products, like CO_2, CO and N_2O. As the gaseous products are being released, they are swept from the combustion chamber by a carrier gas (helium) into a reduction tube, operating at a cooler temperature of ~ 600 °C. While the gaseous products are being swept off, they are contacted over copper. The excess oxygen is removed, and the NO_x traces are converted to N_2, following the copper oxidation to copper (II) oxide.

The CO gas produced during the combustion process oxidizes to CO_2 gas over the copper oxide generated. Before being passed through a high sensitivity gas chromatographic (GC) column, these reduced gases mixed up where they are separated at different rates. Upon the separated gases exiting the GC column, they are detected by a thermal conductivity detector cell in the order of N_2, CO_2 and water. The samples' sulphur contents were below the detection limit and were considered negligible, and also given that the CHN components constitute ~ 97-99% of organic biomass fraction [233]. The relative errors for each element analysed are - C (0.1 – 0.8), while the H and N were < 0.2%. The oxygen contents of the IR and SP samples analysed in triplicates were determined by difference, using Equation 3.10.

$$O\% = 100 - C\% - N\% - H\% \qquad \text{Equation 3.9}$$

Additionally, from the CHN analysis, the torrefied carbon's atomic ratio for its fuel properties was determined using a linear function represented by Equation 3.11. Equation 3.11 shows the relationship of the hydrogen to carbon ratio (H/C), as well as the oxygen to carbon (O/C) ratio, proposed by Jones *et al.* [234]:

$$\frac{H}{C} = 1.4125\left(\frac{O}{C}\right) + 0.5004 \qquad \text{Equation 3.10}$$

where

H = hydrogen content

C = carbon content

O = oxygen

3.4.3 Analysis of the higher heating value of the samples

Although the HHV of the untreated and torrefied biomass samples can be determined experimentally using a bomb calorimeter, an alternative correlation proposed by Friedl *et al.* was adopted for the current study [235]. The HHV was aimed at assessing the impact of each torrefaction condition on the biomass samples, as this would be beneficial for energy balances in CCS applications. The model proposed by Friedl *et al.* utilised some experimental data based on the elemental composition of ~ 122 different biomass samples. Two regression models, namely – the ordinary least squares (OLS) and the particle least square (PLS) model, were developed as represented in Equation 3.12 and 3.13:

$$HHV\ (OLS\ model) = 1.87C^2 - 144C - 2820H + 63.8C\ \times H + 129N + 20147 \quad \text{Equation 3.11}$$

$$HHV\ (PLS\ model) = 5.22C^2 - 319C - 1647H + 38.6C\ \times H + 133N + 21028 \quad \text{Equation 3.12}$$

Friedl *et al.* found that the OLS and PLS models generated nearly identical results. An average value of both models was used to arrive at a generic Equation 3.14 to estimate the HHV of the untreated and torrefied products [235].

$$HHV = 3.55C^2 - 232C - 2230H + 51.2CH + 131N + 20{,}600 \quad \text{Equation 3.13}$$

3.4.4 Analysis of the torrefied carbon sample functional group using Fourier transform infrared (FTIR) spectroscopy

FTIR technique was employed to elucidate the structural and chemical composition of the samples before and after torrefaction. Since organic and inorganic compounds constitute individual elements and specific functional groups, the chemical bonds inherent in them vibrates at characteristic frequencies that match their vibration modes when exposed to IR

radiations. The absorption spectrum corresponds to the vibration frequency between the atomic bonds that make up the species [236] [237]. Because each material has a unique composition and different atomic arrangements, no two compounds produce the same IR spectrum [237]. Additionally, the size of a peak in a spectrum is a direct indication of the amount of material present.

Each vibration frequency depends on the strength of bonding between the atom and the mass of the atom. For an infrared activity to occur, the pre-requisite is a net change in dipole moment during molecular vibration [236]. Dipole moments are dynamic, as they change with vibration, and during vibrations, charged entities move around, and if the dipole moment at such transition is zero, absorption will not occur. The atomic energy levels, such as electronic, rotational, vibrational, and translational, are exposed by the IR electromagnetic radiation based on the light absorbance at their different regions. The IR region is divided into three, namely - near-IR (400–10 cm^{-1}), mid-IR (4000–400 cm^{-1}), and far-IR (14,000–4000 cm^{-1}) [237]. The vibrational energy, being a higher energy level, corresponds to the energy absorbed by a molecule, occasioned by vibration around the mean centre position of their inherent chemical bonds [236].

For each sample analysed, about 0.5 g (+/- 5%) of the finely grounded sample, as described in Section 3.4, were collected and loaded into the sample trough of the ABB MB3000 ATR-FTIR instrument. The FTIR spectrometer has three components - the radiation source, an interferometer and a detector. The sample loaded in the trough was clamped into position to enable a single reflection diamond / ZnSe ATR crystal on the ABB MB3000 ATR-FTR instrument to collect the spectra information after detection. The spectra measurements were taken at a resolution of 16 cm^{-1} over an average of 32 consecutive scans. The 16 cm^{-1} resolution is considered moderate to permit the spectra production; otherwise, the spectra information would be lost if the resolution is too low and might threaten the sample's correct functional groups identification. However, if the resolution is too high, time taking for measurements would be longer than necessary. The sample results were recorded and reported as %absorbance, covering the wavenumber of 500 cm^{-1} and 4000 cm^{-1}, described as the lower and upper limits of frequency, respectively.

Figure 3-5-The photograph of the ABB MB3000 FTIR spectroscopy used for the study

3.4.5 Cell wall composition analysis of the samples

The determination of lignocellulosic (cellulose, hemicellulose and lignin) fractions of the untreated and torrefied IR and SP samples were obtained from a gravimetric analysis of the Neutral Detergent Fibre (NDF), Acid Detergent Fibre (ADF), and Acid Detergent Lignin (ADL). The analyses were carried out by the Institute of Biological, Environmental and Rural Sciences (IBERS), Analytical Chemistry Unit at the University of Aberystwyth. A Gerhardt Fibrecap system (FOSS UK Ltd, Warrington, UK); being an improved version of the van Soest's method for fibre analysis [238], was employed for the NDF, ADF and ADL determination, allowing for the samples to be analysed in a reduced timeframe with a minimal systematic error. Correction factors were determined for every measurement within run precision of 0.030%.

Before analysis, the untreated and torrefied samples were milled using IKA A11 analytical milling instrument to ensure homogeneity. The recovered samples were passed through a nominal 1 mm sieve before sub-sampling. During the analyses, the NDF content, regarded as the cross-linked matrix of the plant cell wall (corrected for acid-insoluble ash), was determined after heating and refluxing ~1 g of selected sample in 100 ml neutral detergent solution,

containing 0.5 g of sodium dodecyl sulphate and several drops of n-octanol for 1 h. The resulting residue, being the NDF, was filtered out and washed with warm water and triethylene glycol before drying at 105 °C for 8 h. The % NDF was determined using the residue weight recorded [101].

Similarly, the ADF, which is loosely regarded as the cellulose plus the lignin fraction of the sample residue (corrected for ash) residue, was determined following the boiling and refluxing of 1 g of sample in 100 ml of an acid detergent solution containing cetyl trimethyl ammonium bromide, dissolved in 2 M sulphuric acid. The %ADF was determined using the residue weight recorded after filtering the mixture. After obtaining the ADF residue, the ADL was determined, which was then treated with ~5 mL of 72% concentrated sulphuric acid) and allowed to mix for ~3 h to dissolve the cellulose fraction in the ADF. The resulting mixture was diluted with ~140 mL of distilled water, followed by refluxing for 4 h) to enable the lignin fraction isolation. After this, the acid-insoluble fraction was recovered by filtration and washed twice with excess water before drying in a hot air oven at 100 °C for 8 h. The weight per cent was estimated and corrected for ash [101, 239]. The hemicellulose, cellulose and lignin fractions of the samples were determined using Equations 3.15 to 3.17, and the results relative to the torrefaction conditions are discussed in Chapter 4.

$$Hemicellulose\ (\%) = NDF\ (\%) - ADF\ (\%) \qquad \text{Equation 3.14}$$

$$Cellulose\ (\%) = ADF(\%) - ADL\ (\%) \qquad \text{Equation 3.15}$$

$$Lignin\ (\%) = ADL\ (\%) \qquad \text{Equation 3.16}$$

3.5 Gas adsorption analysis of the samples

To further investigate the torrefied carbons' physical and chemical properties, it was necessary to probe their surface area and pore size characteristics. Adsorption analysis was carried out on each torrefied sample using volumetric and gravimetric techniques. A volumetric technique was employed to characterise the torrefied carbon, while the gravimetric technique was

employed for the CO_2 adsorption studies. The choice of adsorptive (N_2) for the volumetric analysis was based on the gas's physical property, such as having low physisorptive energy.

Although some inert gases, such as argon and krypton, have been used for porous solids' characterisation, krypton adsorption at -196 °C (77 K) for surface area exploration may not be suitable for porosity study. This is given its low saturation pressure of 0.35 Kpa against 101.3 Kpa for N_2 at -196 °C, which may require more krypton being used for a given sample analysis [180]. Also, the number of krypton molecule in a free space of sample cell, at any P/P^o, compared to N_2 is reduced, even though the adsorption quantity will be slightly less. Hence the choice of N_2 against argon (Ar) was based on N_2 being the standard adsorptive for analysis of mesoporous character [201].

Secondly, the availability of N_2 is not questionable, and it has been reported to produce a well-defined monolayer on classical adsorbents. However, recent studies have shown that it adsorbs on a selected number of sorbents' polar sites and exhibits a quadrupole moment, resulting in localised adsorption [201]. Therefore, to minimise further experimental error in the use of liquid nitrogen at -196 °C, it is recommended that a given quantity of sample (> 1 g) is used for analysis [201]. Additionally, to contain evaporation of the liquid nitrogen in the Dewar, which serves as a coolant, the liquid nitrogen level should be kept constant and at a maximum height to the sample tube.

3.5.1 Volumetric analysis of torrefied carbon samples by N_2 gas adsorption

As explained in the preceding section, nitrogen adsorption measurements were carried out on the torrefied IR and SP samples using the Micromeritics Accelerated Surface Area Porosity (ASAP) 2420 analyser, shown in Figure 3-6. The volumetric analysis measures the amount of nitrogen gas adsorbed by the sample loaded within an evacuated system under a change in pressure conditions.

Figure 3-6-The photograph of the Micromeritics Accelerated Surface Area Porosity (ASAP) 2420 analyser

For each torrefied sample, a dry sample tube was weighed and the mass recorded. Following this, ~1.2 g (+/- 5%) of the sample selected for analysis was loaded into the sample tube, and the weight recorded. The tube containing the sample was then attached to the ASAP 2420 system's degassing station, where an independently controlled heating mantle enclosed the bulb end of the sample tube. Outgas conditions were applied by reducing the tube's atmospheric pressure down to a partial vacuum (5 mmHg) prior to full vacuum at 10 mmHg. Upon achieving full vacuum, the degas process was initiated by raising the sample temperature to 110 °C, at a heating rate of 10 °C min^{-1}, where it was held for ~4 h (this was to prevent sample sintering or deformation of the pore structure). The outgas condition chosen was predicated on the basis that some microporous carbon and zeolites have, in the past, been outgassed under a temperature of ~100 °C, for limited periods to avoid thermal damage [180]. After degassing, the sample was cooled down to room temperature, and the tube was backfilled with N_2 gas before being removed from the degassing port and the dry weight recorded. The sample tube was attached to the analysis port, where it was enclosed in an isothermal jacket to enable characterisation with N_2 at -196 °C. The ASAP 2420 instrument was programmed to collect 40 adsorption data points (P/P^o range of 0. 001 to 1.0) and 30

desorption points (P/P^o range of 1 to 0.1). The data were used to determine the surface area and pore volume of the torrefied samples.

3.5.2 Gravimetric analysis of the torrefied carbon samples for CO_2 adsorption studies

CO_2 adsorption studies of the torrefied carbon samples were carried out using an Intelligent Gravimetric Analyser (IGA-003), supplied from Hiden Isochema Limited. The gravimetric technique can precisely measure the magnitude and dynamic of CO_2 adsorption for a given loaded sample, thus making it possible to analyse the kinetics associated with a process through changes in mass. The IGA shown in Figure 3-7 comprises a highly sensitive vacuum microbalance, a gas flow and monitoring system, and a PC that runs the IGA Swin software, enabling a user interface with the instrument.

Figure 3-7-Photograph of the Intelligent Gravimetric Analyser (IGA-003) supplied by Hiden Isochema Limited at the University of Strathclyde Chemical and Process Engineering department

For each sample analysis, the sample bulb was carefully removed and cleaned before hanging on the balance for the bulb weight to be zeroed. After zeroing the weight, the bulb was removed from the balance, and a given amount of selected torrefied carbon sample (< 90 mg) was

loaded into the sample bulb. Once a stable weight was achieved, the chamber was sealed to enable outgassing operation to be carried out. The outgassing procedure at a rate of 6 kPa min^{-1} was performed to remove guest species that may be present on the sample. However, once the vacuum condition was established, the sample was degassed at a temperature of 120 °C, at a ramp rate of 3 °C min^{-1} for about 7 h (420 min) using a fast response furnace supplied by Hiden Isochema Limited.

After degassing the sample, the dry mass was recorded, and an isothermal pressure step from 0 to 1 bar for each adsorption analysis was programmed. Same time, the analysis temperatures of (30, 40 and 50 °C) were set for each torrefied sample to be analysed. The temperature of adsorption was kept constant for each adsorption case using a Grant water bath. Once the set temperature was attained, ~ 99.9% CO_2 gas was admitted into the sample chamber at the rate of 5 kPa min^{-1} over the chosen pressure steps of 0 to 1 bar. The IGA unit was programmed to collect 10 pressure points for the adsorption and 9 pressure points for desorption for each process cycle. After each cycle was completed, based on the pressure swing adsorption (PSA), the chamber was repressurised to atmospheric condition and the sample removed for further characterisation. The adsorption/desorption isotherms and the associated data for each of the static and PSA processes, such as the weight, time, pressure, temperature and concentration for each pressure step, were extracted using the IGA Swin software.

3.5.3 CO_2 adsorption kinetic studies

The IGA Swin software collects the data on a real-time basis for each pressure point of the adsorption during the mass profile relaxation. The data obtained were used in the modelling of the kinetic study of the CO_2 adsorption. The method used for modelling the kinetic study was the diffusion model, based on double exponential. The results of the kinetic studies and other experimental investigation are discussed in Chapter 5.

Chapter 4 : CHARACTERISATION OF TORREFIED CARBON AS FUEL

4.1. Physical analysis of samples

The physical characteristics of the untreated IR and SP samples provide an estimate of the moisture, volatile matter (VM), ash, and fixed carbon (FC) contents inherent in the materials. These parameters have been known to influence the combustion behaviour of fuels and plants' design performance [240]. On the contrary, the chemical analysis provides information on the elemental composition and functional groups present in the IR and SP samples. For typical woody biomass, the major elemental components such as carbon, hydrogen, nitrogen and oxygen were analysed and discussed.

4.1.1 Proximate analysis

As per the procedure described in Section 3.2.1, data extracted using the Proteus software of the NETZSCH Simultaneous Thermal Analyser for the temperature-time and mass-loss dependent profiles were used for determining the proximate analysis. The mass loss regimes were divided into three temperature heating zones, namely - 105 °C, 900 °C and 750 °C. The initial loss in mass occurred at a temperature of 105 °C, resulting in free moisture removal from the biomass.

The second heating segment during which the samples were heated to 900 °C, results in higher mass losses, accounting for the liberation of volatile contents. The third heating segment occurred during complete combustion of the samples at 750 °C, accounting for the loss of fixed carbon. Following the combustion at 750 °C, ash consisting of mineral and inorganic matters, an integral part of the plant, was left as the residue. The result of the proximate analysis is shown in Table 4-1.

Table 4-1-Proximate analysis of the samples

Constituents	IR (feed) wt. % (dry basis)	SP (feed) wt. % (dry basis)
Moisture	0.82	1.40
Volatile matter	76.96	76.58
Fixed Carbon	18.91	17.32
Ash	3.31	4.69

As shown in Table 4-1, the effect of mass loss relative to the percentage fraction of the biomass constituents, such as the moisture (M), volatile matter (VM), fixed carbon (FC), and ash (ASH) compositions, varied for both IR and SP samples. The moisture contents are expressed as the quantity of water per unit mass of the dry sample in mass percentage. The conventional oven drying method adopted for the proximate analysis for moisture determination at 105 ^{o}C, without prolonging the heating, was to avert a high loss of volatile matters due to possible decomposition at more extended heating periods. Although high moisture content in biomass has been reported to decrease the combustion yield of biomass [240], as their water contents must be evaporated before they give up their real heating value, however, the small fractions reported in this work may suggest that both samples may not negatively affect the combustion behaviour of the materials to a great extent. Woody biomass with moisture contents ranging from 10% to 20% has been considered ideal for wood burning by stove manufacturers. By comparing this with the present work, the proximate analysis shows that the SP sample (1.40%) has more moisture content than its IR counterpart (0.82%), indicating that both samples would be suitable as fuel candidates following their torrefaction treatment.

As evident in Table 4-1, the % mass fraction of VM and FC are higher in the IR sample than in the SP by a few per cent. Although the VM and FC % mass fractions for both samples are

somehow close, their ash content varies significantly. The results obtained from the proximate analysis suggests that the VM accounts for the largest share of the constituents, followed by FC. High VM in biomass could reduce combustion efficiency and may propel high pollutant emissions when the untreated biomass samples are used for cofiring applications. Additionally, although the VM and FC % mass fraction determined were as expected, they are closer to those reported in [126] [241], for soft and hardwood of similar biomass category. As reported in the proximate analysis of a black locust (BL) and the eucalyptus woody biomasses, the VM and FC for BL are 77.85% and 14.32% [242], while those of eucalyptus wood are 81.1% and 18.9% [137], respectively. Compared with this work's findings, the VM for IR (76.96%) is closer to those of the BL (77.85%), as both woody biomass are classified as hardwoods. However, although the eucalyptus wood, which can be considered a hardwood, contained higher % mass fractions of the VM and FC, relative to those of IR and SP, the variations may be related to the geographical location of the sourced materials.

For the ash content, the % mass fraction of the SP was slightly higher than those of IR. The ash content, which indicates the extent of non-volatile matter and non-combustible fraction present in the biomass, may also vary depending on biomass type. The variation was evident from the % fraction of the ash content reported in another study [241], for both softwood and the hardwood counterpart, which were higher than those reported for the IR and SP that are relatively lower. From the proximate analysis result, it can be concluded that the high VM and relatively low ash contents of the IR and SP samples suggest their potential for use as a fossil fuel alternative if their inherent properties could be enhanced by a torrefaction treatment. These are also supported by their < 10% moisture contents, as the woods would quickly burn away, sucking in too much air and cooling the flue gases as it does, thus increasing unwanted emissions.

4.1.2 Overall mass balance of torrefaction process

As explained in Chapter 2, the products of torrefaction processes are grouped into solid and volatile products. These products vary with selected torrefaction condition and fuel types. For each torrefaction condition listed in Table 3-1, a material balance was performed on the initial

and final solid product (torrefied carbon), with the volatile fraction obtained by difference. Figure 4-1 presents the linear relationship of the torrefied carbon and the volatiles given off relative to the initial mass (Mf1) (i.e., 1.6 g +/- 10%) of the untreated IR and SP. The volatile fractions comprising the condensable and non-condensable gases are not taken forward, as the analysis is not part of the research scope. The mass balance of the torrefaction process is shown in the Appendix (torrefaction parameters).

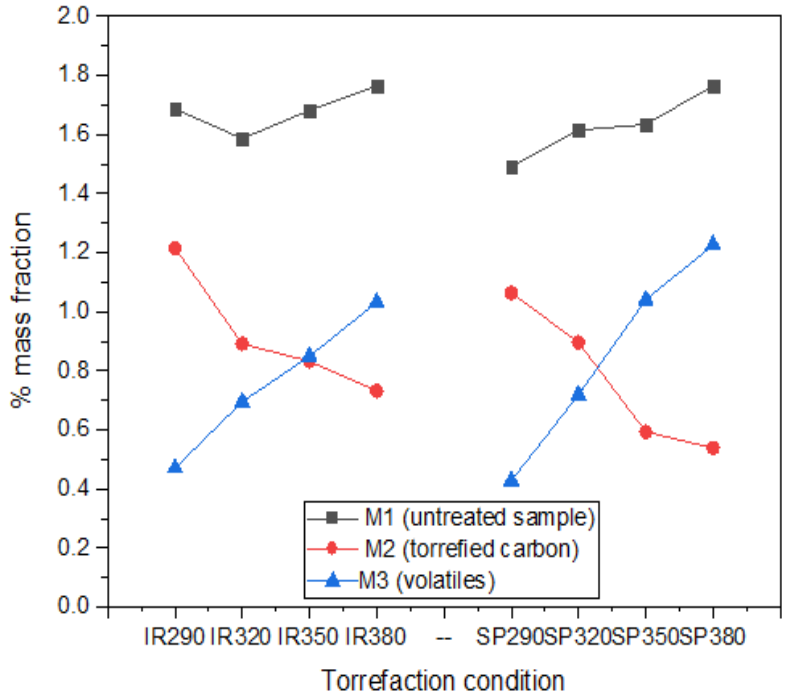

Figure 4-1-Mass balance of the IR and SP samples before and after torrefaction by percentage

As observed with increasing torrefaction condition in Figure 4-1, the volatiles liberated from the samples increases proportionally. A similar trend was observed for the solid product (M2), which continues to decline proportionally. Although both samples followed a similar trend, the volatiles given off under each condition varies with increasing torrefaction severity. These variations may be related to the IR and SP sample reactivity levels with increasing temperature and the selected residence time of 60 min, which concurs with the findings in [241]. Comparing the percentage mass fraction of the IR and SP, the dry solid mass fraction, as shown for IR, is higher than those of SP for all the torrefaction conditions, suggesting that more volatile fractions were produced for the SP sample. While this may suggest that the temperature of a

torrefaction process plays a significant role, even though the residence time is kept constant, the variation in components of the IR and SP samples can explain this behaviour.

Aside from this, it can be concluded that the SP sample shows more reactivity than the IR counterpart. The SP classified as softwood (coniferous), and the IR (dedicious) also share varying characteristics, as evident from the proximate analysis result. It is also anticipated that the three major constituents of plant biomass, namely hemicellulose, cellulose and lignin, would vary in these samples. As explained in Section 2.3.1, lignin contents in hardwoods are of range 18-25%, while those of softwood are ~25-35%; and the same variation applies for the hemicellulose in softwoods and hardwoods, having about 20-32% and 18-25% fraction, respectively as reported in [117]. However, for the cellulose component, 35-50% and 40-50% have been reported for soft- and hardwoods, respectively [117]. These variations in the composition of the lignocellulose constituents would be impacted differently under different heating environments, resulting in the change in the percentage of the mass and volatile fractions, as shown in Figure 4-1.

4.2 Chemical analysis of torrefied carbon from torrefaction

As the products from torrefaction processes vary, depending on process severity, it is necessary to characterise the resulting property of the torrefied carbon based on the selected condition. This would help ascertain the changes that may have occurred to the physicochemical properties of the treated material.

4.2.1 Ultimate Analysis

The ultimate analysis results for the coal, the untreated and torrefied IR and SP samples are shown in Table 4-2. The coal sample analysis was performed to determine the CHN/O constituents compared to the untreated and torrefied material.

Table 4-2-Elemental composition of coal, IR and SP samples

Sample	Condition	C% (d.a.f)	H% (d.a.f)	N% (d.a.f)	O% (d.a.f)
	Coal	50.81	4.17	1.44	43.58
IR	untreated	45.86	6.14	0.55	47.45
	290	59.01	5.72	0.47	34.80
	320	67.12	4.49	0.40	27.99
	350	67.94	4.40	0.32	27.41
	380	68.49	4.30	0.29	27.17
SP	untreated	45.27	6.46	0.30	47.97
	290	54.64	6.24	0.26	38.86
	320	63.73	5.69	0.21	30.37
	350	72.11	4.63	0.19	23.07
	380	74.47	4.39	0.17	22.52

(*O = estimated by difference)

As shown in Table 4-2, the CHN/O analysis shows some variation between the untreated and torrefied carbon counterparts. The carbon contents of the torrefied carbon at 380 °C were seen as having the highest percentage fraction. As with the carbon content (wt.%), a mass balance, based on the untreated and the residual solid, may account for the difference in the volatile constituents' carbon contents by the mere rule of conservation. Whilst the concentration of carbon in the torrefied carbon generally increases with increasing torrefaction condition; it was evident that for IR, the torrefaction at 290 and 320 °C seems to show higher carbon content than those of the SP. However, at torrefaction conditions beyond this regime, the SP carbon contents become more pronounced.

The disparity at higher torrefaction conditions for both samples would also impact the volatile fractions' carbon contents. According to Table 4-2, the volatile fraction continuously increases in the SP sample to account for this. Although more carbon is lost during the torrefaction process, the loss rate may be relative to the carbon content of the untreated IR and SP samples. As mentioned in Section 2.3.3, the hemicellulose fractions in hardwood are more reactive than those in softwood, which may have accounted for the quicker mass loss rate in the SP sample. Therefore, whilst the SP sample exhibited an increasing mass loss with increasing torrefaction condition than IR, it also experienced a greater loss in the low-energy volatile constituents, as shown in Table 4-2. The impacts were shown in the van Krevelen plot, Figure 4-2, where the H/C and O/C ratios varied with increasing torrefaction severity. Generally, the carbon content evident in the IR and SP samples increases with increasing torrefaction condition, while the hydrogen, nitrogen, and oxygen contents decrease correspondingly.

Regarding the hydrogen content, torrefaction has been known to result in the liberation of low energy volatile constituents, comprising the condensable and non-condensable gases. The volatiles from the biomass results in low calorific value products, which are occasioned by the loss of energy-rich elements, such as carbon and the non-oxidising hydrogen confined within the -OH groups present in the lignocellulose components. As with the carbon balance, the hydrogen balance may also be compared with the percentage fraction available in both the untreated and the residual solid product, whose difference may account for those contained in the volatile fraction. The variations in hydrogen content in the samples over increasing torrefaction conditions are shown in Table 4-2.

As expected, the volatile fractions liberated results in a greater loss of the hydrogen constituents. Although hydrogen is non-oxidising and contributes to the high energy contents in solid biofuels, it is also instructive to note that it does not contribute to energy when combined covalently with oxygen to form moisture in fuels. Based on the elemental analysis shown in Table 4-2, it was estimated that the total percentage of hydrogen lost from the SP sample was 36.01%, compared with 32.61% lost from the IR sample, over the entire torrefaction condition. Additionally, the hydrogen content generally decreases with increasing

torrefaction condition. The distribution of hydrogen along the torrefaction condition infers that the IR sample loses fewer hydrogen species than the SP sample. The percentage fraction of hydrogen liberated at the conditions of 350 and 380 °C, for the SP are 18.62% and 5.18%, respectively, while those of IR equates to 2% and 2.27%, respectively, owing to increased volatile production in the SP sample. The loss of hydrogen species in the SP may be ascribed to bond breakages within the OH groups, concurrent with the oxygen losses within the cellulose structure. The OH group predominant in the cellulose structure of woody biomass is due to its hydration water level [93]. Additionally, whilst non-condensable gases liberated during this time may contain gases like methane (CH_4) and some other low molecular alkanes, the condensable fractions such as acids and water were not undertaken as they are not part of the scope for this study.

Another important element for consideration is nitrogen. It has long been established that nitrogen constituents in biomass are found in the linear and cyclic N-compounds of the biomass structures, likened to some class of proteins, such as amino acids and free enzymes [243]. A number of studies have reported the decomposition routes of nitrogen-containing groups, which often result in the formation of ammonia and hydrogen cyanide, are competitive during biochar formation [243] [244]. While it is believed that NH_3 production occurs during char production, the volatile cyclic amides result from bonds cleavage within the biomass structure. As with the percentage of nitrogen fraction liberated during the selected torrefaction condition, this may be accounted for by difference, considering the percentage fraction contained in the untreated and torrefied solid product. As shown in Table 4-2, it is evident that as the torrefaction condition increases, the amount of nitrogen liberated decreases correspondingly.

This suggests that, aside from the temperature variation, longer residence time, as used in this study, results in more volatile-N fraction liberation. The increase in volatile fraction agrees with the findings reported by Jones *et al*., where longer torrefaction times results in more volatile production during char formation [245]. Also, with longer residence times appearing to affect the nitrogen constituents, shorter residence times, although not investigated in this work, are anticipated to favour the retention of nitrogen species in the torrefied solid. It is also

instructive to note that, although extended residence time and higher temperature promotes more nitrogen emission, the feed size is also a determinant factor. The evolution of protein-related nitrogen species from woods/chars into gaseous products have been reported to commence at a temperature of about 200 °C during torrefaction processes. Despite this, the char and volatile elemental constituents' ratio still depends on the fuel type and torrefaction process condition.

Comparing the IR and SP samples, the total % fraction of the nitrogen species lost from the SP samples was about 52.57%, compared with 58.81% from the IR samples, over the entire selected torrefaction condition, relative to the untreated samples. Given this, it can be concluded that the IR samples retained more nitrogen species in their torrefied carbons compared to those of the SP sample. This is aside from the fact that nitrogen content in the untreated IR sample (0.55% d.a.f) is much greater than those in the SP (0.30% d.a.f). Also, a number of researchers have shown that nitrogen contents in untreated biomass are not of primary concern during thermochemical conversion processes in biomass [246]; however, the preferential loss of nitrogen towards the char formation is beneficial regarding the emission of volatiles when used for energy application purposes.

4.2.2 Atomic ratio of torrefied carbon fuel

The torrefied carbons atomic ratios were estimated from the ultimate analysis results compared with those of coal, being the selected comparator in this study. The O/C and H/C ratios over the selected torrefaction conditions were determined from Equation 3.11 and represented in Figure 4-2.

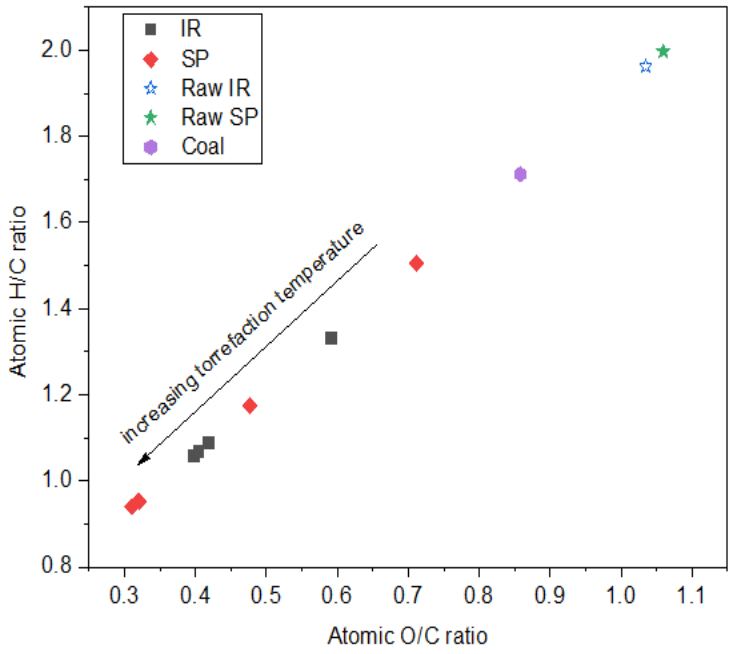

Figure 4-2-van Krevelen plot showing H/C and O/C atomic relationship

The van Krevelen plot presents the changes in the O/C and H/C ratios of the torrefied carbon relative to their untreated counterparts. According to the van Krevelen plot, it is evident that, with increasing torrefaction condition, there is a general decline in the H/C and O/C ratios. Although both samples show an improvement in their H/C and O/C relationships, there were marked differences between them compared with the coal and the untreated counterparts. The SP sample seems to experience a significant impact on its H/C and O/C over the torrefaction condition, compared with the IR samples, despite having slightly higher O/C (SP: 1.06, IR: 1.03) and H/C (SP: 1.99, IR: 1.96) ratios in their untreated sample.

Additionally, it is instructive to note that, while the torrefied carbon uniqueness at the varying torrefaction conditions is dependent on feedstock type, this would vary for both soft- and hardwoods owing to their lignocellulosic compositions [247]. Although the trend in the behaviour of the atomic species following the torrefaction processes aligned with the findings reported in other studies [248] [126], the release of the volatile-rich hydrogen and a reduction in the atomic oxygen contents in the water and CO_2 gases produced may have contributed to the H/C and O/C ratio variations. A reduction in oxygen constituent present in the torrefied carbons, by implication, suggests the extent of improvement of the fuel quality of the torrefied

carbons since more oxygen is lost relative to carbon. With carbon content being a significant energy source, this also associates with the calorific value.

Consequently, since the atomic ratios vary with the torrefaction conditions, this provides a means of predicting the torrefied carbons' energy behaviour compared with other fuels. As shown in Figure 4-2, the H/C and O/C ratios of the torrefied IR and SP carbons exceeded those of the coal sample investigated, suggesting that the untreated biomass shifted away from its original biomass resemblance towards the coal characteristics. For the samples torrefied above 290°C, the atomic ratio makes them suitable for consideration as a coal alternative. Li *et al*. asserted that torrefied wood with HHV > 20 MJ kg^{-1} and H/C and O/C ratios of 0.8 and 0.4, respectively, can serve as coal substitutes, with the potential to offer a 10% reduction in power system efficiency [249]. This demonstrates that the torrefied carbon developed in this study will behave like other fuels for energy applications.

4.2.3 Higher heating value of torrefied carbon

The higher heating value (i.e., the calorific value) correlates with the C and O contents of a given fuel, based on the H/C and O/C relationship. As is evident in Figure 4-3, the HHV of the torrefied samples is noted to be increasing with an increase in torrefaction severity relative to the untreated counterparts. Although the increase in HHV may be associated with the amount of carbon, ash, and other extractives, the constituents also influence the HHV of fuel. Carbon content plays a crucial role in the exothermic processes that occur during the combustion of fuels, while, by contrast, oxygen governs the endothermic reactions.

Although oxygen is not a reactive element, it decreases the HHV of lignocellulosic fuels when present at higher levels with ash. Also, the principal role of oxygen is to consume the hydrogen available through an oxidation process [93]. High ash levels have been reported to make biofuel less desirable for energy applications, whereas high extractives have been known to promote their potential for energy utilisation [250]. The HHV of coal, untreated and torrefied samples used in this work were determined by calculation, using the model proposed by Friedl *et al.* in Equation 3.14. The trend in the HHV value of the IR and SP samples is shown in Figure 4-3.

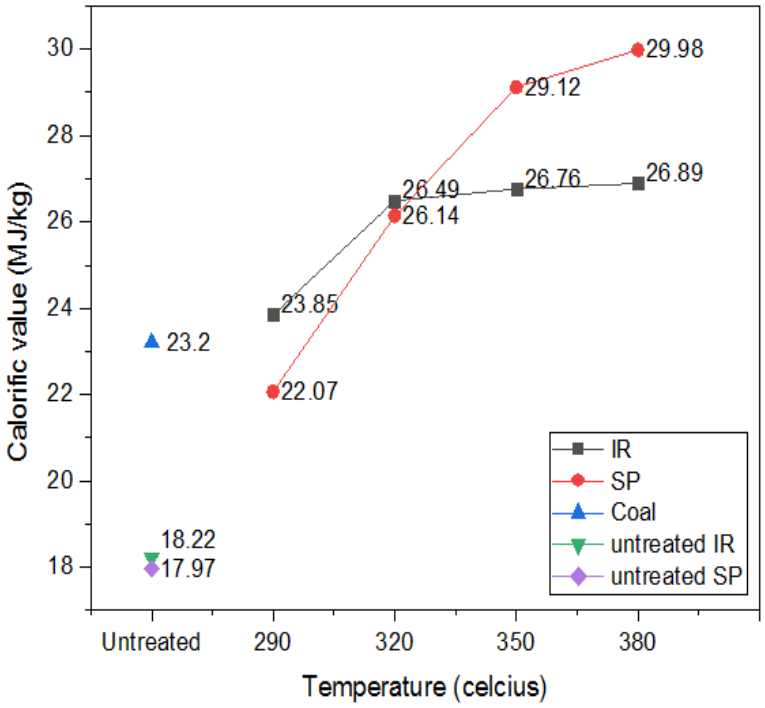

Figure 4-3-High heating value of the IR and SP samples investigated

As the increased HHV for the IR and SP samples corresponds with an increase in the torrefaction condition, the reduction in low-energy bonds within the biomass matrix, like the H-C and O-C, in addition to the corresponding increase in high-energy bonds (C-C), may account for this behaviour [251]. These behaviour suggest that the HHV of the torrefied carbons developed intensifies following the torrefaction process. Aside from the influence of torrefaction temperature, the HHV of the different samples may be associated with other factors, such as physiological differences. The impact of seasonal changes and the investigated materials' geographic location may have contributed to the moisture content variation and the HHV of the torrefied IR and SP carbons. Basu asserts that increasing HHV of fuels could be linked to plant biomass ageing properties [93].

As mentioned in Chapter 2, the fraction and composition of the lignocellulose present in biomass is another contributing factor to HHV variation. Lignin contents found in plant biomass are known to exist in various proportions, with the extractives. This suggests that, for grasses, hardwoods, and softwoods, varying amounts of lignin are expected. Their composition is controlled by methoxyl substitution and C-C bonds linking their phenyl group [250] [252]. The aromatic and phenolic characteristics, which are more pronounced in softwood due to C-C

bonding, prevent reversion to monomeric units under mild temperature processes [250]. Contrary, for hardwoods, their aromatic character is controlled by the coniferyl alcohol (i.e. 3-methoxy-4-hydroxycinnamyl) that produces the guaiacly lignin. The difference in the lignin constituent is responsible for the variation in the HHV reported for the SP and IR samples, above the temperature of 320 °C, due to their chemical reactivity. The study carried out by Demibras further emphasised the relationship between lignin and the HHV, where the HHVs of extractive-free biomass samples reported a lower value than the case of unextracted samples [253].

The HHV of softwoods, which have been reported to be in the range of 20-22 MJ kg^{-1}, and those of hardwoods in the range of 19-21 MJ kg^{-1} [253], are closer to the results obtained in this study. Although a slight difference in the value of the HHVs was observed for the SP samples above this range, the variation of extractives (fats, fatty alcohols, phenols, terpenes, resin acids) present in the SP may have accounted for the difference reported. Also, it is instructive to note that these values of HHVs reported for the IR and SP samples in this study are specific to these materials, based on the inherent properties of their untreated counterparts and not a representation of the entire IR and SP species. Generally, the implication of variations in the HHV seems to correlate with the lignin contents, suggesting an associated improvement in the fuel properties, potentially reducing greenhouse gas emissions that are likely when utilised for energy applications.

4.2.4 Fourier transform infrared spectroscopy of IR and SP sample

The chemical changes within the untreated IR and SP samples following the torrefaction processes were investigated using the FTIR. Figures 4-4 and 4-5 are the FTIR spectrum for the untreated and torrefied IR and SP carbons developed at different torrefaction conditions. To better understand the infrared spectral interpretation, it is instructive to start at the root of most organic compounds, namely the fundamental backbone or the parent hydrocarbon structure [236]. Given that aliphatic hydrocarbons exist in simple linear and branched chains, however, in cyclic structures, the introduction of unsaturation in the form of a double or triple bond has a profound effect on the molecule's chemistry. Similarly, this also has a significant influence on the infrared absorption spectrum.

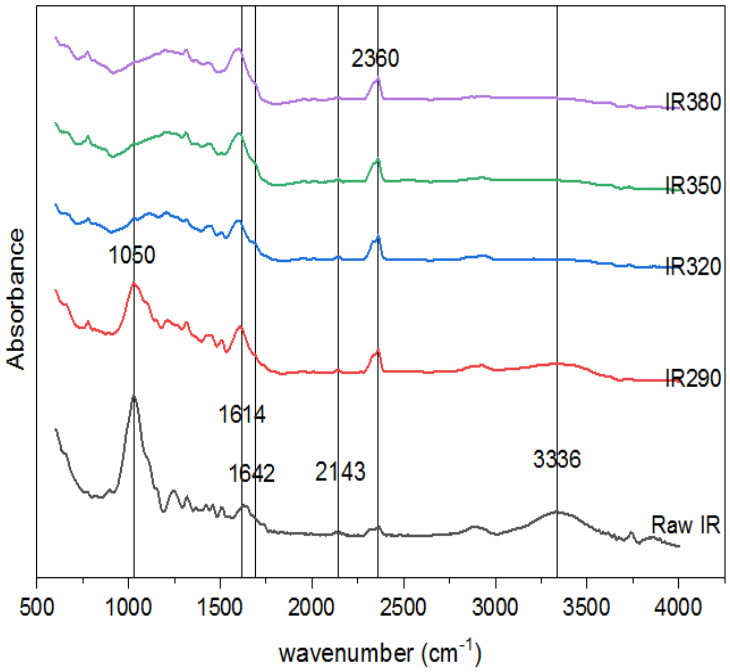

Figure 4-4- FTIR spectra of IR samples

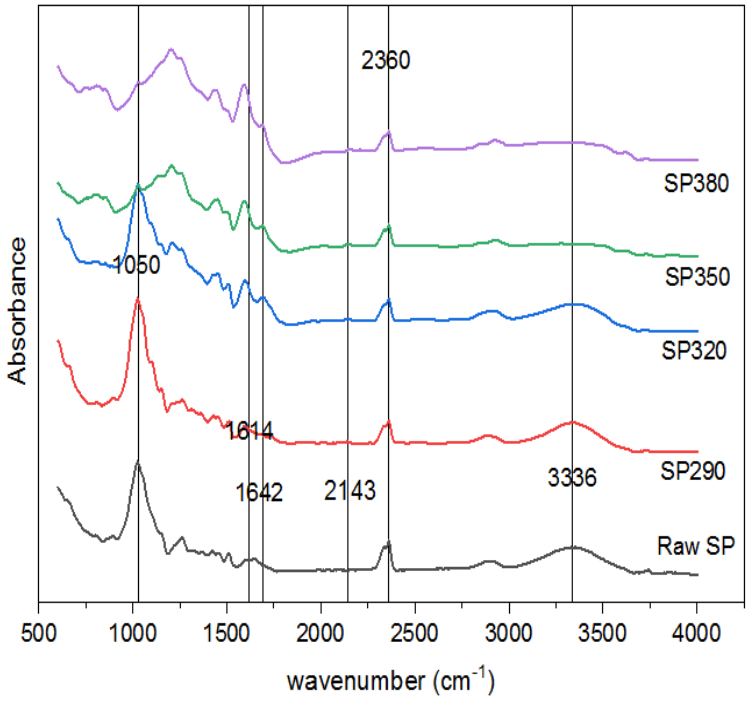

Figure 4-5- FTIR spectra of SP samples

Starting with the absorption spectrum of a molecule, as can be noticed at region 2330 - 2360 cm^{-1}, in Figures 4-4 and 4-5, there is evidence of an increasing peak for all the torrefied carbons. The band 2360 cm^{-1} which lies in this region, represents an antisymmetric stretching

of a physisorbed CO_2 by the torrefied carbons and the subsequent vibration of the CO_2 gas molecule [254]. Molecular vibrations are often determined by their normal modes, depending on the nature of the structure. Each absorption in a vibrational spectrum corresponds to a given normal mode. Since CO_2 has a linear structure, the vibrational mode is determined from the 3n−5 normal mode (where n = the number of atom present). Therefore, for the CO_2 molecule with four vibrational modes, namely - symmetric stretch, asymmetric stretch and two bending vibrations (i.e., scissoring, twisting, rocking and wagging), the nature of vibration depends on the net change in dipole moment, which a pre-requisite for an atomic or molecular specie to become IR active. This asymmetric stretching and bending of the CO_2 make it possible for IR absorption, as evident in band 2360 cm^{-1}.

As shown at band 3336 cm^{-1}, the untreated IR and SP peaks were higher than those of their torrefied carbon counterparts. The peak at 3336 cm^{-1}, which lies in region 3250 - 3650 cm^{-1}, suggests a polymeric OH^- group associated with the hydrogen bonds within the alcohol and phenol compounds of the samples' structures [236] [255]. The impact of the hydrogen bond is to produce significant band broadening and lower the mean absorption frequency. It is instructive to note that the OH^- group does not exist in isolation. A high degree of its association is due to the extensive hydrogen bonding, reflected by the peak height of the SP at this region, due to the higher moisture content (Table 4-1). As can be seen with increasing torrefaction condition, the broad peak at 3336 cm^{-1} disappears, occasioned by the dehydration reactions under intense heating during the torrefied carbon development. The lowering of the O-H bond intensity is a function of the degree of burn-out and the hydrogen bonding strength [236]. As a result, the OH^- degradation contributes to the formation of non-polar and unsaturated compounds that could condense on the torrefied carbon surfaces, thus increasing their hydrophobicity.

Furthermore, as shown in Figures 4-4 and 4-5, band 1642 cm^{-1}, which lies in region 1650 - 1850 cm^{-1}, evident a small shoulder, which suggests the presence of a carbonyl-containing compound [236]. The absorption of a carbonyl-containing group depends on the electronic characteristic of the substituent group, which defines the chemical characteristic and reactivity of the specific carbonyl compound [236]. Although the absorption spectrum of various

carbonyl-containing compounds often overlapped at this region, which creates difficulties in identifying the dominant functional group; however, as the absorption spectrum at this region occurred at the low-end shoulder, the identified functional group is that of carboxylate [236]. Due to the stretching of the C=O bond, the carboxylate bond disappears with increasing torrefaction condition following carbohydrate degradation, occasioned by decarboxylation reactions, under the intense heat treatment during the torrefied carbon development. Additionally, the carboxylic acid level from the hemicellulose constituents, including the xyloglucan, arabinoglucuronoxylan and galactoglucomannan, are all affected by the increasing torrefaction conditions as new products form.

At region 1050 - 1260 cm^{-1}, the stretched peak at band 1050 cm^{-1}, shown in both IR and SP spectrum, may be ascribed to the aromatic compounds, likened to syringyl rings and ethers containing the C-O bonds [236]. The syringyl is a class of alcohol found in the lignin components of the hard- and softwoods. Although the syringyl contents may vary, as may be supported by the heights of the peak for the IR and SP, however, with increasing torrefaction conditions, the aromatic C-O peak stretches and disappear, with a more pronounced effect noticeable for the IR torrefied carbon developed at 320 ^{o}C, compared with the SP. The suggests that the C-O bonds in the IR are more reactive than those found in the SP due to variations in the lignin coniferyl alcohol and syringyl alcohol units. This may also be attributed to the extent of the lignin constituent present in hardwoods, which have also been reported to be more reactive than those in softwoods [106]. Additionally, ether bonds often exhibit strong absorption at this region; however, their identification can be difficult in complex cases, as alcohols, esters, and other compounds containing the C-O bond also stretch at this region. The ether bond identified may be present in the β-glycosidic bonds of the wood samples' hemicellulose and cellulose components, whose peaks decreased with increasing torrefaction conditions. These components were known to degrade at temperatures beyond 250 °C [251].

Figures 4-4 and 4-5 shows evidence of a small peak at band 1614 cm^{-1}, in region 1580 - 1615 cm^{-1}, suggesting an aromatic ring C=C bonded compound. The band's peak intensity at this region gradually disappears with increasing torrefaction conditions, which may be attributed to the stretching of the aromatic C=C bond [236]. The vibration of the aromatic ring in this region

varies slightly, and it is a function of orientation and the substituents' nature on the aromatic ring. Another unclear peak observed from the IR and the SP absorption spectrum was at band 2143 cm^{-1}, where the height of the peak for the SP seems smaller than that of IR, occasioned by variations in their functional groups. Although nitrile (C≡N) absorption peaks often exist in region 2200 - 2300 cm^{-1}, which are closer to those of the alkyne (C≡C bonds) group [237], the peak notable in the spectrum may be associated with an N-functional group that may be contained in these materials. As observed, it was evident that, with increasing torrefaction conditions, the effects on the N-functional groups were not much pronounced. However, previous studies have shown that where a different gas medium such as nitrogen is utilised for the torrefaction, increasing band intensity at this region is expected. Such an increment has also been reported in a similar study, following the pyrolysis of hickory wood and bagasse for biochar production, where an increase in nitrogenous groups on the pyrogenic carbon was reported for the material developed at 600 °C, with the FTIR bands falling within 2000 - 2400 cm^{-1} [256]. The summary of the functional groups identified in both samples is shown in Table 4-3.

Table 4-3- Identified functional group on the Torrefied carbons

Origin	Group frequency cm^{-1}	Assignment cm^{-1}	Ref
adsorbed CO_2	2330 – 2360	2360	[254]
O-H	3250 – 3650	3336	[236]
C=O	1650 – 1850	1642	[236]
C-O	1050 – 1260	1050	[236]
C=C	1580 – 1615	1614	[236] [237]
C≡N	2200 - 2300	2143	[237]

4.2.5 Effects of torrefaction on cell wall composition

As per the procedure described in Section 3.4.5, the IR and SP samples' compositional changes relative to their untreated counterparts are shown in Figures 4-6 and 4-7, respectively.

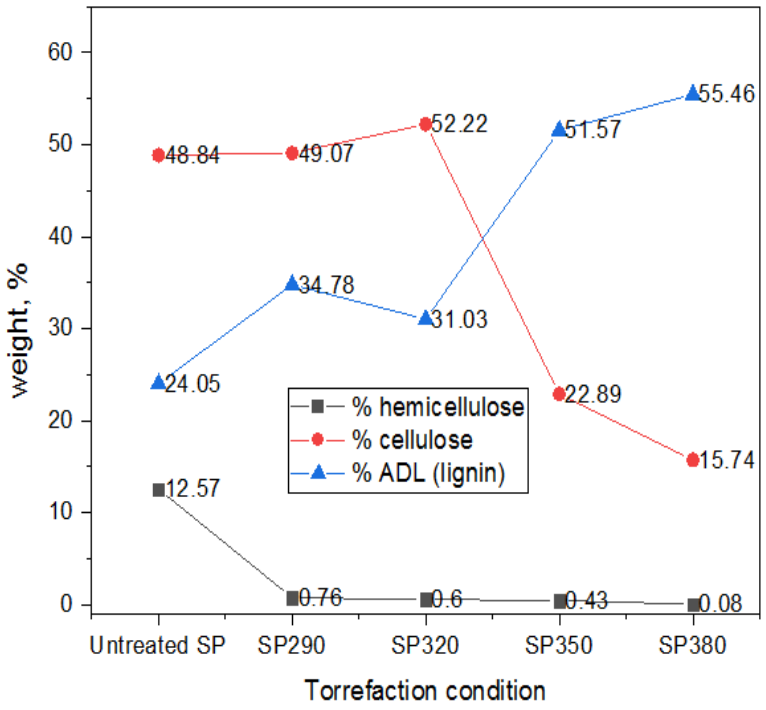

Figure 4-6- Cell wall composition of the SP sample with increasing torrefaction condition

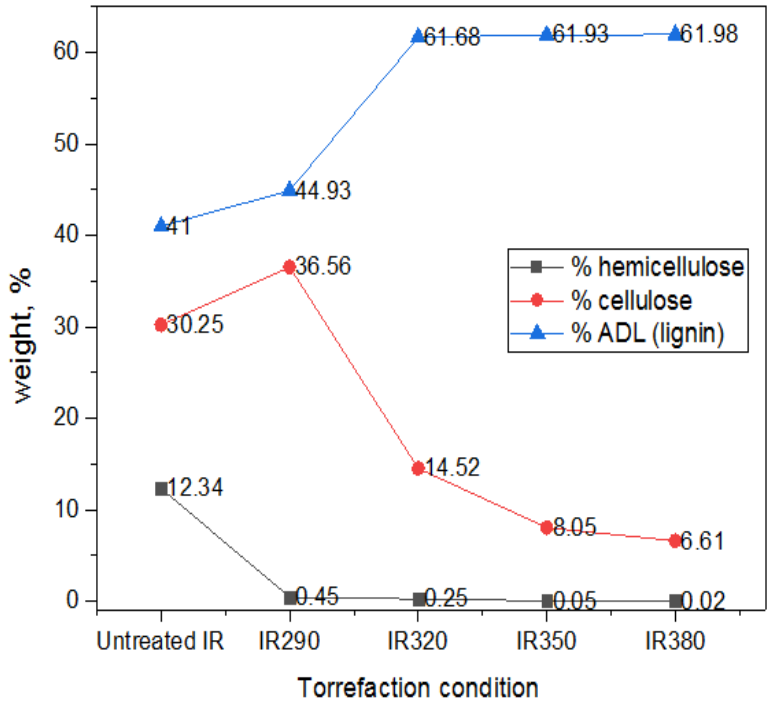

Figure 4-7- Cell wall composition of the IR sample with increasing torrefaction condition

For the untreated samples, the chemical composition of the hemicellulose, cellulose and lignin constituents for the IR sample are 12.34%, 30.25% and 41%, while their proportions in the SP are 12.57%, 48.84% and 24.05%, respectively. The total fraction of the lignocellulose content, representing the sum of hemicellulose, cellulose and lignin present in the IR sample, is around 83.59%, while those of SP is 85.46%. The variation may be associated with higher amounts of the extractive compounds present in the SP sample. Also, the hemicellulose and cellulose fractions were greater in the SP sample than the IR, despite the IR having more lignin content, which is uncommon for hardwoods. Ragland, Aerts and Baker have reported that softwoods typically have more extractives and lignin than their hardwood counterparts [116]; hence, the discrepancy noted in this case may be connected with the distribution of the components due to their originating sources. The variation of the components, based on the source of origin, also agree with the findings in the study reported by Phanphanich and Mani, where the hemicellulose, cellulose and lignin fractions of a pinewood chip, obtained from Oglethorpe, Georgia, United States, showed a fraction of 11.9%, 54% and 25% respectively [257], compared to the SP sample investigated in this study.

During torrefaction, the lignocellulosic components of the IR and SP samples known to decompose based on the temperature condition employed are a function of the heating effects of the dominant components in the biomass, such as the glucan, xylan and arabinan [242]. As shown in Figures 6-15 and 6-16, the hemicellulose is noticed to decrease with increasing torrefaction severity. Although hemicellulose degradation has been reported to occur within a temperature range of 220 °C - 315 °C [241], the results obtained in the study suggest that hemicellulose is the least thermally stable component and usually accounts for the distribution of the mass yield in torrefied solid, as previously discussed in Section 6.6. As investigated, the fraction of the hemicellulose fraction that decomposed at the torrefaction condition of 290 °C, relative to the untreated SP and IR counterparts, are 93.95% and 96.35%, thus reducing to 0.76% and 0.45% respectively, an indication that more hemicellulose fraction is lost from the IR sample. Also, with an increase in torrefaction severity, the hemicellulose fraction drastically reduces, with minor traces (for IR - 0.02% and SP - 0.08%) evident at torrefaction condition of 380 °C. The greater loss of the hemicellulose fraction may be connected with the xylan polysugar constituent dominant in hardwoods relative to other carbohydrate species. It has also been reported to be more reactive than the glucomannan polysugars dominant in softwoods [242].

Also, regarding the cellulose content, which seems to decrease, but not with the same trend as for hemicellulose, the rate of decline may be connected with the heating impact of the inherent hydrogen bonds, alongside the glycosidic bonds that bridged the glucan constituents, being the dominant polysugar found in the cellulose structure. As the torrefaction temperature was increased to 290 °C, the cellulose fraction in both IR and SP sample increased slightly, from 48.84 % to 49.07% in SP and 30.25% to 36.56% in IR. Such an increase may be occasioned by the volatile fractions produced from the hemicellulose degradation, reacting with the phenolic units found in the lignin structure to form heavier acid-insoluble products leading to a relative increase in the cellulose concentration [258]. The study by Li *et al.,* on the torrefaction of Bamboo wood under a CO_2 atmosphere, also found that, at the torrefaction temperature of 280 °C, the cellulose fractions of the torrefied bamboo also increased in concentration, which seems to agree with the findings in this work [248]. Although light and mild torrefaction regimes were not investigated in this study, where cellulose degradation is

considered minimal [107], by comparing the impact of torrefaction at 380 °C, the cellulose content in the IR reduces to 6.61%, as against 15.74% witnessed for the SP. The reduction may be due to acid hydrolysis of the cellulose, which is common during torrefaction with increasing severity, and it is considered faster in IR (hardwood) compared to the SP (softwood), owing to differences in the unstructured region of their cellulose, containing water of hydration [259]. The hydrolysis involves a case where protic acid catalyses the cleavage of chemical bonds via a nucleophilic susbtitution reaction, in the presence of water, hence the conversion of cellulose to glucose substrates.

Furthermore, for the lignin component, a significant increase of the content was evident in the IR sample, with increasing torrefaction condition. Although lignin degradation has been reported to increase with an increase in carbonisation temperature, their proportional mass also increases with increasing temperature conditions, consistent with the findings reported in other studies [260] [156]. As evident in Figure 4-6, the SP did not follow a similar trend; the lignin content declined by 3.75% between the torrefaction condition of 290 °C and 320 °C. Chen and Kuo have previously argued that the reactivity levels of lignocellulosic components vary with their nature, which may have resulted in the variation observed [150]. Other possible reasons for this may be associated with the polymeric cellulose dissociation, resulting in some acid-insoluble condensable products being formed, including the benzenoid aromatic groups. A study by Shoulaifar investigated the changes in the lignin structure of birch wood following torrefaction and reported that an increase in the p-hydroxyphenyl constituent of the lignin follows the dissociation of the methoxyl groups within the lignin constituent [261]. While such a dissociation reaction is likely, the intrinsic structural differences bridging the lignocellulosic components cannot be overlooked. The nature of chemical interaction may also induce some side reactions imposed by external conditions. Jin *et al.* employed carboxymethylation experiments and found that covalent bonding is more pronounced in softwoods [262]. The nature of this bond may account for the decline in the SP sample, observed in this work at 320 °C due to possible local reactions taking place [262].

4.2.6 Torrefaction performance parameters

4.2.6.1 Mass Yield

Since torrefaction is concerned with the changes within the organic constituents present in a biomass structure on a dry basis (db), the mass yield represents the percentage fraction of the original organic constituents retained in the solid product. The polymeric constituents in biomass, such as hemicellulose, cellulose and lignin, often dominate the biomass structure. These constituents react differently based on changes in torrefaction conditions. Equation 65 expresses the relationship between the torrefied solid product and their untreated counterparts. Results of the torrefied solid product and their untreated counterparts are presented in Figure 4-8 for both IR and SP samples. As observed in both cases, the mass yield continues to decline with an increase in torrefaction severity. The solid product, which represents the extent of the individual organic constituent's reactivity, accumulates into the total mass loss experience. Chen *et al.* assert that mass loss resulting from torrefaction is the sum of degradation of the polymeric constituents [150]; however, the type of treatment gas employed also contributes to this effect.

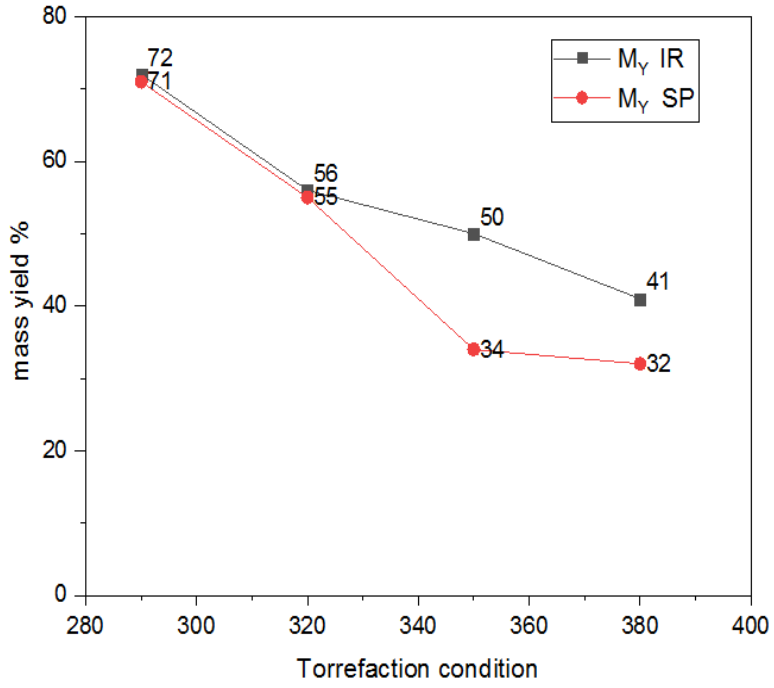

Figure 4-8-Mass yield of IR and SP samples

As shown in Figure 4-8, the mass yield accounted for by the treatment gas (CO_2) is not the same for IR and SP samples. The CO_2 gas seems to affect the SP samples' solid conversion more significantly than the IR counterpart at temperatures beyond 320 °C. The behaviour exhibited by the organic constituents in the two samples were almost similar at the torrefaction condition of 320 °C, where the values of 56% and 55% were reported for the IR and SP samples, respectively. A similar trend in mass loss behaviour had also been reported in a previous study [135] regarding the influence of CO_2 gas on torrefaction, but the effect of the CO_2 gas was not pronounced for torrefaction occurring within the light and mild temperature regimes (< 280 °C). While the study reported higher mass losses for the hardwood than the softwood investigated, the mass of moisture present in the hardwood was greater than for the softwood, which may have accounted for this behaviour. Additionally, although the softwood shows lower hemicellulose content, it exhibited higher mass losses than the hardwood with a higher hemicellulose content. By comparing the findings in [135] and the present work, the % mass fraction of moisture in the SP (1.40%) is greater than those of IR (0.82%), as per Table 4-1. This suggests that aside from the variation of organic constituents present in the biomass structure, the percentage fraction of moisture in the untreated sample may contribute to the reactivity of the CO_2 gas at higher torrefaction conditions, resulting in higher mass losses in the SP sample.

Furthermore, the SP samples' behaviour at higher torrefaction conditions may be associated with the thermal conductivity of the CO_2 gas (32 mW m^{-1} K^{-1}), enabling higher heat transfers across the sample surface gas film, which helped induce significant mass losses at higher torrefaction condition. Also, it is instructive to note that higher ash contents in biomass have been reported to catalyse torrefaction processes, mainly where CO_2 is used as the inert gas medium [226]. Consequently, the ash content determined for the IR and SP samples, as per Table 4-1, which shows a percentage fraction of 3.31% and 4.69%, respectively, may be responsible for the variation in the mass losses for the IR and SP samples, which agrees with the findings reported in other studies [126] [226]. The Boudard reaction, where CO_2 gas reacts with carbon to form carbon monoxide (CO), have also been investigated in the study by Uemura *et al*. for the torrefaction of oil palm kernel shell [135]. In the study, a mass yield of 77.3% was reported for the torrefaction of oil palm kernel shell at a temperature of 300 °C

[135], which is somewhat closer to the mass yield of 72% and 71% for the IR and SP samples, respectively, at the temperature condition of 290 °C. The mass yield differences may be linked to the 15 vol% of CO_2 applied for the oil palm kernel shell's torrefaction, compared with 100% CO_2 used in the present study. Comparing the mass loss of the IR and SP in this work with other torrefaction cases, where a different inert gas, such as nitrogen, was utilised for a similar biomass sample, the result reported a higher mass yield torrefaction with nitrogen compared with CO_2 gas [241]. The higher mass yield suggests that Boudard reactions taking place within biomass samples during torrefaction with CO_2 gas may contribute to low mass yield of torrefied carbons at higher torrefaction temperature conditions.

4.2.6.2 Energy yield

The energy yield (E_Y) accounts for the mass loss effect associated with biomass torrefaction. As the mass loss effect relates to the degradation of the polymeric constituents, the fraction of energy-rich constituents retained in the original sample following torrefaction and relative to the loss of the energy-lean fractions impacts the overall energy contents of torrefied solids [93]. The energy yield serves as a performance indicator when evaluating the 'extent of torrefaction' from the perspective of energy conversion. For this work, the E_Y of the torrefied carbons were estimated using Equation 3.6 and are shown in Figure 4-9. An increase in E_Y value suggests an increase in heating value, occasioned by mass loss behaviour under the varying torrefaction conditions.

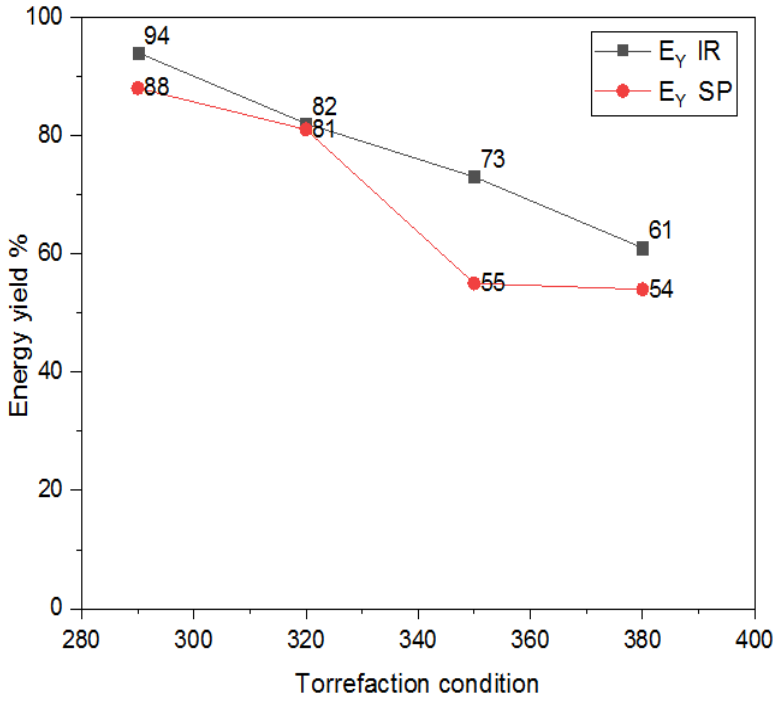

Figure 4-9-Energy yield of IR and SP samples

As evident in Figure 4-9, the torrefied IR and SP samples showed higher E_Y values at the torrefaction condition of 290 °C, representing the optimal condition for the minimal losses in combustible volatile matters. Although the E_Y obtained is high at this condition, the HHV equivalent shown in Figure 4-3 was relatively low, making the torrefied solid unsuitable for energy application. This was as expected, given that the E_Y value is dependent on M_Y, which were also affected by the selected torrefaction conditions. While a further increase in torrefaction severity shows a continuous decline in the E_Y for both samples, the volatile matters, which constitute oxygenated compounds, are further released with increasing torrefaction severity. The consequence is that the heating value of the volatile fractions remaining in the biomass will show higher values than those of the untreated sample. Also, as evident in Figure 4-9, the IR samples seem to show a higher E_y value across the entire torrefaction condition investigated, which indicates the influence of the CO_2 gas medium on the E_Y. Despite the CO_2 gas playing a significant role, the size of the untreated sample is another contributing factor. A higher E_Y value of between 98-100% has been reported in the case of eucalyptus (10 x 40 x 80 mm) torrefaction under an oxygen environment at 280 °C [136]. However, compared with the IR and SP samples used in this work, with a dimension of

4-7 mm, the 97% and 88% E_Y values obtained, respectively, would somewhat agree with the impact of sample size on E_Y. Previous works [136] [154] also concur with these findings that E_Y of hardwoods are greater than those of softwoods and fibrous biomass types, following torrefaction, which can be linked to the higher particle densities of hardwoods (0.4-0.7 g cm^{-3}), relative to those of softwoods (0.3-0.5 g cm^{-3}) [263]. Additionally, as observed in Figure 4-9, the E_Y of the torrefied IR samples were greater than those of SP, thus lending further support to the effect of particle density. Therefore, this suggests that the lower mass loss experience in the IR samples, as shown in Figure 4-8, result in higher E_Y due to reduced loss of the volatile fractions in the samples.

4.2.6.3 Energy gain and energy input of torrefaction

As discussed in Sections 4.2.6.1 and 4.2.6.2, the correlations between M_Y and E_Y suggests that a decrease in mass yield results in a corresponding increase in energy yield. This view aligns with the findings from Cardona *et al*.[231], where the M_Y and E_Y of torrefaction showed a linear correlation of $R^2 = 0.97$.

Table 4-4-Enhancement factor of IR and SP sample at different temperatures ($E_F > 1$ means gain)

Temperature (ºC)	E_F (IR)	E_F (SP)
290	1.30	1.23
320	1.45	1.45
350	1.47	1.62
380	1.48	1.67

Despite the linear correlation between the M_Y and E_Y, Table 4-3 showed that the enhancement factor (E_F) obtained for all the torrefied cases exceeded the theoretical limit of 1, indicating a satisfactory degree of torrefaction [148]. The E_F values are a reflection of the energy output level and densification of the torrefied solid product. Additionally, the IR and SP samples torrefied at 380 ˚C produced the highest value of the enhancement factor, based on the

residence time of 60 min applied for all cases. Although the E_F values obtained for each torrefaction condition exceeded the theoretical limit; however, the HHV obtained at 380 ˚C, which is the highest, relative to the other conditions, are to the detriment of high mass losses in the solid products. Also, for the samples torrefied at 290 °C, the HHV(s) values are lower than that of the coal sample investigated, which is a concern for the intended system's performance. Therefore, it is necessary to determine the optimum torrefaction performance condition for the E_Y and M_Y.

The concept of Energy Gain (E_G), as mentioned in Section 3.3.3.3, was explored to determine the optimum condition for the torrefaction performance, as it neither correlates with the M_Y (R^2 = 0.66) nor the energy densification (R^2 = 0.09), as reported in [231]. As shown in Figures 4-8 and 4-9, the (E_Y, M_Y) values of IR (94%,72%) and SP (88%, 71%) samples for the torrefaction condition at 290 °C suggests that high energy recovery would be expected from such product. The E_G values for the IR and SP samples, following the torrefaction process, were determined from Equation 69 and represented in Figure 4-10.

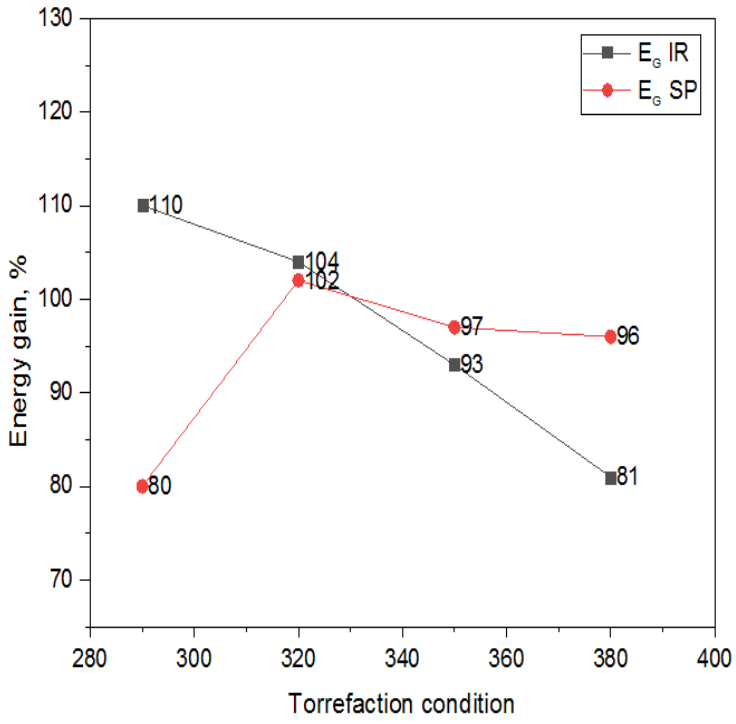

Figure 4-10-Energy gain factor for IR and SP sample

As shown in Figure 4-10, although the E_G reported for the IR sample at 290 °C was the highest (110%), the lower HHV reported makes the sample not too suitable for cofiring applications. As the current work aims to characterise torrefied carbon that may be utilised for CO_2 capture and cofiring applications, this would require the use of torrefied carbons with relatively higher HHV and E_G value. The E_G values reported for torrefaction at 320 °C, for the IR (104) and SP (102), appear somewhat close, with a difference of 2%, indicating that the torrefied samples would share an almost similar characteristic. Similarly, for the case of torrefaction at 350 °C, an almost linear pattern was evident, with an E_G value difference of 4% for the IR and SP samples.

Additionally, since the values of E_Y for the torrefied carbons at the conditions of 320 and 350 °C are relatively high, and with lower mass loss experience, compared to the samples torrefied at 380 °C, it is recommended that the torrefied product should reflect mass losses that are sufficient enough to guarantee the availability of organic species, capable of providing the required energy to meet any energy shortfall in processes [231]. Cardona *et al.* also employed the energy gain parameter to determine an optimum condition for the torrefaction performance of eucalyptus tree residue, which agrees with the findings in the current work [231]. Interestingly, since the E_G parameter had become the basis for selecting the optimum conditions (320 °C and 350 °C) for the torrefied carbon development as investigated, another parameter worth considering is the energy consumption of the torrefaction process, which defines the energy spent in developing the carbons.

Energy consumption is a concern, given that torrefaction processes are often executed under heat energy supply, resulting in partial degradation of the untreated biomass. The extent of energy supplied is governed by temperature and choice of residence time for any given case. Since torrefaction occurs under the influence of treatment gases, the heat supplied is also carried by the gas media during the fuel upgrading. As heat supply progresses, the gas enthalpy also increases due to temperature variations within the reactor. Such heat increments may be expressed in terms of the specific heat of the gas [264]. However, since the treatment gas flow rate is constant, the average heat capacity of the gas would account for the difference between the inlet (room temperature at 25 °C) and outlet temperature conditions for estimation

of energy requirement. As the specific heat capacity of gas is temperature-dependent, the energy input must also consider the residence time of the torrefaction process. Equation 2.13 was employed to determine the energy input of each torrefaction condition, as shown in Table 4-5. The relationship between the energy input and the enhancement factor is also shown in Figure 4-11.

Table 4-5-Enthalpy increment of CO_2 during heating at various torrefaction condition

Torrefaction condition (°C)			
290	320	350	380
CO_2 enthalpy increment (kJ $kmol^{-1}$)			
8,160.94	9,284.51	10,443.78	11,637.31
Energy input (kJ)			
2.00	2.27	2.56	2.85

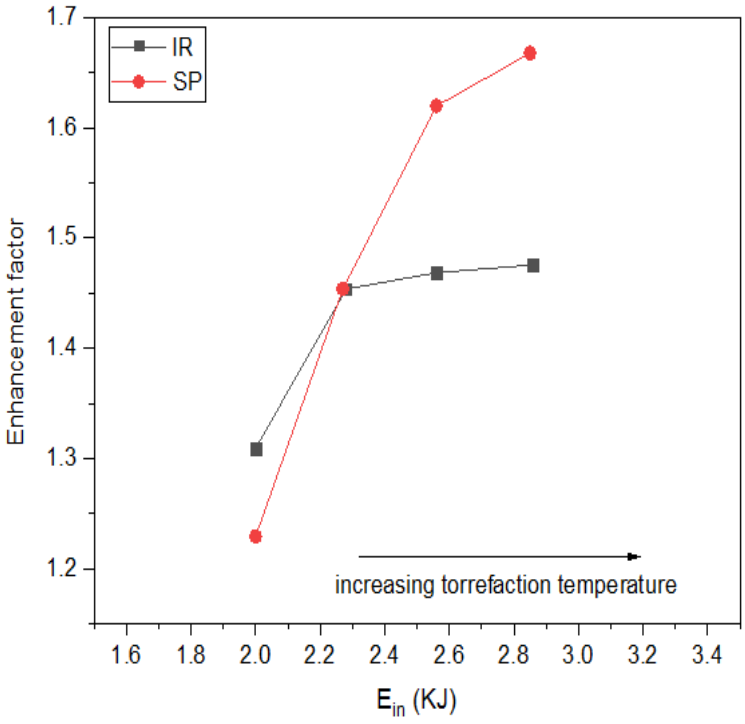

Figure 4-11-Energy Input vs Enhancement factor for IR and SP sample

As shown in Table 4-5, the torrefaction condition at 380 °C shows the highest energy input, which also aligned with the highest enhancement factor, over the residence time of 60 min applied in all cases. Similarly, the energy input also impacted the enthalpy of the CO_2 gas, which may have accounted for the changes in the physicochemical properties of the torrefied carbons. The findings suggest that aside from the reactor's heat supply, the treatment gas also provides heating through the pores of the untreated samples loaded in the reactor. Despite the effect of the gas media, a study by Chen *et al.* using nitrogen as a carrier gas also reported the impact of a combination of high temperature and shorter residence time, resulting in energy efficiency improvement [148]. This suggests that torrefied carbons with lower HHVs would require less energy input for the development.

However, the choice of different carrier gases will also result in different values of the HHV, as well as the enhancement factor, despite having a similar energy input value. As shown in this work, the residence time of 60 min applied would also impact the energy input requirement. This agrees with Ohliger *et al*., for beechwood torrefaction, where the influence of temperature was not considered a controlling parameter, but the residence time, which seems to show a more significant impact along the torrefaction conditions investigated [265]. As per Figure 4-11, the increasing energy input trend shows that developing a torrefied carbon with higher HHV would require more energy input during the torrefaction process. Therefore, given the need to minimise energy consumption in processes, the E_G factor, as a determinant parameter for selecting the optimum condition for torrefaction performance in this work, has been considered, thus eliminating torrefaction condition 380 °C, due to its higher energy consumption requirement.

4.2.6.4 Hydrophobicity of the torrefied carbons

An increase in energy input following the torrefaction process would ultimately impact the torrefied carbon physical property, such as hydrophobicity. As the hydrophobic nature of torrefied biomass makes them suitable for consideration as adsorbents for CO_2 capture applications, it is necessary to determine the extent of hydrophobicity, which defines their moisture repellant tendency. Since moisture in carbonaceous materials reduces their HHV

and, by implication, increases stack losses when employed for energy applications via combustion, the contact angle measurement, based on the drop size analysis, helps determine the extent of surface wettability torrefied carbon. Figure 4-12 presents the contact angle measurement results of the IR and SP samples.

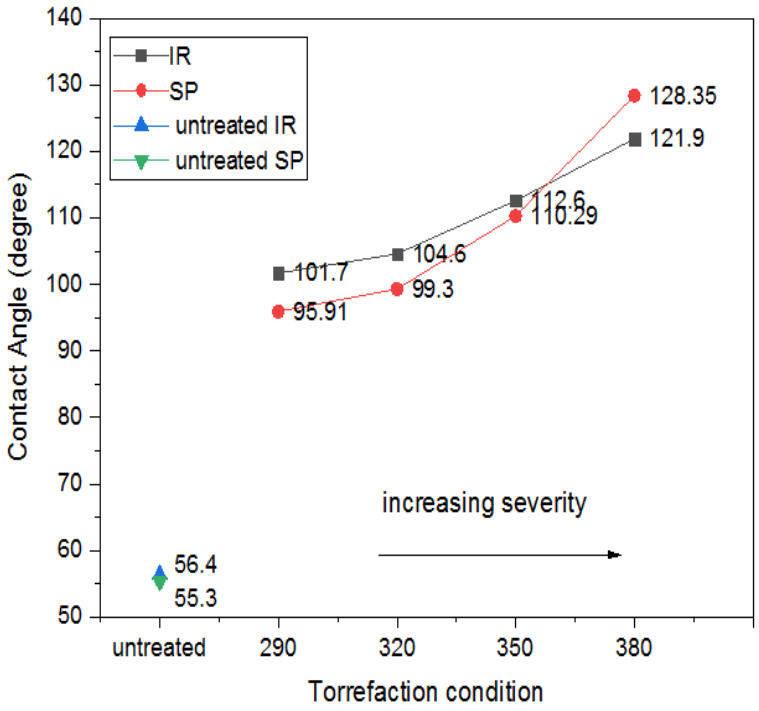

Figure 4-12-Contact Angle measurement with increasing torrefaction condition

As evident in Figure 4-12, there seems to be a continuous increase in the contact angle value reported for both IR and SP samples over increasing torrefaction condition. The obtained values exceeded the theoretical limit of 90^{o}, defining the limit a material can be classified as hydrophobic [266]. The adsorption of water in porous media, which are a function of capillary forces, is also affected by the materials' surface chemistry [266]. A hydrophobic surface with a contact angle < 90° can initiate positive capillary pressures that could permit moisture penetration through the porous solid product. By contrast, where the contact angle is > 90^{o}, the negative capillary pressures that may result would help prevent moisture penetration through porous solids [266]. Unlike the untreated IR and SP samples, the torrefied carbon can retain their contact angle values (always > 90 ^{o}) for a long time. With the increase in contact angle values with torrefaction severity, such behaviour may be attributed to hemicellulose

degradation and the amorphous cellulose within the biomass structures, resulting from the decline of the -OH and the -COOH groups. Also, tar condensation that may have occurred within the pores created during the torrefaction would help repel moist air access into the pores.

The impact of this is the reduced ability of the torrefied carbons to form hydrogen bonding when contacted with polar molecules, such as moisture in flue gases during CO_2 capture applications. As suggested by Felfli *et al.,* the non-polar characteristic of the condensed unsaturates further hinders the access of moist air that could condense within the pores developed within the torrefied solid [252]. Although variations exist in the contact angle values obtained for the IR and SP samples, as shown in Figure 4-12, this explains the influence of temperature on the biomass lignocellulosic constituents. The results concur with Yan et al., where hydrophobicity of the torrefied biomass becomes more pronounced at torrefaction conditions beyond 250 °C [118]. Also, previous studies have reported that the type of torrefaction technique, such as wet torrefaction, makes the solid product more hydrophobic compared to the conventional torrefaction method used in this study [118]. While this may be true, it is also anticipated that the feedstock's nature and the type of treatment gas would influence the quality of the torrefied solid, given the possibility of the gas reacting with the carbon surface, thus producing varying values of the contact angle.

4.3 Summary

In conclusion, Chapter 4 of this work has discussed the potential application of torrefied carbons as fuel for cofiring application, given the HHV and hydrophobicity values established for the IR and SP samples. The values obtained demonstrate that the optimum torrefaction condition, based on the energy gain values, were for the torrefied carbons developed at 320 and 350 °C for both IR and SP samples. Similarly, the atomic ratios of the torrefied carbons developed at these conditions suggest that they would provide similar combustion characteristic with those of the low-ranked coal investigated in this work. As the optimum torrefaction condition has now been established, Chapter 5 of this work will take forward the selected torrefied carbons developed at 320 and 350 °C for CO_2 adsorption studies and

analysis to determine their suitability for CCS applications. Analysing the gas adsorption with N_2 and CO_2 will provide more insight into the applicability of these torrefied carbons for the dual-purpose application of the intended system, which would help in meeting the study objectives

Chapter 5 : CO_2 ADSORPTION STUDIES OF TORREFIED CARBON

5.1 Analysis of surface area

Following the volumetric analysis, the changes in surface morphology of the torrefied carbons were evident from the surface area and pore volume results, shown in Table 5-1. As expected, the torrefaction process under the CO_2 atmosphere had a small impact on the torrefied carbons' porosity. The BET surface area (S_{BET}), determined with the aid of an inbuilt software in the Micromeritics Accelerated Surface Area Porosity (ASAP) 2420 analyser, were based on a plot of V (1-P/P^o) against P/P^o, with the values obtained within the P/P^o range of 0.05 - 0.35. The total pore volume (V_p) was estimated from the amount of nitrogen that may have been adsorbed by the torrefied carbon at *P/P^o* 0.95. The micropore volume (V_{micro}) and the micropore area (S_{DR}) were determined from the DR equation, using CO_2 saturated liquid density value of 0.599 g cm^{-3} [267] and saturated vapour pressure of 71.94 bar [268] at a temperature of 30 °C.

The use of N_2 and CO_2 helped provide more insight into the porous nature of the torrefied carbons. N_2 adsorption is usually employed for probing larger pore sizes but limited for application to narrower pores; however, CO_2 adsorption is limited to narrower pore sizes than 1 nm [187]. Although the result of the S_{BET} and total pore volume (V_p) determined by the (ASAP) 2420 Analyser Software were based on the N_2 adsorption analysis; however, the adsorption isotherm generated by the software did not match any of the IUPAC standard classifications [187], shown in Figure 2-22, and therefore, were deemed uninformative for presentation, as discussed below which may be as a result of adsorption effects within the system.

Table 5-1- BET Surface Area and Total Pore Volume of the Torrefied IR and SP samples

Sample	Torrefaction Condition	BET surface area ($m^2 g^{-1}$)	Total Pore Volume ($cm^3 g^{-1}$)
1	IR290	0.235+/-0003	0.0002
2	**IR320**	**0.454+/-0.008**	**0.0002**
3	**IR350**	**0.695+/-0.016**	**0.0007**
4	IR380	0.756+/-0.005	0.0005
5	SP290	0.204+/-0.015	0.0002
6	**SP320**	**0.384+/-0.016**	**0.0005**
7	**SP350**	**0.562+/-0.005**	**0.0008**
8	SP380	0.652+/-0.042	0.0002

(*samples in bold taken forward for further analysis)

The reason for the low uptakes, affecting the isotherm shape [187], and the low values reported here may be connected with the inability of the N_2 gas to access the pores of the torrefied carbons studied in this work. There is a possibility that the N_2 adsorbed initially may have blocked the pore entrances and also possibly interacted with a specific surface functional group on the torrefied carbon; hence the pore filling pressure would not correlate with the pore structure at the characterisation operational temperature of -196 °C. Additionally, it is known that if the pore dimensions are insufficiently large, then the low temperatures used in the N_2 adsorption may prevent the adsorbate molecules from overcoming the activation energy associated with entering the pore, and hence, the gas molecules are excluded, and adsorption is hindered.

As shown in Table 5-1, the S_{BET} of the IR and SP samples were all ≤ 1 $m^2 g^{-1}$, with some variation notable with an increase in torrefaction condition. For the IR samples, the S_{BET} and V_p are seen to increase with increasing torrefaction severity, up to the temperature limit of 350 °C. However, with further increase in temperature above 350 °C, a reduction in V_p was

evident, which may be associated with pore contraction within the torrefied carbon, in agreement with a similar study by [269]. At 380 °C, the reduced V_p may be due to high burn-off experienced by the torrefied IR and SP samples. The SP samples did not follow a similar trend as the IR, which may be associated with the extent of N_2 affinity on the SP sample at this condition. At higher temperatures > 400 °C, structural disordering, pore widening, and coalescing have been reported to result in pore volume and surface area reductions [269], which seems to agree with the results shown in Table 5-1.

Also, given that the choice of torrefaction condition resulted in partially blocked pores development, the low heating rate of 10 °C min^{-1} applied may have caused the volatile products emitted to diffuse slowly within the solid particle due to sufficient contact time permitted by the low heating rate. As a result, this had impacted the porosity of the IR and SP samples. Although the values of the S_{BET} reported were much smaller, they are consistent with other values reported for wood char pyrolysis under N_2 at 330 °C (< 0.8 m^2 g^{-1}) in [270]. A related study on the torrefaction of mesquite wood at 300 °C reported an internal S_{BET} of 0.750 m^2 g^{-1} [226]. Consequently, this shows that the moderately lower torrefaction temperatures of 320 °C and 350 °C would result in partial volatile losses; hence the extent of surface area and pore volume obtained, compared with those at 380 °C, depending on material type.

Furthermore, while it can be seen that the values of the S_{BET} obtained were relatively low, which may suggest the existence of non-porous solid, it is instructive to note that such analysis was carried out using N_2 at -196 °C, and the capacity for adsorption at such condition is dependent on the surface microstructure of the torrefied carbons, as well as the temperature of analysis. Adsorption capacity at a relatively high temperature may be larger than in cases where adsorption occur at lower temperatures, even when applied in the same gas / solid system [271]. Due to the insufficient kinetic energy of the nitrogen gas (kinetic diameter ~ 0.36 nm) at the cryogenic analysis temperature of -196 °C, following pore network constriction that induces activated diffusion effect, which is temperature-dependent [271], the value of the S_{BET} and the V_p determined may not be an accurate representation of the pore character of the torrefied carbons. The establishment of a sufficient temperature gradient may permit for higher

adsorption uptake, as well as the use of other gas species, such as CO_2 due to its kinetic dimension (0.33 nm) and characteristic, which may provide for a realistic analysis of the S_{BET} and the V_p of the torrefied carbon [187].

5.2 Pore characterisation using CO_2

The scope of this project was always to investigate the adsorption of CO_2 for CCS applications. However, given the diffusional restrictions of the N_2 adsorptive into narrowest pores ≤ 0.45 nm [264], further analysis of the torrefied carbons was also available using the data obtained for CO_2 adsorption at 30 °C, which is close to the standard room temperature of 25 °C, used in other studies. Microporous analyses of carbon materials at 0 °C have been reported in the literature over the pressure range of 0 to 1 bar [187]. As a result of the estimated longer equilibration time for such analysis at 0 °C, CO_2 adsorption at 30 °C was instead employed for pore characterisation of the torrefied carbons. Given that adsorption of CO_2 at 25 °C, carried out during the initial probe of the torrefied carbon took several days, reducing the temperature further still would have resulted in a significantly longer experimental timeframe, of the orders of several weeks for a single sample. Hence, CO_2 adsorption at 30 °C, in the pressure range of 0 - 1 bar, was utilised, which is still below the critical temperature of CO_2 (31 °C), and thus gas condensation would occur within the pores, enabling pore analysis.

5.2.1 Adsorption analysis of Torrefied Carbon IR320 and IR350

The data obtained for the CO_2 adsorption of the IR320 and IR350 torrefied carbons at 30 °C is shown in Figure 5-1. The isotherm obtained shows a Type I IUPAC classified isotherm [187], with small CO_2 uptake notable at the isotherm's low-pressure region, producing a hysteresis. Based on the Type I isotherm, a Langmuir fit was applied to estimate the monolayer capacity and the Langmuir surface area of the torrefied carbons. A linear regression of the Langmuir plots, Figure 5-2, also showed good experimental data fit.

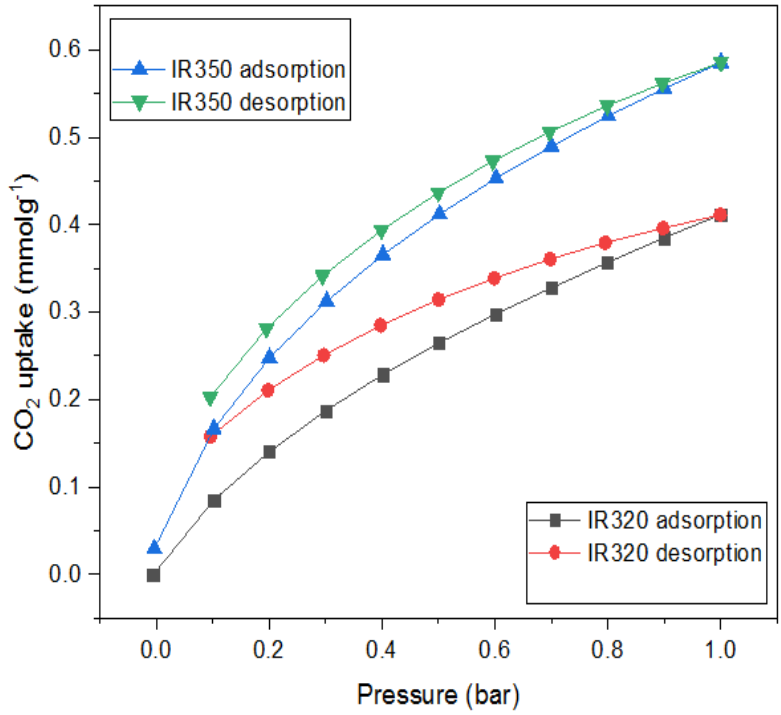

Figure 5-1- CO_2 adsorption analysis of IR320 and IR350 at 30 °C, showing Type I isotherm

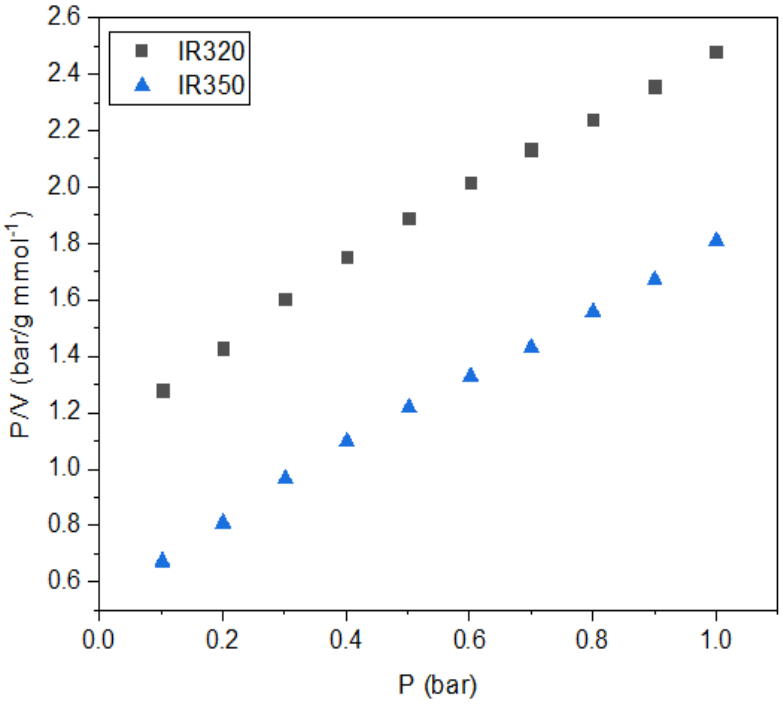

Figure 5-2- Langmuir linear plot of CO_2 adsorption of IR320 and IR350 at 30 °C

Following the Langmuir fit, the experimental data were tested for fitness using the DR equation to estimate the micropore volume (V_{micro}) and area (S_{DR}) of the torrefied IR carbons. Figure 5-3 shows a linear plot of the DR equation for both sorbent, using a CO_2 gas density of 0.599 g cm^{-3} [267].

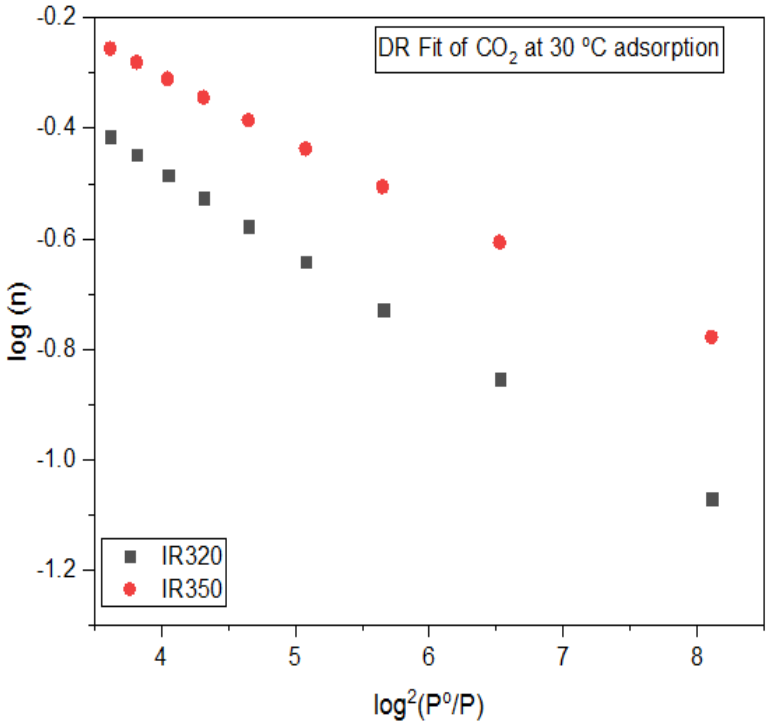

Figure 5-3- DR plot of CO_2 adsorption for IR320 and IR350 at 30 °C

5.2.2 Adsorption analysis of Torrefied Carbon SP320 and SP350

Furthermore, pore characterisation of the SP320 and SP350 torrefied carbons were carried out under similar adsorption condition as the IR to compare the soft- and hardwood. As evident from the Type I isotherm shown in Figure 5-4, the hysteresis produced were smaller than those found in the torrefied IR carbons. Additionally, the CO_2 uptakes of the SP carbons were lower than the case reported for the IR due to enhanced porosity. This may also be related to the anatomical changes that may have occurred within the softwood structures, although their adsorption behaviours are similar. Based on the Type I isotherm, a Langmuir fit was applied to estimate the monolayer capacity and the Langmuir surface area of the torrefied carbons, as shown in Figure 5-5.

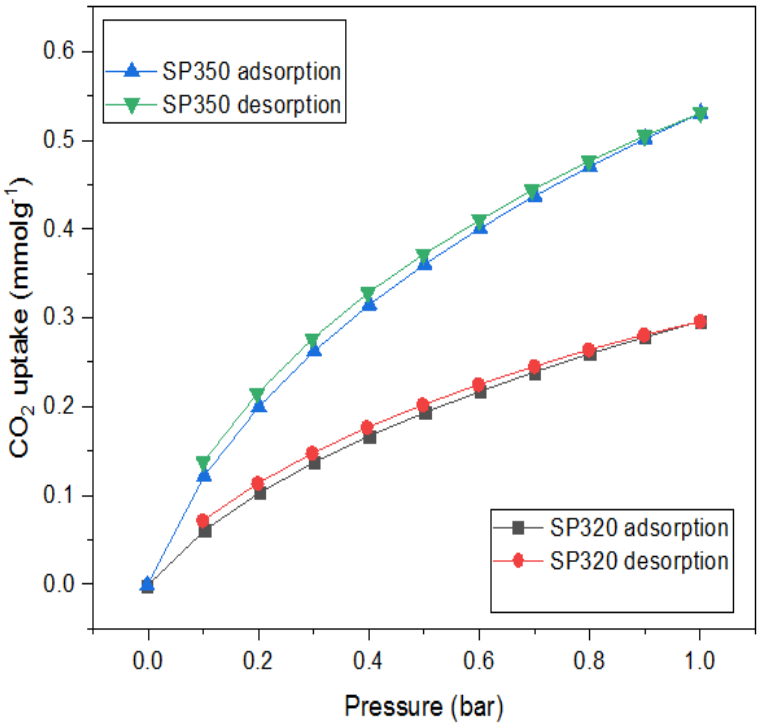

Figure 5-4- CO_2 adsorption analysis of SP320 and SP350 torrefied carbons at 30 °C, showing Type I isotherm

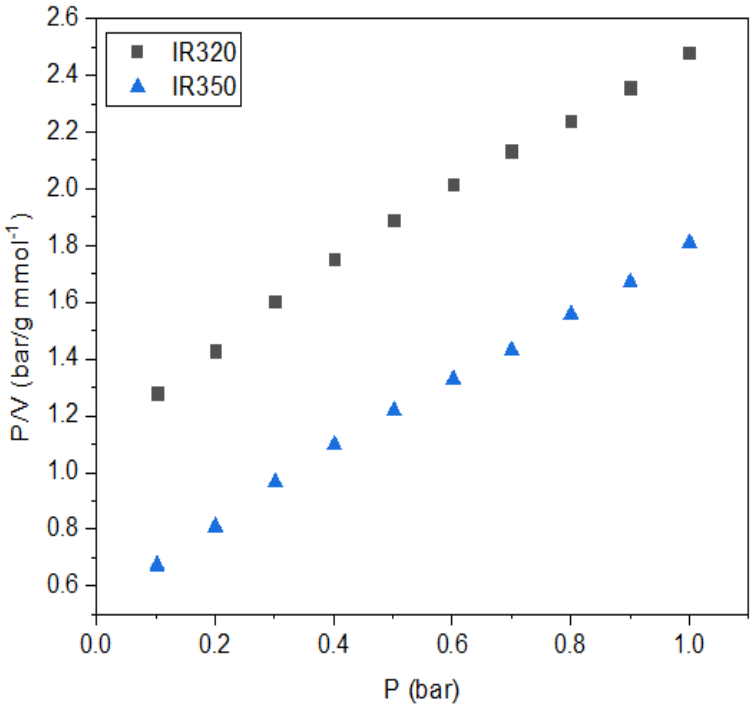

Figure 5-5- Langmuir linear plot of CO_2 adsorption of SP320 and SP350 at 30 °C

Similarly, following the Langmuir fit, the experimental data were tested for fitness using the DR equation to estimate the micropore volume (V_{micro}) and area (S_{DR}) of the torrefied SP carbons. Figure 5-6 shows a linear plot of the DR equation for torrefied carbons SP320 and SP350, using a CO_2 gas density of 0.599 g cm^{-3} [267]. As shown in the DR plot, there was no deviation from linearity over the entire pressure range.

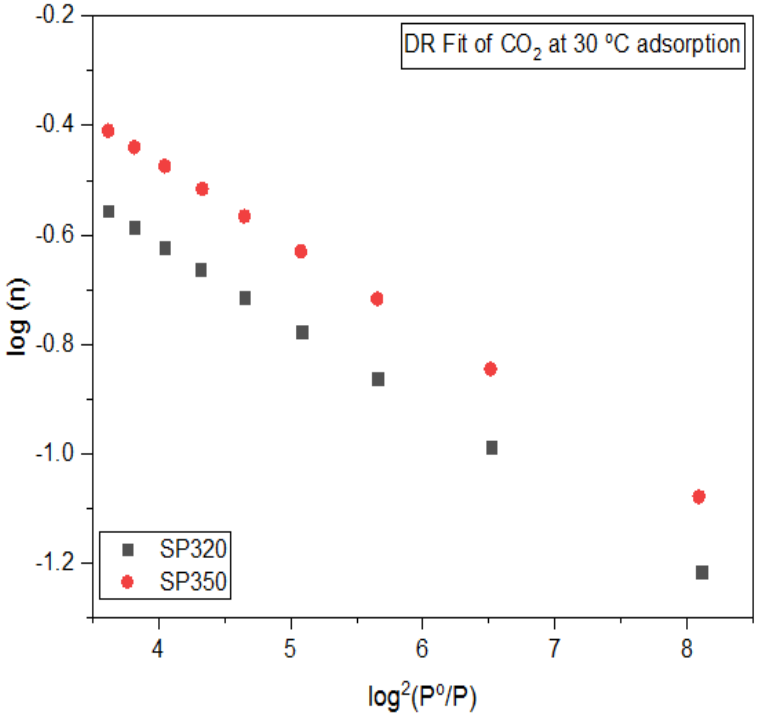

Figure 5-6- DR plot of CO_2 adsorption for SP320 and SP350 at 30 °C

Given the dissimilarities evident in the adsorption isotherm, the Langmuir plots and the DR plots of the torrefied IR and SP carbons, Table 5-2 shows the pore characteristics of the different torrefied carbons.

Table 5-2- BET surface area using N_2 and maximum CO_2 uptake of Torrefied IR and SP carbons

	BET	maximum CO_2 uptake
Sample	S_{BET} $m^2 g^{-1}$	V_m mmol g^{-1}
IR320	0.45+/-0.008	0.4115
IR350	0.69+/-0.016	0.5855
SP320	0.38+/-0.016	0.2959
SP350	0.56+/-0.005	0.5305

Table 5-3- Pore characteristics of Torrefied IR and SP carbons determined from adsorption measurements at 30 ºC

	Langmuir			DR		
Sample	V_m mmol g^{-1}	S_L $m^2 g^{-1}$	R^2	V_{micro} $cm^3 g^{-1}$	S_{DR} $m^2 g^{-1}$	R^2
IR320	0.75 +/-0.04	77.05+/-3.71	0.97	0.09+/-0.06	132.58+/-0.01	0.99
IR350	0.85+/-0.01	86.61+/-0.01	0.98	0.10+/-0.06	149.87+/-0.06	0.99
SP320	0.54 +/-0.03	55.30+/-2.05	0.98	0.06+/-0.01	96.81+/-0.01	0.99
SP350	0.77 +/-0.02	78.97+/-2.21	0.99	0.09+/-0.07	139.12+/-0.01	0.99

5.3 Discussion: pore structure characteristics

It is evident from Figures 5-1 and 5-4 that CO_2 adsorption of the torrefied carbons exhibited a similar shape, regardless of the precursor material. The variation in CO_2 uptakes is a reflection of the extent of porosity developed within the torrefied carbons. When the samples undergo torrefaction, the thermal transformation resulting in the torrefied carbon correlates with their untreated counterpart inherent properties. Tables 5-2 and 5-3 show a comparison of the torrefied IR and SP carbons' porous characteristics at the different selected torrefaction conditions.

Interestingly, the low-cost torrefied carbon IR and SP sorbents exhibited a progressive pattern in the value of the V_{micro} obtained from the DR plot. As evident from the Type I adsorption isotherm displayed for each torrefied carbon, the open knee at the low-pressure region is an indication that the torrefaction with CO_2 induced the formation of narrow micropore (ultramicropore), being the reason for the N_2 gas adsorption limitations previously explained in Section 7.0. As the torrefaction condition increases from 320 °C to 350 °C, the V_{micro} of both torrefied carbon IR and SP also increased slightly, a consequence that may be attributed to the shrinkage of the carbon matrix of their precursor materials, resulting in hysteresis formation, shown in their isotherms. Hysteresis occurrence during torrefied wood/water sorption has been associated with molecular conformational changes around the cell wall matrix, induced by external factors [156], which may have also occurred in the case of CO_2 adsorption with the torrefied carbon.

Aside from this, it is instructive to note the likelihood of new pores creation within the cell wall and their subsequent destruction during the adsorption process, resulting in the adsorption and desorption processes taking place on cell wall substrates that are of different physical state, bringing about hysteresis formation. A study by Jeromenok and Weber on CO_2 adsorption of a polymeric material also found that aside from the creation of new pores, occasioned by volume swelling, other processes related to kinetic and diffusional resistances could also induce hysteresis formation during adsorption processes in microporous polymeric materials [272]. The adsorption process itself can induce adsorbent surface alteration, and

such influence by adsorption has been found in the case of nitrogen and water vapour adsorption on montmorillonite [168]. Additionally, the cell wall matrix relaxation processes may have contributed to hysteresis formation of the CO_2 adsorption on the torrefied carbons, especially where the CO_2 adsorption temperature is further from the glass transition temperature (T_g) of the torrefied carbon, known to contain polymeric substances. The glass transition temperature is defined as the limiting temperature in which the polymeric substrates, present in woody biomass, transforms from a rigid glassy state to a soft substrate (i.e., rubbery or viscoelastic) [273]. The rigid substrates are developed below the T_g level, while the soft ones are formed above the T_g level. The amorphous polymers in woody biomass structures, such as lignin and cellulose, may become softened, following the re-organisation and relief of some internal tension within their microstructure as they attain their glass transition temperature limits. The glass transition temperature of hemicellulose has been reported to be ~40 °C, while those of lignin lies in the range of 50 - 100 °C, and for the cellulose, it is above 100 °C [273]. More so, since the torrefied carbons developed in this study are hydrophobic, given the result of the contact angles, shown in Section 4.2.6.4, the consequence of an increase in hydrophobicity correlates with an increase in glass transition temperature of the torrefied carbons. Also, as the adsorption process occurs at 50 ^oC, relative to the polymeric constituents' glass transition temperature within the torrefied carbons, these may have also contributed to the hysteresis formation, owing to likely increase in motion of the lignocellulose molecular chains.

Furthermore, following an increase in torrefaction severity, the transformational changes within the cell wall structure, which resulted in the formation of small hysteresis in the SP samples, relative to those of IR, can be related to the rigidity of the torrefied carbon. The rigidity of carbon materials has been considered a determinant factor in carbon swelling. Less rigid carbons are prone to developing larger pores that foster the opening of closed pores. Since woody biomass, by nature, have narrow pores, the thermal treatment would further enhance their porosity, causing the pores developed within to become enlarged and coalesce with neighbouring pores in the cell wall matrix. This suggests that micropores formed at the selected torrefaction conditions, under the heating rate of 10 °C $min^{-1,}$ are a function of torrefaction degree.

Given that torrefaction in this work was carried out under a CO_2 atmosphere, the modified IR and SP samples at 320 and 350 °C could have been induced by CO_2 reaction with the fixed carbon contained in the constituents to form hot corrosion. The hot corrosion helped pores development, bringing about the narrower hysteresis shown in the SP adsorption isotherm, compared to the IR torrefied carbons. However, the broad hysteresis evident for the 320 °C torrefied carbons may be associated with the existence of ill-defined pore connectivity. As per the results shown in Table 5-3, it is evident that the torrefaction process, based on the selected temperature conditions of 320 and 350 °C, did not result in very high surface area for the torrefied carbons.

The S_L of the IR and SP torrefied carbons seem to be increasing with an increase in the torrefaction condition, similar to that of the S_{BET}. The S_{BET} and S_L values for the torrefied IR carbons were also more remarkable than those of SP in each of the torrefaction condition investigated. The values of S_L and V_{micro} for the torrefied IR carbons, relative to SP, suggests that the IR torrefied carbons would offer more adsorption space under similar adsorption conditions, enhancing CO_2 adsorption. Also, the reduced surface area and pore volume of the torrefied SP carbons would likely increase the mass transfer resistance of CO_2 gas during the adsorption, compared with the torrefied IR carbons. Also, while it was evident that the S_L of the torrefied IR carbons are higher than those of the SP, this correlates with the reduction in the V_{micro} over increasing torrefaction severity. A similar trend has been reported in a study by Kercher and Nagle, where such behaviours were attributed to the 'condensation of carbon into denser crystallites, leaving behind the formation of nanometre-sized pores in the pyrogenic carbon [274].

Since V_{micro} of the torrefied IR and SP carbons increased slightly with an increase in torrefaction condition, this further confirms the influence of temperature and residence times on pore development in the torrefied carbons. A number of researchers have also investigated the influence of temperature on the pore cross-sectional area of torrefied woody biomasses [226] [275]. Hass *et al*. reported a rapid increment in macropores' cross-sectional area, using wood offcuts from poplar wood under a fast pyrolytic environment (temperature range of 50 to 500 °C) [275], which lends further credence to the findings in the current study. While such

increments were associated with the evolution of liquid and volatile products, occasioned by the thermal decomposition of the biomass structure, a similar investigation by Keiluweit *et al*., using grass and pine wood, pyrolysed at temperatures ranging from 300 to 400 °C, suggests that such temperature regimes represent the end of the transition from an untreated feedstock character to a thermally modified biochar [276], which falls within the temperature range investigated in this study. High temperatures above 400 °C, as investigated by Yuan et *al*., for the pyrolysis of pinewood straw, resulted in a lower surface area biochar (8.9 m^2 g^{-1} at 1200 °C), attributed to melting of the pinewood particles [277]. This lends further support to the choice of less than 400 ^oC employed in the current work for the torrefied carbon development for CO_2 adsorption.

The pore characterisation initially carried out using N_2 at -196 °C revealed the pore characteristics of the torrefied carbons. Although such analysis helped provide quantitative information regarding the porous nature of the torrefied carbon, the technique may not reflect the accurate pore characteristics of the torrefied carbons. Further analysis using the DR equation shows that the V_{micro} calculated is close to the range of 0.1 – 0.4, explained in Section 2.17.1.1. As described in Section 2.20.2, and given the Gaussian pore size distribution shown in Figure 2-25, a close comparison of the Gaussian distribution and the DR plots for the torrefied carbon IR and SP showed evidence of an unclear deviation from linearity, at the low $\log^2 (P^o/P)$ region of the DR plot, particularly for the IR samples, an indication that the pores developed within the torrefied carbon are too narrow to permit adsorption at the experimental temperature.

Values close to 0.1 – 0.4 were obtained for V_{micro}, and the CO_2 adsorption condition of 30 °C may have affected the results obtained, as CO_2 adsorption analysis is usually carried out at a temperature of 0 °C, over an estimated longer time, which may allow true characteristics of the torrefied carbon to be revealed. The effect of N_2 gas on the surface area analysis has been explained previously in Section 5.1; however, using CO_2 for surface area analysis has resulted in a more reliable result. The CO_2 utilisation aligns with the findings on the comparative analysis of S_{BET} carried out by Della Rocca et *al.,* using a hardwood char, developed at temperature conditions of 350 and 850 °C, in which N_2 was used for the BET analysis and

CO_2 employed for the DR model. The work showed that CO_2 / N_2 surface area ratio was as high as 245, which may be nearer to what may be obtained in this study [278]. Also, while the values of the S_{BET} and those of S_L and S_{DR} are different, it would be ill-judged to assume that those determined from CO_2 analysis are more realistic. It is also possible that CO_2 may have interacted strongly with some surface groups resulting in the values obtained.

5.4 CO_2 adsorption of torrefied carbon at 50 °C

Section 5.3 of this work has discussed the results obtained from the pore characterisation of the torrefied carbon at an adsorption temperature of 30 °C. However, Section 5.4 would look at the adsorption performance of the torrefied carbons at 50 °C, being a condition that may simulate CO_2 capture from flue gas streams during post-combustion capture. This would compare performance for the torrefied carbons with other sorbent used in CO_2 capture processes. Figures 5-7 and 5-8 shows the adsorption isotherm of the IR and SP torrefied carbons, respectively.

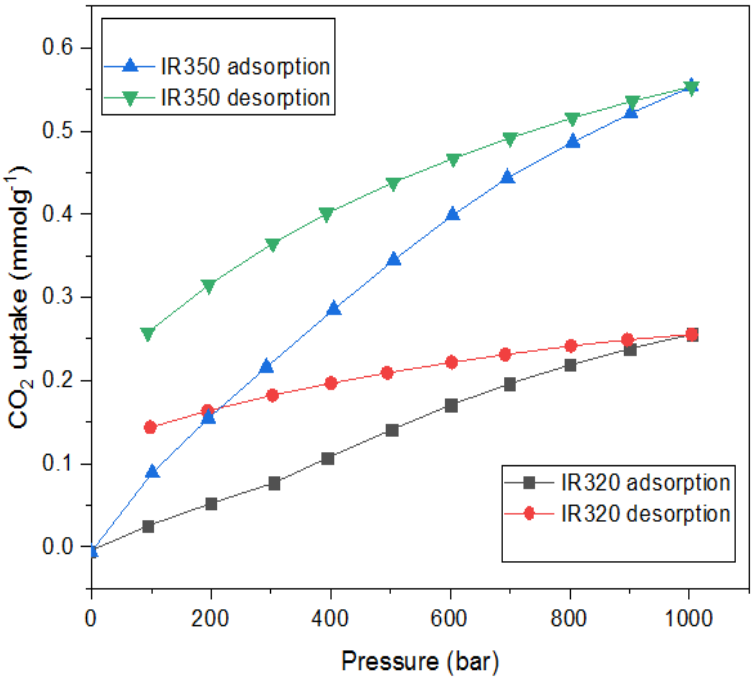

Figure 5-7-The adsorption isotherm of CO_2 on IR320 and IR350 at 50 °C

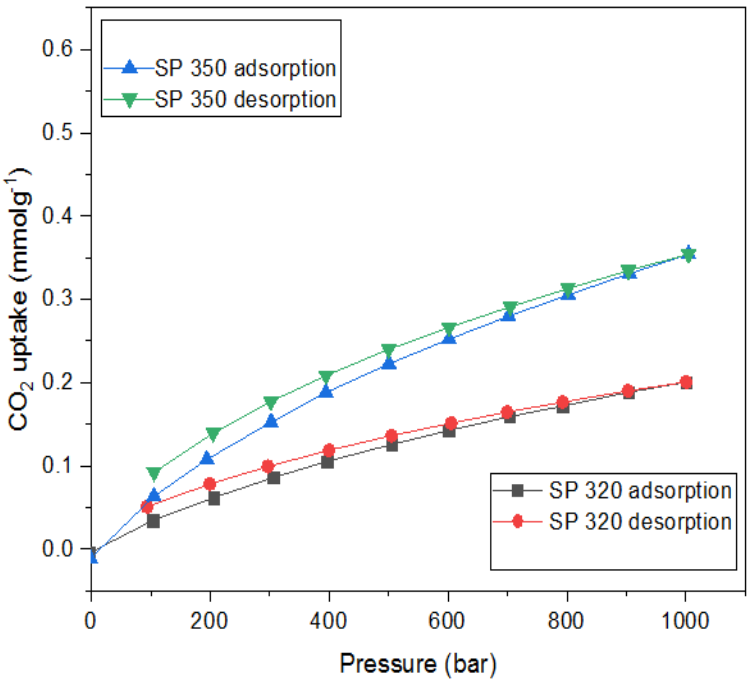

Figure 5-8- The adsorption isotherm of CO_2 on SP320 and SP350 at 50 °C

5.4.1 CO_2 sorption performance

As shown in Figures 5-7 and 5-8, it was evident that the adsorption isotherm at 30 °C followed a similar trend with those at 50 °C. This suggests that both processes are governed by physisorption; however, lower uptakes were experienced for the adsorption at 50 °C. The lower CO_2 uptake experienced was as expected, which may be attributed to the higher thermal energy of the CO_2 during adsorption at 50 °C. The CO_2 uptake at the adsorption temperature of 50 °C are in the order of IR350 > SP350 > IR320 > SP320, which seems to correspond with the influence of an increase in torrefaction conditions on the torrefied carbons. As shown, it can be concluded that the increasing torrefaction condition correlates with the S_{BET} and V_{micro} values determined since the CO_2 adsorption capacity of the torrefied carbons depends on their pore characteristics. More so, it has been established that V_{micro} ranging from 0.1 – 0.4 is preferred for CO_2 adsorption, as such pores are known to have a high affinity for gas adsorption [279] [175]. Furthermore, as evident from Figures 5-7 and 5-8, the isotherms also appeared steeper with increasing adsorption pressure, suggesting the effect of porosity on the torrefied carbons relative to the CO_2 uptake. For all the torrefied carbons investigated, the reduced CO_2 uptake at the temperature of 50 °C, compared to the case at 30 °C, confirms that

the adsorption process is exothermic, in agreement with a previous study on CO_2 adsorption on activated carbon developed from other carbon-based materials [76].

Based on the CO_2 adsorption capacity, it is possible that aside from surface area, other factors, such as CO_2 interaction with the surface functional groups on the torrefied carbons, might have played a contributing role to the CO_2 adsorption. A number of researchers have studied the influence of N-containing groups on the CO_2 adsorption of carbon-based adsorbents [226] [280]. Some N-functional groups, such as pyrrolic N and -C=NH, have been found to offer strong anchor sites for CO_2, with a potential to induce acid-based chemical interactions [279]. Additionally, since CO_2 has a strong quadrupole moment (13.4×10^{-40} C m^2), with no dipole moment, there is a likelihood that the gas would interact with the N-containing group on the torrefied carbon via the polar bonds available on either end of its linear structure [48]. Although a detailed analysis of the N-containing groups using some technique such as X-ray photoelectron spectroscopy (XPS) was not employed in this work due to limited resources, the FTIR confirms the presence of some N-containing groups on the torrefied carbon surfaces. The N-containing groups does not only influence the CO_2 adsorbed phase but also, they exert influence on the adsorptive gas occluded within the micropore of the torrefied carbon, as the adsorptive further pressed against each other within the pores space due to pore wall overlapping effects.

A similar study on N-containing compounds' influence has also been reported for CO_2 adsorption on carbonised hickory wood and sugarcane bagasse, following a slow pyrolytic process [256]. Although the hickory wood, in this case, presented a higher surface area, the bagasse biochar seemed to adsorb more CO_2 than the hickory biochar, owing to the presence of more N-containing group on its surface. While the N-containing group may have played a role in the CO_2 adsorption of the torrefied IR and SP carbons, it is instructive to note that, where an additional N- containing group is doped on the torrefied carbons, although not within the scope of this work, the possibility of the torrefied carbons adsorbing more CO_2 is likely at the adsorption temperature of 50 °C. A previous study has confirmed that doping N-containing groups onto carbon surfaces helps facilitate hydrogen bonding / CO_2 interaction, and the production of acid-base complexes have not been found [281]. As a result, it can be concluded

that the pore volume of the torrefied carbons, as well as the presence of some N-containing groups, may have been responsible for the CO_2 adsorption by these materials. Although the elemental composition of nitrogen present in the torrefied carbons continued to decline with increasing torrefaction condition, the extent of decline may affect the level of the N-containing group; hence, the fraction of the N-group remaining may have induced multipoles on the CO_2, leading to its adsorption.

Regarding the CO_2 adsorption performance of the torrefied carbons, the monolayer capacity for the adsorption at 50 °C, determined from the Langmuir model, shows that the IR350 torrefied carbon has the highest uptake (0.81 +/- 0.04), while those of IR320 (0.56 +/- 0.04), SP320 (0.45 +/- 0.02) and SP350 (0.76 +/- 0.02 mmol g^{-1}) reported lower values. Compared with the CO_2 adsorption at 30 °C, the reduced monolayer capacity at 50 °C may be attributed to the increased kinetics of the CO_2 due to higher adsorptive energy. Additionally, the S_L and S_{BET} of the torrefied IR carbons were all higher than those of the SP carbons developed at the same torrefaction condition of 320 and 350 °C. As observed, the IR torrefied carbons seem to adsorb more CO_2 than those of SP, which may be related to the IR torrefied carbons, having more nitrogen-containing functional groups, as seen from the ultimate analysis and the FTIR results. More so, the results of the ultimate analyses further supported this view, as the elemental nitrogen content in the torrefied IR carbons were more than those contained in the SP carbons, despite the increase in torrefaction severity. Whilst the capacity for CO_2 adsorption by the IR torrefied carbons may have resulted from stronger interactions of surface groups with the CO_2 molecules, being an acidic gas and a specific N-containing group on the IR, which may have provided the basic character, it is instructive to note that sorbents' possessing various N-functional moieties would exhibit similar higher CO_2 uptake compared with those containing lesser N-functional moieties [280]. Therefore, this suggests that higher CO_2 uptake reported for the IR torrefied carbon, compared to those of SP, may be attributed to the presence of functional groups and their levels.

More so, as evident in the CO_2 adsorption isotherm of the SP samples at 50 °C, the isotherms showed an almost nearly reversible desorption pathway, given the presence of narrow hysteresis near the low-pressure region, compared with those of the IR torrefied carbons. As

previously witnessed for the CO_2 adsorption at 30 °C, the hysteresis formed were not as broad as those evident in the torrefied carbon adsorption at 50 °C. Given the variations, it is likely that CO_2 adsorption at 50 °C may have induced temporary structural distortion within the torrefied carbon structure at this condition. This effect may have enabled the opening of initially inaccessible pores within the torrefied carbon structure, which were not recovered during the short time of the desorption process; hence, the CO_2 molecules become trapped in the pores leading to broader hysteresis formation in the torrefied IR carbons. Such behaviour has also been supported in a previous study by Bailey et *al.* on the adsorption of organic vapours on porous carbon [282]. Although the phenomena of elastic deformation have been experienced by a number of porous sorbents, such as charcoal, activated carbon, aerogel, etc., the effect does not show much impact on the adsorption isotherm, except in the case of polymeric-related adsorbents [183], which may be likened to the behaviour displayed by the torrefied carbons in the present study.

5.5 Thermodynamic of CO_2 adsorption of torrefied carbon

Furthermore, for an in-depth analysis of the CO_2-torrefied carbon interactions, it was necessary to characterise the torrefied carbon, using some thermodynamic parameters, such as the isosteric heat of adsorption (ΔH_{ads}). The quantification of such parameter is crucial for system design, and since ΔH_{ads} depends on the extent of surface interaction when an adsorptive is exposed to a sorbent, it would help in the future analysis of regeneration energy associated with the use of torrefied carbons for CO_2 capture. The ΔH_{ads} was determined as a function of CO_2 loading from three different adsorption isotherms employed at close temperatures (30, 40 and 50 °C) (ΔT = 10 °C in each case), as shown in Appendix, and then applying the Clausius-Clapeyron equation.

The close temperature of adsorption was selected to increase the statistical significance and minimise errors since ΔH_{ads} is temperature-dependent. Wide temperature intervals may introduce errors, as have been reported in [175]. Fixed surface coverage of CO_2 loading (n) across the three adsorption isotherms was fitted as a function of pressure for a given loading to enable comparison of sorption sites with uneven energy distribution. Values of n (0.01, 0.02,

0.03, 0.04, 0.05, 0.10, 0.13, 0.15 and 0.19), representing a range of surface coverage were selected from the lower regions of the three isotherms. The values at these lower regions are also closer to the partial pressure of CO_2 (0.15 bar) in flue gas during post-combustion CO_2 capture, where adsorption often occur on the most energetic sites [283].

Extrapolating beyond the minimum and maximum CO_2 uptakes were also considered since CO_2 adsorption on SP320 torrefied carbon at 50 °C has the lowest uptake. By considering this, the fitting produced a sequence of n/p_1, n/p_2, and n/p_3 data pairs from the three isotherms (30, 40 and 50 °C), for each torrefied carbon, and these were used to determine the differential heat of adsorption on the various energy sites present on the torrefied carbon. A linear plot resulting from ln *P* against 1/*T* gave a slope of $(-\Delta H_{vap}/R)$, from where $-\Delta H_{vap} = \Delta H_{ads}$ values were determined (sample plots of the first two coverage (n -0.01 and 0.02) is shown in the Appendix). Then for each ΔH_{ads} determined from the linear plot, ΔH_{ads} is plotted against their corresponding 'n' value, and the ΔH_{ads} (n=0) was estimated. Figures 5-9 and 5-10 represents the isosteric heat of adsorption for torrefied carbons IR and SP.

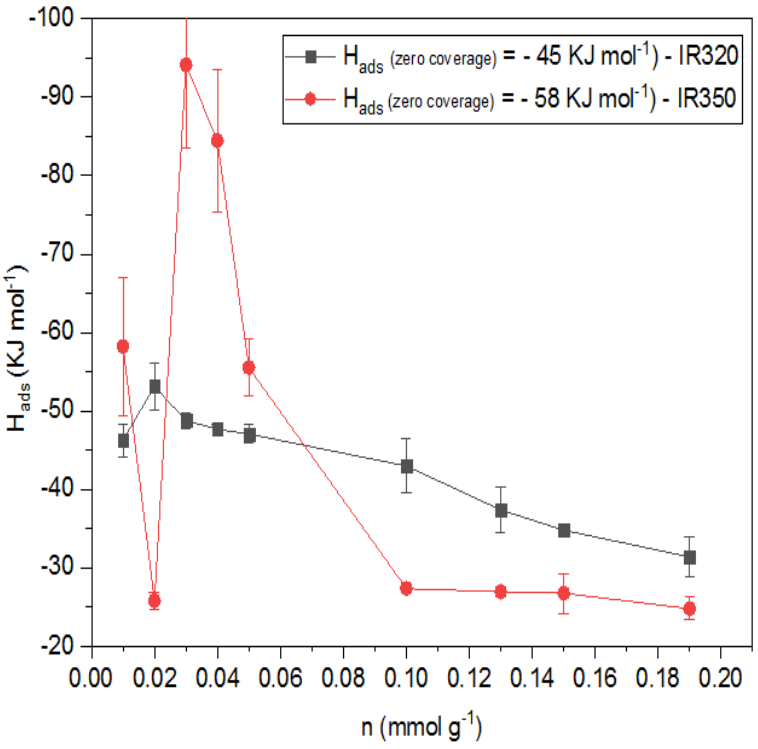

Figure 5-9- Isosteric Heat of adsorption of CO_2 on IR320 and IR350

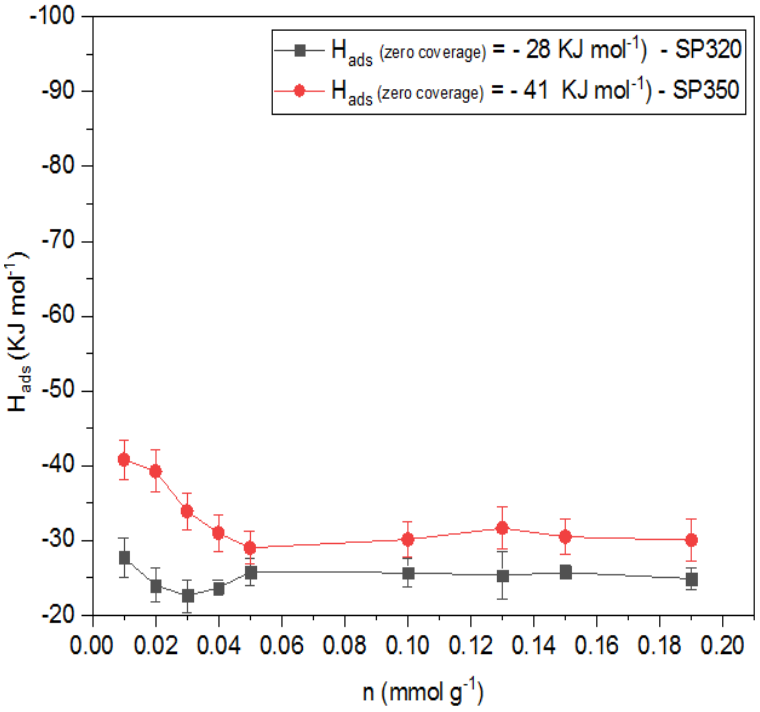

Figure 5-10- Isosteric Heat of adsorption of CO_2 on SP320 and SP350

It is evident from the plots of ΔH_{ads} against the corresponding surface coverage that the estimated ΔH_{ads} (n=0) were all < 80 KJ mol^{-1}, an indication that van der Waals intermolecular forces govern CO_2 adsorption on the torrefied carbons. Physical sorption processes, which can generally be reversed and are by nature exothermic, have been reported in adsorption enthalpy values < 50 KJ mol^{-1} [40], which can be compared with the ΔH_{ads} values obtained in the present work. ΔH_{ads} in porous materials have been described as the summation of individual contributions of the varying surface coverage on an adsorbent, starting from fluid-fluid interaction prior to the fluid-solid interaction within the porous solid during adsorption processes [284]. At the onset of adsorption, low fluid-fluid interaction often dominate. During this time, the fractional filling pores experience is insufficient to provide a meaningful contribution towards intermolecular interaction enthalpy. However, with an increase in pore filling, the adsorptive would deviate from its ideal behaviour and contributes to the build–up of intermolecular enthalpy of adsorption.

Additionally, other non-specific fluid-solid interaction and their contribution towards the build-up of the enthalpy of adsorption also depend on the pore characteristics and availability of

high energy sites [284]. Aside from these, it is instructive to note that specific fluid-solid interactions induced by polarised functional groups' may also contribute to the intermolecular interaction enthalpy. The effects from these levels of interactions would undoubtedly contribute to an initial enthalpy value of adsorption, represented at the highest binding energy site on the adsorbent. The highest binding sites are often occupied at the low-pressure region of the adsorption isotherm [168]. As the ΔH_{ads} defines the binding strength of an adsorbent-adsorbate pair, it is anticipated that such binding strength will vary with an increase in surface coverage, occasioned by the nature of adsorbent, adsorbate and extent of interaction between the adsorbed molecules themselves [168].

Given the selected surface coverage, the ΔH_{ads} curve may be explained using three regions, namely – the ΔH_{ads} at zero surface coverage ($n = 0$), ΔH_{ads} at low surface coverage ($0 < n \leq 0.1$) and the ΔH_{ads} at the moderately high surface coverage ($0.1 < n$). As observed, the shape of the ΔH_{ads} curves of the IR and SP torrefied carbon suggests that heterogeneous surfaces exist on the torrefied carbons, given the variation in values of the ΔH_{ads}, obtained at different CO_2 loadings. Such variations can also be associated with the effects of corresponding torrefaction conditions, which may have resulted in the CO_2 adsorption occurring at the crevices within the pore channels created, where adsorption may have been influenced by different atomic species, amongst other functional groups available on the surface of the torrefied carbons. Similar adsorption of an acidic gas (SO_2) on charcoal has been reported to result in an initial decline in ΔH_{ads}, due to surface heterogeneity, as atoms present on the surface of the charcoal, separated by distance, and at different geometrical configuration induced different interaction energies on the SO_2 molecules [285].

The estimated values of the ΔH_{ads} from the curves are IR320 (-45 KJ mol $^{-1}$), IR350 (-58 KJ mol $^{-1}$), SP320 (-28 KJ mol $^{-1}$) and SP350 (-41 KJ mol $^{-1}$). These ΔH_{ads} values represent the binding strength of the CO_2 that first adsorb at the most active sites on the torrefied carbon near the zero surface coverage ($n=0$) region, where pore wall interaction effects on the CO_2 show great attraction force. From the zero to the low coverage region, the magnitude of ΔH_{ads} is mainly dependent on the binding strength of CO_2 on the active sites, which are rapidly saturated in this region. The maximum value of the ΔH_{ads} in this region may result from a small

fraction of the torrefied carbon surface being covered by the adsorbed CO_2. After the adsorbed CO_2 occupied the high energy sites, it can be seen that the differential enthalpy of adsorption continues to decrease with an increase in the CO_2 loading, particularly for the torrefied SP carbon samples. The decrease in the value of ΔH_{ads} is as expected, given that the more negative the value of the ΔH_{ads}, the more the amount of gas species that can be accommodated by the adsorbent [175]. This is also because subsequent CO_2 intake is possible as the interaction energy of adsorption is still above the enthalpy of liquefaction of CO_2 (- 17 kJ mol^{-1}) [175].

As observed from the ΔH_{ads} curve, the IR torrefied carbons exhibited an ascending value in the ΔH_{ads}, after the initial ΔH_{ads} for the zero coverage region. Although the expectation is that ΔH_{ads} would continue to decrease with an increase in surface coverage in the range (0.02 to 0.05); however, CO_2 interaction with initially inaccessible high energy sites may likely have coincided where high fluid-fluid interaction is taking place, resulting in high ΔH_{ads} value at this region. The shape of the ΔH_{ads} curve in this region would depend on the competing forces between the CO_2-high energy sites still available and the fluid-fluid interaction. Also, as reported in a similar study, in the case of ether vapour adsorption on charcoal, the maxima and minima points, resulting in a significant variation in ΔH_{ads}, due to the oscillating nature of the ΔH_{ads} curve at the low coverage region, have been attributed to the superposition of opposing orientation and dispersion effect of the adsorbate-adsorbent interactions [168]. Additionally, the views from Palmer affirmed that such ascending behaviour of ΔH_{ads} at low uptake region is attributed to the tendency of an adsorbate to self-associate, in which the resulting attraction energy, plus the interaction emanating from the adsorbate-adsorbent interaction at the same time may result in the ΔH_{ads} increase, as demonstrated in the adsorption of methyl alcohol on vitreous silica [286]. This suggests that fluid-fluid interaction experienced at the low uptake region of the torrefied IR ΔH_{ads} curve may be higher than the CO_2-high energy site interaction at this region, which has also accounted for the higher CO_2 adsorption of the IR torrefied carbon.

For the moderately high surface coverage region ($0.1 < n$), ΔH_{ads} is seen as decreasing with increasing CO_2 loading for both IR and SP torrefied carbons. As the name implies, the high

surface coverage encompasses fluid-fluid interaction, which would most likely dominate in wider micropore within the torrefied carbon structure. As a result, the high uptake region may witness the completion of specific fluid-solid interaction, with further adsorption nearing the CO_2 heat of liquefaction. Although the values of the ΔH_{ads} obtained for the ΔH_{ads} curve of the torrefied carbon investigated are still further from the enthalpy of liquefaction of CO_2 (i.e., -17 kJ mol^{-1}), this may be due to the adsorption isotherm not reaching the pore-filling regime at the maximum pressure of 1 bar employed for the torrefied carbon characterisation. The Clausius-Clapeyron equation was derived based on the assumption that ΔH_{vap} of adsorbate from an adsorbent surface is non-variant; however, in practice, the adsorption enthalpy may vary, depending on surface heterogeneity [168], which has been proven by the torrefied carbons investigated in this study. Also, since enhanced heat of adsorption indicates preferential adsorption of CO_2 on torrefied carbons, with the ΔH_{ads} < 80 KJ mol^{-1}, suggesting physisorption process taking place, lower regeneration energy would be required for the CO_2 capture, where the torrefied carbon is employed for CCS applications. Therefore, having investigated the ΔH_{ads}, as a crucial thermodynamic parameter relevant for energy consumption analysis in adsorption processes, it is crucial to study the associated kinetics governing the minimal equilibrium uptake of the torrefied carbons adsorption at a temperature of 50 °C to assess their performance.

5.6 Adsorption kinetics of CO_2 on torrefied carbon

As explained in Section 2.22, the diffusion model recognises the steps involved in an adsorption process, with adsorption proceeding via film diffusion, through to pore (internal or intra-particle) diffusion, and then to mass action (i.e., the adsorption and desorption to and from the active sites [210]. Interpretation of data through the application of kinetic models provided insight into the processes involved in the CO_2 adsorption by the torrefied carbons. Therefore, it is crucial to ensure the validity of a suitable kinetic model used for such modelling. As described in Section 2.22.1.2, the linear driving force model (LDF) has been applied in modelling a wide range of adsorption kinetics; however, it provides for a single rate-determining step, which is limited to molecular diffusion at pore entrances [287]. Given the expected chemical surface interaction of the torrefied carbons, in addition to pore diffusion, it

was expected that the LDF would provide an inadequate description of the adsorption processes; hence fitting the kinetic data using the LDF model showed this to be the case with poor fitting obtained for the LDF model. The fit provided by the LDF model for CO_2 adsorption on the IR320 sample is shown in the Appendix.

Consequently, more complex forms of the nested models, namely: the stretched exponential (SE), represented by Equation 58 and the double exponential (DE) model, Equation 59, were considered and tested for their fitness with the kinetic data of the CO_2 adsorption on the IR and SP torrefied carbons. The kinetic data for each pressure step (100 – 1000 mbar) on the adsorption isotherm (at 50 °C) for IR320, IR350, SP320 and SP350, were extracted from the IGA Swin software. As shown in the Appendix for the SE and DE models, the DE model seems to reproduce a better CO_2 adsorption fitting on a time-dependent function. The DE model was also fitted with the least number of variables, with the linear regression meeting the criteria of an acceptable fit, with a residual range of +/-0.04; an indication of conformance of the DE model of a normalised kinetic profile, with two distinct processes. Figures 5-11 to 5-14 shows the CO_2 adsorption kinetics of the torrefied carbons.

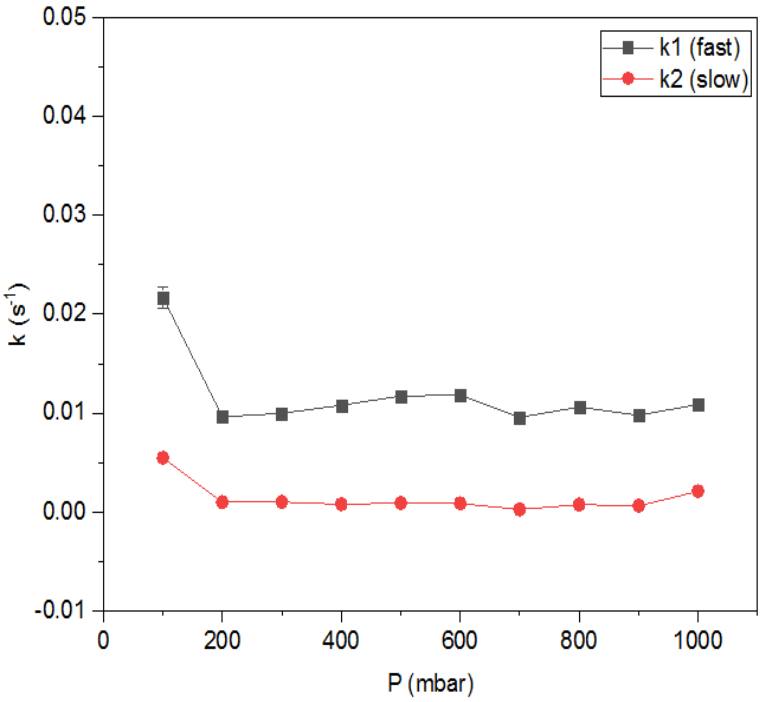

Figure 5-11- Adsorption kinetics of CO_2 against pressure for IR320 at 50 °C

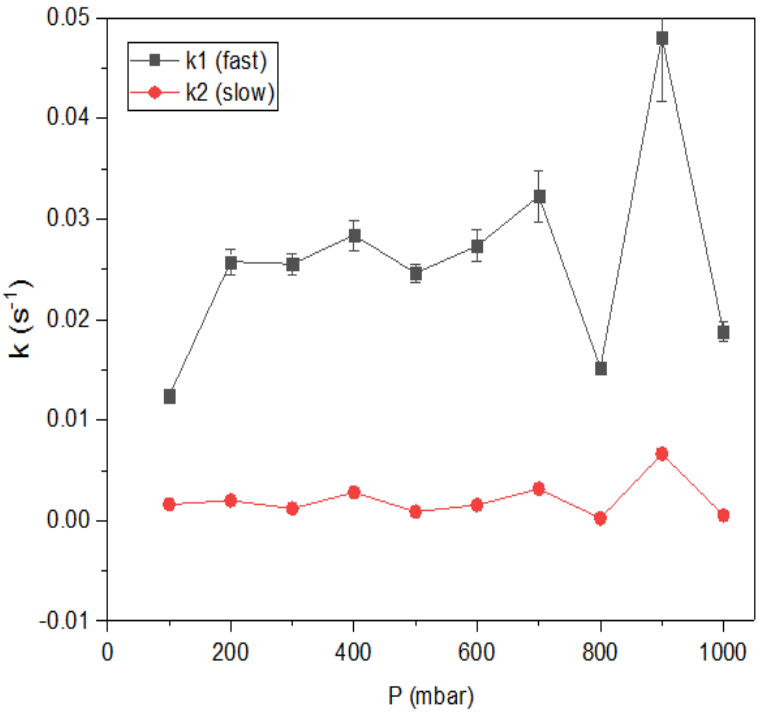

Figure 5-12- Adsorption kinetics of CO_2 against pressure for IR350 at 50 ^oC

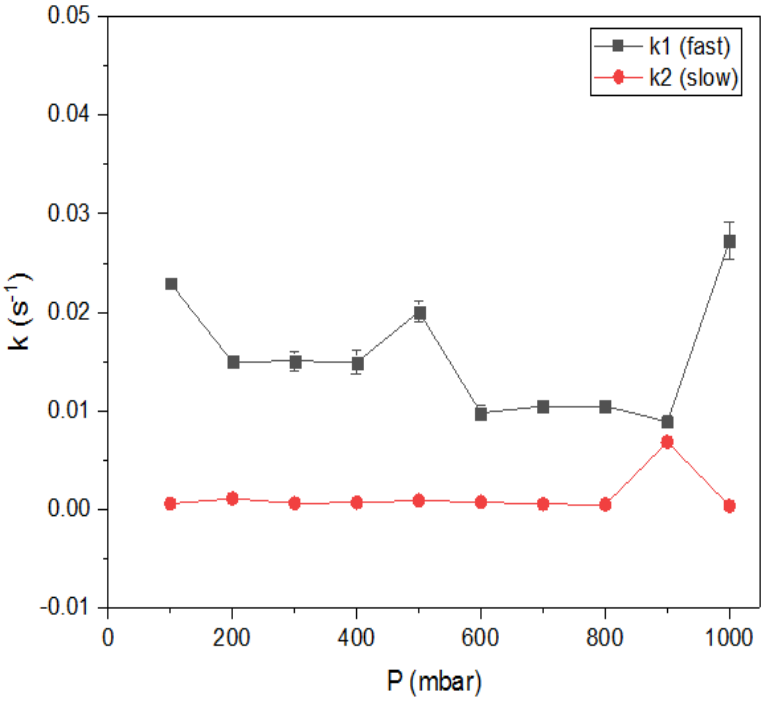

Figure 5-13- Adsorption kinetics of CO_2 against pressure for SP320 at 50 ^oC

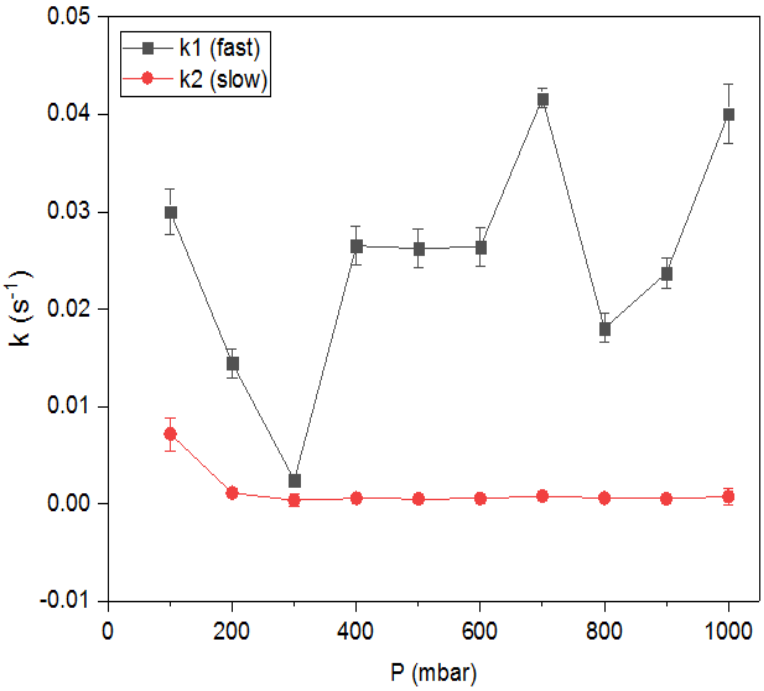

Figure 5-14- Adsorption kinetics of CO_2 against pressure for SP350 at 50 ºC

As deduced from Figures 5-10 - 5-14, the kinetic profiles suggest that the CO_2 adsorption kinetics of the torrefied carbons followed the DE model. This indicates that molecular diffusion of CO_2 into the torrefied carbons' micropores is controlled by two distinct kinetic processes - one fast and the other slow, with a distribution of mass relaxation times. The fast process is with rate constant (k_1), ranging from 2.46 x 10^{-2} – 6.64 x 10^{-2} s^{-1}, while the slow process with rate constants (k_2), ranges from 6.1 x 10^{-5} – 5.6 x 10^{-4}. Diffusion processes have been known to control the rate-determining steps of physical adsorption processes. Also, such processes may involve gas, Knudsen and surface diffusion regimes, depending on the mean free path of the gas, as explained in Section 3.9.1. Given this, it is crucial to explore how diffusion and pore dimension influences the adsorption rate of CO_2 in torrefied carbon.

Furthermore, the first (fast) process with rate constant k_1 describes CO_2 diffusion along the pore cavities due to the interaction of CO_2 molecules with the surface functional groups available on the torrefied carbon, once at proximity, as reported in [222]. Also, the permanent quadrupole moment of the CO_2 may have contributed to the fast kinetic nature, as permitted by the structural environment of the torrefied carbons. At the low-pressure regions of the adsorption isotherm, say < 0.15 mbar, surface functional groups have been known to promote

increased adsorption rates of CO_2. Such fast kinetics are consistent with a site to site hopping mechanism, which has been associated with the influence of surface functional groups on adsorption rates, as reported in the adsorption of polar molecules on activated carbons [222]. As observed for the torrefied carbons developed at 350 °C, the rate constant of the fast process seems to be increasing, though not at a progressive pattern, compared with the rate constant of the torrefied carbon developed at 320 °C. The difference in adsorption behaviour could be attributed to the structural changes that may have occurred within the torrefied carbon during their development.

For the slow processes, the rate of CO_2 diffusion may be related to the pore window of the torrefied carbon, of < 2 nm, as expected. However, since the pore size governs the molecular diffusion of gases in porous media, gas molecules' orientation as they approach the pore entrance becomes crucial. For a CO_2 molecule with a kinetic diameter of 0.33 nm to pass through the pore window, it must first orient itself for ease of access into the pores. As evident from the kinetic profile, the rate constants decline slightly with an increase in adsorption pressure. This decline is because, as the fractional loading of the CO_2 into the pores increases with an increase in adsorption pressure, the effective pore width developed in the torrefied carbon would be affected by the pore filling, and the rate with which CO_2 diffuses through the pores would be slowed. The fractional filling increase would also limit CO_2 access to the initially exposed surface functional groups on the torrefied carbon, causing the slow process to be independent of the torrefied carbon surface chemistry at higher fractional loading. However, following the orientation of the CO_2 and the subsequent access of a few molecules, the molecules may further compete against each other for adsorption energy sites within the torrefied carbon structure. And with further increase in adsorption pressure, the CO_2 gas may begin to cluster. As a result, the pore entry would be limited; hence the pore width originally controlling the slow kinetic process becomes affected. Such an effect on the pore size will induce further a barrier to the surface diffusion; hence the slow kinetic process experienced. The slow process can also be associated with the longer time it takes to surmount the activation energy barrier, leading to the CO_2 adsorption following the system equilibration.

Conclusively, although the two diffusion processes occur concurrently, given the rate at which adsorption processes occur, the fast process would be affected by the reduced effects (pore filing) from the slow process. As a result, the slow process becomes the rate-determining step of the CO_2 adsorption, occurring at the high energy sites of the torrefied carbons. As per Equation 59 of the DE model, the pre-exponential factors (A_1 and A_2) as variables also contribute to the kinetic model fitting. The contribution from the pre-exponential factors is shown in Figures 5-15 – 5-18.

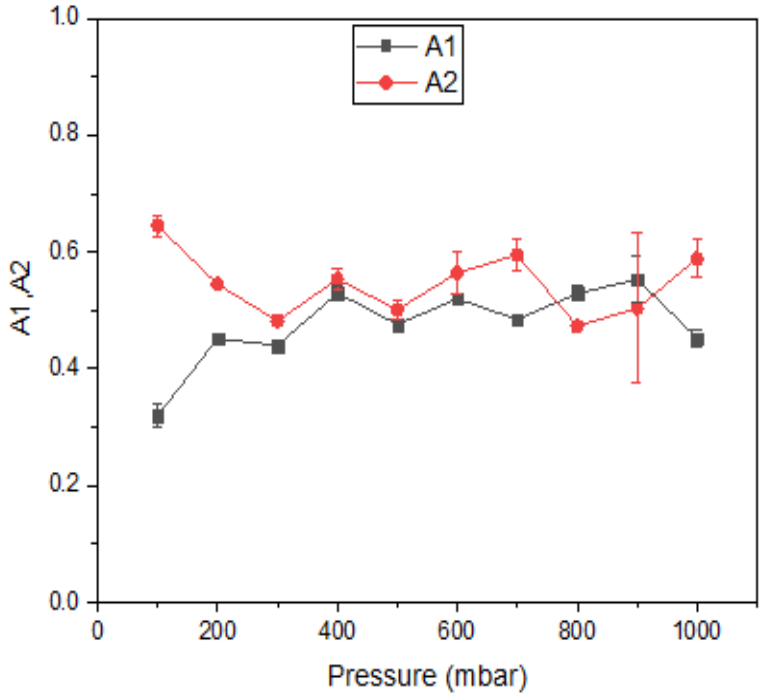

Figure 5-15- Pre-exponential factor A1 and A2 contribution for CO_2 adsorption on the torrefied carbon IR320, based on the DE model at 50 ^oC

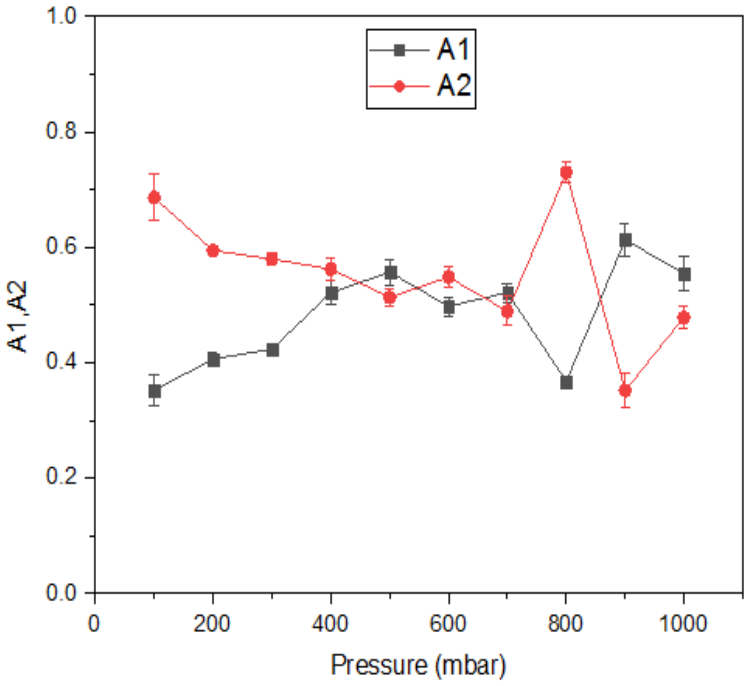

Figure 5-16- Pre-exponential factor A1 and A2 contribution for CO_2 adsorption on the torrefied carbon IR350, based on the DE model at 50 ºC

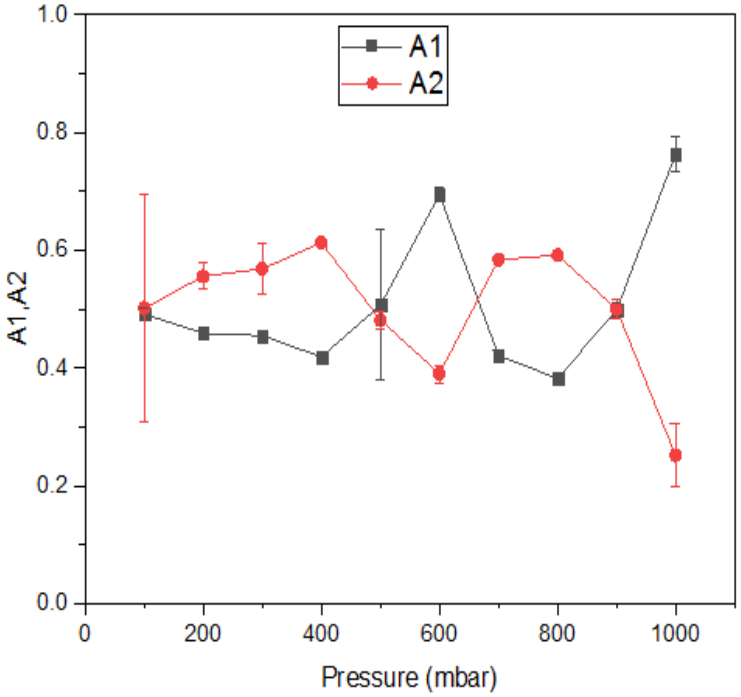

Figure 5-17- Pre-exponential factor A1 and A2 contribution for CO_2 adsorption on the torrefied carbon SP320, based on the DE model at 50 ºC

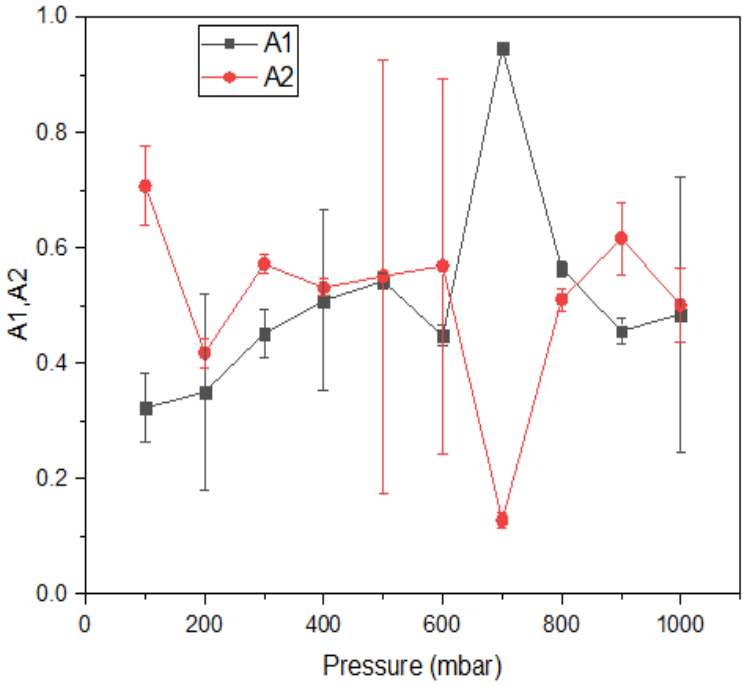

Figure 5-18- Pre-exponential factor A1 and A2 contribution for CO_2 adsorption on the torrefied carbon SP350, based on the DE model at 50 ^oC

Having analysed the contribution from the pre-exponential factors (A1 and A2) against increment in adsorption pressure, the (A1, A2) trends suggest that process 2 contributes more to the CO_2 adsorption. The A2 trend seems to converge more towards the centre (0.5 value) of the (A1, A2) axis of the plots, in which for pressure equilibration, A1 + A2 must be = 1. However, it is crucial to note that neither of the two processes is entirely dominant as both play a vital role in CO_2 adsorption on the torrefied carbons. Kinetic consideration is an essential aspect and performance measurement metric in every adsorption process in the industry. Adsorption cycles with shorter cycle time < or = 12 min for a PSA process have often been recommended, as working towards the achievement of lesser time of adsorption, increases the system performance [288]. As evident from the DE model shown in the Appendix, the CO_2 adsorption rate by the torrefied carbon is fast, given the equilibration time of an average of < 8 min for the IR carbon and about 11 min as observed for the SP carbon sample. Consequently, the short time of approaching equilibrium is an indication that there is potential from these materials on a kinetic basis.

5.7 Post CO_2 adsorption HHV analysis of torrefied carbon

As the scope of this work was to investigate CO_2 adsorption of torrefied carbons for CCS applications, the objectives included determining whether torrefied carbons can be recycled as fuel in the same coal-powered plant integrated with the CCS unit after the torrefied carbon would have been entirely spent for CO_2 capture. The torrefied carbon intended for such application would be employed for CO_2 capture based on a Temperature Swing Adsorption (TSA) technique. The TSA process aimed to utilise low-grade waste heat that may be recovered from the combustion stacks of the coal-fired power plant's boiler system for regeneration purposes.

However, given the limitations of this work, this aspect of the research framework could not be achieved. The pressure swing adsorption (PSA) process employed was limited to the torrefied carbon characterisation. The result obtained shows the likely performance of torrefied carbons in future adsorption systems. Despite adopting the PSA, it was necessary to assess the energy value of the spent torrefied carbons. As a result, ultimate analysis of the spent torrefied carbons were carried out, as described in Section 3.4.2. The HHV of the spent torrefied carbons were estimated using the model equation stated in Section 3.4.3. The post-CO_2 adsorption HHV of the torrefied carbon were compared with those of the pre-CO_2 adsorption, as shown in Figures 5-19 and 5-20, to assess the torrefied carbon fuel quality.

5.7.1 Calorific value analysis (pre and post - CO_2 adsorption) torrefied carbon

As shown in Table 5-4, it was evident that the carbon contents of the torrefied carbons increased slightly, following the CO_2 adsorption at 50 °C. Besides the likely interaction of CO_2 gas with the torrefied carbon during the adsorption process, which may have contributed to an increase in the carbon contents, the adsorption system's temperature may have also impacted the fuel’s quality. Additionally, while the carbon content increased slightly, the hydrogen and nitrogen species also declined slightly, with oxygen following a similar trend.

Table 5-4-Elemental composition of post-CO_2 adsorption IR and SP torrefied carbon sorbent at 50 ^oC.

Sample (Post)	C% (d.a.f)	H% (d.a.f)	N% (d.a.f)	O% (d.a.f)	Pre-CO_2 HHV (MJ kg^{-1})	Post-CO_2 HHV (MJ kg^{-1})
IR320	67.89	4.43	0.39	27.29	**26.49**	**26.78**
IR350	68.20	4.38	0.30	27.12	**26.75**	**26.85**
SP320	63.98	5.64	0.19	30.19	**26.13**	**26.21**
SP350	73.01	4.59	0.15	22.25	**29.12**	**29.52**

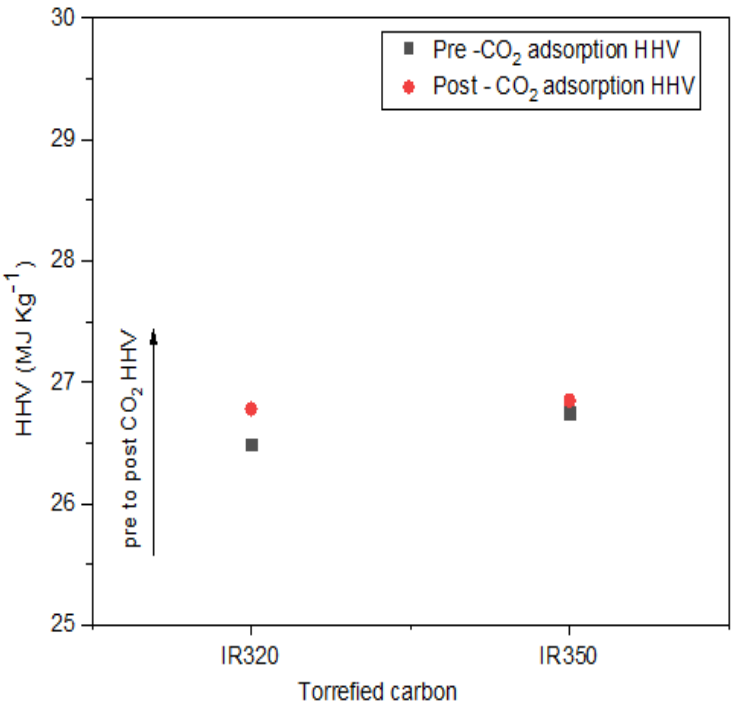

Figure 5-19- Post-CO_2 (at 50 ^oC) and Pre-CO_2 HHV comparison of IR320 and IR350 torrefied carbons

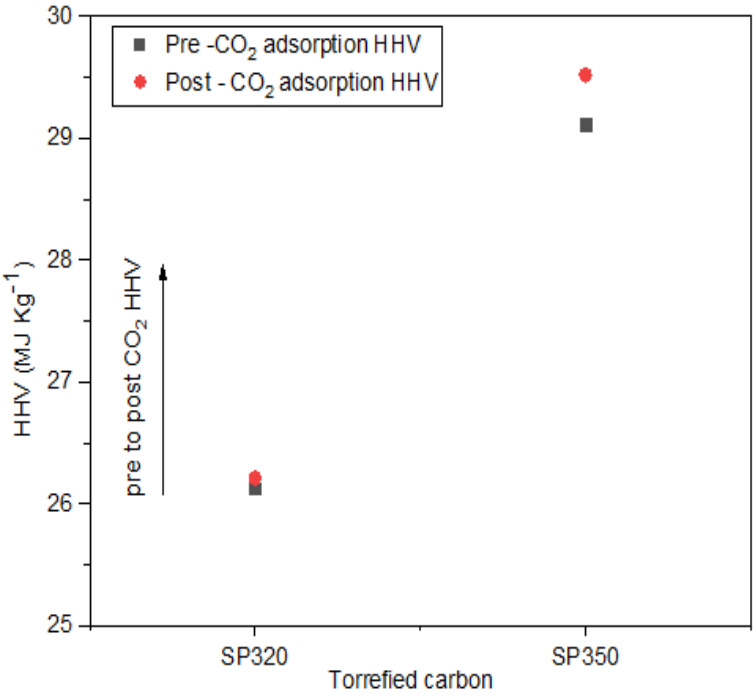

Figure 5-20- Post-CO_2 (at 50 ^oC) and Pre-CO_2 HHV comparison of SP320 and SP350 torrefied carbons

Also, as evident in Figures 5-19 and 5-20, the HHV of the spent torrefied carbon improved slightly, an indication that the spent torrefied carbon can be employed for co-firing applications in the same coal-powered plant integrated with a CCS unit. However, from an energy consumption perspective, assuming a TSA process was employed for testing the CO_2 adsorption performance, the total energy that would have been spent for the development of the entire process would equal:

$$E_{in} + Q_{reg}$$

The parameters associated with the above expression (E_{in} and Q_{reg}) have been defined earlier in Equation 1.6, Equation 2.13, and the ΔH_{ads} explained in Section 5.5. It is anticipated that low ΔH_{ads} of CO_2 using the torrefied carbons would require less energy during CO_2 regeneration (Q_{reg}). Energy consumption using the PSA process were not estimated in this work, as it is not within the initial research framework. A change in ΔH_{ads} would affect how much CO_2 is captured in future applications. This also has a direct relationship with the sensible heat that may be required for regeneration processes under a TSA arrangement. The

total energy consumption from the combination of the terms above would be compared with the regeneration energy applicable in CO_2 capture, using MEA as the industry benchmark, estimated around 4530 kJ kg^{-1} of CO_2 capture [82]. The HHV of the spent torrefied carbon, which would be exploited for the co-firing purposes, would be an added value to the CCS application, allowing reduction of the amount of fresh coal that may be required to power the coal-fired plant, thus compensates for energy penalty and meeting some objectives of this study.

Chapter 6 : CONCLUSION AND FUTURE WORK

6.1 Research limitations

The initial framework of this research was to study the adsorption performance of torrefied carbons under a Temperature Swing Adsorption (TSA) process arrangement and relate the findings to how energy penalties associated with sorbents' materials performance in Carbon Capture and Sequestration (CCS) applications can be drastically reduced. This would have ensured a closed-loop system of using the same torrefied carbon developed under a CO_2 torrefaction environment for CO_2 capture, as fuel once the torrefied carbon is entirely spent for the CCS processes. Unfortunately, this aspect of the original research plan could not be realised due to limitations within the project; hence, an understanding of the applicability of the torrefied carbons would require detailed characterisation of the torrefied carbons based on standard conditions.

The characterisation of the torrefied carbon in this work, using CO_2 adsorption data obtained at 30 °C, as opposed to 0 °C reported in previous adsorption analysis, was based on technical constraints imposed by the adsorption system used to run such analysis at 0 °C. This was in addition to anticipated longer durations for such analyses, which were further impacted by the constraints on laboratory working hours that resulted from the COVID-19 global pandemic. As a result, CO_2 adsorption data at 30 °C was used to characterise the torrefied carbons. This temperature is below the critical temperature of CO_2 gas (31 °C) and still within an acceptable standard room temperature, as suggested in previous studies in the literature. The results obtained here may not fully represent accurate pore characteristics of the torrefied IR and SP carbons; however, the general trends obtained are expected to be the same at lower temperatures of analysis.

Aside from the above, other criteria for assessing adsorption performance such as selectivity, adsorption capacity, resistance to attrition, and the torrefied carbon's chemical stability would have offered a more detailed analysis of CO_2 adsorption performance of the torrefied carbons. However, the timeline to conduct these analyses was affected by universities' national

lockdown for several months. As a result, the results presented in this work could serve as a foundation for future works on the use of torrefied carbon for CO_2 capture and cofiring applications, based on the optimum condition of performance established using the materials investigated.

6.2 Overview

Torrefaction is a thermochemical conversion process that has been used over the years in the production of a range of bioenergy resource alternatives. Recent studies have shown that such technology can be integrated with other industry areas, such as CCS. As a result, this work has evaluated the application of torrefaction technology for carbon-based adsorbent 'torrefied carbons' development for CO_2 capture and co-firing applications. Within the work, two woody biomass materials (Iroko (IR) and Scottish Pine (SP)) were studied extensively for their potential use for adsorbent development. The impacts of torrefaction on the physicochemical characteristics of the torrefied carbon were discussed. Also, CO_2 adsorption studies were performed to assess the torrefied carbons' potential for utilisation in CCS applications. During the thermochemical conversion processes, the changes that occurred within the materials' inherent properties enhanced their fuel quality and the capacity for CO_2 adsorption.

The lignocellulosic constituents of the woody materials, namely – hemicellulose, cellulose and lignin, reacted differently, given the change in selected torrefaction conditions. The degradation of these constituents led to the enhanced calorific value and hydrophobicity of the torrefied carbons. The torrefaction performance indicators, such as energy yield, energy density and energy gain, amongst others, were used to assess the fuel quality of the torrefied carbon for suitability in cofiring applications. The torrefied carbon also showed some characteristic tendency as a potential material for CO_2 capture. The microporous character of the torrefied carbons is shown by the results of the Langmuir and DR analyses. The adsorption capacities obtained are higher than those of other non-carbonaceous adsorbents that have been discussed in other studies within the literature. Therefore, it is instructive to note that the torrefaction process employed was carried out at lesser energy requirements than what may

be obtainable in typical pyrolysis for pyrogenic sorbent development, which may come at a much higher temperature condition and cost.

6.3 Overall conclusion

In conclusion, given the torrefied carbon developed in this work, it was evident that those developed at the torrefaction temperature condition of 350 °C showed the highest adsorption capacity for both IR and SP carbons. This is in addition to having a higher heating value and hydrophobicity, with all values > 90 ^{o}C. The results from the characterisation of the torrefied carbons show a high degree of performance, given the energy gain (104) for SP and (102) for IR, at the torrefaction conditions of 320 °C. The temperatures of 320 and 350 °C were investigated extensively, despite the other 290 and 380 °C temperature conditions, given the limitations discussed. The temperature of 320 and 350 °C are considered the optimum performance conditions for such material to be taken forward for CO_2 capture application. This is as a result of the need to preserve the mechanical strength of the torrefied carbons since the calorific values of the torrefied carbons developed at these conditions, for example, IR (26.49 MJ kg^{-1} and 26.75 MJ kg^{-1}) and SP (26.13 MJ kg^{-1} and 29.12 MJ kg^{-1}) were higher than that of the low-ranked coal (23.20 MJ kg^{-1}) investigated.

The characterisation of the torrefied carbons, given the FTIR results, suggests the existence of some N-containing functional groups on the torrefied carbon surface, which may have attracted CO_2, causing adsorption. Consequently, it is anticipated that the torrefied carbons can be employed for CCS and cofiring applications. Additionally, the CO_2 adsorption performance of the torrefied carbons were assessed from both thermodynamic and kinetic perspectives. The thermodynamic study results suggest that the torrefied carbons would require relatively lower regeneration energy if employed for CO_2 capture application. This is given the values of the isosteric heat of adsorption for the torrefied carbons investigated, which were lower than 80 KJ mol^{-1}, indicating that the CO_2 adsorption is physisorption-controlled. The kinetics of CO_2 adsorption shows two distinct processes (one fast and one slow), based on the double exponential model, which helped describe the adsorption mechanism as diffusion controlled.

Based on the above, it was evident that using CO_2 as the treatment gas for the torrefaction enhanced the torrefied carbons' physicochemical characteristics, which has been justified. The advantage of using CO_2 compared with other inert gases, such as nitrogen, argon, amongst others, is a potential reduction in the cost of the CCS process. As a result, it is highly recommended for CO_2 to be utilised for torrefied carbon development for application in other industrial processes in the future. Another supporting argument for CO_2 utilisation is that, it is possible for the CO_2 emitted from the stacks of boiler systems of coal-powered plants to be effectively recycled for use in further development of the torrefied carbons, thus helps in promoting the sustainability of such system and the use of renewable materials for CCS applications.

6.4 Future work

Given the limitations experienced in this research, there is no doubt that additional work would be required to fully justify the use of torrefied carbon for CO_2 capture and cofiring application in the CCS process. Some of the suggested future work for the torrefied carbon sample developed include:

Characterisation of the torrefied carbons at 0 °C to compare the case with the results obtained in this work and the wider literature. This may enable the true porous character of the torrefied carbon to be known; however, the overall trends in pore sizes are expected to remain the same.

Also, given that the current work was based on the traditional torrefaction technique, it may be worth demonstrating other types of torrefaction processes to compare the performance with the current method. Additionally, some characterisation techniques, such as x-ray photoelectron spectroscopy, pycnometer (for mechanical strength) and scanning electron microscopy, may be employed to reveal more in-depth characteristics of the torrefied carbons, as these were not utilised in this work due to the research constraints experienced.

As this study focused on using two woody biomass materials, it is also recommended that other wood types such as waste woods and other forms of carbon materials are assessed for

performance. This would enable comparison of their adsorption performance and strengthen the sustainability of the proposed system and the intended dual purpose of the torrefied carbon in this research framework.

Finally, given that the study's initial framework was to develop a torrefied carbon for use in a TSA process, it would be necessary to assess the performance of these materials under cyclic adsorption performance to inform the behaviour of the entire system, thus completes the close-loop approach intended.

Chapter 7 : APPENDIX

7.1 - Excel calculation of the atomic ratio of the torrefied carbon fuel using Equation 3.11.

$$\frac{\mathrm{H}}{\mathrm{C}} = 1.4125 \left(\frac{\mathrm{O}}{\mathrm{C}}\right) + 0.5004$$

	A	B	C	D	E	F	G	H
1								
2								
3	**Sample**	**C**	**H**	**N**	**O**	**O/C**	**H/C**	**H/C = 1.4125 [O/C] + 0.5004**
4								
5	**IR380**	68.49	4.3	0.29	27.17	0.3967	1.060739101	1.060739101
6	**IR350**	67.94	4.4	0.32	27.41	0.403444	1.070264954	1.070264954
7	**IR320**	67.12	4.49	0.4	27.99	0.417014	1.089432703	1.089432703
8	**IR290**	59.01	5.72	0.47	34.8	0.589731	1.333394408	1.333394408
9	**Untreated IR**	45.86	6.14	0.55	47.45	1.034671	1.961872416	1.961872416
10								
11	**SP380**	72.47	4.39	0.17	22.52	0.310749	0.939333352	0.939333352
12	**SP350**	72.11	4.63	0.19	23.07	0.319928	0.952298142	0.952298142
13	**SP320**	63.73	5.69	0.21	30.37	0.476542	1.173515095	1.173515095
14	**SP290**	54.64	6.24	0.26	38.86	0.711201	1.504970827	1.504970827
15	**Untreated SP**	45.27	6.46	0.3	47.97	1.059642	1.997144533	1.997144533
16								
17	**Coal**	50.81	4.17	1.44	43.58	0.857705	1.711908561	1.711908561

7.2- Energy input of torrefaction using Equation 2.13

$$E_{(in)} = \Delta H_T \times Q \times t$$

Q = molar volume of CO_2 gas (i.e., converted from ml min^{-1} to kmol min^{-1})

Hence for CO_2 volume flowrate of 100 ml min^{-1} applied through the furnace, being considered as an open system, the molar volume equivalent = 4.082 x 10^{-6} kmol min^{-1}, as reported in [148]

$$\Delta H_T = \int_{25}^{T} C_p \, dC$$

$$C_p = a + bC_p + cC_p^2 + dC_p^3$$

Where

a = 22.26 KJ $(kmol.K)^{-1}$, b = 5.981 x 10^{-2} KJ $(kmol.K)^{-1}$, c = - 3.501 x 10^{-5} KJ $(kmol.K)^{-1}$

d =7.469 x 10^{-9} KJ $(kmol.K)^{-1}$

	A	B	C	D	E	F	G	H	I
1									
2				**Carbon dioxide Torrefaction**					
3									
4				ΔH (upper - lower)				**ΔH x Qx t**	
5	Sample	Cp T	Cp T	CpT	CpT	Residence Time	Gas flowrate	E(in)	Enthalpy
6	Condition	(upper limit)	(lower limit)	(upper)	(lower)	t (min)	Q (kmol/min)	KJ	change
7									
8	290	290	25	8698.58	537.63	60	4.08E-06	2.00E+00	8160.95
9	320	320	25	9822.14	537.63	60	4.08E-06	2.27E+00	9284.51
10	350	350	25	10981.4	537.63	60	4.08E-06	2.56E+00	10443.8
11	380	380	25	12174.9	537.63	60	4.08E-06	2.85E+00	11637.3
12									

7.3 - Calculation for the HHV of coal, the untreated and torrefied carbon IR and SP using Equation 3.14

$$\mathrm{HHV} = 3.55\mathrm{C}^2 - 232\mathrm{C} - 2230\mathrm{H} + 51.2\mathrm{CH} + 131\mathrm{N} + 20{,}600$$

	A	B	C	D
1				
2		Calorific value		
3	**Sample**	**Torrefied carbon**	**Coal**	**Untreated**
4		**Pre - CO2 adsorption HHV**		
5		($MJkg^{-1}$)	($MJkg^{-1}$)	($MJkg^{-1}$)
6				
7	**IR290**	23,859.29	23,203.00	18223.39
8	**IR320**	26,491.03	23,203.00	18223.39
9	**IR350**	26,759.61	23,203.00	18223.39
10	**IR380**	26,890.69	23,203.00	18223.39
11				
12	**SP290**	22,097.83	23,203.00	17979.28
13	**SP320**	26,138.15	23,203.00	17979.28
14	**SP350**	29,124.05	23,203.00	17979.28
15	**SP380**	29,981.53	23,203.00	17979.28
16				
17		**Torrefied carbon**		
18		**Post - CO2 adsorption HHV**		
19		($MJkg^{-1}$)	($MJkg^{-1}$)	
20				
21	**IR320**	26782.38	23,203.00	18223.39
22	**IR350**	26855.66	23,203.00	18223.39
23				
24	**SP320**	26211.42	23,203.00	17979.28
25	**SP350**	29,562.70	23,203.00	17979.28
26				

7.4 - Excel calculations of the torrefaction parameters, using Equations 3.5 - 3.9

$$\text{Mass Yield } (MY_{db}) = \frac{M_{f2}}{M_{F1}} \times 100\%$$

$$E_y(\text{wt.}\%) = (MY_{db}) \times (HHV_{torrefied} / HHV_{untreated})$$

$$Energy\ Density, E_D = E_Y / M_Y$$

$$\text{Enhancement factor } (E_F) = \frac{HHV_{torrefied}}{HHV_{untreated}}$$

$$\text{Energy gain } (E_G) = \frac{\left[\frac{HHV_{torrefied} - HHV_{untreated}}{HHV_{untreated}}\right]}{\left[\frac{Mass_{untreated} - Mass_{torrefied}}{Mass_{untreated}}\right]} * 100$$

F	G	H	I	J	K	L	M	N	O
				Performance Parameters					
					mass balance				
Sample	EY	ED	EF	Untreated	Torrefied Carbon	Volatile	MY	MY	EG
	(wt. %)	(> 1 = gain)		MF1(g)	MF2 (g)	(MF3)		(%)	
				(+/- 10%)		(Mf1 - MF2)			
IR290	94.372	1.309267	1.31	1.6869	1.2159	0.471	0.721	72.08	110.76
IR320	81.668	1.453683	1.45	1.5864	0.89124	0.69516	0.562	56.18	103.53
IR350	72.687	1.468421	1.47	1.6817	0.83252	0.84918	0.495	49.5	92.765
IR380	61.223	1.475614	1.48	1.764	0.732	1.032	0.415	41.49	81.297
SP290	87.608	1.229072	1.23	1.4922	1.0637	0.4285	0.713	71.28	79.772
SP320	80.627	1.453793	1.45	1.6147	0.8956	0.7191	0.555	55.46	101.9
SP350	54.865	1.619867	1.62	1.6343	0.5936	1.0407	0.363	33.87	97.343
SP380	54.663	1.66756	1.67	1.765	0.5386	1.2264	0.305	32.78	96.073

7.5 - Adsorption isotherms of the torrefied carbons at temperatures (30, 40 and 50 °C)

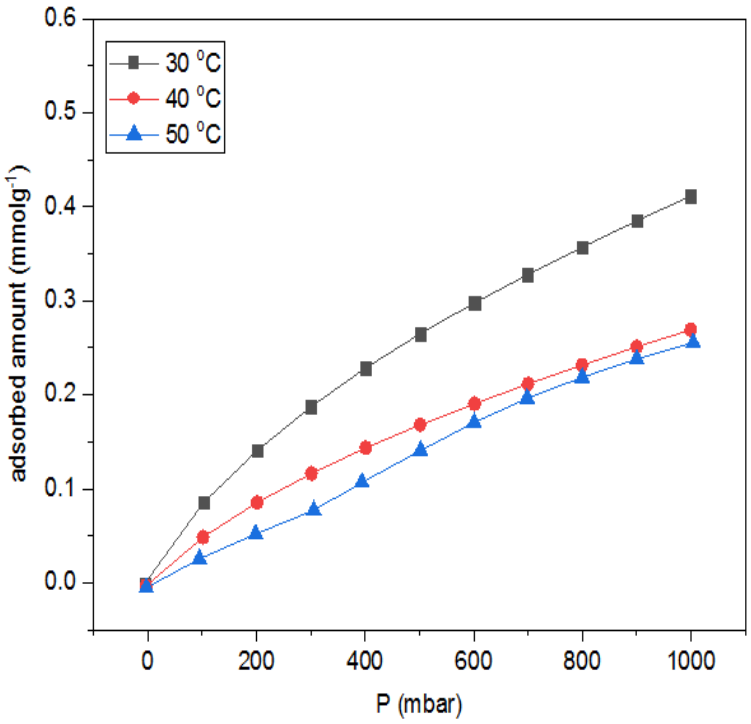

Figure 7-1- CO_2 adsorption isotherm at three temperature for IR320 for the heat of adsorption determination

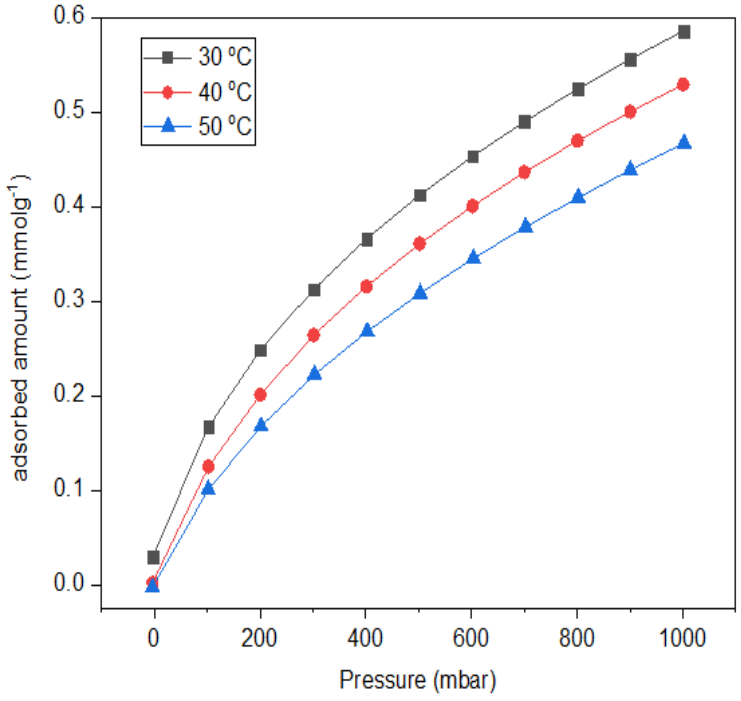

Figure 7-2- CO_2 adsorption isotherm at three temperatures for IR350 for the heat of adsorption determination

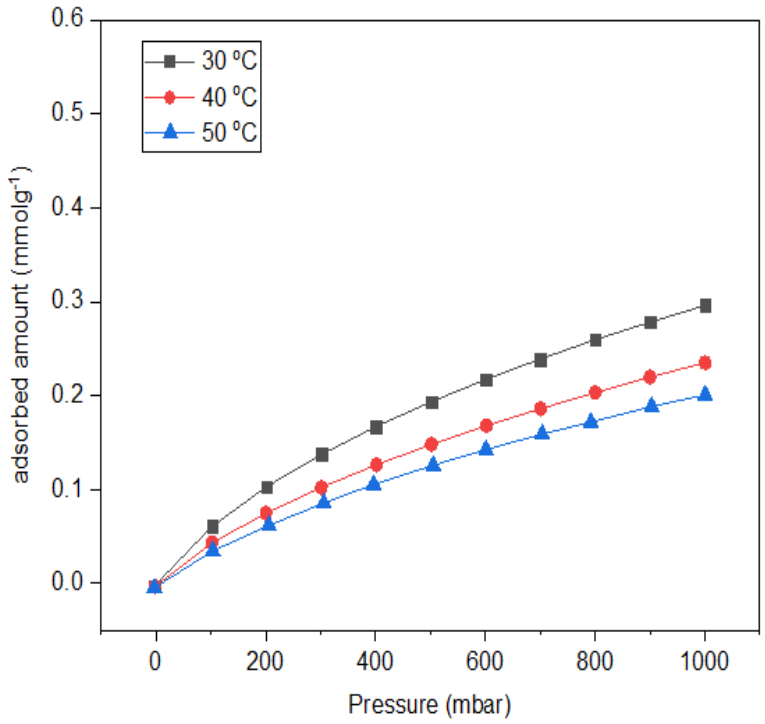

Figure 7-3 - CO_2 adsorption isotherm at three temperatures for SP320 for the heat of adsorption determination

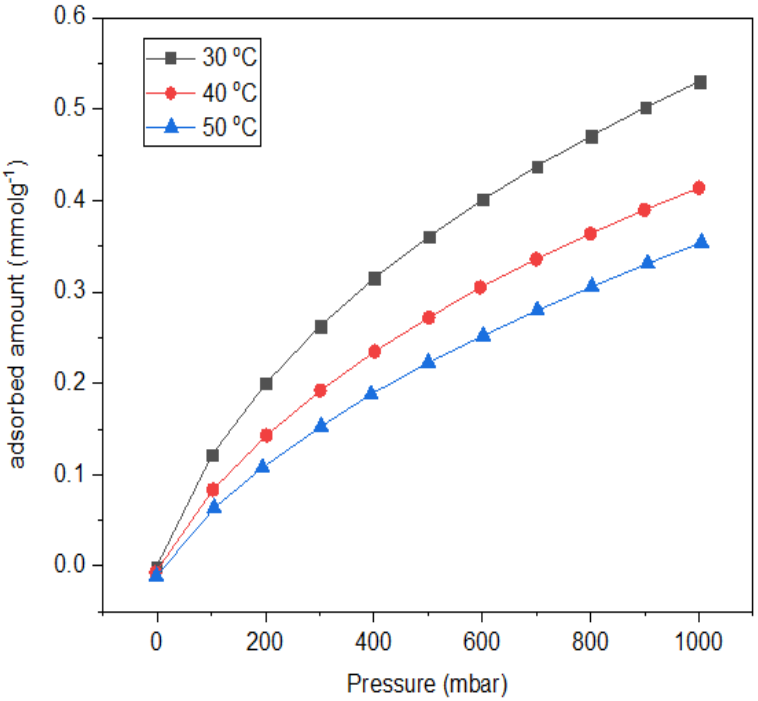

Figure 7-4 - CO_2 adsorption isotherm at three temperature for SP350 for the heat of adsorption determination

7.6 - Plots of Differential heat of adsorption for IR320 fixed coverage values – (0.01 and 0.02)

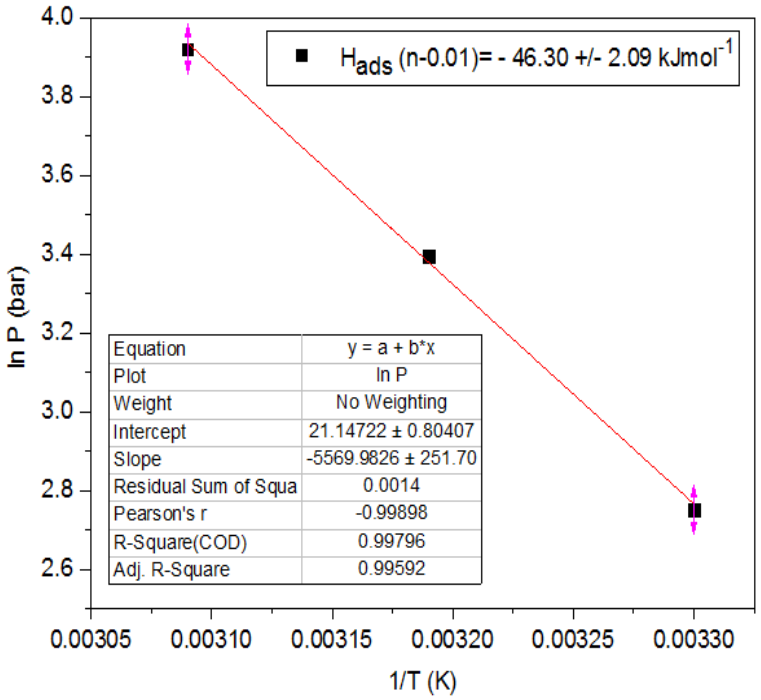

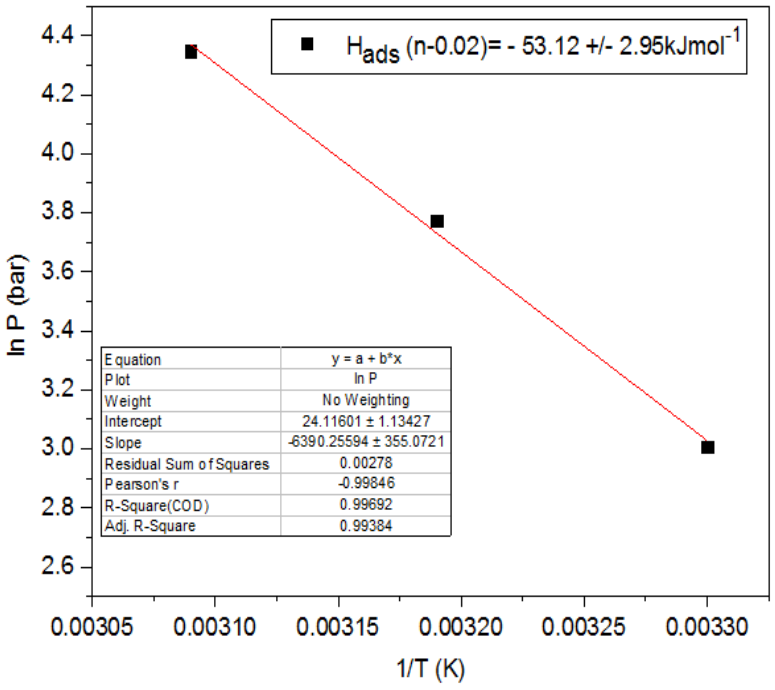

7.7- Plots of Differential heat of adsorption IR350 fixed coverage value (0.01 and 0.02)

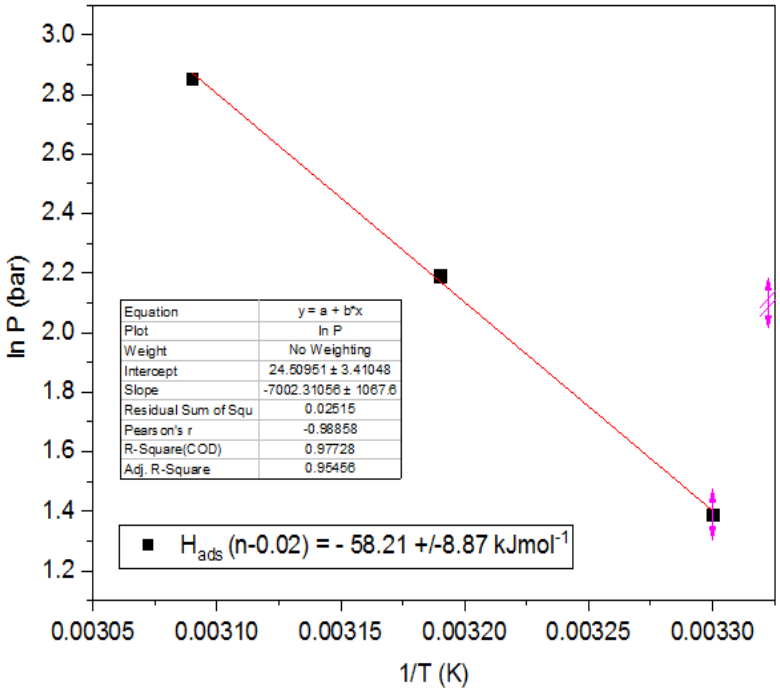

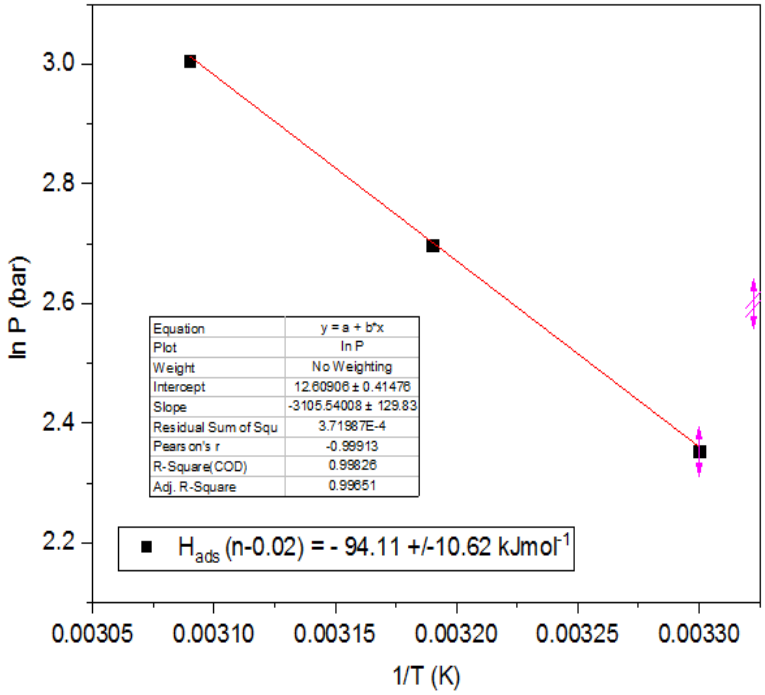

7.8 - Plots of Differential heat of adsorption SP320 fixed coverage value (0.01 and 0.02)

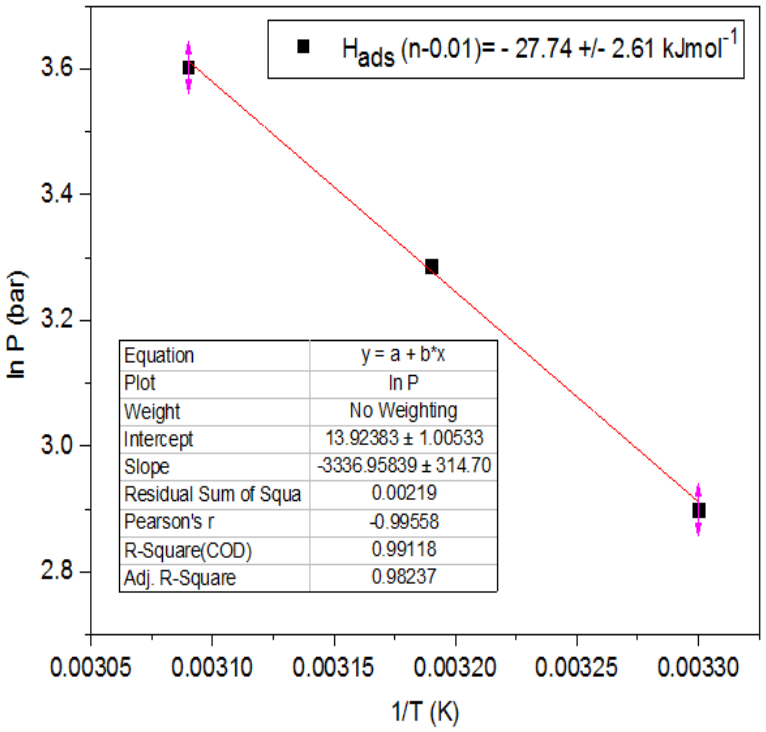

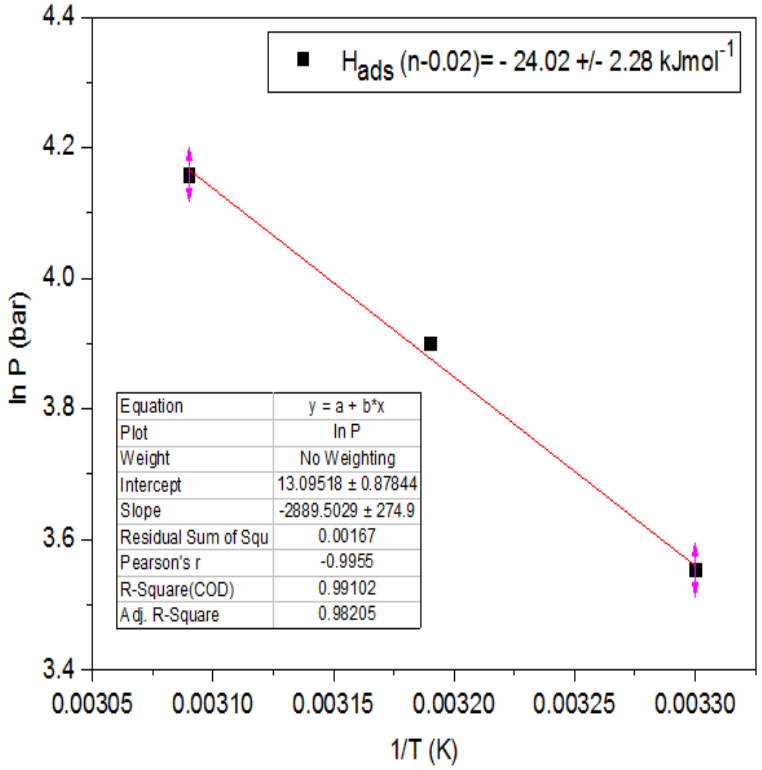

7.9 - Plots of Differential heat of adsorption SP350 fixed coverage value (0.01 and 0.02)

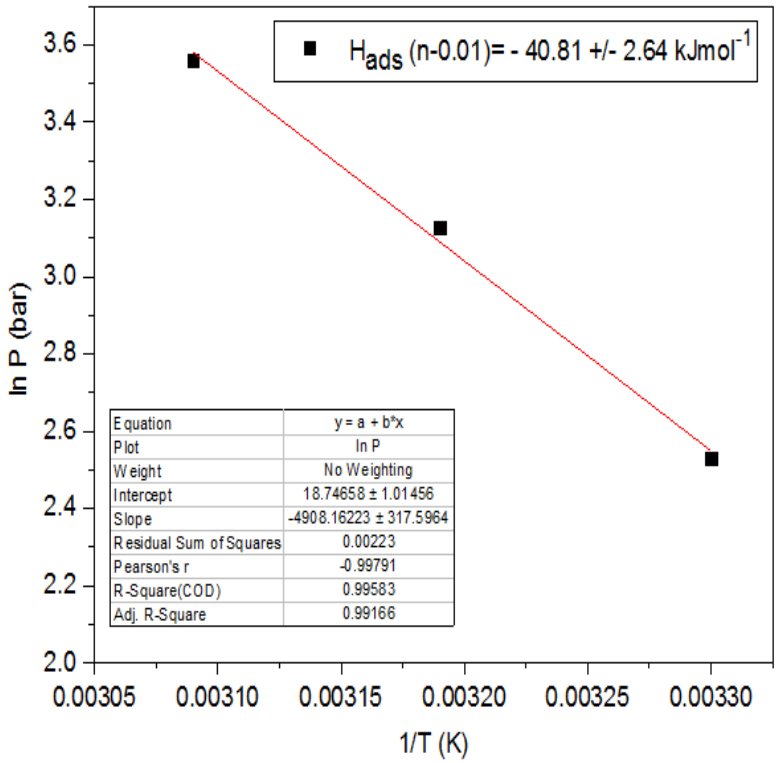

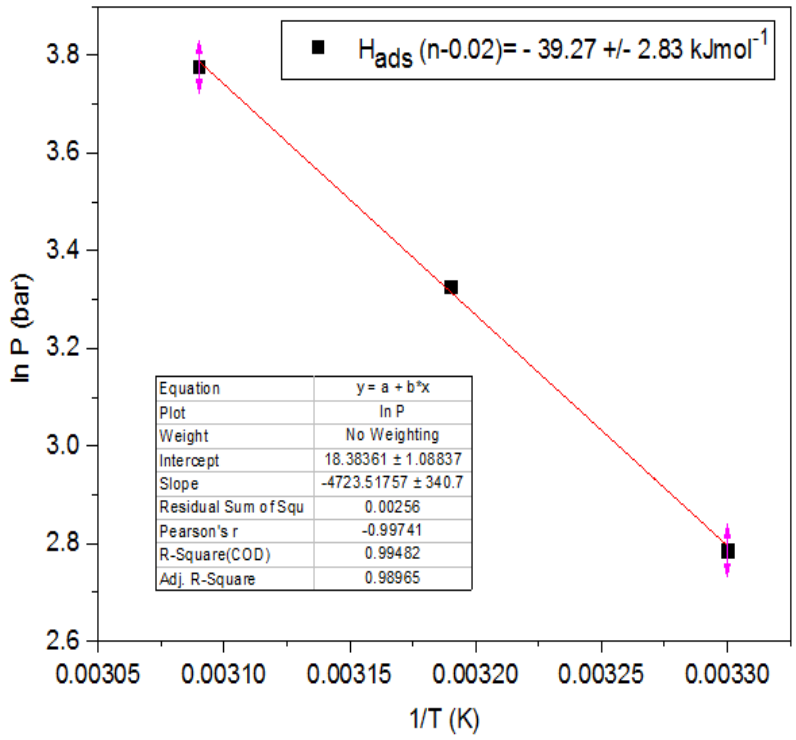

7.10 - Kinetic modelling of IR320 torrefied carbon at 50 ºC

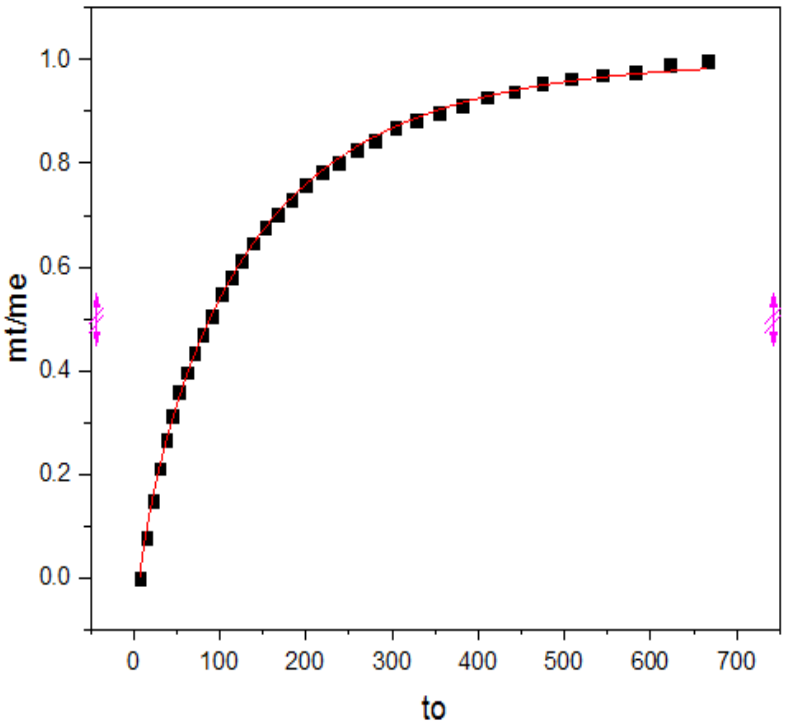

Unfitted Linear driving force model for IR320

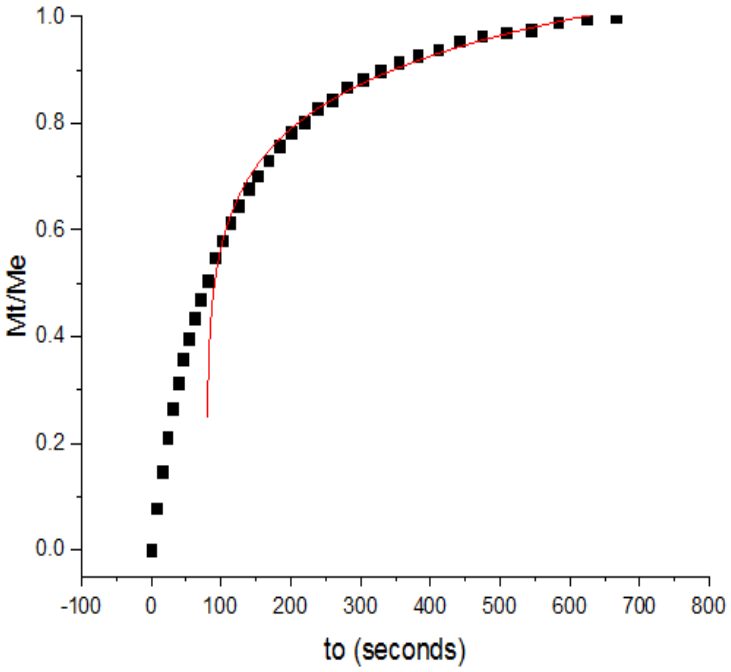

Unfitted Stretched exponential model for IR320

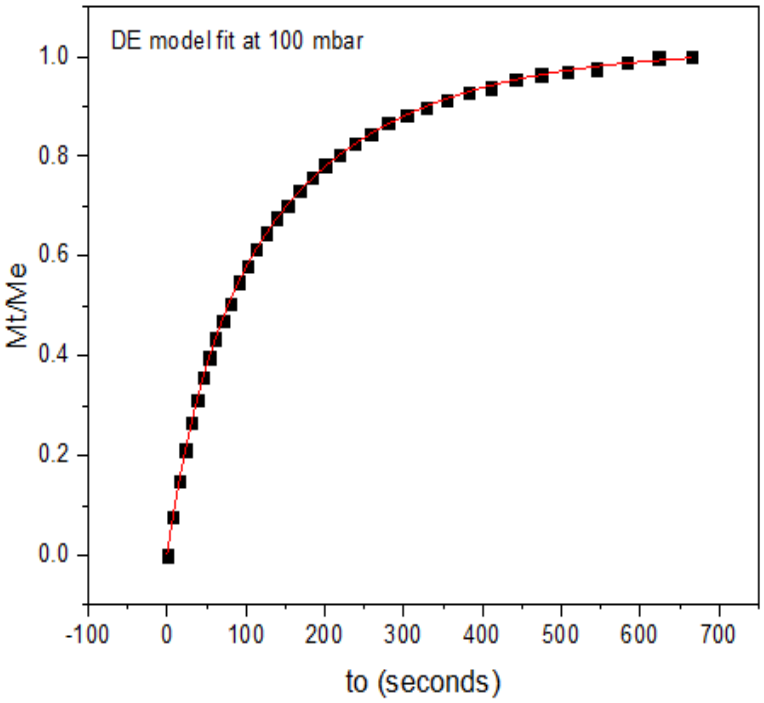

Double exponential model fitting for IR320

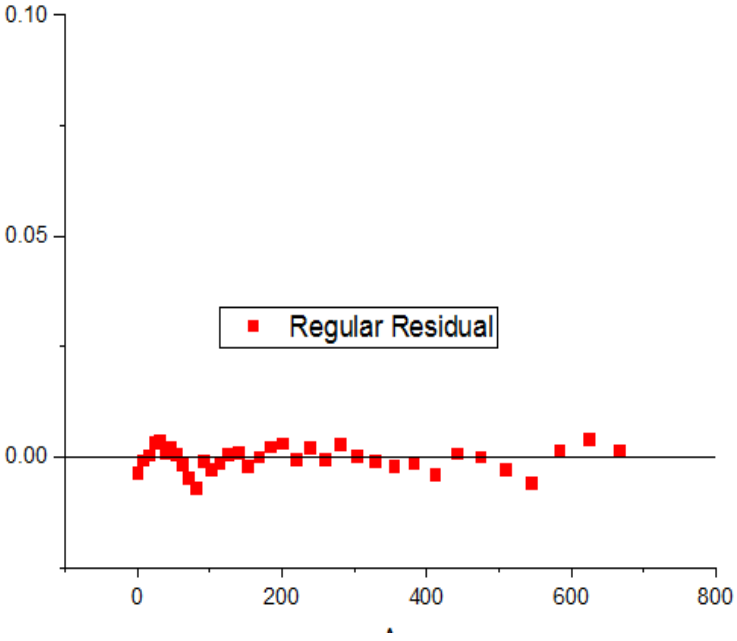

Double exponential model residual fitting for IR320

7.11 - Kinetic modelling of IR350 torrefied carbon at 50 ºC

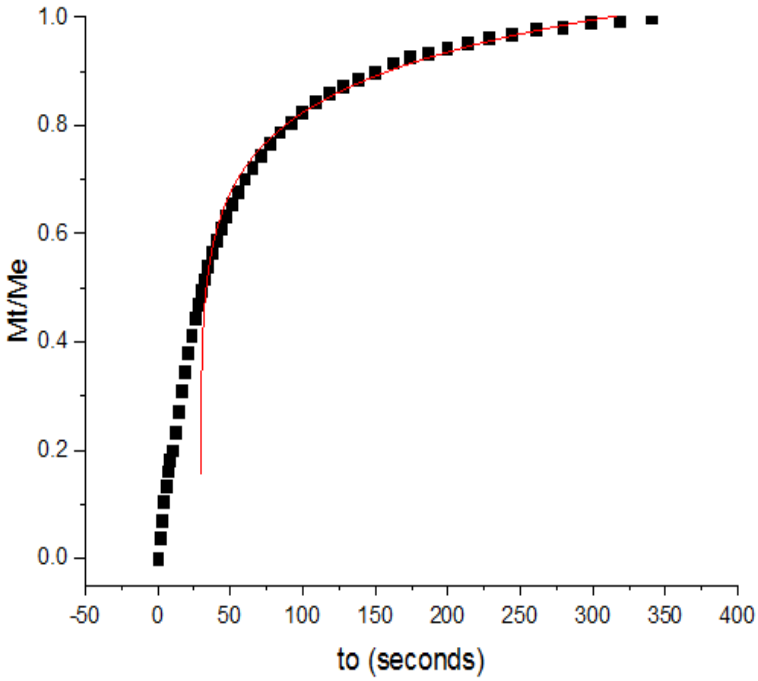

Unfitted Stretched exponential model for IR350

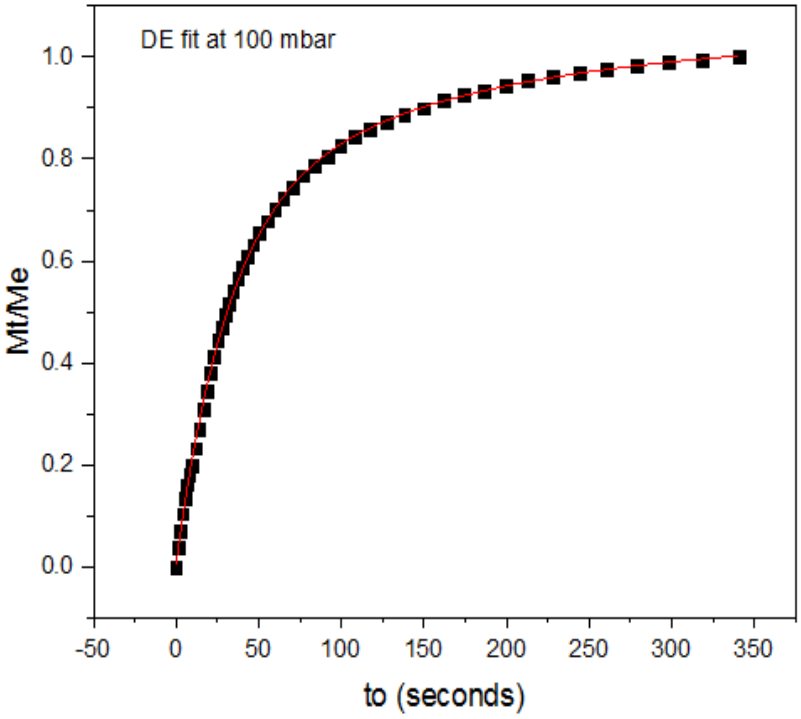

Double exponential model fitting for IR350

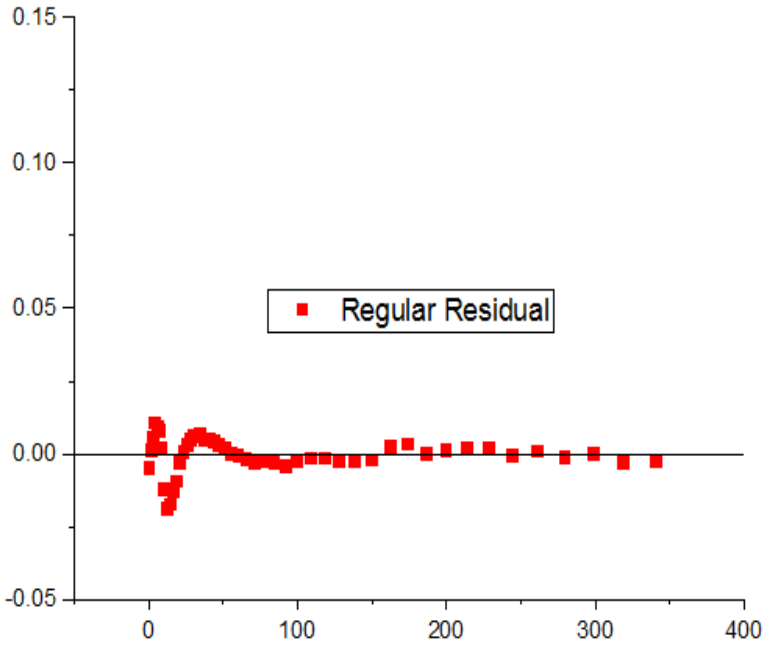

Double exponential model residual fitting for IR350

7.12 - Kinetic modelling of SP320 torrefied carbon at 50 ºC

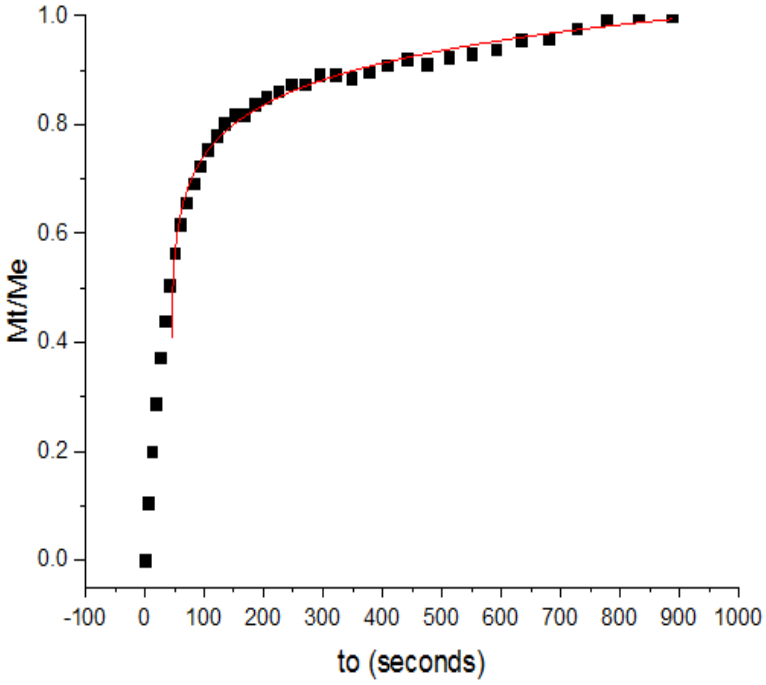

Unfitted Stretched exponential model for SP320

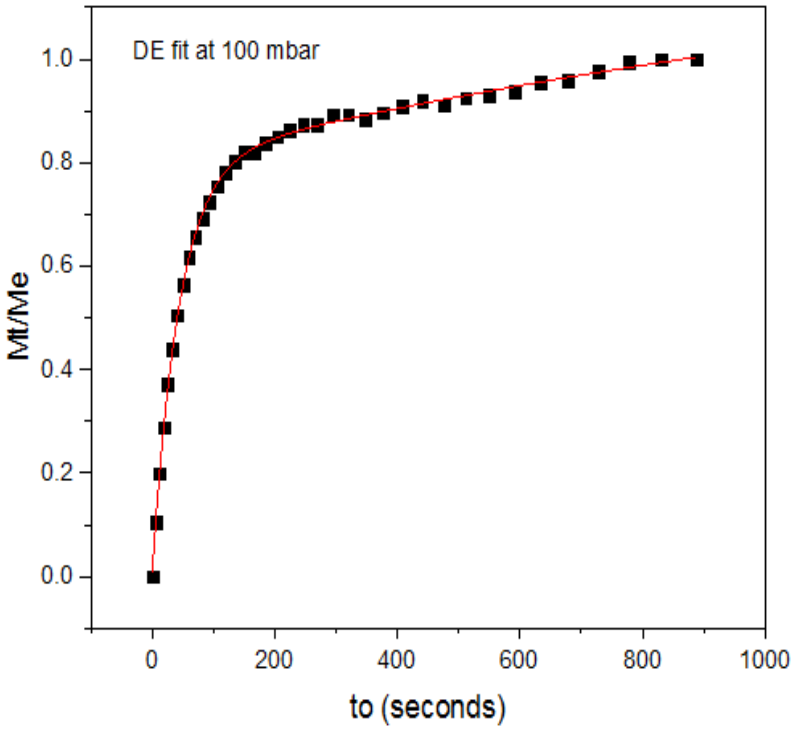

Double exponential model fitting for SP320

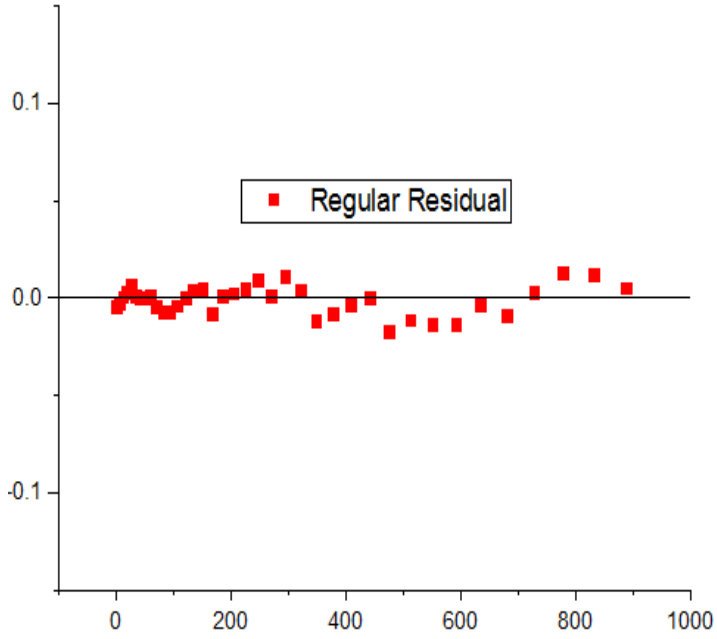

Double exponential model residual fitting for SP320

7.13 - Kinetic modelling of SP350 torrefied carbon at 50 ºC

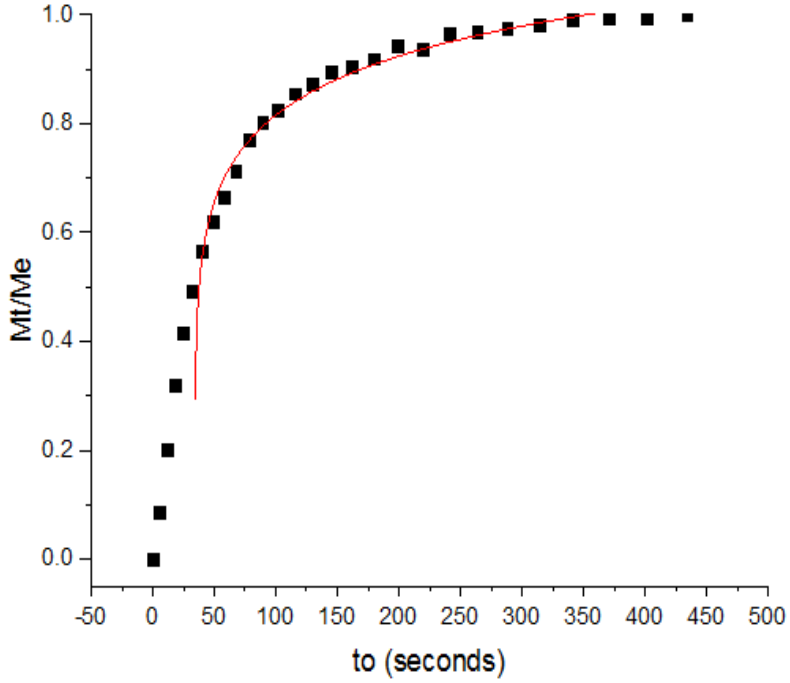

Unfitted Stretched exponential model for SP350

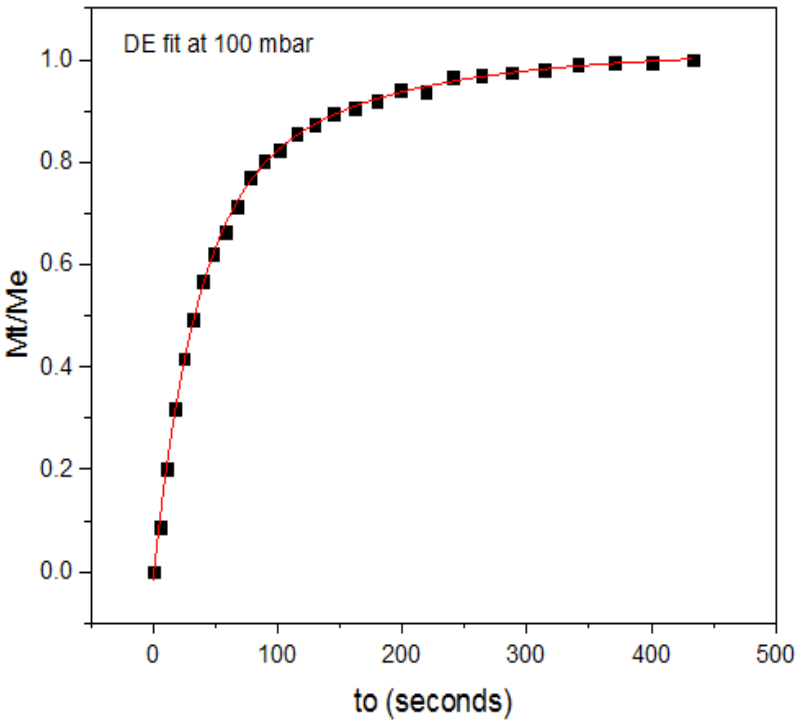

Double exponential model fitting for SP350

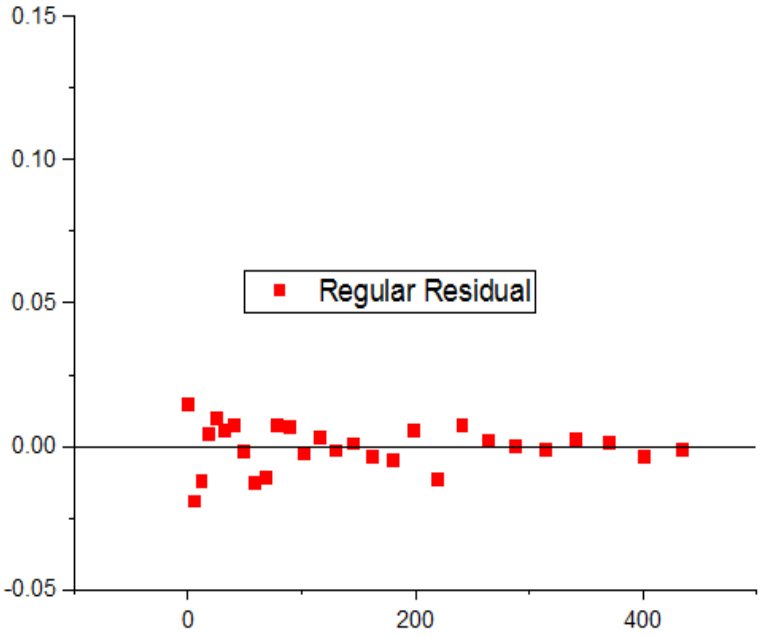

Double exponential model residual fitting for SP350

Chapter 8: REFERENCES

1. Hester, R.E. and Royal Society of Chemistry., *Carbon capture sequestration and storage*. Issues in environmental science and technology -29, ed. R.M. Harrison and R.E. Hester. 2010, Cambridge, UK Royal Society of Chemistry.
2. Le Quéré, C., Andrew, R.M., Friedlingstein, P., Sitch, S., Hauck, J., *Global Carbon Budget 2018.* Earth System Science Data, 2018. **10**(4): p. 2141-2194.
3. Vortmeyer, N., Schneider, R., Hohe, S.,, *Post Combustion Carbon Capture Leading Mature Technology for Decarbonisation of Fossil Power Generation*, in *World Energy Congress*. 2013, Siemens AG: Daegu, South Korea, Oct 13 - 17.
4. Drage, T.C., Snape, C.E., Stevens, L.A., Joseph, W., Wang, J., Cooper, A.I., Dawson, R., Guo, X., Satterley, C., Irons, R.,, *Materials challenges for the development of solid sorbents for post-combustion carbon capture.* Journal of Materials Chemistry, 2012. **22**(7): p. 2815-2823.
5. Bae, T., Hudson, M. R., Mason, J .A., Queen, W. L., Dutton, J.J., Sumida, K., Micklash, K . J., Kaye, S.S., Brown, C.M., Long, J.R.,, *Evaluation of cation-exchanged zeolite adsorbents for post-combustion carbon dioxide capture.* Energy & Environmental Science, 2013. **6**(1): p. 128-138.
6. Lenntech BV. *Carbon dioxide*. [cited 2019 April 12]; Available from: https://www.lenntech.com/carbon-dioxide.htm.
7. Mazzoldi, A., Hill,T., Colls, J.J.,, *CO2 transportation for carbon capture and storage: Sublimation of carbon dioxide from a dry ice bank.* International Journal of Greenhouse Gas Control, 2008. **2**(2): p. 210-218.
8. McBroom, R., *Polar Molecules Tutorial: How to determine polarity in a molecule*. 2017, Crash Chemistry Academy.
9. SEI., G., *Radiative Forcing* in *Carbon Offset and Research Education*. 2011, Stockholm Environmental Institute and Greenhouse Gas Management Institute: Aviation Information.
10. Institute, S.E.I.a.G.G.M. *Radiative Forcing*. 2011 [cited 2017 June 15]; Available from: http://www.co2offsetresearch.org/aviation/RF.html.
11. Arrhenius, S., *On the influence of carbonic acid in the air upon the temperature of the ground.* Philosophical Magazine and Journal of Science 1896. **41**(5): p. 237-276.
12. Derek, M. *Global Warming Effects and Causes: A Top 10 List*. Planetsave 2009 [cited 2017 15/05]; Available from: http://planetsave.com/2009/06/07/global-warming-effects-and-causes-a-top-10-list/.
13. International Energy Agency, *CO2 Emissions from Fuel Combustion*, I. Statistics, Editor. 2015, IEA: France. p. 1-548.
14. International Energy Agency, *Global Energy & CO2 Status Report 2018* in *The latest trends in energy and emissions in 2018* 2018.
15. Zhao, M., Minett, A.I., Harris, A.T.,, *A review of techno-economic models for the retrofitting of conventional pulverised-coal power plants for post-combustion capture (PCC) of CO2.* Energy & Environmental Science, 2013. **6**(1): p. 25-40.
16. Marchal, V., Dellink, R., van Vuuren, D., Clapp, C.,Château, J., Lanzi, E., Magné, **B.,** van Vliet, J.,, *The OECD Environmental Outlook to 2050*. 2011. p. 1-91.
17. Scripps Institution of Oceanography. *The Keeling Curve*. 2017 25/10/2020 [cited 2020 27/10]; Available from: https://www.co2.earth/weekly-co2.
18. Metz, B., Davidson, O., Coninck, H., Loos, M., Meyer, L,. *Carbon Dioxide Capture and Storage*, in *IPCC Special Report*. 2005: New York. p. 431.
19. United Nations Framework Convention on Climate Change. *Background on the UNFCCC: The international response to climate change*. 2016 [cited 2017 21/08]; Available from: http://unfccc.int/essential_background/items/6031.php.

20. United Nations. *What is the Kyoto Protocol?* 2012 [cited 2019 April 29]; Available from: https://unfccc.int/kyoto_protocol.
21. International Energy Agency., *World Energy Outlook 2018*. 2018.
22. Matt, M. *Climate change: US formally withdraws from Paris agreement*. 2017 [cited 2020 15 November]; Available from: https://www.bbc.co.uk/news/science-environment-54797743.
23. Srikanta Dinda, *Development of Solid Adsorbent for Carbondioxide Capture from Flue Gas.* Separation and Purification Technology, 2013. **109**: p. 64-71.
24. Figueroa, J.D., Fout, T., Plasynski, S., McIlvried, H., Srivastava, R.D.,, *Advances in CO2 capture technology—the US Department of Energy's Carbon Sequestration Program.* International journal of greenhouse gas control, 2008. **2**(1): p. 9-20.
25. Philibert, C., *Technology Penetration and capital Stock Turnover-lessons from IEA scenerio analysis*, in *OECD and IEA Information Paper*. 2007, International Energy Agency: Paris.
26. Lee, S., Park, S.,, *A review on solid adsorbents for carbon dioxide capture.* Journal of Industrial and Engineering Chemistry, 2015. **23**(2015): p. 1–11.
27. Global CCS Institute. *Advantages and disadvantages of major CO2 capture technologies*. [cited 2017 November 03]; Available from: https://hub.globalccsinstitute.com/publications/technology-options-co2-capture/advantages-and-disadvantages-major-co2-capture.
28. Davidson, R.M., *Post-combustion carbon capture from coal fired plants: solvent scrubbing*. 2007: IEA Clean Coal Centre London.
29. Dutcher, B., Fan, M., Russell, A.G.,, *Amine-Based CO2 Capture Technology Development from the Beginning of 2013 - A Review.* American Chemical Society, Division of Applied Materials & Interfaces, 2015. **7**(2015): p. 2137-2148.
30. Yu, C.H., Huang, C.H., Tan, C.S.,, *A review of CO2 cpature by Absorption and Adsorption.* Aerosol and Air Quality Research, 2012. **12**(2012): p. 745 -769.
31. Bishnoi, S. and G.T. Rochelle, *Absorption of Carbon Dioxide into Aqueous Piperazine ; Reaction Kinetics, Mass Transfer and Solubility.* Chemical Engineering Science, 2000. **55**(2000): p. 5531 - 5543.
32. Caplow, M., *Kinetics of carbamate formation and breakdown.* Journal of the American Chemical Society, 1968. **90**(24): p. 6795-803.
33. Donaldson, T.L. and Y.N. Nguyen, *Carbon dioxide reaction kinetics and transport in aqueous amine membranes.* Industrial & Engineering Chemistry Fundamentals, 1980. **19**(3): p. 260-6.
34. Sexton, A.J. and G.T. Rochelle, *Reaction Products from Oxidative Degradation of Monoethoanolamine.* Industrial & Engineering Chemistry Research, 2011. **50**(2): p. 667 - 673.
35. Davis, J. and G. Rochelle, *Thermal degradation of monoethanolamine at stripper conditions* Energy Procedia, 2009. **1**(2009): p. 327 - 333.
36. Arnold, D.S., D.A. Barrett, and R.H. Isom, *Carbon Dioxide can be produced from Flue gas.* Oil and Gas Journal, 1982. **80**(1982): p. 130 -136.
37. Rao, A.B., Rubin, E.S.,, *A technical, economic, and environmental assessment of amine-based CO2 capture technology for power plant greenhouse gas control.* Environmental science & technology, 2002. **36**(20): p. 4467-4475.
38. Burr, B., Lyddon, L.,. *A comparison of physical solvents for acid gas removal*. in *87th Annual Gas Processors Association Convention, Grapevine, TX, March*. 2008.
39. United State Environmental Protection Agency., *Environmental Footprints and Costs of Coal-Based Integrated Gasification Combined Cycle and Pulverised Coal Technologies*, EPA, Editor. 2006: Washington, DC.

40. Marsh, H., Rodriguez-Reinoso, F.,, *Activated Carbon*. 2006, Elsevier: Elsevier Science & Technology Books. 542.
41. Hernandez-Montayo, V., Garcia-Servin, J., Bueno-Lopez, J.I.,, *Thermal Traetments and Activation Procedures Used in the Preparation of Activated Carbons*, in *Lignocellulosic Precursors Used in the Synthesis of Activated Carbon- Characterisation Techniques and Applications in the Wastewater Treatment*, V.H. Montayo, Editor. 2012, IntechOpen: London. p. 92.
42. Zuo, S., Yang, J., Liu, J., Cai, X.,, *Significance of the carbonization of volatile pyrolytic products on the properties of activated carbons from phosphoric acid activation of lignocellulosic material.* Fuel Processing Technology, 2009. **90**(7): p. 994-1001.
43. Hayashi, J., Horikawa, T., Takeda, I., Muroyama, K., Nasir Ani, F.,, *Preparing activated carbon from various nutshells by chemical activation with K2CO3.* Carbon, 2002. **40**(13): p. 2381-2386.
44. Sudaryanto Y, H., S.B, Irawaty W, Hindarso H, Ismadji, S,. *High surface area activated carbon prepared from cassava peel by chemical activation.* Bioresourse Technology, 2006. **97**: p. 734-739.
45. Rashidi N.A., Y.S., *An overview of activated carbons utilization for post-combustion carbon dioxide capture.* Journal of CO2 Utilization, 2016. **13**: p. 1-16.
46. Houshmand, A., Wan Daud, W. M. A., Shafeeyan, M.S.,, *Exploring Potential Methods for Anchoring Amine Groups on the Surface of Activated Carbon for CO2 Adsorption.* Separation Science and Technology, 2011. **46**(7): p. 1098-1112.
47. Hedin, N., Andersson, N.,Yan, J., Bergstrom, L.,, *Adsorbents for the post-combustion capture of CO2 using rapid temperature swing or vacuum swing adsorption.* Applied Energy, 2013. **104**: p. 418-433.
48. Yang, R.T., *Adsorbents: Fundamentals and Applications*. 2003, Hoboken, New Jersey: John Wiley & Sons, Inc.
49. Dunne, J.A., Rao, M., Sircar, S., Gorte, R. J., Myers, A. L., *Calorimetric Heats of Adsorption and Adsorption Isotherms. 2. O2, N2, Ar, CO2, CH4, C2H6, and SF6 on NaX, H-ZSM-5, and Na-ZSM-5 Zeolites.* Langmuir, 1996. **12**(24): p. 5896-5904.
50. Jadhav, P.D., Chatti, R. V., Biniwale, R. B., Labhsetwar, N. K., Devotta, S., Rayalu, S. S., *Monoethanol Amine Modified Zeolite 13X for CO2 Adsorption at Different Temperatures.* Energy & Fuels, 2007. **21**(6): p. 3555-3559.
51. Chue, K.T., Kim, J. N., Yoo, Y. J., Cho, S. H., Yang, R. T.,, *Comparison of Activated Carbon and Zeolite 13X for CO2 Recovery from Flue Gas by Pressure Swing Adsorption.* Industrial & Engineering Chemistry Research, 1995. **34**(2): p. 591-598.
52. Wang, Y., LeVan, M. D.,, *Adsorption Equilibrium of Carbon Dioxide and Water Vapor on Zeolites 5A and 13X and Silica Gel: Pure Components.* Journal of Chemical & Engineering Data, 2009. **54**(10): p. 2839-2844.
53. Beltrao-Nunes, A., Sennour, R., Arus, V., Anoma, S., Pires, M., Bouazizi, N., Roy, R., Azzouz, A.,, *CO2 capture by coal ash-derived zeolites- roles of the intrinsic basicity and hydrophilic character.* Journal of Alloys and Compounds, 2019. **778**: p. 866-877.
54. Lively, R.P., Chance, R.R., Koros, W.J.,, *Enabling low-cost CO2 capture via heat integration.* Ind Eng Chem Res, 2010. **49**: p. 7550–62.
55. Millward, A.R., Yaghi, O.M.,, *Metal-Organic Frameworks with Exceptionally High Capacity for Storage of Carbon Dioxide at Room Temperature.* Journal of American Chemical Society, 2005. **127**: p. 17998–17999.
56. Furukawa, H., Ko, N., Bok Go, Y., Aratani, N., Beom Choi, S., Choi, E., Özgür Yazaydin, A., Snurr, R.Q., O'Keeffe, M., Kim, J., Yaghi, O.M.,, *Ultrahigh Porosity in Metal-Organic Frameworks.* Journal of Science, 2010. **329**(5990): p. 424-428.

57. Lin, Y., Kong, C., Chen, L.,, *Direct synthesis of amine-functionalized MIL-101(Cr) nanoparticles and application for CO2 capture.* RSC Advances, 2012. **2**(16): p. 6417-6419.
58. Chen, C., Kim, J., Ahn, W.S.,, *CO2 capture by amine-functionalized nanoporous materials: A review.* Korean Journal of Chemical Engineering, 2014. **31**(11): p. 1919–1934.
59. Kim, S.N., Yang, S.T., Kim, J., Park, J., Ahn, W.,, *Post-synthesis functionalization of MIL-101 using diethylenetriamine: a study on adsorption and catalysis.* CrystEngComm, 2012. **14**(12): p. 4142-4147.
60. Hoffmann, F., Cornelius, M., Morell, J., Fröba, M.,, *Silica-Based Mesoporous Organic–Inorganic Hybrid Materials.* Angewandte Chemie International, 2006. **45**(20): p. 3216 – 3251.
61. Xu, X., Song, C., Andrésen, J.M., Miller, B.G., Scaroni, A.W.,, *Preparation and characterization of novel CO2 "molecular basket" adsorbents based on polymer-modified mesoporous molecular sieve MCM-41.* Microporous and Mesoporous Materials, 2003. **62**(1): p. 29-45.
62. LIU, Z., Yang, T., ZHANG, K., Yan, C., PAN, W.,, *CO2 adsorption properties and thermal stability of different amine-impregnated MCM-41 materials.* Journal of Fuel Chemistry and Technology, 2013. **41**(4): p. 469-475.
63. Zhao, A., Samanta, A., Sarkar, P., Gupta, R.,, *Carbon dioxide adsorption on amine-impregnated mesoporous SBA-15 sorbents: experimental and kinetics study.* Industrial & Engineering Chemistry Research, 2013. **52**(19): p. 6480-6491.
64. Yue, M.B., Chun, Y., Cao, Y., Dong, X., Zhu, J.H.,, *CO2 capture by as-prepared SBA-15 with an occluded organic template.* Advanced Functional Materials, 2006. **16**(13): p. 1717-1722.
65. Qi, G., Wang, Y., Estevez, L., Duan, X., Anako, N., Park, A., Li, W., Jones, C.W., Giannelis, E.P.,, *High efficiency nanocomposite sorbents for CO2 capture based on amine-functionalized mesoporous capsules.* Energy & Environmental Science, 2011. **4**(2): p. 444-452.
66. Son, W.J., Choi, J.S., Ahn, W.S.,, *Adsorptive removal of carbon dioxide using polyethyleneimine-loaded mesoporous silica materials.* Microporous and Mesoporous Materials, 2008. **113**(1-3): p. 31-40.
67. Hicks, J.C., Drese, J.H., Fauth, D.J., Gray, M.L., Qi, G., Jones, C.W.,, *Designing Adsorbents for CO2 Capture from Flue Gas-Hyperbranched Aminosilicas Capable of Capturing CO2 Reversibly.* Journal of the American Chemical Society, 2008. **130**(10): p. 2902-2903.
68. Leal, O., Bolívar, C., Ovalles, C., García, J.J., Espidel, Y.,, *Reversible adsorption of carbon dioxide on amine surface-bonded silica gel.* Inorganica Chimica Acta, 1995. **240**(1-2): p. 183-189.
69. Ji, G., Zhao, M., , *Membrane Separation Technology in Carbon Capture, Recent Advances in Carbon Capture and Storage*, ed. D.Y. Yun. 2017: InTech.
70. Wang, M., Wang, Z., Zhao, S., Wang, J., Wang, S.,, *Recent advances on mixed matrix membranes for CO2 separation.* Chinese journal of chemical engineering, 2017. **25**(11): p. 1581-1597.
71. CO2 Capture Project. *Three basic methods to separate gases*. 2008 [cited 2017 December 18]; Available from: https://www.co2captureproject.org/pdfs/3_basic_methods_gas_separation.pdf.
72. Burt, S., Baxter, A., Baxter, L.,. *Cryogenic CO2 capture to control climate change emissions*. in *Proceedings of the 34th International Technical Conference on Clean Coal & Fuel Systems*. 2009.

73. Song, C., Liu, Q., Deng, S., Li, H., Kitamura, Y.,, *Cryogenic-based CO2 capture technologies: State-of-the-art developments and current challenges.* Renewable and Sustainable Energy Reviews, 2019. **101**: p. 265-278.
74. Xu, G., Jin, H., Yang, Y., Duan, L., Han, W.A.,, *A novel coal-based hydrogen production system with low CO2 emissions.* Journal of Engineering Gas Turbines Power, 2010. **132**(3): p. 307 - 15.
75. Tuinier, M.J., Hamers, H.P., van Sint Annaland, M.,, *Techno-economic evaluation of cryogenic CO2 capture—A comparison with absorption and membrane technology.* International Journal of Greenhouse Gas Control, 2011. **5**(6): p. 1559-1565.
76. Samanta, A., Zhao, A., Shimizu, G. K. H., Sarkar, P., Gupta, R.,, *Post-Combustion CO2 Capture Using Solid Sorbents: A Review.* Industrial & Engineering Chemistry Research, 2012. **51**(4): p. 1438-1463.
77. Rege, S.U., Yang, R.T.,, *A SIMPLE PARAMETER FOR SELECTING AN ADSORBENT FOR GAS SEPARATION BY PRESSURE SWING ADSORPTION.* Separation Science and Technology, 2001. **36**(15): p. 3355-3365.
78. Berger, A.H., Bhown, A.S.,, *Comparing physisorption and chemisorption solid sorbents for use separating CO2 from flue gas using temperature swing adsorption.* Energy Procedia, 2011. **4**: p. 562-567.
79. Sjostrom, S., Denney, J., Senior, C., Morris, W.,, *Evaluation of Solid Sorbents as a Retrofit Technology for CO2 Capture*. 2016: Colorado. p. 1 - 265.
80. Susarla, N., Haghpanah, R., Karimi, I.A., Farooq, S., Rajendran, A., Tan, L.S.C., Lim, J.S.T.,, *Energy and cost estimates for capturing CO2 from a dry flue gas using pressure/vacuum swing adsorption.* Chemical Engineering Research and Design, 2015. **102**: p. 354-367.
81. Ho, M.T., Allinson, G.W., Wiley, D.E.,, *Factors affecting the cost of capture for Australian lignite coal fired power plants.* Energy Procedia, 2009. **1**(1): p. 763-770.
82. Tarka, T.J., Ciferno, J. P., Gray, M. L., Fauth, D.,. *CO2 capture systems using amine enhanced solid sorbents*. in *Annual Conference on Carbon Capture & Sequestration*. 2006. Alexandria, VA, USA.
83. Skarstrom, C.W., *Method and apparatus for fractionating gas mixtures by adsorption*. 1960: U.S.
84. Langmuir, I., *The adsorption of gases on plane surfaces of glass, mica and platinum.* Journal of the American Chemical society, 1918. **40**(9): p. 1361-1403.
85. Grande, C.A., *Advances in pressure swing adsorption for gas separation.* ISRN Chemical Engineering, 2012. **2012**(982934): p. 1 - 13.
86. Riboldi, L., Bolland, O., , *Evaluating Pressure Swing Adsorption as a CO2 separation technique in coal-fired power plants.* International Journal of Greenhouse Gas Control, 2015. **39**: p. 1-16.
87. Mérel, J., Clausse, M., Meunier, F.,, *Carbon dioxide capture by indirect thermal swing adsorption using 13X zeolite.* Environmental progress, 2006. **25**(4): p. 327-333.
88. Jiang, L., Roskilly, A. P., Wang, R. Z.,, *Performance exploration of temperature swing adsorption technology for carbon dioxide capture.* Energy Conversion and Management, 2018. **165**: p. 396-404.
89. Lee, J.H., Kwak, N.S., Lee, I -Y., Jang, K-R., Shim, J-G.,, *Performance analysis of a 500 MWe coal-fired power plant with a post-combustion CO2 capture process.* Proceedings of the Institution of Mechanical Engineers, Part E: Journal of Process Mechanical Engineering, 2013. **227**(3): p. 149-156.
90. Sjostrom, S., Krutka, H.,, *Evaluation of solid sorbents as a retrofit technology for CO2 capture.* Fuel, 2010. **89**: p. 1298–1306.

91. Ntiamoah, A., Ling, J., Xiao, P., Webley, P.A., Zhai, Y.,, *CO2 capture by temperature swing adsorption: use of hot CO2-rich gas for regeneration.* Industrial & Engineering Chemistry Research, 2016. **55**(3): p. 703-713.
92. Loppinet-Serani, A., Aymonier, C., Cansell, F.,, *Current and Foreseeable Applications of Supercritical Water for Energy and the Environment.* ChemSusChem, 2008. **1**(1998): p. 486 – 503.
93. Basu, P., *Biomass Gasification, Pyrolysis and Torrefaction: Practical Design and Theory*. Second Edition ed. 2013: Elsevier.
94. Basu, P., *Biomass gasification and pyrolysis : practical design and theory*. 2010, Kidlington, Oxford, United Kingdom: Elsevier Inc.
95. IFP. *Innovation Energy Environment, Potential biomass mobilization for biofuel production worldwide, in Europe and in France*. 2007 [cited 2017; Available from: http://www.ifpenergiesnouvelles.com/Industrial-development/Biofuels-and-green-chemistry.
96. ASABE, *Terminology and definition for biomass production, harvesting and collection, storage , processing, conversion and utilization.* 2011(ANSI/ASABE S593.1): p. pp 821 - 824.
97. Panda, D., Mishra, S., Swain, K. C., Chakraborty, N.R., Mondal, S.,, *BIO-ENERGY CROPS IN MITIGATION OF CLIMATE CHANGE.* INTERNATIONAL JOURNAL OF BIO-RESOURCE, ENVIRONMENT AND AGRICULTURAL SCIENCES (IJBEAS) 2016. **2**(1): p. 242-250.
98. Madakadze, I.C., Stewart, K. A., Peterson, P. R., Coulman, B.E., Smith, D. L.,, *Switchgrass biomass and chemical composition for biofuel in eastern Canada.* Agronomy Journal, 1999. **91**(1999): p. 696-701.
99. Mohan, J.D., McCarthy K.,, *Ethanol production from energy crops and waste for use as transport fule in Ireland.* Applied Energy, 2005. **82**(2): p. 148-166.
100. Chen, W.H., Peng, J., Bi, X.T.,, *A state-of-the-art review of biomass torrefaction,densification and applications.* Renewable and Sustainable Energy Reviews, 2015. **44**(2015): p. 847–866.
101. Singh, Y.D., Mahanta, P., Bora, U.,, *Comprehensive characterization of lignocellulosic biomass through proximate, ultimate and compositional analysis for bioenergy production.* Renewable Energy, 2017. **103**(2017): p. 490 - 500.
102. Klass, D.L., *Biomass for Renewable Energy, Fuels, and Chemicals*. 1998, San Diego, California: Academic Press.
103. Tumuluru, J.S., Sokhansanj, S., Hess, J.R., Wright, C., Boardman, R.D.,, *A Review on biomass torrefaction process and product properties for energy applications.* Industrial Biotechnology, 2011.
104. Diebold, J.P., Bridgwater, A. V.,, *Overview of Fast Pyrolysis of Biomass for the Production of Liquid Fuels*, in *Developments in Thermochemical Biomass Conversion*, A.V. Bridgwater, Boocock, D. G. B., Editor. 1997, Springer Netherlands: Dordrecht. p. 5-23.
105. Jiang, G., D.J. Nowakowski, and A.V. Bridgwater, *A systematic study of the kinetics of lignin pyrolysis.* Thermochimica Acta, 2010. **498**(2010): p. 61–66.
106. Chen, W.H., Cheng, W.Y., Lu, K.M., Huang, Y.P.,, *An evaluation on improvement of pulverized biomass property for solid fuel through torrefaction.* Applied Energy, 2011. **88**(2011): p. 3636-44.
107. Mohan, D., Pittman , C.U., Steele, P.H.,, *Pyrolysis of wood/biomass for bio-oil: A critical review.* Energy & Fuels, 2006. **20(3)**: p. 848-889.
108. Koppejan, J. and S. van Loo, *The Handbook of Biomass Combustion and Co-firing*. Edn ed. Built Environment, Environment and Sustainability, ed. S.v.L. Jaap Koppejan. 2008, London: Routledge. 464.

109. Kasman, H., Berg, M.,, *Ash related problems in woodfired boilers and effect of additives*. 2006, Vattenfall, AB: Glasgow.
110. EUBIONET. *Biomass Cofiring—An Efficient Way to Reduce Greenhouse Gas Emissions*. 2003 [cited 2018 September 18]; Available from: ec.europa.eu/energy/renewables/. . ./2003_cofiring_eu_bionet.pdf.
111. Tillman, D.A., *Biomass cofiring: The technology, the experience, the combustion consequences.* Biomass and Bioenergy, 2000. **19**(6): p. 365-384.
112. Bergman, P.C., Boersma, A. R., Zwart, R. W. R., Kiel, J. H. A.,, *Torrefaction for biomass co-firing in existing coal-fired power stations (Biocoal)*, in *ECN-C--05-013*. 2005, Energy Research Centre of the Netherlands: Petten.
113. Uemura, Y., Omar,W., Othman,N.A., Yusup,S., Tsutsui,T.,, *Torrefaction of oilpalm EFB in the presence of oxygen.* Fuel, 2013. **103**(2013): p. 156-60.
114. Chen, W.H. and P.C. Kuo, *Torrefaction and co-torrefaction characterization of hemicellulose, cellulose and lignin as well as torrefaction of some basic constituents in biomass.* Energy, 2011. **36**(2): p. 803–811.
115. Cetin, E., Moghtaderi, B., Gupta, R., Wall, T.F.,, *Influence of pyrolysis conditions on the structure and gasification reactivity of biomass chars.* Fuel, 2004. **83**(16): p. 2139 - 2150.
116. Ragland, K.W., Aerts, D. J., Baker, A. J.,, *Properties of Wood for Combustion Analysis.* Bioresource Technology, 1991. **37**(2): p. 161-168.
117. Prins, M.J., Ptasinski, K.J., Jansen, F.J.G.,, *Torrefaction of wood. Part 1. Weight loss kinetics.* Journal of Analytical and Applied Pyrolysis,, 2006. **77**(2006): p. 28-34.
118. Yan, W., Acharjee,T.C., Coronella, C.J., Vasquez,V.R.,, *Thermal Pretreatment of Lignocellulosic Biomass.* Environmental Progress & Sustainable Energy, 2009. **28**(3): p. 435-40.
119. Lynam, J.G., Coronella, C.J., Yan, W., Reza,M.T., Vasquez, V.R.,, *Acetic acid and lithium chloride effects on hydrothermal carbonization of lignocellulosic biomass.* Bioresour Technololgy, 2011. **102**(2011): p. 6192-9.
120. Wang, L., Barta-Rajnai, E., Skreiberg, Ø., Khalil, R., Czegeny, Z., Jakab, E., Barta, Z. and Grønli, M.,, *Effect of torrefaction on physiochemical characteristics and grindability of stem wood, stump and bark.* Applied Energy, 2017.
121. Rousset, P., Macedo,L., Commandré,J.M., Moreira,A.,, *Biomass torrefaction under different oxygen concentrations and its effect on the composition of the solid by-product.* Analytical and Appllied Pyrolysis, 2015. **96**(2012): p. 86-91.
122. Lam, P.S., Sokhansanj,S., Bi,X.T., Lim,C.J., Larsson,S.H.,, *Drying characteristics and equilibrium moisture content of steam-treated Douglas fir (Pseudotsuga menziesii L.) during pelletization.* Bioresource Technololgy, 2012. **116**(2012): p. 396-402.
123. Tooyserkani, Z., Sokhansanj, S., Bi, X., Lim, C.J., Saddler, J., Lau, A., Melin, S., Lam, P.S., Kumar, L., *Effect of steam treatment on pellet strength and the energy input in pelleting of softwood particles.* Transactions of the ASABE, 2012. **55**(6): p. 2265-2272.
124. Deng. J., W., G., Kuang, J., Zhang, Y., Luo, Y.,, *Pretreatment of agricultural residues for co-gasification via torrefaction.* Journal of Analytical and Applied Pyrolysis, 2009. **86**(2): p. 331– 337.
125. Ciolkosz, D. and R. Wallace, *A review of torrefaction for bioenergy feedstock production.* Biofuels, Bioprod. Biorefinery, 2011. **5**(2011): p. 317 - 329.
126. Ibrahima, R.H., Darvella, L.I., Jonesa, J.M., Williams, A.,, *Physicochemical characterisation of torrefied biomass.* Journal of Analytical and Applied Pyrolysis, 2013. **103**(2013): p. 21–30.
127. Pimchuai, A., A. Dutta, and P. Basu, . *Torrefaction of agriculture residue to enhance combustible properties.* Energy and Fuel, 2010. **24**(2010): p. 4638–4645.

128. Arias, B., Pevida, C.C., Fermoso, J., Plaza, M.G., Rubiera, F., Pis, J.J.,, *Influence of Torrefaction on Grindability and Reactivity of Woody Biomass.* Fue Process Technology, 2008. **89**: p. 169-175.
129. Pimchuai, A., A. Dutta, and P. Basu, *Torrefaction of Agriculture Residue To Enhance Combustible Properties.* Energy Fuels, 2010. **24**(2010): p. 4638 – 4645.
130. Van der Stelt, M., et al., *Biomass upgrading by torrefaction for the production of biofuels: A review.* Biomass and bioenergy, 2011. **35**(9): p. 3748-3762.
131. Nunes, L.J.R., Matias, J.C.D.O., Catalao, J.P.D.S.,, *Torrefaction of Biomass for Energy Applications: From Fundamentals to Industrial Scale*. 2017: Academic Press.
132. Di Blasi, C., *Combustion and gasification rates of lignocellulosic chars.* Progress in energy and combustion science, 2009. **35**(2): p. 121-140.
133. Kumar, G., Panda, A.K., Singh, R.K.,, *Optimization of process for the production of bio-oil from eucalyptus wood.* Journal of Fuel Chemistry and Technology, 2010. **38**(2): p. 162-167.
134. Supramono, D., Devina, Y.M., Tristantini, D.,, *Effect of heating rate of torrefaction of sugarcane bagasse on its physical characteristics.* International Journal of Technology, 2015. **6**(7): p. 1084-1093.
135. Uemura, Y., Saadon, S., Osman, N., Mansor, N., Tanoue, K.I.,, *Torrefaction of oil palm kernel shell in the presence of oxygen and carbon dioxide.* Fuel, 2015. **144**(2015): p. 171–179.
136. Rousset, P., Macedo, L., Commandré, J.M., Moreira, A.,, *Biomass torrefaction under different oxygen concentrations and its effect on the composition of the solid by-product.* Journal of Analytical and Applied Pyrolysis, 2012. **96**: p. 86-91.
137. Lu, K.M., Lee, W.J., Chen, W.H., Liu, S.H., Lin, T.C.,, *Torrefaction and low temperature carbonization of oil palm fiber and eucalyptus in nitrogen and air atmospheres.* Bioresource Technology, 2012. **123**: p. 98-105.
138. Wang, C., Peng, J., Li, H., Bi, X.T., Legros, R., Lim, C.J., Sokhansanj, S.,, *Oxidative torrefaction of biomass residues and densification of torrefied sawdust to pellets.* Bioresource technology, 2013. **127**: p. 318-325.
139. Peng, J.H., BiX,T., Sokhansanj, S., Lim,J.,, *A study of particle size effect on biomass torrefaction and densification.* Energy & Fuel, 2012. **26**(2012): p. 3826–39.
140. Jenkins, B.M., *Physical properties of biomass*. Eds ed. Biomass Handbook, ed. O. Kitani, Hall, C.W.,. 1989, Amsterdam.: Gordon & Breach Science Publishers. 876.
141. Tumuluru J.S., S., S., Christopher,T., Richard,W., Boardman, D., Hess, R.J.,, *Review on Biomass Torrefaction Process and Product properties and Design of Moving Bed Torrefaction System Model Development*, in *An ASABE Meeting Presentation*. 2011: Louisville, Kentucky. p. 1-40.
142. TenWolde, A., McNatt, J.D., Krahn, L.,, *Thermal Properties of Wood and Wood Panel Products for use in Buildings*. 1988, Oak Ridge National Laboratory: Oak Ridge, TN.
143. Hurst, J.E., Harrison, B.K.,, *ESTIMATION OF LIQUID AND SOLID HEAT CAPACITIES USING A MODIFIED KOPP'S RULE.* Chemical Engineering Communications, 1992. **112**(1): p. 21-30.
144. MacDougall, F.H., *Chemical Process Principles. Part One: Material and Energy Balances. By Olaf A. Hougen and Kenneth M. Watson.* The Journal of Physical Chemistry, 1944. **48**(4): p. 232-232.
145. Granados, D.A., Velásquez, H. I., Chejne, F.,, *Energetic and exergetic evaluation of residual biomass in a torrefaction process.* Energy, 2014. **74**: p. 181-189.
146. Chen, W.-H., Huang, Ming-Yueh., Chang, Jo-Shu., Chen, Chun-Yen., Lee, Wen-Jhy.,, *An energy analysis of torrefaction for upgrading microalga residue as a solid fuel.* Bioresource technology, 2015. **185**: p. 285-293.

147. Cengel, Y.A., Cimbala, J.M., Turner, R.H.,, *Fundamentals of thermal-fluid sciences*. 2012.
148. Chen, W.H., Huang, M.Y., Chang, J., Chen, C., Lee, W.J.,, *An energy analysis of torrefaction for upgrading microalga residue as a solid fuel.* Bioresource technology, 2015. **185**: p. 285-293.
149. Yan, W., et al., *Mass and Energy Balances of Wet Torrefaction of Lignocellulosic Biomass.* Energy & Fuels, 2010. **24**(9): p. 4738-4742.
150. Chen, W.H., Kuo, P.C.,, *Torrefaction and co-torrefaction characterization of hemicellulose, cellulose and lignin as well as torrefaction of some basic constituents in biomass.* Energy, 2011. **36**(2): p. 803-811.
151. Gomez, C., Velo, E., Barontini, F., Cozzani,V.,, *Influence of secondary reactions on the heat of pyrolysis of biomass.* Ind Eng Chem Res, 2009. **48**(2009): p. 10222–33.
152. Milosavljevic, I., V. Oja, and E.M. Suuberg, *Thermal effects in cellulose pyrolysis: relationship to char formation processes.* Ind Eng Chem Res, 1996. **35**(653 - 62).
153. Yang, H., Yan, R., Chen, H., Lee, D.H., Zheng, C.,, *Characteristics of hemicellulose, cellulose and lignin pyrolysis.* Fuel, 2007. **86**(2007): p. 1781–1788.
154. Prins, M.J., Ptasinski, K.J., Janssen, F.J.J.G.,, *More efficient biomass gasification via torrefaction.* Energy, 2006. **31**(2006): p. 3458-3470.
155. White, R.H. and M.A. Dietenberger, *Wood Products: Thermal Degradation and Fire A2 - Buschow, K.H. Jürgen*, in *Encyclopedia of Materials: Science and Technology (Second Edition)*, R.W. Cahn, et al., Editors. 2001, Elsevier: Oxford. p. 9712-9716.
156. Kymalainen, M., Rautkari, L., Hill, C.A.,, *Sorption behavior of torrefied wood and charcoal determined by dynamic vapour sorption.* Journal of Material Science, 2015. **50**(2015): p. 7673-7680.
157. Shen, D.K., S. Gu, and A.V. Bridgwater, *Study on the pyrolytic behaviour of xylan-based hemicellulose using TG–FTIR and Py–GC–FTIR.* J. Anal. Appl. Pyrolysis, 2010. **87**(2010): p. 199–206.
158. Werner, K., L. Pommer, and M. Broström, *Thermal decomposition of hemicelluloses.* Journal of Analytical and Applied Pyrolysis, 2014. **110** (2014): p. 130–137.
159. Kilzer, F.J. and A. Broido, *Speculation on theNature of Cellulose Pyrolysis.* Pyrodynamics, 1965. **2**(1965): p. 151-163.
160. Mohan, D., C.U. Pittman, and P.H. Steele, *Pyrolysis of Wood/Biomass for Bio-oil: A Critical Review.* Energy & Fuels, 2006. **20**(2006): p. 848-889.
161. Repellin, V., et al., *Modelling anhydrous weight loss of wood chips during torrefaction in a pilot kiln.* Biomass Bioenergy, 2010. **34**(2010): p. 602-609.
162. Di Blasi, C. and M. Lanzetta, *Intrinsic kinetics of isothermal xylan degradation in inert atmosphere.* Journal of Analytical and Applied Pyroiysis, 1997. **40-41**(1997): p. 287-303.
163. Bach, Q., et al., *Torrefaction Kinetics of Norwegian Biomass Fuels.* The Italian Association of Chemical Engineering, 2014. **37**(2014): p. 49-54.
164. Branca, C. and C. Di Blasi, *Kinetics of the isothermal degradation of wood in the temperature range 528–708 K.* Journal of Analytical and Applied Pyrolysis, 2003. **67**(2003): p. 207–219.
165. Rouquerol, J., Rouquerol, F., Llewellyn, P., Maurin, G., Sing, K.,, *Adsorption by powders and porous solids: principles, methodology and applications*. 2nd Edition ed. 2013: Academic Press.
166. Ruthven, D.G., *Principles of Adsorption and Adsorption Processes*. 1984, Canada: John Wiley & Sons, Inc. 433.
167. Atoms In Motion, L. *Atoms In Motion - Chapter 5 - Molecular Dynamics (MD) - A Few Notes on the Atomistic Simulations*. 2018 [cited 2018 January 16]; Available from: http://atomsinmotion.com/book/chapter5/md.

168. Brunauer, S., *The Adsorption Of Gases And Vapors* Vol. I. 1945, London: Oxford University Press. 528.
169. Hutzler, N. *Gas adsorption applications*. [Web page] 2008 27 November 2011 [cited 2017 01/03]; Available from: http://soft-matter.seas.harvard.edu/index.php/Gas_adsorption_applications.
170. Brunauer, S., Emmett, P.H., Teller, E.,, *Adsorption of Gases in Multimolecular Layers.* Journal of the American Chemical Society, 1938. **60**(2): p. 309-319.
171. Brunauer, S., *The Adsorption of Gases and Vapors*. Physical Adsorption. Vol. 1. 1943, London: Oxford University Press.
172. Toth, M., Lobo, C., Friedli, V., Szkudlarek, A., Utke, I.,, *Continuum models of focused electron beam induced processing.* Beilstein journal of nanotechnology, 2015. **6**(1): p. 1518-1540.
173. Atkins, P., de Paula, J.,, *Physical Chemistry*. 10th ed. 2014, London: Oxford University Press.
174. Atkins, P.W., *Physical Chemistry*. 1994, Oxford: Oxford University Press.
175. Nuhnen, A., Janiak, C.,, *A practical guide to calculate the isosteric heat/enthalpy of adsorption via adsorption isotherms in metal–organic frameworks, MOFs.* Dalton Transactions, 2020. **49**(30): p. 10295-10307.
176. Gregg, S.J., K.S. Sing, and H. Salzberg, *Adsorption Surface Area and Porosity.* Journal of The Electrochemical Society, 1967. **114**(11): p. 279.
177. Do Duong D., *Adsorption Analysis: Equilibria & Kinetics.* Series on Chemical Engineering, 1998. **2**: p. 1-913.
178. Sing, K.S.U., Everett, D.H., Haul, R.A.W., Moscou, L., Pierotti, R.A., Rouquerol, J., Siemieniewska, T.,, *Reporting physisorption data for gas/solid systems — with special reference to the determination of surface area and porosity.* Pure and Applied Chemistry, 1985. **57**(4): p. 603-619.
179. Cheremisinoff, P.N., Ellerbusch, F.,, *Carbon Adsorption Handbook*. (eds) ed. 1978: Ann Arbor, Science Publishers Ins.
180. Rouquerol, J., Avnir, D., fairbridge, C.W., Everett,D.H., Haynes, J.H., Pernicone, N., Ramsay, J.D.F., Sing, K.S.W., Unger, K.K.,, *RECOMMENDATIONS FOR THE CHARACTERIZATION OF POROUS SOLIDS* Pure & Appl. Cher, 1994. **66**(8): p. 1739 - 1758.
181. Everett, D.H., *IUPAC, Manual of Symbol and Terminology for Physico -chemical Quantities and Units, Appendix, Definitions, Terminology and Symbols in Colloid and Surface Chemistry, Part I.* Pure Appl. Chem, 1972. **31**(4): p. 579.
182. Zdravkov, B.D., Čermák, J.J., Šefara, M., Janků, J.,, *Pore classification in the characterization of porous materials: A perspective.* Central European journal of chemistry, 2007. **5**(2): p. 385-395.
183. Thommes, M., Cychosz, K.A.,, *Physical adsorption characterization of nanoporous materials: progress and challenges.* Adsorption Science and Technology, 2014. **20**(2014): p. 233-250.
184. Dubinin, M.M., *Characterisation of Porous Solids*. Ed ed, ed. S.G. Gregg, King, K.S.W., Stoeckli, H.F.,. Vol. 1. 1979, London: Society of Chemical Industries.
185. Dabrowski, A., *Adsorption - from theory to practice.* Advances in Colloid and Interface Science, 2001. **93**(2001): p. 135-224.
186. Polanyi, M., *Section III.—Theories of the adsorption of gases. A general survey and some additional remarks. Introductory paper to section III* Transactions of the Faraday Society, 1932. **28**(1932): p. 316-333.
187. Thommes, M., Kaneko, K., Neimark, A.V., Olivier, J.P., Rodriguez-Reinoso, F., Rouquerol, J., Sing, K.S.W.,, *Physisorption of gases, with special reference to the*

evaluation of surface area and pore size distribution (IUPAC Technical Report). Pure Appl. Chem, 2015. **87**(9-10): p. 1051-1069.
188. Leddy, N., *Surface Area and Porosity*. 2012. p. 1-28.
189. Halsey, G., *Physical Adsorption on Non-Uniform Surfaces.* The Journal of Chemical Physics, 1948. **16**(1948): p. 931.
190. Sing, K.S.W., Williams R.T.,, *Physisorption Hysteresis Loops and the Characterization of Nanoporous Materials.* Adsorption Science and Technology 2004. **22**(10): p. 773 - 782.
191. Foster, A.G., *Sorption Hysteresis, Part II - The Role of Cylindrical Meniscus Effect.* Journal of Chemical Society, 1952. **55**(1951): p. 1806 - 1812.
192. Mohave, F. *Why the adsorption desorption branches of mesoporous materials overlap each other below P/P0=0.3?* 2015; Available from: https://www.researchgate.net/post/why_the_adsorption_desorption_branches_of_mesoporous_materials_overlap_each_other_below_P_P003/5627ad1c6225ffa4288b45b7/citation/download.
193. Barrer, R.M., *Zeolites and Clay Minerals*. 1978, London: Academic Press.
194. Gregg, S.J., Sing, K.S.W.,, *Adsorption, Surface Area and Porosity*. Second ed. 1982, London: Academic Press.
195. Duong D. D., *ADSORPTION ANALYSIS: EQUILIBRIA AND KINETICS*. SERIES ON CHEMICAL ENGINEERING, ed. R.T. Yang. Vol. Volume 2. 1998, London: Imperial College Press.
196. Sutherland, J.W., *Porous Carbon Solids*, ed. R.L. Bond. 1967, London: Academic Press.
197. Gregg, S.J., *Sixty Years in the Physical Adsorption of Gases.* Colloids and Surfaces, 1986. **21**(1986): p. 109-124.
198. Drain, L.E. and J.A. Morrison, *Thermodynamic properties of nitrogen and oxygen adsorbed on rutile.* Transactions of the Faraday Society, 1953. **49**(1953): p. 654-673.
199. Rouquerol, J., Llewellyn, P., Rouquerol, F.,, *Is the BET equation applicable to microporous adsorbents.* Stud. Surf. Sci. Catal, 2007. **160**(07): p. 49-56.
200. Lippens, B.C., de Boer, J. H.,, *Studies on pore systems in catalysts: V. The t method.* Journal of Catalysis, 1965. **4**(3): p. 319-323.
201. Webb, P.A., Orr, C.,, *Analytical methods in fine particle technology*. 1997: Micromeritics Instrument Corp.
202. D-6556-01, A.-. *Standard Test Method for Carbon Black-Total and External Surface Area by Nitrogen Adsorption.*
203. Hutson, N.D., Yang, R.T.,, *Theoretical Basis for the Dubinin-Radushkevitch (D-R) Adsorption Isotherm Equation.* Adsorption 1997. **3**(3): p. 189-195.
204. Polanyi, M., *The Potential Theory of Adsorption.* Science, 1963. **141**(3585): p. 1010 - 1013.
205. Hutson, N.D., Yang, R.T.,, *Theoretical basis for the Dubinin-Radushkevitch (D-R) adsorption isotherm equation.* Adsorption, 1997. **3**(3): p. 189–195.
206. Robinson, J.W., Frame, E.M.S, Frame, G.M, Skelly Frame, E.M, Frame, Ii G.M.,, *Undergraduate Instrumental Analysis*. 6th Edition ed. 2005.
207. Marsh, H., *Adsorption methods to study microporosity in coals and carbon - a critique.* Carbon, 1987. **25**(1): p. 49-58.
208. Fletcher, A.J., Thomas, K.M.,, *Compensation effect for the kinetics of adsorption/desorption of gases/vapors on microporous carbon materials.* Langmuir, 2000. **16**(15): p. 6253-6266.
209. Barrett, E.P., L.G. Joyner, and P.P. Halenda, *The Determination of Pore Volume and Area Distributions in Porous Substances. I. Computations from Nitrogen Isotherms.* American Chemical Society, 1951. **73**(1): p. 373–380.

210. Qiu, H., Lv, L., Pan, B., Zhang, Q., Zhang, W., Zhang, Q.,, *Critical review in adsorption kinetic models.* Journal of Zhejiang University-Science A, 2009. **10**(5): p. 716-724.
211. McBain, J.W., *Theories of occlusion and the sorption of iodine by carbon.* Transactions of Faraday Society, 1919. **14**: p. 202-212.
212. Suresh, S., Sundaramoorthy, S.,, *Green Chemical Engineering: An introduction to catalysis, kinetics, and chemical processes*. 2014: CRC Press.
213. Meng, F.W., *Study on a mathematical model in predicting breakthrough curves of fixed-bed adsorption onto resin adsorbent*. 2005, MS Thesis, Nanjing University, China.
214. Xiao, J., Wei, J.,, *Diffusion mechanism of hydrocarbons in zeolites—I. Theory.* Chemical Engineering Science, 1992. **47**(5): p. 1123-1141.
215. Jakes, J.E., Hunt, C.G., Zelinka, S.L., Ciesielski, P.N., Plaza, N.Z.,, *Effects of Moisture on Diffusion in Unmodified Wood Cell Walls: A Phenomenological Polymer Science Approach.* Forests, 2019. **10**(12): p. 1084.
216. De Kee, D., Liu, Q., Hinestroza, J.,, *Viscoelastic (non-Fickian) diffusion.* The Canadian Journal of Chemical Engineering, 2005. **83**(6): p. 913-929.
217. Crank, J., *The mathematics of diffusion*. 1975, Oxford University Press, New York. p. 414
218. Fu, T.Z., Durning, C.J.,, *Numerical simulation of Case II transport.* AIChE journal, 1993. **39**(6): p. 1030-1044.
219. Park, G.S., and Crank, J.,, *Diffusion in polymers*. 1968, London and NY: Academic Press.
220. Frisch, H.L., *Isothermal diffusion in systems with glasslike transitions.* The Journal of Chemical Physics, 1964. **41**(12): p. 3679-3683.
221. Zeng, Q., Xu, S.,, *A two-parameter stretched exponential function for dynamic water vapor sorption of cement-based porous materials.* Materials and Structures, 2017. **50**(2): p. 128.
222. Fletcher, A.J., Uygur, Y., Thomas, K.M.,, *Role of surface functional groups in the adsorption kinetics of water vapor on microporous activated carbons.* The Journal of Physical Chemistry C, 2007. **111**(23): p. 8349-8359.
223. Bagley, E., Long, F.A.,, *Two-stage sorption and desorption of organic vapors in cellulose acetate1, 2.* Journal of the American Chemical Society, 1955. **77**(8): p. 2172-2178.
224. Wilczak, A., Keinath, T.M.,, *Kinetics of sorption and desorption of copper (II) and lead (II) on activated carbon.* Water Environment Research, 1993. **65**(3): p. 238-244.
225. Ottaway, M., *Use of thermogravimetry for proximate analysis of coals and cokes.* Fuel, 1982. **61**(1982): p. 713-716.
226. Thanapal, S.S., Chen, W., Annamalai, K., Carlin, N., Ansley, R.J., Ranjan, D.,, *Carbon Dioxide Torrefaction of Woody Biomass.* Energy & Fuels, 2014. **28**: p. 1147-1157.
227. Saadon, S., Uemura, Y., Mansor, N.,, *Torrefaction in the presence of oxygen and carbon dioxide: the effect on yield of oil palm kernel shell.* Procedia Chemistry, 2014. **9**: p. 194-201.
228. Ibrahim, R.H.H., Darvell, L.I., Jones, J.M., Williams, A.,, *Physicochemical characterisation of torrefied biomass.* Journal of Analytical and Applied Pyrolysis, 2013. **103**: p. 21-30.
229. Matali, S., et al., *Lignocellulosic Biomass solid Fuel Properties Enhancement via Torrefaction.* Procedia Engineering, 2016. **148**(2016): p. 671-678.
230. Nam, H. and S. Capareda, *Experimental investigation of torrefaction of two agricultural wastes of different composition using RSM (response surface methodology).* Energy, 2015. **91**(2015): p. 507–516.

231. Cardona, S., Gallego, L.J., Valencia, V., Martínez, E., Rios, L.A.,, *Torrefaction of eucalyptus-tree residues: A new method for energy and mass balances of the process with the best torrefaction conditions.* Sustainable Energy Technologies and Assessments, 2019. **31**: p. 17-24.
232. British Standards Institution., *BS EN 15104:2011- Solid biofuels. Determination of total content of carbon, hydrogen and nitrogen. Instrumental methods*. 2011.
233. Sheng, C., Azevedo, J.L.T.,, *Estimating the higher heating value of biomass fuels from basic analysis data.* Biomass and Bioenergy, 2005. **28**(2005): p. 499-507.
234. Jones, J.M., Nawaz, M., Darvell, L.I., Ross, A.B., Pourkashanian, M., Yang, R.T., Williams, A.,, *Towards biomass classification for energy applications.* Science in thermal and chemical biomass conversion, 2006. **1**: p. 331-339.
235. Friedl, A., Padouvas, E., Rotter, H., Varmuza, K.,, *Prediction of heating values of biomass fuel from elemental composition.* Analytica Chimica Acta, 2005. **544**(1-2): p. 191-198.
236. Coates, J., *Interpretation of infrared spectra, a practical approach.* Encyclopedia of analytical chemistry: applications, theory and instrumentation, 2006.
237. Dutta, A., *Chapter 4 - Fourier Transform Infrared Spectroscopy*, in *Spectroscopic Methods for Nanomaterials Characterization*, S. Thomas, Thomas, R., Zachariah, A.K., Mishra, R.K.,, Editor. 2017, Elsevier. p. 73-93.
238. Van Soest, P., Robertson, J.B., Lewis, B.A.,, *Methods for dietary fiber, neutral detergent fiber, and nonstarch polysaccharides in relation to animal nutrition.* Journal of dairy science, 1991. **74**(10): p. 3583-3597.
239. Van Soest, P.J., Robertson, J.B., Lewis,B.A.,, *Methods for dietary fiber, neutral detergent fiber and non-starch polysaccharides in relation to animal nutrition.* Journal of Dairy Science, 1991. **1991**(3583 - 3597).
240. García, R., Pizarro, C., Lavín, A.G., Bueno, J.L.,, *Biomass proximate analysis using thermogravimetry.* Bioresource technology, 2013. **139**: p. 1-4.
241. Eseltine, D., Thanapal, S.S., Annamalai, K., Ranjan, D.,, *Torrefaction of woody biomass (Juniper and Mesquite) using inert and non-inert gases.* Fuel, 2013. **113**(2013): p. 379–388.
242. Barta-Rajnai, E., Jakab, E., Sebestyén, Z., May, Z., Barta, Z., Wang, L., Skreiberg, Ø., Grønli, M., Bozi, J., Czégény, Z.,, *Comprehensive compositional study of torrefied wood and herbaceous materials by chemical analysis and thermoanalytical methods.* Energy & Fuels, 2016. **30**(10): p. 8019-8030.
243. Hansson, K.M., Åmand, L.E., Habermann, A., Winter, F.,, *Pyrolysis of poly-l-leucine under combustion-like conditions ☆.* Fuel, 2003. **82**(6): p. 653-660.
244. Ma, Z., Zhang, Y., Li, C., Yang, Y., Zhang, W., Zhao, C., Wang, S.,, *N-doping of biomass by ammonia (nh3) torrefaction pretreatment for the production of renewable n-containing chemicals by fast pyrolysis.* Bioresource technology, 2019. **292**: p. 122034.
245. Jones, J.M., Bridgeman, T.G., Darvell, L.I., Gudka, B., Saddawi, A., Williams, A.,, *Combustion properties of torrefied willow compared with bituminous coals.* Fuel processing technology, 2012. **101**: p. 1-9.
246. Di Nola, G., De Jong, W., Spliethoff, H.,, *TG-FTIR characterization of coal and biomass single fuels and blends under slow heating rate conditions: Partitioning of the fuel-bound nitrogen.* Fuel Processing Technology, 2010. **91**(1): p. 103-115.
247. Kongkeaw, N., Patumsawad, S.,, *Thermal Upgrading of Biomass as a Fuel by Torrefaction*, in *2nd International Conference on Environmental Engineering and Applications*. 2011, IACSIT Press,: Singapore.
248. Li, M.F., Chen, C.Z., Li, X., Shen, Y., Bian, J., Sun, R.C.,, *Torrefaction of bamboo under nitrogen atmosphere: Influence of temperature and time on the structure and properties of the solid product.* Fuel, 2015. **161**: p. 193-196.

249. Li, J.B., A., Yang, W., Blasiak, W.,, *Co-firing based on biomass torrefaction in a pulverized coal boiler with aim of 100% fuel switching.* Applied Energy, 2012. **99**: p. 344-354.
250. Diaz, L.F., Golueke, C.G.,, *Residues and wastes*, in *Biomass Conversion Processes for Energy and Fuels*. 1981, Springer. p. 3-24.
251. Liu, Z., Quek, A., Hoekman, S.K., Balasubramanian, R.,, *Production of solid biochar fuel from waste biomass by hydrothermal carbonization.* Fuel, 2013. **103**(2013): p. 943 - 949.
252. Felfli, F.F., Luengo,C.A., Suarez,J.A., Beaton,P.A.,, *Wood briquette torrefaction.* Energy Sustainable Development, 2005. **9**(3): p. 19-22.
253. Demirbas, A., *Relationships between lignin contents and heating values of biomass.* Energy conversion and management, 2001. **42**(2): p. 183-188.
254. Ma, X., Wang, X., Song, C.,, *Molecular basket" sorbents for separation of CO2 and H2S from various gas streams.* Journal of the American Chemical Society, 2009. **131**(16): p. 5777-5783.
255. Lua, A.C., Yang, T.,, *Characteristics of activated carbon prepared from pistachio-nut shell by zinc chloride activation under nitrogen and vacuum conditions.* Journal of colloid and interface science, 2005. **290**(2): p. 505-513.
256. Creamer, A.E., Gao, B., Zhang, M.,, *Carbon dioxide capture using biochar produced from sugarcane bagasse and hickory wood.* Chemical Engineering Journal, 2014. **249**(2014): p. 174-179.
257. Phanphanich, M., Mani, S.,, *Impact of torrefaction on the grindability and fuel characteristics of forest biomass.* Bioresource Technology, 2010. **102**(2011): p. 1246 - 1253.
258. Pastorova, I., Botto, R.E., Arisz, P.W., Boon, J.J.,, *Cellulose char structure: a combined analytical Py-GC-MS, FTIR, and NMR study.* Carbohydrate research, 1994. **262**(1): p. 27-47.
259. Gaur, S., Reed, T.B.,, *Thermal data for natural and synthetic fuels*. 2020: CRC press.
260. Rousset, P., Lapierre, C., Pollet, B., Quirino, W., Perre, P.,, *Effect of severe thermal treatment on spruce and beech wood lignins.* Annals of Forest Science, 2009. **66**(1): p. 1.
261. Shoulaifar, T.K., *Chemical changes in biomass during torrefaction*, in *Chemical Engineering*. 2016, Åbo Akademi University: Åbo, Finland p. 113.
262. Jin, Z., Katsumata, K.S., Lam, T.B.T., Iiyama, K.,, *Covalent linkages between cellulose and lignin in cell walls of coniferous and nonconiferous woods.* Biopolymers: Original Research on Biomolecules, 2006. **83**(2): p. 103-110.
263. Rowell, R.M., *Handbook of wood chemistry and wood composites*. 2012: CRC press.
264. Çengel, Y.A., *Introduction to Thermodynamics and Heat Transfer*. 2nd ed. ed. 2008, New York, NY: McGraw-Hill.
265. Ohliger, A., Förster, M., Kneer, R.,, *Torrefaction of beechwood: A parametric study including heat of reaction and grindability.* Fuel, 2013. **104**: p. 607-613.
266. Gray, M., Johnson, M.G., Dragila, M.I., Kleber, M.,, *Water uptake in biochars: The roles of porosity and hydrophobicity.* Biomass and Bioenergy, 2014. **61**: p. 196-205.
267. Dortmund Data Bank. *Saturated Liquid Density*. 27/10/2020; Available from: http://ddbonline.ddbst.de/DIPPR105DensityCalculation/DIPPR105CalculationCGI.exe.
268. Dortmund Data Bank. *Saturated Vapor Pressure*. [cited 2020 27/10/2020]; Available from: http://ddbonline.ddbst.com/AntoineCalculation/AntoineCalculationCGI.exe.
269. Angın, D., *Effect of pyrolysis temperature and heating rate on biochar obtained from pyrolysis of safflower seed press cake.* Bioresource technology, 2013. **128**: p. 593-597.

270. Gray, M.R., Corcoran, W.H., Gavalas, G.R.,, *Pyrolysis of a wood-derived material. Effects of moisture and ash content.* Industrial & Engineering Chemistry Process Design and Development, 1985. **24**(3): p. 646-651.
271. Gregg, S.J., Sing, K.S.W., Salzberg, H.W.,, *Adsorption surface area and porosity.* Journal of The electrochemical society, 1967. **114**(11): p. 279C.
272. Jeromenok, J., Weber, J.,, *Restricted access: on the nature of adsorption/desorption hysteresis in amorphous, microporous polymeric materials.* Langmuir, 2013. **29**(42): p. 12982-12989.
273. Furuta, Y., Aizawa, H., Yano, H., Norimoto, M.,, *Thermal-softening properties of water-swollen wood. IV. The effects of chemical cconstituents of the cell wall on the thermal-softening properties of wood.* Mokuzai gakkaishi, 1997. **43**(9): p. 725-730.
274. Kercher, A.K., Nagle, D.C.,, *Microstructural evolution during charcoal carbonization by X-ray diffraction analysis.* Carbon, 2003. **41**(1): p. 15-27.
275. Haas, T.J., Nimlos, M.R., Donohoe, B.S.,, *Real-time and post-reaction microscopic structural analysis of biomass undergoing pyrolysis.* Energy & Fuels, 2009. **23**(7): p. 3810-3817.
276. Keiluweit, M., Nico, P.S., Johnson, M.G., Kleber, M.,, *Dynamic molecular structure of plant biomass-derived black carbon (biochar).* Environmental science & technology, 2010. **44**(4): p. 1247-1253.
277. Yuan, S., Chen, X., Li, Jun., Wang, F.C, *CO2 gasification kinetics of biomass char derived from high-temperature rapid pyrolysis.* Energy & fuels, 2011. **25**(5): p. 2314-2321.
278. Della Rocca, P.A., Cerrella, E.G., Bonelli, P.R., Cukierman, A.L.,, *Pyrolysis of hardwoods residues: on kinetics and chars characterization.* Biomass and Bioenergy, 1999. **16**(1): p. 79-88.
279. Zhang, Z., Zhou, J., Xing, W., Xue, Q., Yan, Z., Zhuo, S., Qiao, S.Z.,, *Critical role of small micropores in high CO2 uptake.* Physical chemistry chemical physics, 2013. **15**(7): p. 2523-2529.
280. Parshetti, G.K., Chowdhury,S., Balasubramanian, R.,, *Biomass derived low-cost microporous adsorbents for efficient CO2 capture.* Fuel, 2015. **148**(2015): p. 246-254.
281. Xing, W., Liu, C., Zhou, Z., Zhang, L., Zhou, J., Zhuo, S., Yan, Z., Gao, H., Wang, G., Qiao, S.Z.,, *Superior CO2 uptake of N-doped activated carbon through hydrogen-bonding interaction.* Energy & Environmental Science, 2012. **5**(6): p. 7323-7327.
282. Bailey, A., Cadenhead, D.A., Davies, D.H., Everett, D.H., Miles, A.J.,, *Low pressure hysteresis in the adsorption of organic vapours by porous carbons.* Transactions of the Faraday Society, 1971. **67**: p. 231-243.
283. Watabe, T., Yogo, K.,, *Isotherms and isosteric heats of adsorption for CO2 in amine-functionalized mesoporous silicas.* Separation and Purification Technology, 2013. **120**: p. 20-23.
284. Madani, S.H., Rodríguez-Reinoso, F., Biggs, M.J., Pendleton, P.,, *Isosteric heats of adsorption of gases and vapors on a microporous carbonaceous material.* Journal of Chemical & Engineering Data, 2018. **63**(8): p. 3107-3116.
285. Roberts, J.K., *Some effects of dipole interactions on heats of adsorption.* Transactions of the Faraday Society, 1938. **34**: p. 1342-1346.
286. Palmer, W.G., *Adsorption on measured surfaces of vitreous silica—II.* Proceedings of the Royal Society of London. Series A-Mathematical and Physical Sciences, 1937. **160**(901): p. 254-267.
287. Zhao, X., Villar-R.S., Fletcher, A.J., Thomas, K.M.,, *Kinetic isotope effect for H2 and D2 quantum molecular sieving in adsorption/desorption on porous carbon materials.* The Journal of Physical Chemistry B, 2006. **110**(20): p. 9947-9955.

288. Grande, C.A., *Advances in pressure swing adsorption for gas separation.* ISRN Chemical Engineering, 2012. **2012**.